

Advances in Meteorology

# Weather and Climate in Monsoon Regions

Guest Editors: Lin Wang, June-Yi Lee, Haishan Chen, Fred Kucharski, Xiaolong Jia, Xiaojing Jia, and Jieshun Zhu





---

# **Weather and Climate in Monsoon Regions**

Advances in Meteorology

---

## **Weather and Climate in Monsoon Regions**

Guest Editors: Lin Wang, June-Yi Lee, Haishan Chen,  
Fred Kucharski, Xiaolong Jia, Xiaojing Jia, and Jieshun Zhu



---

Copyright © 2015 Hindawi Publishing Corporation. All rights reserved.

This is a special issue published in “Advances in Meteorology.” All articles are open access articles distributed under the Creative Commons Attribution License, which permits unrestricted use, distribution, and reproduction in any medium, provided the original work is properly cited.

## Editorial Board

José Antonio Adame, Spain  
Cesar Azorin-Molina, Spain  
Guillermo Baigorria, USA  
Marina Baldi, Italy  
Abderrahim Bentamy, France  
Massimo A. Bollasina, UK  
Stefania Bonafoni, Italy  
Isabella Bordi, Italy  
Claudio Carbone, Italy  
Dominique Carrer, France  
Charles Chemel, UK  
Annalisa Cherchi, Italy  
James Cleverly, Australia  
Jill S. M. Coleman, USA  
Gabriele Curci, Italy  
Mladjen Ćurić, Serbia  
Klaus Dethloff, Germany  
Panuganti C. S. Devara, India  
Julio Diaz, Spain  
Arona Diedhiou, France  
Stefano Dietrich, Italy  
Eugenio Domnguez Vilches, Spain  
Antonio Donateo, Italy  
Igor Esau, Norway  
Stefano Federico, Italy  
Enrico Ferrero, Italy  
Rossella Ferretti, Italy  
Roberto Fraile, Spain  
Charmaine Franklin, Australia  
Jan Friesen, Germany  
M. fhngeles Garca, Spain

Herminia Garca Mozo, Spain  
Eduardo Garca-Ortega, Spain  
Luis Gimeno, Spain  
Jorge E. Gonzalez, USA  
Ismail Gultepe, Canada  
Rafiq Hamdi, Belgium  
Adel Hanna, USA  
Hiroyuki Hashiguchi, Japan  
Tareq Hussein, Jordan  
Bradley G. Illston, USA  
Ivar S A Isaksen, Norway  
Yasunobu Iwasaka, Japan  
Pedro Jiménez-Guerrero, Spain  
Kuruvilla John, USA  
Charles Jones, USA  
Hann-Ming H. Juang, USA  
George Kallos, Greece  
Harry D. Kambezidis, Greece  
Nir Y. Krakauer, USA  
Simon O. Krichak, Israel  
Hisayuki Kubota, Japan  
Haim Kutiel, Israel  
Richard Leaitch, Canada  
Monique Leclerc, USA  
Ilan Levy, Israel  
Gwo-Fong Lin, Taiwan  
Anthony R. Lupo, USA  
Paolo Madonia, Italy  
Andreas Matzarakis, Germany  
Samantha Melani, Italy  
Nicholas Meskhidze, USA

Christophe Messenger, France  
Mario Marcello Miglietta, Italy  
Takashi Mochizuki, Japan  
Andrea Montani, Italy  
Goro Mouri, Japan  
Brian R. Nelson, USA  
Efthymios I. Nikolopoulos, USA  
Sandip Pal, USA  
Giulia Panegrossi, Italy  
Giulia Pavese, Italy  
Kyaw T. Paw, USA  
Olivier P. Prat, USA  
Sara C. Pryor, USA  
Philippe Ricaud, France  
Tomeu Rigo, Spain  
Filomena Romano, Italy  
Jose Antonio Ruiz-Arias, Spain  
Haydee Salmun, USA  
Pedro Salvador, Spain  
Arturo Sanchez-Lorenzo, Spain  
Andres Schmidt, USA  
Shraddhanand Shukla, USA  
Fiona Smith, UK  
Francisco J. Tapiador, Spain  
Yoshihiro Tomikawa, Japan  
Tomoo Ushio, Japan  
Rogier Van Der Velde, The Netherlands  
S. Vicente-Serrano, Spain  
Francesco Viola, Italy  
Alastair Williams, Australia  
Olga Zolina, France

# Contents

**Weather and Climate in Monsoon Regions**, Lin Wang, June-Yi Lee, Haishan Chen, Fred Kucharski, Xiaolong Jia, Xiaojing Jia, and Jieshun Zhu  
Volume 2015, Article ID 143731, 1 page

**Spatiotemporal Variability and Change of the South China Spring Precipitation during 1961-2012**, Hong-Lan Liu, Qiang Zhang, Jun-Qin Guo, Jun-Guo Zhang, and Sheng Wang  
Volume 2015, Article ID 419735, 9 pages

**Recent Trends in Temperature and Precipitation in the Langat River Basin, Malaysia**, Mahdi Amirabadizadeh, Yuk Feng Huang, and Teang Shui Lee  
Volume 2015, Article ID 579437, 16 pages

**Dominant Large-Scale Atmospheric Circulation Systems for the Extreme Precipitation over the Western Sichuan Basin in Summer 2013**, Yamin Hu, Panmao Zhai, Lihong Liu, Yang Chen, and Yanju Liu  
Volume 2015, Article ID 690363, 10 pages

**Fuzzy Clustering-Based Ensemble Approach to Predicting Indian Monsoon**, Moumita Saha, Pabitra Mitra, and Arun Chakraborty  
Volume 2015, Article ID 329835, 12 pages

**Analysis on the Extreme Heat Wave over China around Yangtze River Region in the Summer of 2013 and Its Main Contributing Factors**, Jin Li, Ting Ding, Xiaolong Jia, and Xianchan Zhao  
Volume 2015, Article ID 706713, 15 pages

**Spatiotemporal Characteristics of Evapotranspiration Paradox and Impact Factors in China in the Period of 1960-2013**, Huiping Huang, Yuping Han, Mingming Cao, Jinxi Song, Heng Xiao, and Weili Cheng  
Volume 2015, Article ID 519207, 10 pages

**Impact of Stratospheric Sudden Warming on East Asian Winter Monsoons**, Quanliang Chen, Luyang Xu, and Hongke Cai  
Volume 2015, Article ID 640912, 10 pages

## Editorial

# Weather and Climate in Monsoon Regions

**Lin Wang,<sup>1</sup> June-Yi Lee,<sup>2</sup> Haishan Chen,<sup>3</sup> Fred Kucharski,<sup>4</sup> Xiaolong Jia,<sup>5</sup>  
Xiaojing Jia,<sup>6</sup> and Jieshun Zhu<sup>7</sup>**

<sup>1</sup>*Center for Monsoon System Research, Institute of Atmospheric Physics, Chinese Academy of Sciences and Joint Center for Global Change Studies, Beijing 100190, China*

<sup>2</sup>*Institute of Environmental Studies, Pusan National University, Busan, Republic of Korea*

<sup>3</sup>*School of Atmospheric Sciences, Nanjing University of Information Science and Technology, Nanjing 210044, China*

<sup>4</sup>*Earth System Physics Section, Abdus Salam ICTP, Trieste, Italy*

<sup>5</sup>*National Climate Center, China Meteorological Administration, Beijing 100081, China*

<sup>6</sup>*Department of Earth Sciences, Zhejiang University, Hangzhou 310027, China*

<sup>7</sup>*Climate Prediction Center, NOAA/NWS/NCEP, College Park, MD, USA*

Correspondence should be addressed to Lin Wang; wanglin@mail.iap.ac.cn

Received 27 July 2015; Accepted 27 July 2015

Copyright © 2015 Lin Wang et al. This is an open access article distributed under the Creative Commons Attribution License, which permits unrestricted use, distribution, and reproduction in any medium, provided the original work is properly cited.

Monsoon regions feed about 70 percent of the world's population. The weather and climate variability in these regions often lead to natural hazards such as flooding, droughts, heat waves, and blizzards, which exert strong impacts on both the society and human lives. This is particularly the case over many Asian monsoon regions, where the countries are less developed and the people heavily depend on agriculture. As a result, the monsoon research has traditionally held a very high priority for the international scientific communities of weather and climate. It is an urgent task for the community to gain a deeper understanding of the monsoon variability to meet the rising demand of a better weather forecast and climate prediction.

This special issue consists of seven research papers, all of which focus on the Asian monsoon. Two papers are case studies on the 2013 summer monsoon in China, where both extreme rainfall and heat waves were recorded in the middle and lower reaches of the Yangtze River Valley. One paper discusses the stratospheric and extratropical influences on the East Asian monsoon. The rest of papers discuss the spatiotemporal variability, mechanism, and prediction of the Asian monsoon over China, India, and Malaysia through statistical and diagnostic approaches. Besides the monsoon rainfall, the evaporation that is crucial to understand the

hydrological cycles in monsoon regions and the cold spell that is another important aspect of the monsoon climate are also discussed.

All seven papers in this special issue can be categorized as traditional climate studies. In recent years, an increasing number of scientists from the traditional weather and climate communities are working together and trying to fill the gap of understanding and prediction between the weather and climate. A Subseasonal to Seasonal (S2S) Prediction Project was launched in 2013 under the umbrella of the World Weather Research Program (WWRP), the World Climate Research Program (WCRP), and the Observing System Research and Predictability Experiment (THORPEX), aiming to promote a seamless weather/climate prediction. We sincerely expect that a better and more integrated understanding of weather and climate of monsoon regions could be obtained in the near future.

*Lin Wang  
June-Yi Lee  
Haishan Chen  
Fred Kucharski  
Xiaolong Jia  
Xiaojing Jia  
Jieshun Zhu*

## Research Article

# Spatiotemporal Variability and Change of the South China Spring Precipitation during 1961–2012

Hong-Lan Liu,<sup>1</sup> Qiang Zhang,<sup>2</sup> Jun-Qin Guo,<sup>3</sup> Jun-Guo Zhang,<sup>4</sup> and Sheng Wang<sup>5</sup>

<sup>1</sup>Zhangye Meteorological Bureau, Zhangye 734000, China

<sup>2</sup>Key Laboratory of Arid Climatic Change and Disaster Reduction of Gansu Province, Key Laboratory of Arid Climate Change and Disaster Reduction of China Meteorological Administration, Institute of Arid Meteorology, China Meteorological Administration, Lanzhou 730020, China

<sup>3</sup>Northwest Regional Climate Center, Lanzhou 730020, China

<sup>4</sup>Zhangye Middle School, Zhangye 734000, China

<sup>5</sup>Jinta County Meteorological Bureau, Jinta 735300, China

Correspondence should be addressed to Hong-Lan Liu; [gszylhl@126.com](mailto:gszylhl@126.com)

Received 6 December 2014; Revised 4 March 2015; Accepted 27 April 2015

Academic Editor: June-Yi Lee

Copyright © 2015 Hong-Lan Liu et al. This is an open access article distributed under the Creative Commons Attribution License, which permits unrestricted use, distribution, and reproduction in any medium, provided the original work is properly cited.

We analyze precipitation data from 47 meteorological stations spanning between 1961 and 2012 and NCEP/NCAR reanalysis to understand spatiotemporal variability and change of spring precipitation of South China and their relations to atmospheric circulations. Empirical orthogonal function (EOF) analysis and rotated EOF (REOF) are used to reveal dominant spatial structures of precipitation anomaly and Mann-Kendall testing method to determine the temporal locations of abrupt changes during the analyzed time span. We find that the first spatial mode of the spring precipitation of the South China has a domain uniform structure; the second is dominated by a spatial dipole; and the third contains six variability centers. 1980s was the decade of the largest amount of precipitation while 1960s the decade of the smallest amount of precipitation. The spring precipitation also appeared to have a decreasing trend since 2000. We also find that spring precipitation of the South China has experienced a few abrupt changes: sudden increment at 1964, sudden decrement at 2002, and sudden increment at 1995. In addition to these abrupt changes, the precipitation could also be characterized by variability of multiple temporal scales, with dominant periodicities of 4 years, 8 years, and 14 years. The South China spring precipitation is also closely tied to the atmospheric circulations: when Aleutian Low strengthens, westerly weakens, and the center of the Western Pacific subtropical high shifts southeastward in the early spring; and the South China precipitation tends to be abundant (positive anomaly). In contrast, when Ural ridge strengthens, the southern branch of the East Asian trough weakens and the Western Pacific subtropical high shifts northwestward in the early spring, the South China precipitation tends to be reduced (negative anomaly).

## 1. Introduction

China is one of the most vulnerable countries in the world to natural disasters, with annual loss caused by weather/climate disasters mounts up to 3%–6% of the gross domestic product. The frequent occurrences of draught have been threatening food product and social security and thereby creating tremendous challenge to socioeconomic conditions and environment-ecology [1, 2]. The South China (104°26′–117°20′E, 20°09′–26°24′N) locates in the southeastern edge of the Eurasian continent and has 41 million square kilometers, including Guangdong Province and Guangxi Zhuang

Autonomous Region, spreading over both tropical and subtropical regions surrounded by the South China Sea to the south and the Pacific Ocean to the east. The region is topographically complicated and features diverse stereoscopic climate regimes, especially in the vertical direction. While the region processes abundant climatic resources, it also experiences frequently occurred meteorological disasters [3].

The climate of South China is not only significantly affected by the low latitudes atmospheric circulation but also influenced by the middle to high latitudes atmospheric circulations. Low and high latitude circulation systems interact with each other and lead to diverse weather/climate patterns

in South China. In addition to that, numerous studies have also shown that climate variability and change in China, especially South China, are closely related to the coupled air-sea interactions in low latitudes. In general, the low-level basic flow in South China features three different types: the subtropical westerly, the equatorial westerly, and tropical easterly. Although these three types of basic flow appear in all four seasons, their locations, intensities, and ranges can vary significantly from season to season. Also, these winds are most baroclinic, with alternating easterly and westerly in the vertical. In winter, westerly dominates in upper troposphere and low-level features northeast monsoon. In summer, southwest monsoon prevails in the middle-low troposphere and steady easterly in upper troposphere.

Since 1980s, the region has recorded numerous disastrous extreme climatic events which are believed to tie with the global climate change [4, 5]. It appeared that the South China spring drought occurred with increasing frequency most recently and some of drought events even lasted for a few seasons, for example, the 2003 drought event that influenced most regions of China south to the Yangtze River and continued through the summer and autumn, the 2005 drought in South China that lasted from autumn to spring, and 2010 severe spring drought in South China [6–9], which caused drastic consequences in agricultural, industrial, and civil water usage. Wen et al. [10] performed a quantitative diagnosis for the mechanisms of spring droughts in South China. Gu et al. [11] analyzed the variation and precursor of Guangzhou spring rainfall. Zhou et al. [12] provided April-May persistent drought events in South China and the related general circulation background. Li et al. [13] demonstrated the zonal seesaw-like distribution of spring precipitation over South China and characteristics of atmospheric circulation in anomalous climate years. Li et al. [14] found the characteristics of the atmospheric water vapor and its relationship with rainfall in South China in northern autumn, winter, and spring. Wan et al. [15] discussed temporal variations of the spring persistent rains and SCS subtropical high and their correlations to the circulation and precipitation of the East Asia summer monsoon. Han et al. [16] revealed the interannual variation of spring precipitation and circulation in South China as simulated by a coupled model. Since the spring is the most important season for crop growing, the study of the characteristics of South China spring precipitation and their physical causes bears significant meanings.

Previous studies using statistical analysis have showed that the South China spring droughts were often of large scales, in contrast to the relatively spatiotemporally fragmented character of summer-autumn droughts. In this study, we aim to provide more detailed spatiotemporal characteristics of spring precipitation in South China.

## 2. Data and Methods

The South China in this study refers to the territory of China enclosed by a rectangle from  $104^{\circ}26'$  to  $117^{\circ}20'E$  and from  $20^{\circ}09'$  to  $26^{\circ}24'N$ , as shown in Figure 1. This part of China includes Guangdong Province and Guangxi

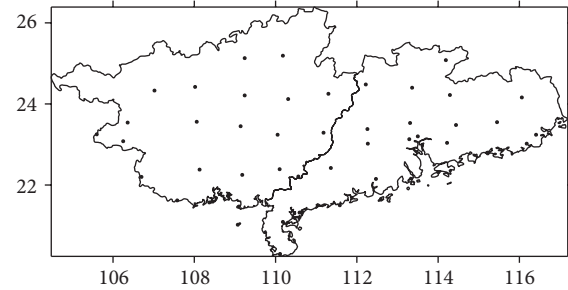


FIGURE 1: Locations of meteorological stations (dots) providing precipitation data.

Zhuang Autonomous Region. The data analyzed include (1) spring (March to May) precipitation (see Figure 2) and (2) NCEP/NCAR reanalysis with a resolution of  $2.5^{\circ} \times 2.5^{\circ}$ .

Precipitation data used in this paper is monthly precipitation data of 730 stations from 1961 to 2012, provided by the National Climate Center (China). The daily NCEP/NCAR reanalysis data during the same period includes wind, water vapor flux, geopotential height field, and vertical velocity field.

We selected all of the stations located in the east of  $104^{\circ}E$  and the south of  $27^{\circ}N$  on behalf of South China. There are 47 stations evenly distributed in the region, which could well represent South China (Figure 1).

The empirical orthogonal function (EOF) analysis and rotated EOF (REOF) [17, 18] are used to determine the basic characteristics of South China spring precipitation as well as their spatiotemporal structures of variability and change. Mann-Kendall testing method [17, 18] is used to determine the temporal locations of abrupt changes of spring precipitation, at an a priori set  $\alpha = 0.05$  significance level. The trend is a fifth order running trend and its statistical significance is also tested using nonparametric Mann-Kendall method. The periodicity information of the spring precipitation is obtained using spectrum analysis.  $t$ -testing [17, 18] is also used to test statistical significance of abrupt changes.

## 3. Characteristics of South China Precipitation

**3.1. Basic Climate Characteristics.** The South China features a wide spread of spring precipitation from 212.1 mm to 808.3 mm, with a mean value 487.8 mm. Spring precipitation consists of 15.3% to 40.2% of its annual total for different regions, with a mean value 28.9%. Figure 2 plots the mean and the standard deviation of precipitations over the whole South China region. As revealed by Figure 2 the eastern part of South China has abundant rainfall in spring while the western part has much less rainfalls. The center of the fewest spring precipitation locates at Weizhou Island ( $109^{\circ}06'E$ ,  $21^{\circ}02'N$ ) of Guangxi Zhuang Autonomous Region, with spring precipitation of only 212.1 mm. The largest spring precipitation occurs in Fuogang ( $113^{\circ}31'E$ ,  $23^{\circ}53'N$ ) of Guangdong Province, with a value over 800 mm. The large ratio (about 4) between the values of maximum and of minimum precipitation indicates the unevenness of the precipitation distribution over South

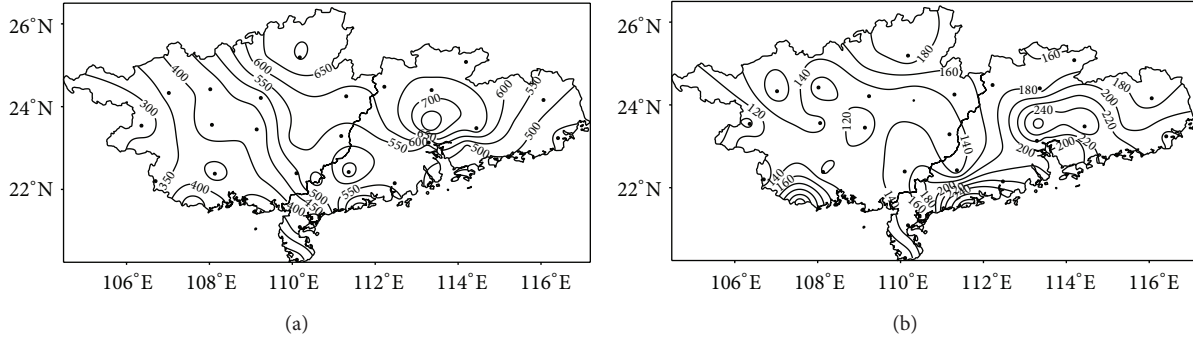


FIGURE 2: Long-term mean spring precipitation (a) and its standard deviation (b) in South China.

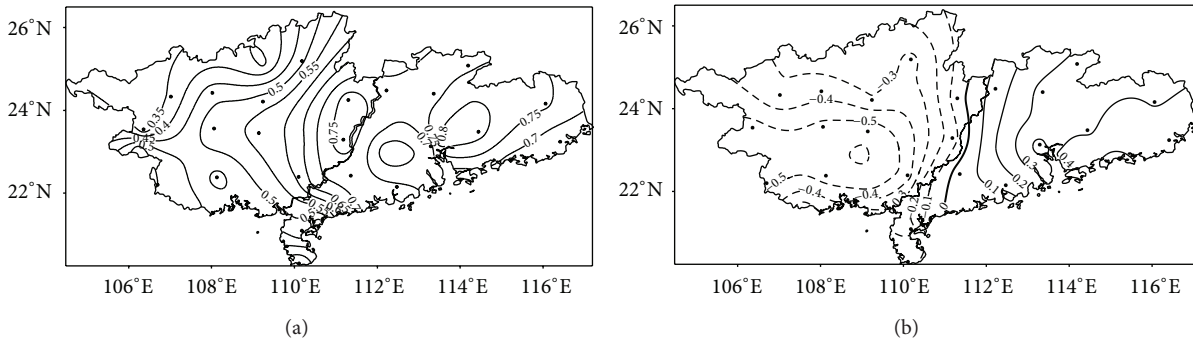


FIGURE 3: The first (a) and the second (b) eigenvectors of spring precipitation in South China.

China. The standard deviation of the precipitation has similar spatial structure of the precipitation itself, with its maximum (349.3 mm) locating at Yangjiang (111°58'E, 21°50'N) of southern Guangdong Province and a minimum (92.3 mm) striped along Napo (105°50'E, 23°25'N) and Baise (106°36'E, 23°54'N) region of western Guangxi Zhuang Autonomous Region. In general, the eastern and southeastern regions of the South China have abundant rainfall; and the remaining parts of South China have much less rainfall. This pattern of the spring precipitation indicates that the spring precipitation in the South China may be significantly influenced by the monsoon southeasterly from the Pacific Ocean.

**3.2. Spatial Structure of Precipitation Anomaly.** Table 1 presents the variance contribution from the first eight eigenvectors (empirical orthogonal functions). The convergence of the sum of eigenvectors for South China precipitation is relatively slow: the accumulated variance contribution from the first two eigenvectors is 52.1%, the first four 63.1%, and the first eight 76.6%. The first two eigenvectors are displayed in Figure 3. The first eigenvector (EOF) has positive values all over the domain, with the maximum value at Zengcheng (113°50'E, 23°20'N) of central Guangdong Province. The result implies that the South China may be considered as one natural climatological regime for the spring precipitation over the South China, with its representative station being Zengcheng (113°50'E, 23°20'N) of Guangdong Province which has a value 0.82. The second eigenvector is dominated by a dipole, with

a north-southward zero line passing the neighborhoods of Hezhou (111°30'E, 24°25'N) of Guangxi and Luoding (111°36'E, 22°42'N) of Guangdong, coincided with the border between Guangxi and Guangdong. To the east of the zero line, the representative station is Wuhua (115°45'E, 23°55'N) of Guangdong Province, with a value of 0.46; and to the west, the representative station is Laibin (109°14'E, 23°45'N) of Guangxi Zhuang Autonomous Region, with a value of -0.58, implying that the precipitation of South China spring precipitation has a component of contrasting changes in the east and west parts of the South China.

To maximize the variance explained by different spatial structures, we rotate the first eight eigenvectors obtained using EOF. The first five rotated EOFs explain 67.2% of variance. The sum of these five rotated EOFs illustrates six distinctive natural climatological regimes: (1) the northern part of the South China which features hilly areas of both Guangdong and Guangxi; (2) the northwestern region of Guangxi; (3) the southwestern region of Guangxi; (4) the central South China (including the central parts of both Guangdong and Guangxi); (5) the southern South China region (including the central regions of both Guangdong and Guangxi); and (6) Leizhou Peninsula region.

**3.3. Interannual and Decadal Variability of the South China Spring Precipitation.** Based on the first time coefficient sequence of EOF and precipitation anomaly percentage of each station, the variation law of was analyzed. By the first time coefficient curve shown in the newly added Figure 4,

TABLE 1: Different EOF variance contributions of spring precipitation in South China.

Number	1	2	3	4	5	6	7	8
Variance contribution (%)	39.0	13.1	5.7	5.3	4.1	3.7	2.9	2.8
Accumulated variance contribution (%)	39.0	52.1	57.8	63.1	67.2	70.9	73.8	76.6

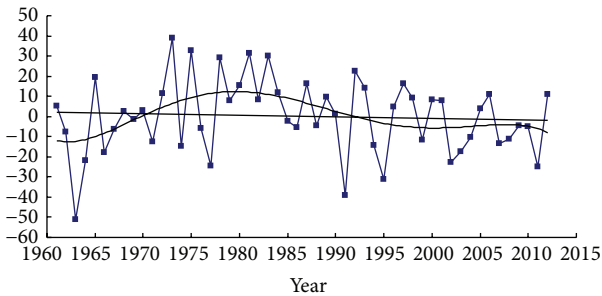


FIGURE 4: Yearly variation of the first time series of precipitation of South China spring precipitation.

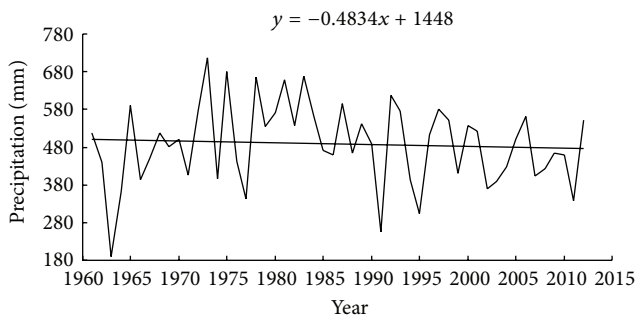


FIGURE 5: The overall variability and changes of spring precipitation in South China.

it could be found that spring precipitation in South China decreased slowly in overall tendency since the 1960s. There are two relatively wetter periods in the 1970s and the 1980s. The precipitation shows a decreasing trend since the late 1980s.

To quantify the variability of South China spring precipitation, we calculate the percentages of positive anomaly and negative anomaly. Over the temporal span of data, 27 years had positive anomaly and 25 years negative anomaly. The interannual variability of spring precipitation is evident, for example, the fluctuation in 1973 reached a maximum value of 716.5 mm while the fluctuation in 1963 is as small as 189.9 mm. The maximum interannual fluctuation is almost four times as large as that of the minimum. From Figure 5, it can be identified that the fluctuating spring precipitation in South China has been slowly decreasing in the last 52 years. Further analysis of the increased percentages of positive or negative anomalies over different decades (with respect to 1981–2010 mean) is presented in Figure 6. In 1960s, the increased percentage of anomaly is positive in northwestern Guangxi and negative elsewhere. The increased positive percentage of spring rainfall anomaly was most evident in Fengshan ( $107^{\circ}02'E$ ,  $24^{\circ}33'N$ ) region of Guangxi, reaching

a value of 21%. In contrast, Shantou ( $116^{\circ}41'E$ ,  $23^{\circ}24'N$ ) of eastern Guangdong has a decreased positive (increased negative) anomaly percentage of  $-35\%$ . In 1970s, except the southeastern coastal region of Guangdong, the whole South China was dominated by positive anomalies. The positive anomaly percentage was most evident in southern coastal Guangxi, with an increased positive anomaly percentage of 50%. In contrast, the southern coastal Guangdong had a negative anomaly percentage of  $-24\%$ . In 1980s, the South China was dominated by positive anomaly percentage except the northwestern region of Guangxi. The largest positive anomaly percentage (31%) appeared in the southeastern coastal area of Guangdong while the largest negative anomaly percentage ( $-5\%$ ) appeared in Liuzhou ( $109^{\circ}24'E$ ,  $24^{\circ}21'N$ ) of Guangxi. In 1990s, the northern part of the South China and Leizhou Peninsula had positive anomaly percentage while the other regions of the South China had negative anomaly percentages. The largest positive percentage anomaly, with a value of 14%, appeared in Zhanjiang ( $110^{\circ}18'E$ ,  $21^{\circ}09'N$ ) of Leizhou Peninsula while the largest negative anomaly percentage appeared in Huilai ( $116^{\circ}18'E$ ,  $23^{\circ}02'N$ ) of coastal southeastern Guangdong and Baise ( $106^{\circ}36'E$ ,  $23^{\circ}54'N$ ) of western Guangxi. In 2000s, the positive anomaly percentage was small and only appeared at Guangzhou ( $113^{\circ}29'E$ ,  $23^{\circ}13'N$ ), Dianbai ( $110^{\circ}59'E$ ,  $21^{\circ}32'N$ ) of Guangdong, and Baise ( $106^{\circ}36'E$ ,  $23^{\circ}54'N$ ) of Guangxi, with its largest value only reaching 8% at Baise ( $106^{\circ}36'E$ ,  $23^{\circ}54'N$ ). Elsewhere, negative anomaly percentage dominated, with the largest value ( $-19\%$ ) appeared in eastern Guangdong.

In summary, 1980s was the decade of largest amount of spring precipitation in the last half century in the South China. 1960s was dominated by above normal spring precipitation in northwestern part of South China and below normal spring precipitation elsewhere. 1970s featured above normal spring precipitation over most of the South China. 1990s had above normal spring precipitation in northern part of South China and below normal in the southern part. In 2000s, spring precipitation was generally below average.

**3.4. Multiscale Analysis of the South China Spring Precipitation.** The linear fitting to spring precipitation anomaly in the South China shows a slow steady decrease of spring precipitation, with a slope of  $-0.48$ . From Figure 5, it is identified that the spring precipitation of South China was above normal during 1968–1992 and was below normal during 1961–1967 and 1993–2000. The below normal spring precipitation in the first decade of 21st century indicates that the amount of South China spring precipitation had reduced during the first decade of the 21st century.

To better quantify the multiscale nature of the South China spring precipitation, wavelet analysis [17, 18] of spring

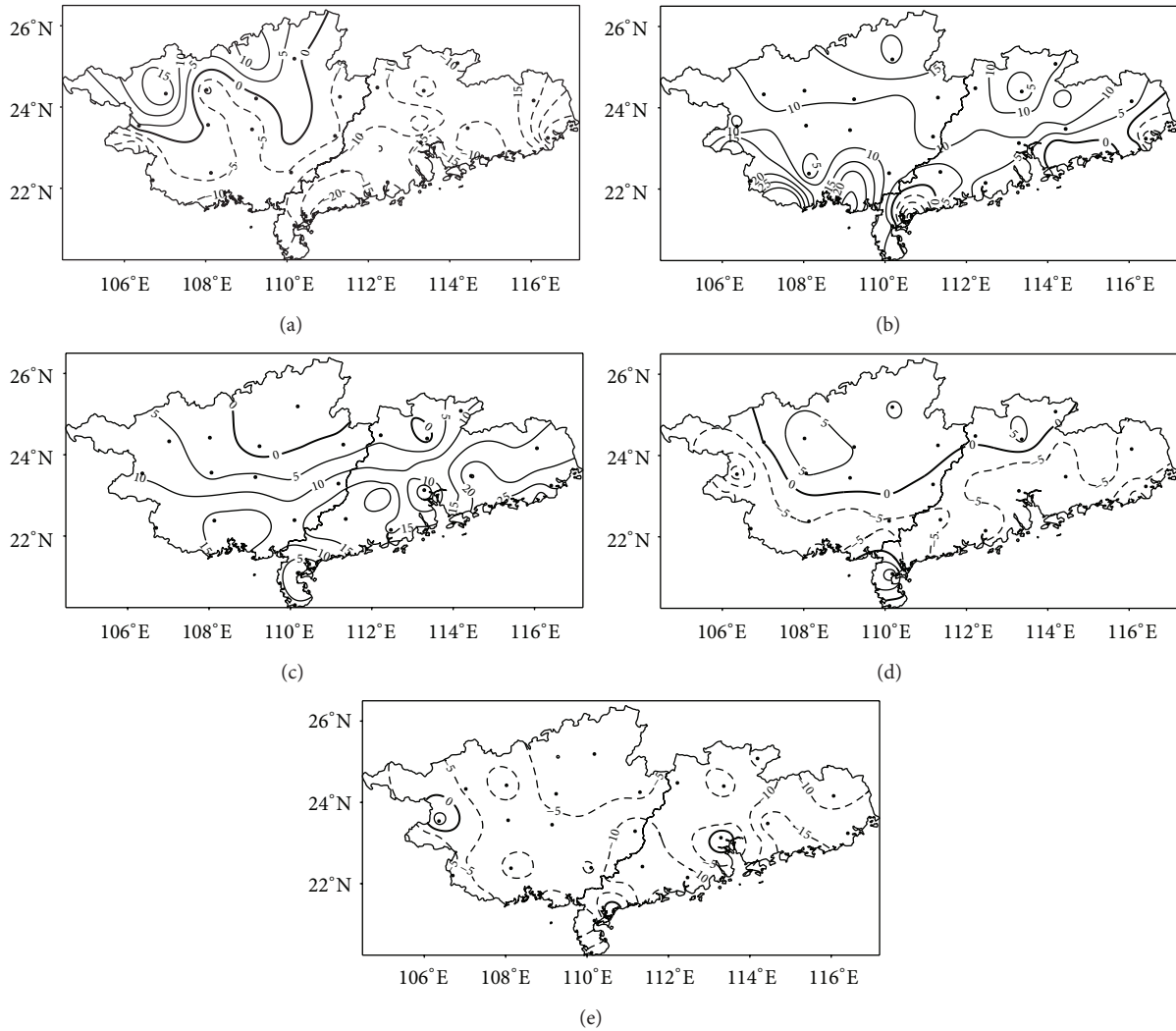


FIGURE 6: The spring precipitation anomaly percentage in the South China ((a) 1960s, (b) 1970s, (c) 1980s, (d) 1990s, and (e) 2000s).

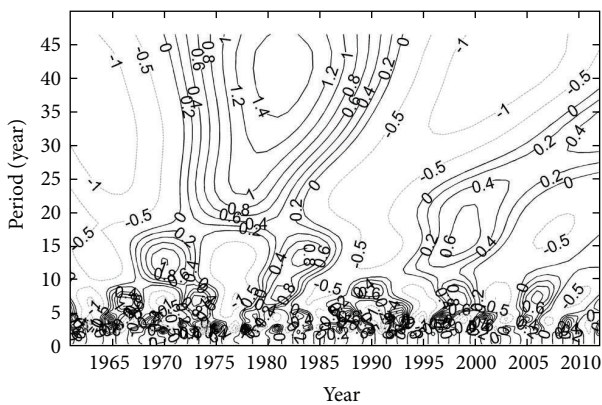


FIGURE 7: Wavelet analysis of spring precipitation in South China.

precipitation of South China is carried out, with the corresponding results presented in Figure 7. The dominant

timescales of variability of the South China spring precipitation are 7 years, 12 to 14 years, and 40 years. The 12- to 14-year variability occurred between 1961 and 2012; and the variability of South China spring precipitation had a below-above-below-above-below-above-below pattern, with 1961–1967, 1975–1980, 1987–1994, and 2004–2010 below normal and 1968–1974, 1981–1986, and 1995–2003 above normal. The latest below normal pattern appeared to have already well passed its peak and it is likely that the above normal precipitation will occur in the next decade. On the timescale of about 40 years, the South China spring precipitation has experienced below-above-below normal pattern, with below normal precipitation occurring during 1961–1972 and after 1992 and above normal during 1973–1992. The latest below-normal period appears to be close to or to have reached its zero-crossing phase, implying that the variability South China spring precipitation on that timescale may enter above normal phase in the coming years. The variability of the time scale of around 7 years has large amplitude modulation and has much complicated patterns. Prediction using the

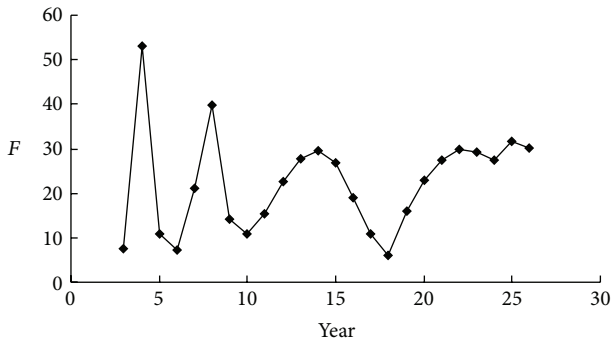


FIGURE 8: Spectral analysis of the South China spring precipitation.

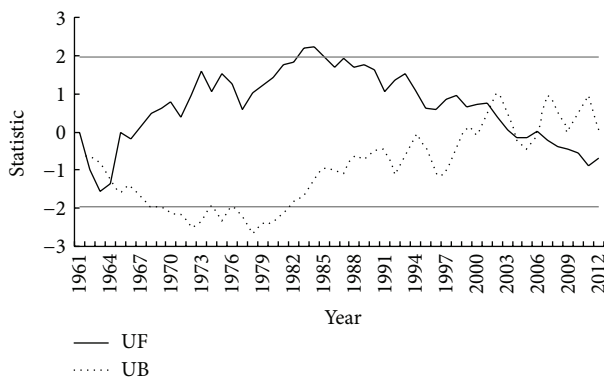


FIGURE 9: Mann-Kendall testing of abrupt changes of the South China spring precipitation (The  $\alpha = 0.05$  significance level is given by the straight line).

periodicity but not the amplitude modulation may lead to larger error.

Spectral analysis of the spatial mean of spring precipitation of South China shows peaks of 4 years, 8 years, and 14 years in spectral diagram, which is presented in Figure 8. This kind of periodicity passes the significance test at level 0.05.

#### 4. Abrupt Changes of Spring Precipitation in South China

To determine whether the spring precipitation of South China has experienced abrupt changes, we use Mann-Kendall [17, 18] testing method to analyze area averaged precipitation series. Mann-Kendall testing method is a nonparametric method and widely used. The method does not assume any a priori distribution of sample and is not sensitive to small number of abnormal extremes. The method can be applied to both categorized data and series albeit it only involves intuitively simple calculation. One of the advantages of Mann-Kendall testing method is its capability of determining the locations of mean or slope changes; and therefore, it is a method that can detect abrupt changes. Figure 9 presents the detecting results. It is evident that the spring precipitation increment started at mid-1960s and maintained until mid-1980s. From mid-1980s, the spring precipitation

began to decrease. An abrupt increment occurred in 1964 and an abrupt decrement occurred in 2002. These two abrupt changes are statistically significant at a significance level of  $\alpha = 0.05$  ( $u_{0.05} = \pm 1.96$ ) [17, 18].

#### 5. The South China Spring Precipitation and the Abnormal Atmospheric Circulations

The South China spring climate is significantly influenced by subtropical and mid and high latitude atmospheric circulations. From the composites of 850 hPa level wind fields and geopotential height fields for abundant South China spring precipitation years and for scarce South China spring precipitation years (figures omitted), one can identify that the abundant (scarce) spring precipitation of the South China coincides with abnormally strong (weak) and wide (narrow) subtropical high, stronger (weaker) Eastern Asia low, and larger (smaller) geopotential gradient between these two systems. Such a coincidence is also reflected in the composite of geopotential gradient at 500 hPa (Figure 10(a)). The larger positive geopotential gradient center, with its maximum value exceeding 9 dagpm, appears in the  $10^{\circ}$ – $20^{\circ}$ N zone of the western Pacific, implying the strengthening of the subtropical high. At the same time, a negative center to the east of the Tibetan Plateau appears, indicating a stronger low. From the basic dynamics, it can be inferred that such type of anomalous pressure gradient can lead to the strengthening of the southwesterly [19, 20] at low levels. It is clear that the years of abundant (scarce) spring precipitation in the South China correspond to the strengthened (weakened) low-level southwesterly, which is also evident from the composite of the difference of the wind field at 850 hPa level between the abundant spring precipitation and scarce spring precipitation years (Figure 10(b)). Figure 10(b) also displays that anomalous anticyclonic circulation appears in the western Pacific subtropical high region, centered in the vicinity of ( $138^{\circ}$ E,  $17^{\circ}$ N), and an anomalous cyclonic circulation appears to the east of Tibetan Plateau centered around  $25^{\circ}$ N. The anomalous southwesterly between these two systems covers the eastern part of the Indochina, South China, and southeastern coastal China. The anomalous southwesterly weakens significantly when it reaches the Yangtze River region.

The strengthened southwesterly provides both the convergence-induced upward motion and moisture source for South China. Figure 10(c) displays the composite of the difference of the low-level (from surface to 700 hPa) convergence between the abundant spring precipitation years and scarce spring precipitation years in South China. It is evident that large scale convergence occurs in South China region and western Pacific subtropical high region, with its maximum value reaching  $-40 \times 10^{-3} \text{ s}^{-1}$ . This large anomalous convergence leads to strong vertical motions in the South China region, as shown in Figure 10(d). The strong vertical motion (with its value exceeding the absolute value of  $-20 \times 10^{-3} \text{ Pa s}^{-1}$ ) appears from  $20^{\circ}$ – $30^{\circ}$ N and extends from surface to 200 hPa level, with strongest vertical motion reaching a value of  $-36 \times 10^{-3} \text{ Pa s}^{-1}$ . The strong anomalous vertical motion and abundant low-level moisture

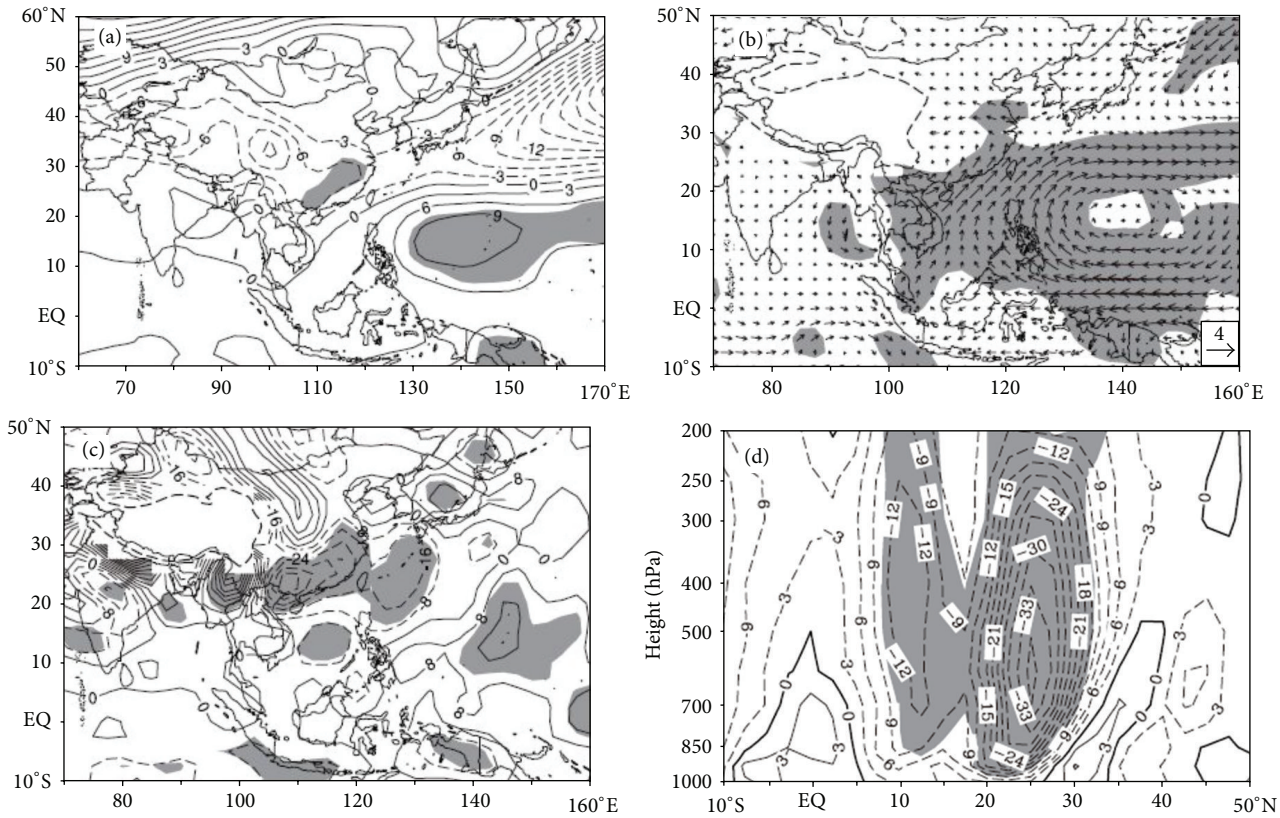


FIGURE 10: The differences of physical fields between the abundant spring precipitation years and scarce precipitation years in the South China: (a) the 500 hPa geopotential height (dagpm); (b) the 850 hPa wind ( $\text{ms}^{-1}$ ); (c) the low-level convergence ( $10^{-3} \text{ s}^{-1}$ ); and (d) the zonally averaged (along  $110^{\circ}$ – $120^{\circ}\text{E}$ ) vertical velocity in p-coordinate ( $10^{-3} \text{ Pa s}^{-1}$ ).

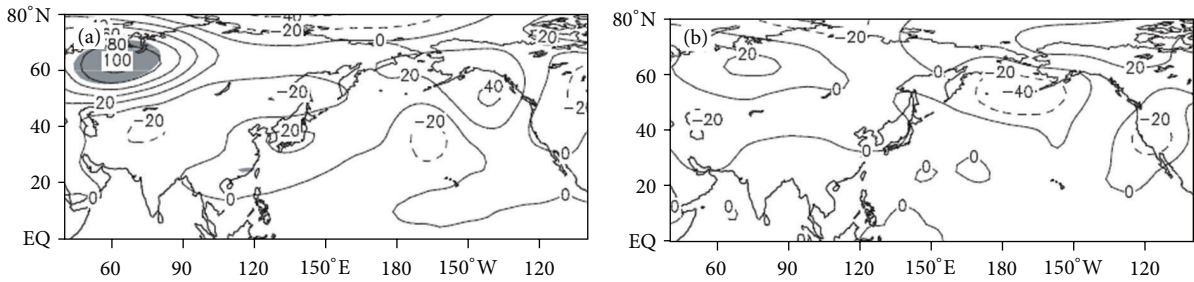


FIGURE 11: Composite 500 hPa level geopotential height for flooding spring years (a) draught spring years (b) in in South China (unit: gpm).

convergence generates the abnormal precipitation in the abundant South China spring precipitation years.

It could be found from Figure 11 that there are abnormal regions passed the significant test located in the western tropical Pacific, northwestern North America, and mid latitude in northwest Atlantic in the 500 hPa height field. Similar to the Pacific-North American teleconnection pattern, it is positive difference in the western tropical Pacific and from northwestern North America to North Pole; negative difference at mid latitude in Asia and mid latitude in North America. It results in higher geopotential height over the western tropical Pacific and stronger Aleutian Low in March in years when spring precipitation in South China is abundant.

Coincident with the tropical-subtropical circulations, the Aleutian Low strengthens and the westerly in midlatitudes east Asia weakens in the early spring of the abundant spring precipitation years in South China. Such type of mid and high latitude circulation pattern provides a favorable environment for the mid and high level cold air mass to move southward, leading to the dropping of the temperature of the tropical western Pacific and further strengthening the western Pacific subtropical high. The southeastward retreating of the western Pacific subtropical high leads to the large moisture transport from ocean reaching only to the latitudes of the South China. The meeting of the cold air from midlatitude and warm moist air from tropics leads to the abnormal precipitation in the

South China region [21]. In the years of scarce spring precipitation in the South China, there is an anomalous anticyclonic circulation over the vicinity of the South China [22]. Such an anticyclonic circulation maintains the anomalous downward motion. At the same time, positive large scale geopotential height anomaly appears in the vicinity of Ural mountains, so as in the eastern China, Japan, and its eastern neighboring regions, coincident with the weakening of the grand eastern Asian trough. Such a circulation pattern prevents the cold air in mid and high latitude to move southward, thereby forming an environment not favoring the occurrence of spring precipitation in the South China.

## 6. Conclusions and Discussions

Consider

- (1) The precipitation in South China is spatiotemporally uneven, with the scarcest spring precipitation (212.1 mm) at Weizhou Island (109°06'E, 21°02'N) of Guangxi Zhuang Autonomous Region and most abundant spring precipitation (808.3 mm) at Fuogang (113°31'E, 23°53'N) of Guangdong Province. In general, the eastern and southeastern regions of South China are rainfall abundant area; and the remaining parts of South China are rainfall scarce area. The first eigenvector resulting from EOF analysis is uniform over the whole South China; the second eigenvector features two natural climatological regimes; and the third eigenvector has six distinctive natural climatological regimes: (1) the northern part of South China which features hilly areas of both Guangdong and Guangxi; (2) the northwestern region of Guangxi; (3) the southwestern region of Guangxi; (4) the central South China (including the central parts of both Guangdong and Guangxi); (5) the southern South China region (including the central regions of both Guangdong and Guangxi); and (6) Leizhou Peninsula region.
- (2) The spring precipitation in the South China contains significant multiscale variability. The largest interannual fluctuation occurred in 1973 and had a value of 716.5 mm while the smallest interannual fluctuation occurred in 1963 with a value of 189.9 mm. The maximum interannual fluctuation is almost four times as large as that of the minimum. The South China spring precipitation experienced variability of a below-above-below-above-below-above-below pattern. Spectral analysis of the spatial mean spring precipitation in South China shows periodicity of 4 years, 8 years, and 14 years.
- (3) The spring precipitation in the South China contains significant interdecadal variability. The 1980s is the decade of most abundant spring precipitation while the 1960s is the decade of the fewest spring precipitation. An abrupt increment occurred in 1964 while an abrupt decrement occurred in 2002. These two abrupt changes are statistically significant at a significance level of  $\alpha = 0.05$  ( $u_{0.05} = \pm 1.96$ ).
- (4) The atmospheric circulation patterns associated with the abundant spring precipitation and scarce spring precipitation in South China are significantly different. In the abundant years, on the one hand, the Aleutian Low strengthens and the westerly in midlatitudes east Asia weakens in the early spring, favoring the mid and high level cold air mass moving southward. On the other hand, the western Pacific subtropical high retreats southeastward, leading to the large moisture transport from ocean reaching only the latitudes of South China. The meeting of the cold air from midlatitude and warm moist air from tropics leads to the abnormal precipitation in the South China region. In the years of scarce spring precipitation in the South China, there is an anomalous anticyclonic circulation over the vicinity of the South China. Such an anticyclonic circulation maintains the anomalous downward motion. In the meantime, positive large scale geopotential height anomaly appears in the vicinity of Ural mountains, as well as in the eastern China, Japan, and its eastern neighboring regions, causing the weakening of the southern branch of the grand eastern Asian trough and the northwestward shift of the western Pacific subtropical high. Such a circulation pattern prevents the cold air in mid and high latitude to move southward, thereby not favoring the occurrence of spring precipitation in the South China.

## Conflict of Interests

The authors declare that there is no conflict of interests regarding the publication of this paper.

## Acknowledgments

This work has been funded by the National Basic Research Program of China (Grant no. 2013CB430200 (2013CB430206)) and the Sixth Program Ten Talented People of the Gansu Province Meteorological Bureau, China (Grant no. 06).

## References

- [1] H. L. Liu, Q. Zhang, W. C. Hu, and J. Q. Guo, "The changing characteristics of spring precipitation in Northwest China and their spatial differentiation during 1961–2011," *Journal of Glaciology And Geocryology*, vol. 35, no. 4, pp. 857–864, 2013 (Chinese).
- [2] H. L. Liu, Q. Zhang, J. Q. Guo, S. Wang, Y. Cui, and X. Y. Wen, "Anomaly space distribution and decadal variability of spring precipitation in Gansu Province," *Journal of Glaciology and Geocryology*, vol. 36, no. 5, pp. 1143–1150, 2014 (Chinese).
- [3] S. J. Lu, *Climate of South China*, Meteorological Press, Beijing, China, 1990, (Chinese).
- [4] H. L. Liu, Q. Zhang, S. Wang, J. Q. Guo, and H. Yang, "Abnormal spatial distribution of spring precipitation and its decadal variability in the Hexi corridor in the arid area of

- Northwest China,” *Journal of Desert Research*, vol. 34, no. 5, pp. 1386–1392, 2014 (Chinese).
- [5] H. L. Liu, Q. Zhang, J. Q. Guo, S. Wang, and H. W. Zhang, “Spatial differentiation of spring precipitation in the Heihe River basin and its correlation with the river flow,” *Journal of Desert Research*, vol. 34, no. 6, pp. 1633–1640, 2014 (Chinese).
- [6] H. X. Duan, S. P. Wang, and J. Y. Feng, “The drought situation and its influence and cause in 2010 spring,” *Journal of Arid Meteorology*, vol. 28, no. 2, pp. 238–244, 2010 (Chinese).
- [7] Z. X. Hao, J. Y. Zheng, Q. S. Ge, and X. Z. Zhang, “Spatial patterns of precipitation anomalies for 30-yr warm periods in China during the past 2000 years,” *Acta Meteorologica Sinica*, vol. 26, no. 3, pp. 278–288, 2012.
- [8] X. X. Bai, C. Y. Li, and L. Li, “Numerical simulation study of the Madden-Julian Oscillation in influences on spring precipitation in China,” *Acta Meteorologica Sinica*, vol. 70, no. 5, pp. 986–1003, 2012 (Chinese).
- [9] R. J. Wan and G. X. Wu, “Temporal and spatial distributions of the spring persistent rains over Southeastern China,” *Acta Meteorologica Sinica*, vol. 23, no. 5, pp. 598–608, 2009.
- [10] Z. P. Wen, N. G. Wu, Y. R. Feng, L. X. Lin, Z. J. Yuan, and B. H. Chen, “A quantitative diagnosis for the mechanisms of spring droughts in South China,” *Chinese Journal of Atmospheric Sciences*, vol. 31, no. 6, pp. 1223–1236, 2007 (Chinese).
- [11] D. J. Gu, Z. P. Ji, A. L. Lin, and L. S. Hao, “The variation and precursor of Guangzhou spring rainfall,” *Journal of Tropical Meteorology*, vol. 21, no. 6, pp. 579–587, 2005 (Chinese).
- [12] M. S. Zhou, M. Q. Jian, and Y. T. Qiao, “April-May persistent drought events in South China and the related general circulation background,” *Acta Meteorologica Sinica*, vol. 71, no. 1, pp. 76–85, 2013 (Chinese).
- [13] H. Y. Li, Z. H. Lin, Y. Song, and H. Chen, “Zonal seesaw-like distribution of spring precipitation over South China and characteristics of atmospheric circulation in anomalous climate years,” *Meteorological Monthly*, vol. 39, no. 12, pp. 1616–1625, 2013 (Chinese).
- [14] X. Z. Li, W. Liang, and Z. P. Wen, “Characteristics of the atmospheric water vapor and its relationship with rainfall in South China in northern autumn, winter and spring,” *Journal of Tropical Meteorology*, vol. 26, no. 5, pp. 626–632, 2010 (Chinese).
- [15] R. J. Wan, T. M. Wang, and G. X. Wu, “Temporal variations of the spring persistent rains and SCS subtropical high and their correlations to the circulation and precipitation of the East Asia summer monsoon,” *Acta Meteorologica Sinica*, vol. 66, no. 5, pp. 800–807, 2008 (Chinese).
- [16] J. P. Han, H. J. Wang, and D. B. Jiang, “Interannual variation of spring precipitation and circulation in South China as simulated by a coupled model,” *Climatic and Environmental Research*, vol. 11, no. 2, pp. 194–202, 2006 (Chinese).
- [17] F. Y. Wei, *The Modern Technology of Climate Statistics and Diagnose*, Meteorological Press, Beijing, China, 2nd edition, 2007, (Chinese).
- [18] H. L. Liu, Q. Zhang, J. G. Zhang, W. C. Hu, J. Q. Guo, and S. Wang, “Changing characteristics and spatial differentiation of spring precipitation in Southwest China during 1961–2012,” *Chinese Physics B*, vol. 24, no. 2, Article ID 029201, 2015.
- [19] D. S. Yang and Y. B. Liu, *Dynamic Meteorology*, Meteorological Press, Beijing, China, 1983, (Chinese).
- [20] P. P. Jiang and P. Zhao, “The interannual variability of spring rainy belt over southern China and the associated atmospheric circulation anomalies,” *Acta Meteorologica Sinica*, vol. 70, no. 4, pp. 681–689, 2012 (Chinese).
- [21] L. P. Deng and Q. Q. Wang, “On the relationship between precipitation anomalies in the first raining season (April–June) in southern China and SST over offshore waters in China,” *Journal of Tropical Meteorology*, vol. 18, no. 1, pp. 45–55, 2010 (Chinese).
- [22] H. Y. Li, Z. H. Lin, Y. Song, H. Chen, and J. Y. Xu, “Analysis of the possible factors that influence March precipitation anomalies over south China,” *Chinese Journal of Atmospheric Sciences*, vol. 37, no. 3, pp. 719–730, 2013 (Chinese).

## Research Article

# Recent Trends in Temperature and Precipitation in the Langat River Basin, Malaysia

Mahdi Amirabadizadeh,<sup>1</sup> Yuk Feng Huang,<sup>2</sup> and Teang Shui Lee<sup>1</sup>

<sup>1</sup>Faculty of Engineering, Universiti Putra Malaysia, 43300 Serdang, Selangor, Malaysia

<sup>2</sup>Faculty of Engineering and Science, Universiti Tunku Abdul Rahman, 53300 Kuala Lumpur, Malaysia

Correspondence should be addressed to Mahdi Amirabadizadeh; [mamir692@gmail.com](mailto:mamir692@gmail.com)

Received 10 September 2014; Revised 7 November 2014; Accepted 20 November 2014

Academic Editor: Lin Wang

Copyright © 2015 Mahdi Amirabadizadeh et al. This is an open access article distributed under the Creative Commons Attribution License, which permits unrestricted use, distribution, and reproduction in any medium, provided the original work is properly cited.

A study was undertaken to detect long-term trends in the annual and seasonal series of maximum and minimum temperatures. Measurements were taken at 11 meteorological stations located in the Langat River Basin in Malaysia. The rainfall and maximum and minimum temperature data were obtained from the Malaysia Meteorological Department (MMD) and the Department of Irrigation and Drainage (DID) Malaysia. The procedures used included the Mann-Kendall test, the Mann-Kendall rank statistic test, and the Theil-Sen's slope method. The analytical results indicated that when there were increasing and decreasing trends in the annual and seasonal precipitation and temperature, only the increasing trends were significant at the 95% confidence level. The Theil-Sen's slope method showed that the rate of increment in the annual precipitation is greater than the seasonal precipitation. A bootstrap technique was applied to explore uncertainty about significant slope values for rainfall, as well as the maximum and minimum temperatures. The Mann-Kendall rank statistics test indicated that most of the trends in the annual and seasonal time series started in the year 2000. All of the annual and seasonal significant trends were obtained at the stations located in the north, east, and northeast portions of the Langat River Basin.

## 1. Introduction

Quantitatively speaking, climate change refers to the statistically significant variations of the mean state of the climate or that of its variability for decades or even over a longer period [1]. Although climate change happens globally, its effects, however, can be deterministic, dependent on the region of study. Temperature and precipitation variables are the most important measures that indicate the signs of climate change. The Intergovernmental Panel on Climate Change (IPCC) AR4 specified that the average global surface temperature has increased by 0.074°C per year from 1906 to 2000 [2]. Furthermore, the IPCC AR5 report indicated that increases in mean temperature will continue for the 2016–2035 period [1]. The reports from IPCC also indicated that the frequency of extreme rainfall events have increased over most land areas, consistent with growing temperatures and atmospheric water vapour [3]. An analysis of the long-term changes in climate variables is very crucial for water resource planning

and management, as well as to put things into their proper perspective and context [4].

Many trend analyses have been carried out on climate variables, especially with temperature and precipitation. Many of researchers applied the nonparametric Mann-Kendall method in the detection of trend in hydrologic variables [5, 6]. The Mann-Kendall rank statistics test and Theil-Sen's slope method are other methods that are widely used to declare trends and magnitude changes in the climate variables in annual and seasonal time scales [7, 8].

The comparison between the trend detection methods is the main subject of many studies. Yue et al. [9] compared the power of the Mann-Kendall and Spearman tests for detecting the monotonic trend in time series. They stated that the power of the test depends on the slope of trend, level of significance, sample size, and properties of the datasets, such as skewness and variation. The test results also demonstrated that both of the tests provided the same consequences in the absence of autocorrelation.

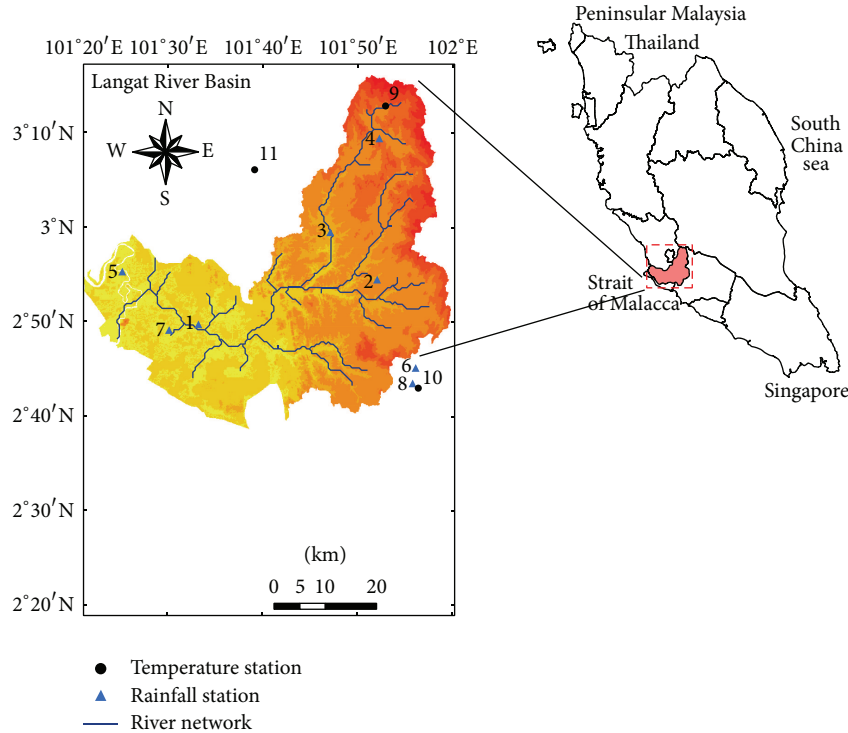


FIGURE 1: Geographic location and spatial distribution of stations in the Langat River Basin.

While there were interests in the examination of the existence of trends for many climatic variables in Malaysia, a limited number of studies have been done in this country. Meng et al. [10] investigated the trend of regional warming in Malaysia using a mean annual temperature time series of approximately 50 years. Their findings showed complete agreement with the temperature increments reported by the IPCC for Malaysia, which are 0.99 to 3.44°C per 100 years. Tangang et al. [11] applied the Mann-Kendall test for 32 stations over whole peninsula of Malaysia for the period of 1974–2004. The MK test for mean, variability, and persistence of wet spells revealed positive and negative trends in the stations east of the peninsula during the northeast monsoon and southwest monsoon seasons, respectively. They also concluded that there is a wide gap in the knowledge of climate change throughout Malaysia.

Suhaila et al. [12] investigated the existing trends in daily rainfall in peninsular Malaysia based on seasonal rainfall during 1975–2004. The results of the Mann-Kendall test indicated a decreasing trend in the total amount of rainfall and frequency of wet days, as well as the increasing trend in rainfall intensity during the southwest monsoon. On the contrary, the results of the test showed reverse trends in the parameters for northeast monsoon flow.

The comparison associated with preceding studies in climate change in Malaysia indicated that there is a gap in many climate parameters such as maximum temperature, minimum temperature, and annual precipitation—one of the most important factor. Furthermore the beginning of trend is actually another concern that was not addressed in the past researches.

In this study, we analysed and examined the signs of change in the annual precipitation, as well as the maximum and minimum temperature regime, specific to Langat River Basin (a strategic basin), located in Malaysia (Figure 1). The Langat River Basin is the most urbanised river basin in Malaysia, located in the southern part of Klang Valley. During the last decade, this watershed has experienced rapid development in urbanisation, agriculture, and industrialisation. This watershed supplies water to two-thirds of the state of Selangor for its domestic, hydroelectric plant, industry, and agricultural consumption. As Selangor State is currently facing a water shortage problem, especially during the southwest monsoon season, analysing the trends of rainfall and the maximum and minimum temperatures is a vital activity in management of the water resources for the future. The objectives of this research were achieved using the Mann-Kendall and Mann-Kendal rank statistic methods. The rates of changes in these variables were then determined using the Theil-Sen's slope method.

## 2. Materials and Methods

**2.1. Study Area.** The total area of the Langat River Basin is approximately 2352 km<sup>2</sup>. It lies between latitudes 2°40'15" to 3°16'15" N and longitudes 101°17'20" to 101°55'10" E in the southern part of the Klang Valley region. The northern part of the basin is a mountainous area, while its southern part consists of a flat area. The mean areal annual rainfall of the Langat River Basin is 1994.1 mm. The highest recorded monthly rainfall is about 327.1 mm, occurring in November, while the lowest is 97.6 mm in June. These two maximum and

TABLE 1: Geographic characteristics of stations for recorded precipitation data.

Station ID	Number	Longitude (E)	Latitude (N)	Altitude (m)	Period
2815001	1	101° 32'	2° 49'	3	1971–2011
2818110	2	101° 52'	2° 53'	36	1971–2011
2917001	3	101° 47'	2° 59'	39	1976–2011
3118102	4	101° 52'	3° 10'	91	1971–2011
2913001	5	101° 23'	2° 55'	3	1974–2011
2719001	6	101° 56'	2° 45'	93	1971–2011
44256	7	101° 30'	2° 49'	8	1974–2011
45241	8	101° 56'	2° 43'	64.1	1974–2011
Ampangan	9	101° 53'	3° 13'	233.3	1985–2011
Hospital Seremban	10	101° 56' 37''	2° 42' 33''	64.1	1971–2011
Petaling Jaya	11	101° 39'	3° 6'	60.8	1974–2011

minimum precipitations occurred in the northeast monsoon and the southwest monsoon periods, respectively.

Besides global warming, the climate of Malaysia is associated with many global and regional phenomena, such as monsoons, El Nino/La Nina, and the Indian Ocean Dipole (IOD). These phenomena could affect the severity of extreme events in the country. Scientists state that global warming will directly affect systems, such as hydrological cycles, and extreme events, such as El Nino/La Nina [13].

In the seasonal time scale, the surface climate in Malaysia is affected by two monsoon regimes, namely, the southwest (SW) monsoon and northeast (NE) monsoon patterns. The SW monsoon season that is dominated by the low level southwesterly winds begins in May and lasts through August. On the other hand, the NE monsoon season that is controlled by the northeast wind commences in November and ends in February of the following year [14].

The recorded data for rainfall (subdaily measurements) and maximum and minimum temperature (daily measurements) were obtained from the Malaysia Meteorological Department (MMD) and Department of Irrigation and Drainage (DID). The daily data for precipitation was extracted from subdaily data at each station. The series of annual and monsoon seasonal recorded data, which included the maximum temperature ( $T_{Max}$ ), the minimum temperature ( $T_{Min}$ ), and total precipitation ( $P$ ), were analysed for the existence of monotonic trends.

The seasonal and annual values of  $T_{Max}$  and  $T_{Min}$  were computed as the average values over the season and year, respectively. The study periods were matched to all the available records at each station, which varied between 27 and 41 years. The recorded daily data were available at three temperature stations and eight precipitation stations. Monthly values were averaged to obtain the NE monsoon (winter) and SW monsoon (summer) temperature for each of the three stations. Spatial distribution and geographic characteristics of the precipitation and temperature stations are shown in Figure 1 and Table 1, respectively.

These stations were chosen as the database due to the good quality datasets, suitable length (close to 30 years) of data recorded, which is considered to be long enough for studying the changes in climate, and good spatiality

distribution in the mountainous and flat regions to cover the whole area of the river basin.

In the analysis of climate variables, it is primarily important to investigate the quality of the recorded climatic data, such as looking for missing values, analysing the outliers, and also administering the consistency test. In the case of missing observations, the daily missed values were repaired using the Ameliaview1.1 package in R software [15], which is based on the bootstrap method. Also, for the longer missed observations, the recorded values in neighbouring stations that had high correlations were used to complete the temperature and precipitation time series.

Outliers in the data sets can lead to false trend results and inaccurate statistical properties [16]. Bremer [17] found that the interquartile ratio (IQR) method reduces biases in the dataset caused by outliers, while also keeping the information for extreme events as well. In the IQR method, the higher and lower thresholds are described by  $Q75\% + 5 * IQR$  and  $Q25\% - 5 * IQR$ , respectively [18]. Then, each value greater or smaller than the higher and lower bands, respectively, is set as an outlier and eliminated from the data sets.

The homogeneity of the time series has been investigated by many researchers [19]. In this study, the double-mass curve procedure [20] was applied to test the consistency of climate variables. The double-mass curve method is a graphical procedure to identify the inconsistency of station records by comparing the time trend in one station with other relatively stable records at other stations or the average of several nearby stations [6]. Results of the double mass-curves for all of the stations are straight lines, and no apparent breakpoints are detected in the time series

The mean value of precipitation ( $P$ ) at the observed stations varied between 1658.3 in Station 1 and 2351.6 mm in Station 8, which are located in the flat and mountainous areas, respectively. This pattern was repeated for the mean of the seasonal precipitation in the SW monsoon and NE monsoon seasons. This is shown in Table 2 and Figure 2.

As shown in Figure 2, the ranges of variation at Stations 9 and 11 are the smallest and greatest values in the temperature time series, respectively. These differences in  $T_{Max}$  and  $T_{Min}$  between stations were more related to the land use and altitude of gauging stations. Station 9, located in forest and

TABLE 2: Statistical properties of annual and seasonal rainfall and temperature in the Langat River Basin.

Station	Variable	Annual			Seasonal					
		Mean	S.D.	Skew	Mean	S.D.	Skew	Mean	S.D.	Skew
1	Precipitation	1658.3	304.9	-0.14	583.5	182.37	0.03	468.8	143.64	0.06
2		1883.8	366.3	0.35	594.5	181.72	0.73	517.5	144.83	0.68
3		2191.2	417.3	-0.31	773.3	245.15	0.13	562.8	175.61	0.15
4		2128.7	379.5	0.36	662.1	198.53	-0.14	638.0	178.20	0.39
5		1750.3	396.6	-0.16	687.9	219.40	0.45	460.4	122.03	0.68
6		1951.9	363.1	0.01	620.5	188.53	0.24	539.7	141.00	0.1
7		1965.6	470.9	2.43	677.2	206.92	1.35	606.7	188.01	1.45
8		2351.6	345.4	-0.38	786.1	224.75	-0.09	648.6	140.17	0.58
9	$T_{Max}$	31.7	0.46	0.07	31.1	0.62	-0.08	32.0	0.42	0.67
	$T_{Min}$	21.6	0.47	-0.88	21.5	0.44	-0.79	21.7	0.50	-1.23
10	$T_{Max}$	31.9	0.36	0.48	31.9	0.54	0.61	31.8	0.28	0.52
	$T_{Min}$	23.5	0.55	-0.18	23.4	0.58	-1.08	23.6	0.55	-0.08
11	$T_{Max}$	32.8	0.42	0.04	32.4	0.66	0.49	32.9	0.4	0.13
	$T_{Min}$	24.0	0.57	0.31	23.7	0.61	0.27	24.2	0.58	0.23

mountainous regions, demonstrated less variation in the maximum and minimum temperatures than did the two other stations near the urban area and lower altitudes. The 5-year moving average indicated an approximate monotonic increasing trend for the annual maximum temperature in Station 9 and the annual minimum temperature in Stations 10 and 11.

As shown in Figure 3(b), the stations that are located north and east of the Langat River Basin receive more rainfall than do those stations west of the basin during the study period. These results are consistent with those obtained by Deni et al. [21]. The mean annual  $T_{Max}$  and  $T_{Min}$  range from 31.6 to 33°C and 21.6 to 24.2°C respectively.

**2.2. Trend Analysis.** There are two main ways to declare the significant trends in the climatic data sets: parametric and nonparametric trend methods. In the parametric trend analysis, data should be independent and normally distributed, while in the nonparametric method, the only requirement is to be independent. In this study, the nonparametric Mann-Kendall was used for the detection of significant trends, the Mann-Kendall rank statistic test was used for determining the beginning of trend, and the Theil-Sen's slope procedure was applied to measure the quantity of change in the climatologic time series.

**2.2.1. Mann-Kendal Test.** The Mann-Kendall (MK) test is a robust method of detecting a monotonic trend in hydroclimate data. The MK method is a rank-based procedure, with a strength being the application in skewed data. Another suitable property of this test is that it has a low sensitivity to abrupt breaks, which may be caused by inhomogeneous data.

For an observed time series  $x = x_1, x_2, x_n$ , the trend test statistic  $S$  is given by

$$S = \sum_{i=1}^{n-1} \sum_{j=i+1}^n \text{Sgn}(x_j - x_i), \quad (1)$$

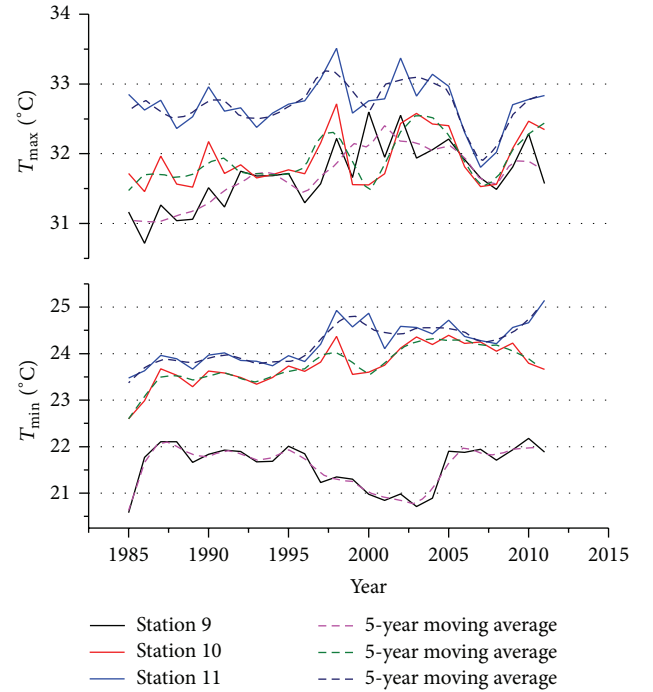


FIGURE 2: Annual maximum and minimum temperatures and their 5-year moving average in the Langat River Basin.

where

$$\text{Sgn}(x) = \begin{cases} 1, & x > 0 \\ 0, & x = 0 \\ -1, & x < 0. \end{cases} \quad (2)$$

And  $i$  and  $j$  are the rank of observation of the  $x_i, x_j$  of time series.

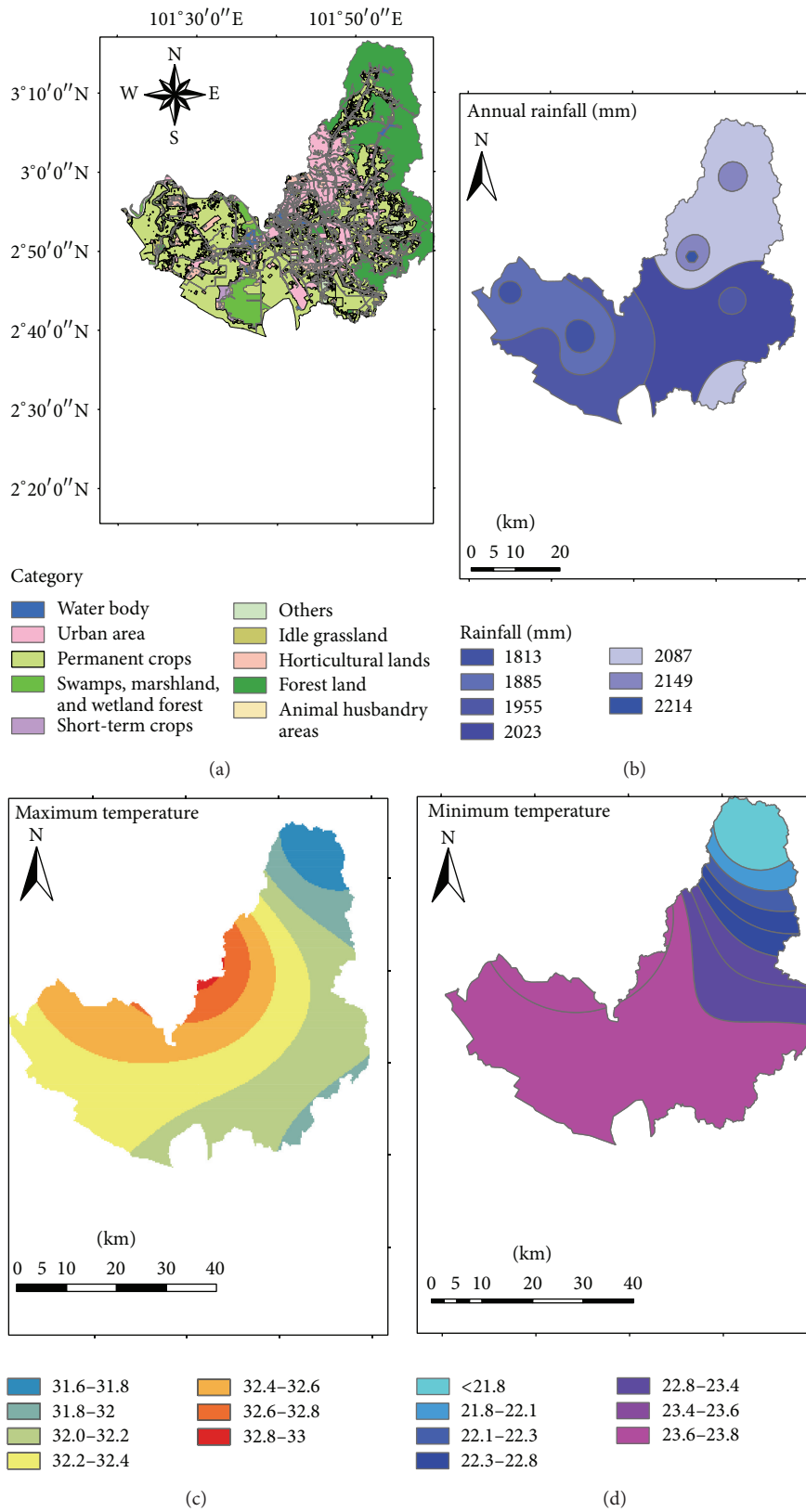


FIGURE 3: Spatial characteristics of the Langat River Basin include (a) land use map, (b) annual precipitation, (c) minimum temperature, and (d) maximum temperature.

The variance is computed as

$$V = \frac{n(n-1)(2n+5)}{18} - \sum_{i=1}^g \frac{t_i(t_i-1)(2t_i+5)}{18}, \quad (3)$$

where  $g$  is the number of groups of tied rank and  $t_i$  is number of ties in group  $i$ . For a sample size of 30 or larger, the  $S$  statistic is normally distributed and the value of the standard deviation is computed by

$$Z = \begin{cases} \frac{s-1}{\sqrt{0.5}} & S > 0 \\ 0 & S = 0 \\ \frac{s+1}{\sqrt{0.5}} & S < 0. \end{cases} \quad (4)$$

When  $|Z| > Z_{1-\alpha/2}$  or the  $P$  value is smaller than the significance level ( $\alpha$ ), the null hypothesis is rejected and there is a significance trend in the time series. The  $Z_{1-\alpha/2}$  and  $P$  value are obtained from the standard normal distribution table. In this study, the significance level is  $\alpha = 0.05$  and therefore the null hypothesis of no trend is rejected while  $|Z| > 1.96$ .

The MK test analysis technique was widely used in detecting trends in climate variables [5, 8, 22–26]. The prewhitening procedure was carried out before completing the MK test to eliminate the influence of autocorrelation on the results of the test. The prewhitening procedure is described in Section 2.3.

**2.2.2. Mann-Kendall Rank Statistic Test.** According to Sneyers [27], the Mann-Kendall rank statistic (MKRS) test is used to determine the approximate beginning year of significant trends (e.g., [6, 14, 28]). Two sequential values,  $U_t$  and  $U'_t$ , are determined from progressive and backward time series, respectively. This method uses relative values of each element in the time series ( $x_1, x_2, \dots, x_n$ ). The following steps are utilised in four sequences.

- (1) The magnitudes of  $x_i$  annual or seasonal time series ( $i = 1, \dots, n$ ) are compared with  $x_j$  ( $j = 1, \dots, i-1$ ). At each comparison, the number of cases  $x_i > x_j$  is counted and indicated by  $n_i$ .
- (2) The test statistic  $t_i$  variable is computed using

$$t_i = \sum_{i=1}^i n_i. \quad (5)$$

- (3) As the  $t_i$  distribution is asymptotically normal, the mean and variance of  $t_i$  are calculated as follows:

$$E(t) = \frac{n(n-1)}{4}, \quad (6)$$

$$\text{Var}(t_i) = \frac{1}{72} [i(i-1)(2j+5)].$$

- (4) Finally, the sequential values of the  $U_t$  are computed by

$$U_t = \frac{t_i - E(t)}{\sqrt{\text{Var}(t_i)}}. \quad (7)$$

Similarly, these four steps are followed to compute the  $U'_t$  in backward direction, from the end of the time series. If the time series of  $U_t$  and  $U'_t$  intersect each other and at least one of them is greater than a chosen level of significance, then there is a statistically significant trend. The point where the  $U_t$  and  $U'_t$  cross each other indicates the approximate beginning year of a developing trend within the time series. In this study, as the level of significance  $\alpha = 0.05$ , then the absolute values of calculating  $U_t$  and  $U'_t$  are compared with the Gaussian distribution value 1.96.

**2.2.3. Theil-Sen's Slope Method.** The Theil-Sen's slope method [29] is used to estimate the rate of change the rate of change:

$$\beta = \text{Median} \left( \frac{x_j - x_i}{j - i} \right) \quad i < j, \quad (8)$$

where  $x_j$  and  $x_i$  are the data values in times  $j$  and  $i$ , respectively. The  $\beta$  sign represents the direction of change and its value indicates the steepness of change [7, 25]. According to Yue et al. [9], the slope estimated by Theil-Sen's slope (TSS) estimator is a robust estimation of the magnitude of the trend. In order to determine the magnitude of TSS, an algorithm in R programme that corresponds to an extension of original TSS test was applied. This technique is frequently used in determining the slope of trend in climate variable time series (e.g., [5, 30–33]).

**2.3. Influence of Serial Correlation.** In time series analysis, it is essential that the data sets used for trend analysis be free of serial correlation in the time series. von Storch and Navarra [34] found that the presence of serial correlation in the time series can complicate the results of the identification of the trend detection for the Mann-Kendall test since the positive first-order autocorrelation can increase the expected number of false positive outcomes. In this study, the trend-free prewhitening (TFPW) approach that was modified by Burn et al. [35] was used prior to the application of the Mann-Kendall and Theil-Sen's slope procedures to remove the significant serial correlation from the time series. This procedure can be followed in five steps.

- (1) Compute the TSS,  $\beta$ , using (8).
- (2) Remove the monotonic trend from the original data sets using

$$Y_t = X_t - \beta t, \quad (9)$$

where  $X_t$  is the time series value at time  $t$  and  $Y_t$  is the detrended series.

- (3) Compute  $r_1$ , the lag-1 serial correlation of the new series. If the value of  $r_1$  is not statistically significant at the 5% level, the estimated  $\beta$  is accepted. Otherwise, the detrended series is prewhitened through

$$Y'_t = Y_t - r_1 Y_{t-1}, \quad (10)$$

where  $Y'_t$  is the prewhitened series.

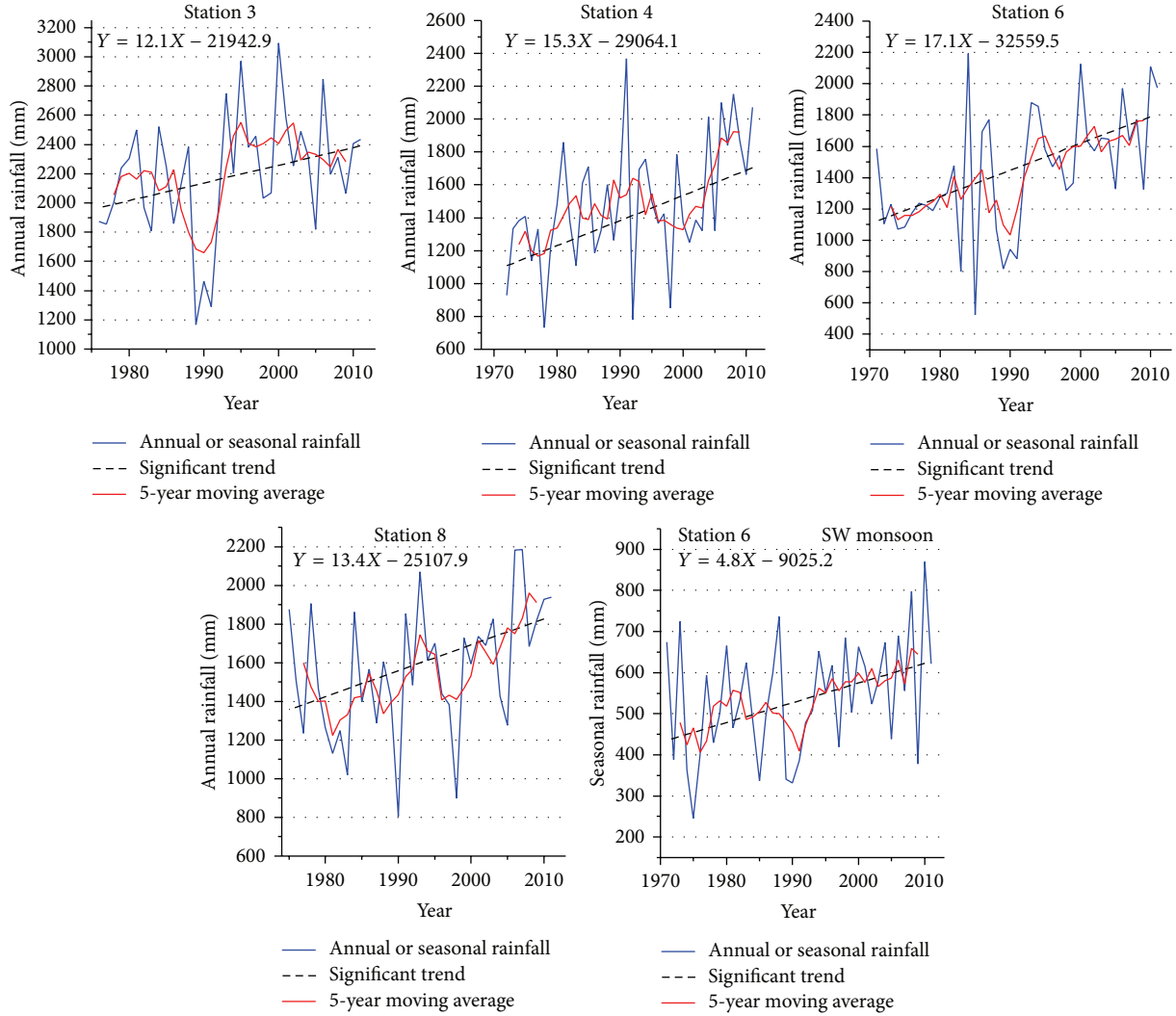


FIGURE 4: The plot of significant trends for annual and seasonal precipitation in the Langat River Basin at the 95% confidence level.

- (4) Add the monotonic trend to the prewhitened series through

$$Y''_t = Y'_t + \beta t, \tag{11}$$

where  $Y''_t$  is the trend-free prewhitened series.

- (5) Calculate the MK statistic on  $Y''_t$  series and examine the local significance of the calculated statistics.

### 3. Results and Discussion

**3.1. Analyses of Lag-1 Autocorrelation and the Prewhitening Process.** The results of lag-1 autocorrelations and the prewhitening process of the annual and seasonal precipitation and temperature in the related situations are shown in Tables 3 and 4. As shown, while the serial correlations for the annual  $P$ ,  $T_{Min}$ ,  $T_{Max}$  before the TFPW process were all positive, positive and negative serial correlations were obtained at the seasonal time series of precipitation and temperature. While the temperature variables required

the TFPW process before the MK test, the majority of the precipitation variables did not require any prewhitening procedure. The strongest and weakest autocorrelation were found in the annual  $T_{Min}$  (Station 9) and SW monsoon  $T_{Min}$  (Station 11), respectively. Generally, the temperature variables have a higher autocorrelation than did the precipitation variables. The majority of the seasonal precipitation time series is free of significant lag-1 serial correlation.

**3.2. Trend in Precipitation and Temperature Variables.** The results of the MK test, the TSS estimator, and MKRS test for  $P$ ,  $T_{Max}$ , and  $T_{Min}$  are presented in Tables 5, 6, and 7. The results of the MK test for the annual and seasonal time series are also presented in Figures 3 and 4.

**3.2.1. Analysis of Precipitation.** The results of the MK test of the annual and seasonal precipitation time series are shown in Table 5 and the significant trends at the 95% confidence level are illustrated in Figure 4. The results of the MK test

TABLE 3: Lag-1 serial correlation values for temperature variables before and after prewhitening.

Station	Critical $r_1$	$T_{Max}$		$T_{Min}$		NE $T_{Max}$		SW $T_{Max}$		NE $T_{Min}$		SW $T_{Min}$	
		$r_1$	$r_1'$	$r_1$	$r_1'$	$r_1$	$r_1'$	$r_1$	$r_1'$	$r_1$	$r_1'$	$r_1$	$r_1'$
9	0.37	0.48*	-0.01	0.58*	-0.02	0.36	—	-0.03	—	0.55*	-0.05	0.45*	0.34
10	0.31	0.37*	0.08	0.02	—	0.12	—	0.17	—	-0.09	—	0.42*	0.04
11	0.30	0.39*	0.02	0.75*	0.07	0.15	—	0.16	—	0.16	—	0.02	—

\*Significant at the 5% significance level.  
 —No need to follow TFPW process.

TABLE 4: Lag-1 serial correlation values for annual and seasonal precipitation before and after TFPW process ( $r_1'$ ).

Station	Critical $r_1$	P (mm)		NE monsoon		SW monsoon	
		$r_1$	$r_1'$	$r_1$	$r_1'$	$r_1$	$r_1'$
1	0.31	0.11	—	-0.18	—	-0.05	—
2	0.31	0.06	—	-0.07	—	0.1	—
3	0.33	0.27	—	0.06	—	-0.03	—
4	0.31	0.36*	0.05	-0.03	—	0.2	—
5	0.32	0.21	—	-0.16	—	0.09	—
6	0.31	0.29	—	-0.13	—	-0.23	—
7	0.32	0.15	—	0.07	—	0.03	—
8	0.32	0.36*	0.27	-0.08	—	0.10	—

\*Significant at the 5% level of significance.  
 —No need to follow TFPW process.

TABLE 5: The results of the MK and TSS methods for annual and seasonal precipitation in the Langat River Basin.

Site	Annual P (mm)				NE monsoon				SW monsoon			
	S	Z	P value	$\beta$ (mm/yr)	S	Z	P value	$\beta$ (mm/yr)	S	Z	P	$\beta$ (mm/yr)
1	110	1.22	0.22	+4.5	28	0.30	0.76	+0.8	104	1.16	0.24	+2.5
2	59	0.65	0.54	+3.0	72	0.80	0.43	+1.7	-44	-0.48	0.63	-1.1
3	146	2.03	0.04*	+12.6	110	1.43	0.14	+5.8	26	0.33	0.73	+1.0
4	252	2.92	0.004*	+15.3	138	1.54	0.12	+5.4	122	1.36	0.17	+3.2
5	-83	-1.0	0.30	-5.8	-37	-0.45	0.65	-1.5	-83	-1.03	0.30	-1.6
6	280	3.13	0.002*	+17.1	136	1.52	0.13	+4.1	198	2.21	0.02*	+4.8
7	73	0.91	0.37	+4.5	43	0.53	0.59	+0.7	89	1.11	0.27	+2.5
8	188	2.45	0.014*	+13.4	91	1.13	0.26	+3.9	77	0.96	0.34	+2.2

\*Statistically significant at the 95% confidence level.

TABLE 6: Results of the MK and TSS methods for annual temperature variables in the Langat River Basin.

Station	$T_{Max}$ (°C)				$T_{Min}$ (°C)			
	S	Z	P value	$\beta$ (°C/yr)	S	Z	P value	$\beta$ (°C/yr)
9	145	3.00	0.003*	+0.035	52	1.06	0.287	+0.01
10	135	1.68	0.09	+0.008	370	4.83	0.000*	+0.03
11	-29	-0.34	0.75	-0.002	401	4.84	0.000*	+0.04

\*Statistically significant at 95% confidence level.

TABLE 7: The results of the MK and TSS methods for seasonal temperature variables in the Langat River Basin.

Station	Variable	NE Monsoon				SW Monsoon			
		S	Z	P value	$\beta$ (°C/yr)	S	Z	P value	$\beta$ (°C/yr)
9	$T_{Max}$	117	2.42	0.015*	+0.04	149	3.09	0.002*	+0.03
	$T_{Min}$	-3	-0.04	0.98	+0.0001	-29	-0.62	0.54	-0.007
10	$T_{Max}$	71	0.88	0.38	+0.007	87	1.08	0.28	+0.005
	$T_{Min}$	411	5.15	0.000*	+0.046	420	5.48	0.000*	+0.04
11	$T_{Max}$	-114	-1.27	0.204	-0.012	12	0.12	0.902	+0.001
	$T_{Min}$	558	6.26	0.000*	+0.043	568	6.39	0.000*	+0.041

\*Statistically significant at the 95% confidence level.

for prewhitened annual precipitation showed that there are significant positive trends at Stations 3, 4, 6, and 8, which represents 50% of the precipitation stations. As shown in Figure 3(b), by considering the spatiality of these stations, the significance trends were obtained in these stations, which are located east and north of the basin. In addition, as illustrated by the altitude and DEM (Table 1 and Figure 1) of these stations, the positive significant trends are obtained in higher altitude areas. The land use of the area around Stations 3 and 4 are urban and forest, respectively.

The score values of this variable conformed to the  $P$  values at these stations. In addition, the largest  $S$  value obtained at Station 6 adapted to the most powerful significance trend test at that station. On the contrary, among these four stations with significant trends, Station 3 has the smallest  $S$  value and the largest  $P$  value. This indicates the smallest rate of change at this station. Nevertheless, the majority of trends for the seasonal precipitation time series were insignificant at the 95% confidence level. The only significant trend at the 95% confidence level was detected at Station 6 for SW monsoon precipitation.

The results of Theil-Sen's test of annual and seasonal precipitation time series are shown in Table 5 and significance trends at the 95% confidence level are illustrated in Figure 4. As indicated in Table 5, the largest increasing slope of significant annual precipitation occurred at Station 6, while the smallest rates were obtained at Station 3, which were 17.1 and 12.6 mm/year, respectively. Based on the results of the MK test for the annual and seasonal precipitations, the test could not detect any significant negative trends in the time series.

The consequences of the MKRS test for significant annual and seasonal precipitation and temperatures are shown in Figure 5. The sequential values of the  $U(t)$ ,  $U'(t)$ , and the confidence limits are depicted by solid red, blue, and dashed lines, respectively. As shown in Figure 5(a), the intersection point of the  $U(t)$  and  $U'(t)$  curves has changed the regime of the downward trend to the increasing trend around year 1990, which became significant in the year 2002. In spite of the existence of significant positive trends at Stations 4, 6, and 8, the MKRS test was not capable of determining the approximate beginning year of the trends. During the study period of these stations, the  $U(t)$  and  $U'(t)$  have become significant, especially around the year 2000 and after.

**3.2.2. Analysis of  $T_{Max}$ .** The outputs of the trend detection analysis for annual and seasonal maximum temperature in the Langat River Basin are presented in Tables 6 and 7 and also in Figures 5 and 6.

Concerning the annual and seasonal analysis of  $T_{Max}$ , there were downward and upward trends at the stations. Three out of seven upward trends were statistically significant and none of the decreasing trends were significant at the 5% significance level. All of the significant trends are related to Station 9, located in the mountainous area, and forest land use category. The findings also indicate that the largest  $S$  value for the annual  $T_{Max}$  was found at Station 9. The strongest warming trend in  $T_{Max}$  was conformed to the lowest  $P$  value at this station. The slope estimator test indicated an increase

of 3.5°C per century in the maximum temperature at this station, which is close to the highest rate of temperature increments, 0.99–3.44°C, in a century, reported by the IPCC in Malaysia. The rates of significant seasonal changes in SW monsoon and NE monsoon seasons for  $T_{Max}$  were 3 and 4°C per century, respectively. Thus, the warming slope of  $T_{Max}$  in the annual period is higher than the SW monsoon season and lower than NE monsoon season. These results indicate that the monsoons' winds are active regional phenomena, which influence the observed maximum temperature during these seasons.

Regarding the annual significant trend at Station 9, the MKRS test was not able to indicate any mutation point for this powerful upward trend, as shown in Figure 5(c). The series of  $U(t)$  passed the 95% confidence level in 1990, while the MKRS test detected the beginning years of trend for the annual  $T_{Max}$  at Stations 10 and 11 in 1998 and 2003, respectively. However, none of these trends are significant at the 95% confidence level. As illustrated in Figure 5(e), the warming trend for the NE monsoon  $T_{Max}$  at Station 9 began in 1997 and became significant during the same year. The MKRS test detected other intersections between  $U(t)$  and  $U'(t)$  series in the NE monsoon and SW monsoon seasons at Stations 10 and 11 after 1990, and none of them were significant at the 95% significance level.

**3.2.3. Analysis of  $T_{Min}$ .** The trend analyses for annual and seasonal  $T_{Min}$  in the three stations, Stations 9, 10, and 11, of the Langat River Basin obtained by the MK, MKRS, and TSS methods are given in Tables 6 and 7 and Figures 6 and 7. The annual MK trend test results identified the maximum  $S$  value at Station 11 and the smallest one at Station 9. Therefore, Station 9, which had the most powerful trend in  $T_{Max}$ , was replaced by Station 11 for  $T_{Min}$ . The increasing significant trend of the annual  $T_{Min}$  at Stations 10 and 11 were significant at the 95% confidence level, while it was not as strong as the annual increment in  $T_{Max}$  at Station 9.

According to the results, the highest value of the slope for the annual minimum temperature was identified at Station 11 (0.4°C/decade), while the lowest value was obtained at Station 9 (0.1°C/decade). As shown in Table 6, the probability of this trend being obtained randomly is close to zero, and thus the test results are significant at the 95% confidence level. The MK trend test for the SW monsoon and NW monsoon seasons indicated significant trends at Stations 10 and 11. The MK trend analysis of the seasonal  $T_{Min}$  showed a strong significant increasing trend at Stations 10 and 11 in the seasonal time periods. The altitudes of Stations 10 and 11 are less than the altitude of Station 9. The rates of seasonal increasing in  $T_{Min}$  at these two stations are about 4°C per century, which is near the NE monsoon trend in  $T_{Max}$  at Station 9.

The sequential MK test could not detect any beginning point for significant seasonal and annual positive trends. The result of this test showed a mutation point only at Station 9 for annual and seasonal trends in 2001 that passed the significant confidence levels in this year.

Therefore, the results of the present study indicated a climate change signal for annual rainfall, as well as the

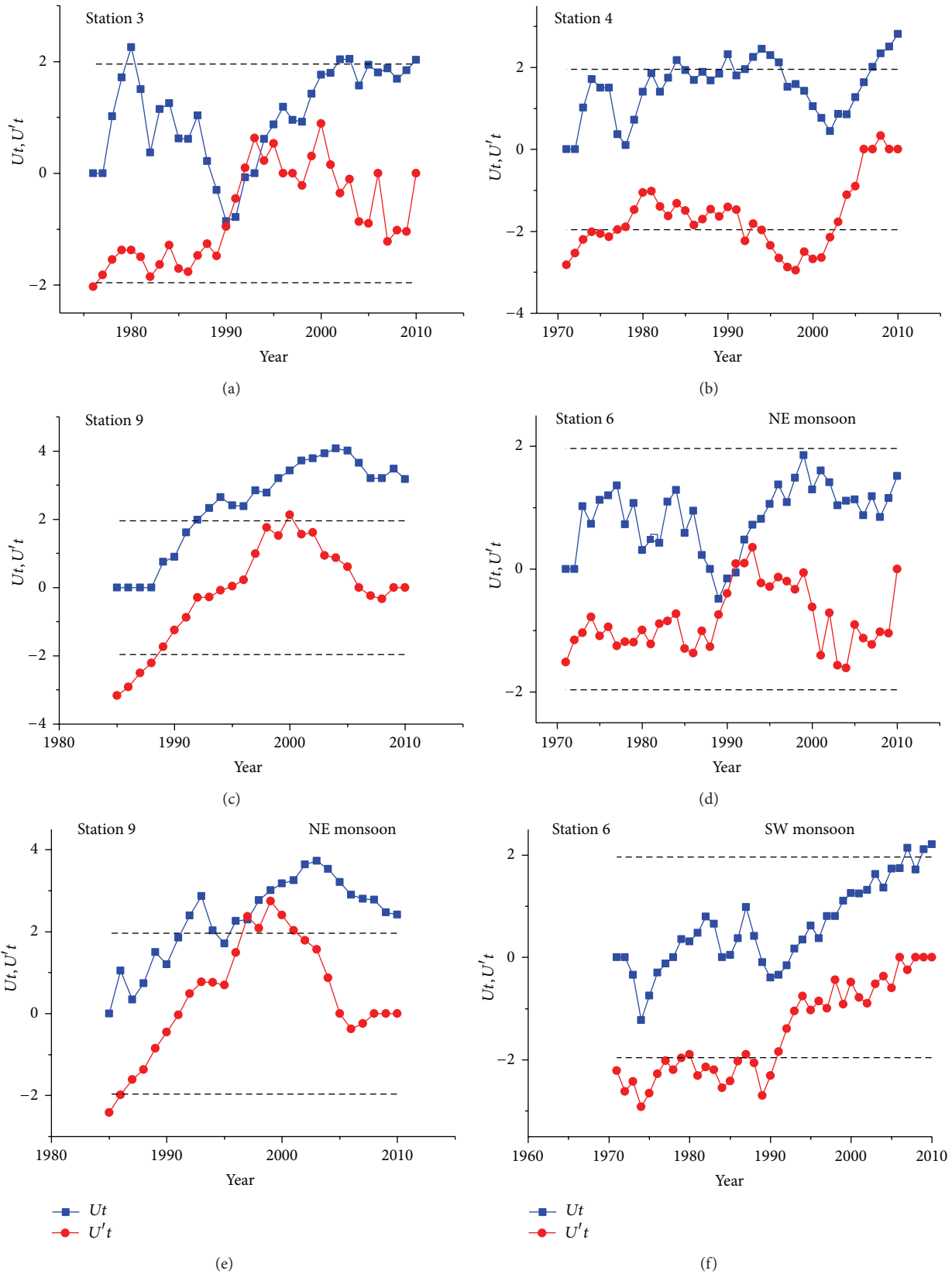


FIGURE 5: Graphical example of  $U(t)$  and backward series  $U'(t)$  of the MKRS test for annual analysis ((a), (b), and (c)), NE monsoon season ((d), and (e)), and SW monsoon (f) for precipitation and temperature at the stations with significant trends at the 95% confidence level.

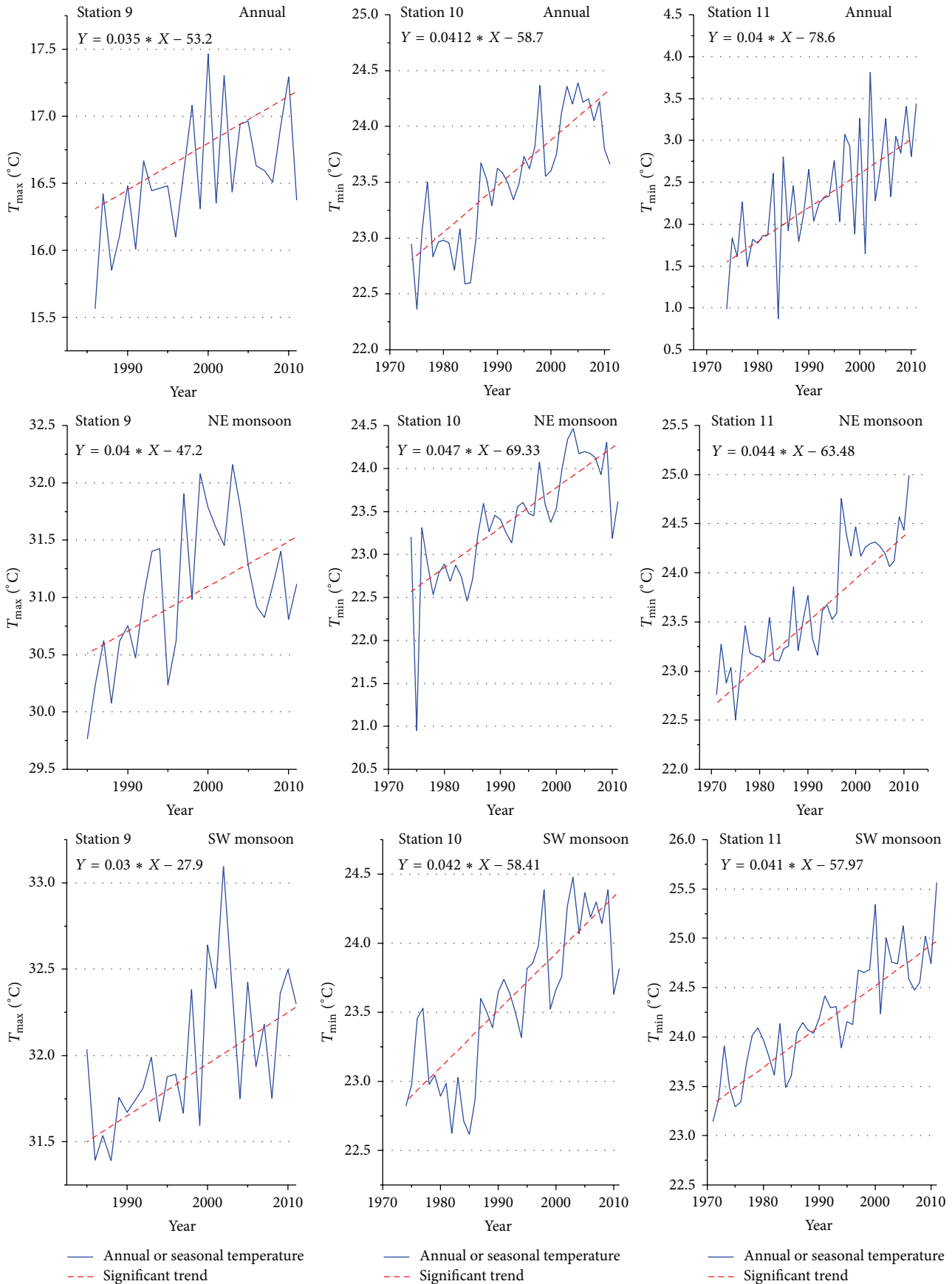


FIGURE 6: Results of significant MK trends for annual and seasonal temperature variables in the Langat River Basin at the 95% confidence level.

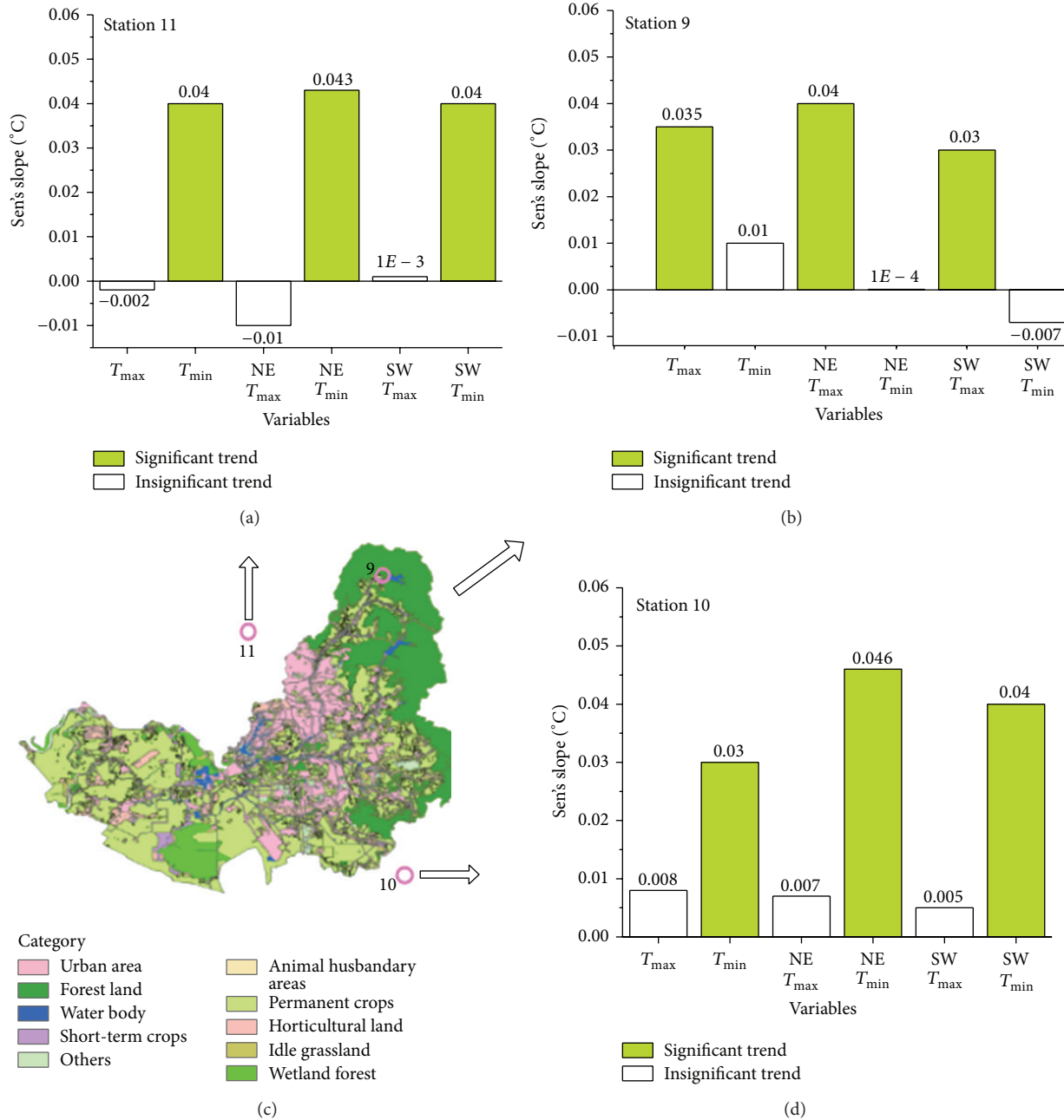


FIGURE 7: The spatial distribution of significant and insignificant trends for annual and seasonal temperatures along with corresponding Sen's slope values per year.

maximum and minimum temperatures in the Langat River Basin. These findings reflect other researchers that looked for signs of climate change for discrete climate parameters in Malaysia [10, 36, 37]. As far as we are aware, the present study is the only one that simultaneously focused on the slope of the trend in  $P$ ,  $T_{Max}$ , and  $T_{Min}$  besides the beginning time of change in climate parameters in the Langat River Basin.

**3.3. Uncertainty in Trends.** A bootstrap method was applied herein on the database to assess the uncertainty in the estimated significant slopes associated with the slope estimator method in significant trends for the annual and seasonal

precipitation and maximum and minimum temperatures by using 1000 resampling times. The bootstrap histogram, box plot, confidence intervals, and other useful statistics of the bootstrapped slope values at these stations are shown in Table 8 and Figures 8 and 9. The 95% confidence intervals of the median bootstrapped slopes were computed using the percentile method. As shown in Table 7, all of the measured Theil-Sen's slope values are placed at the 95% confidence intervals. The box-plot figure also illustrated more nonnormality in the slopes' distribution for temperature than with the precipitation in the significant stations.

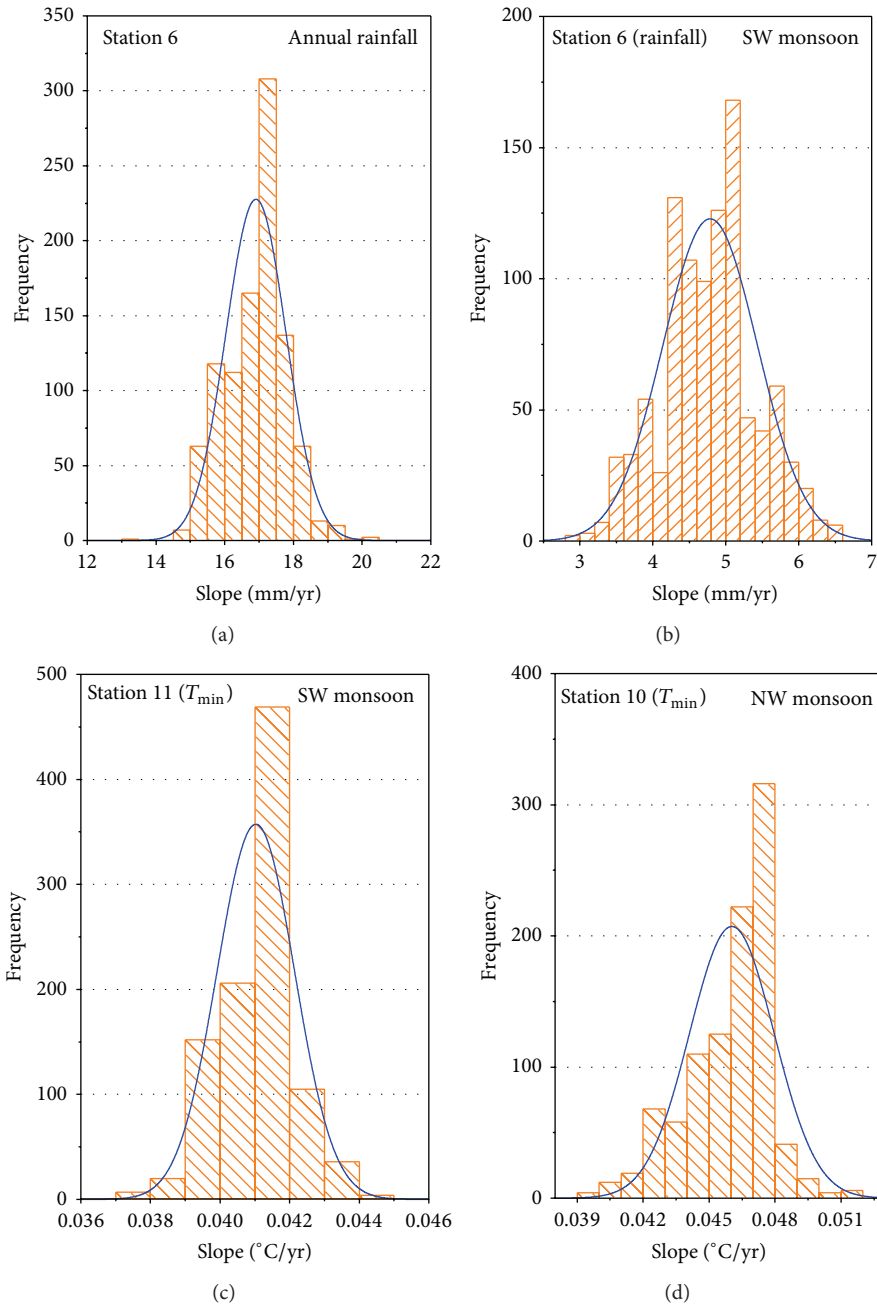


FIGURE 8: Examples of histogram of bootstrap slopes in significant trend for annual and seasonal temperatures ( $T_{Max}$ ,  $T_{Min}$ ) and precipitation.

#### 4. Conclusions

Changes in the climate variables due to global warming and regional systems, such as monsoon phenomena, were investigated at the Langat River Basin to precisely determine the rate of changes in this strategic river basin. The main objective of this study was the annual and seasonal trend analysis for  $P$ ,  $T_{Max}$ , and  $T_{Min}$  at the 11 selected stations in this river basin to support the water management policymakers for planning for the future. Three nonparametric methods, the MK, MKRS test, and TSS, were applied to complete the

detection of trends for the variables. The analyses of the MK and TSS were performed after eliminating the influence of significant lag-1 serial correlations from the time series using the TFPW technique. The results of these trend tests showed significant increasing trends at four stations (Stations 3, 4, 6, and 8) for annual precipitation, one station for the SW monsoon season (Station 6), one station for the seasonal and annual  $T_{Max}$ , and two stations for the annual and seasonal  $T_{Min}$ , at the 95% confidence level. The rate of changes in this river basin showed that north and east of basin have faced a moderate change in the maximum and minimum

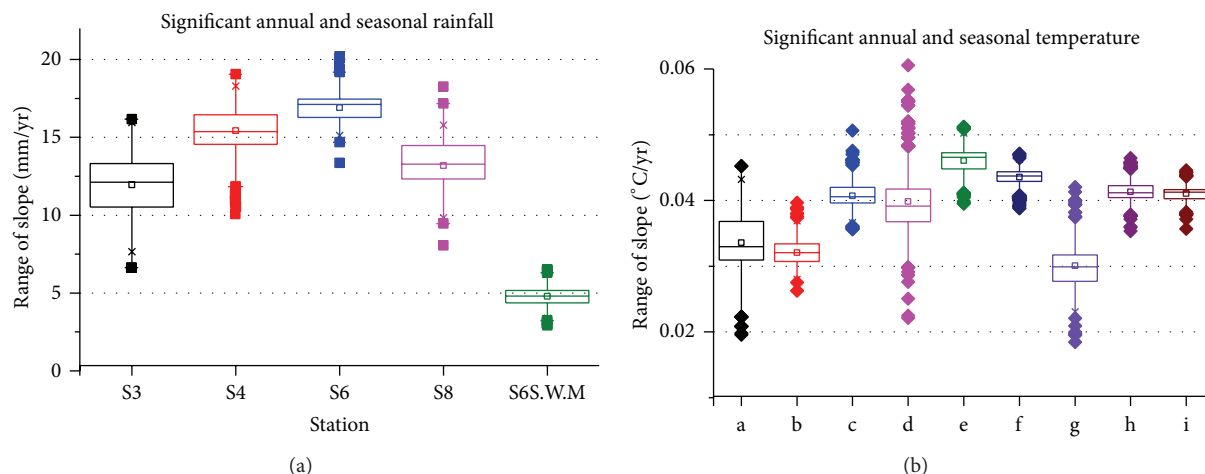


FIGURE 9: Boxplot of slope obtained from bootstrap method for the significant trends of annual and seasonal rainfall and temperatures (a: S9 ( $T_{Max}$ ), b: S10 ( $T_{Min}$ ), c: S11 ( $T_{Min}$ ), d: S9 ( $T_{Max}$  NE monsoon), e: S10 ( $T_{Min}$  NE monsoon), f: S11 ( $T_{Min}$  NE monsoon), g: S9 ( $T_{Max}$  SW monsoon), h: S10 ( $T_{Min}$  SW monsoon), i: S11 ( $T_{Min}$  SW monsoon)).

TABLE 8: The bootstrap results for slopes in significant trends for rainfall and maximum and minimum temperatures in the Langat River Basin.

Station	Parameter	Estimated Theil-Sen's slope	Bootstrap results of slope			
			The 95% confidence intervals		Mean	Standard deviation
S3	Precipitation	12.6	8.369	15.738	12.01	1.95
S4		15.3	12.732	18.293	15.34	1.11
S6		17.1	15.244	18.748	16.89	0.91
S8		13.4	10.172	15.516	13.25	1.46
S6 (SW monsoon)		4.8	3.477	6.051	4.77	0.67
S9 ( $T_{Max}$ )	Temperature	0.035	0.023	0.042	0.034	0.005
S10 ( $T_{Min}$ )		0.03	0.029	0.037	0.032	0.002
S11 ( $T_{Min}$ )		0.04	0.036	0.046	0.041	0.002
S9 ( $T_{Max}$ NE monsoon)		0.04	0.033	0.052	0.04	0.005
S10 ( $T_{Min}$ NE Monsoon)		0.046	0.042	0.05	0.047	0.002
S11 ( $T_{Min}$ NE monsoon)		0.043	0.040	0.046	0.044	0.001
S9 ( $T_{Max}$ SW monsoon)		0.03	0.025	0.038	0.03	0.003
S10 ( $T_{Min}$ SW monsoon)		0.04	0.038	0.045	0.041	0.002
S11 ( $T_{Min}$ SW monsoon)		0.04	0.039	0.043	0.041	0.001

temperatures and rainfall during the past four decades. In other words, the weather north and east of basin became warmer and wetter during the study period.

While the rates of upward significant changes for annual precipitation ranged from 12.6 to 17.1 mm per year, for the rate of change in SW monsoon, a significant trend was found to be about one-third (4.8 mm per year). The TSS test determined the slope of an upward trend for the annual and seasonal  $T_{Max}$  in a range of 3.5 to 4°C per century. It is the same for the annual and seasonal significant trends for the  $T_{Min}$  variable. Also, all of the significant trends were found at the stations located in the north, east, and northeast parts of the basin. Their elevations are higher than those stations in the west region of the river basin. The land use of these stations is forest or urban area. The other important result is that all of the significant long-term trends in precipitation and temperature gradually increased during the study period.

Also, it showed that the monsoon system is a powerful phenomenon among all other active systems in the region. This rate of change in the annual and seasonal rainfall,  $T_{Max}$  and  $T_{Min}$  temperature may drive some changes in land cover/land use of the basin therefore increasing the flood frequency in this region, especially during the NE monsoon season. Furthermore, changes in the water demand pattern for all type of usage in the region is another consequence, due to the alterations in climate parameters. Future studies in trend analysis for extreme rainfall events and other indices of precipitation in the Langat River Basin would be very useful for future water resource planning.

### Conflict of Interests

The authors declare that there is no conflict of interests regarding the publication of this paper.

## Acknowledgments

The authors would like to thank the Department of Irrigation and Drainage Malaysia (DID) and the Malaysian Meteorological Department (MMD), both under the Ministry of Natural Resources and Environment Malaysia (NRE), for providing data and technical support. The authors would also like to sincerely thank the Ministry of Science, Technology and Innovation (MOSTI) for the financial support.

## References

- [1] T. F. Stocker, D. Qin, G.-K. Plattner et al., "Climate change 2013: the physical science basis," in *Intergovernmental Panel on Climate Change, Working Group I Contribution to the IPCC Fifth Assessment Report (AR5)*, Cambridge University Press, New York, NY, USA, 2013.
- [2] IPCC2007, *Climate Change 2007: The Physical Science Basis*, IPCC, Geneva, Switzerland, 2007.
- [3] S. Solomon, *Climate Change 2007—The Physical Science Basis: Working Group I Contribution to the Fourth Assessment Report of the IPCC*, vol. 4, Cambridge University Press, 2007.
- [4] P. Nyeko-Ogiramoi, P. Willems, and G. Ngirane-Katashaya, "Trend and variability in observed hydrometeorological extremes in the Lake Victoria basin," *Journal of Hydrology*, vol. 489, pp. 56–73, 2013.
- [5] D. H. Burn and M. A. H. Elnur, "Detection of hydrologic trends and variability," *Journal of Hydrology*, vol. 255, no. 1–4, pp. 107–122, 2002.
- [6] H. Tabari, B. S. Somee, and M. R. Zadeh, "Testing for long-term trends in climatic variables in Iran," *Atmospheric Research*, vol. 100, no. 1, pp. 132–140, 2011.
- [7] M. Gocic and S. Trajkovic, "Analysis of changes in meteorological variables using Mann-Kendall and Sen's slope estimator statistical tests in Serbia," *Global and Planetary Change*, vol. 100, pp. 172–182, 2013.
- [8] D. Liu, S. Guo, X. Chen, and Q. Shao, "Analysis of trends of annual and seasonal precipitation from 1956 to 2000 in Guangdong Province, China," *Hydrological Sciences Journal*, vol. 57, no. 2, pp. 358–369, 2012.
- [9] S. Yue, P. Pilon, B. Phinney, and G. Cavadias, "The influence of autocorrelation on the ability to detect trend in hydrological series," *Hydrological Processes*, vol. 16, no. 9, pp. 1807–1829, 2002.
- [10] W. N. Meng, C. Alejandro, A. Wahab, and A. Khairi, "A study of global warming in malaysia," *Jurnal Teknologi F*, pp. 1–10, 2005.
- [11] F. T. Tangang, L. Juneng, E. Salimun, K. M. Sei, L. J. Le, and H. Muhamad, "Climate change and variability over Malaysia: gaps in science and research information," *Sains Malaysiana*, vol. 41, no. 11, pp. 1355–1366, 2012.
- [12] J. Suhaila, S. M. Deni, W. A. N. Zawiah Zin, and A. A. Jemain, "Trends in peninsular Malaysia rainfall data during the southwest monsoon and northeast monsoon seasons: 1975–2004," *Sains Malaysiana*, vol. 39, no. 4, pp. 533–542, 2010.
- [13] R. Nurmohamed and S. Naipal, "Trends and variation in monthly rainfall and temperature in suriname," in *Proceedings BALWOIS Conference on Water Observation and Information-System for Decision Support, Ohrid, FY Republic of Macedonia, 25–29 May 2000*, p. 3, 2004.
- [14] J. Taubenheim, "An easy procedure for detecting a discontinuity in a digital time series," *Zeitschrift für Meteorologie*, vol. 39, pp. 344–347, 1989.
- [15] J. Honaker, G. King, and M. Blackwell, "Amelia II: a program for missing data," *Journal of Statistical Software*, vol. 45, no. 7, pp. 1–47, 2011.
- [16] C. Data, *Guidelines on Analysis of Extremes in a Changing Climate in Support of Informed Decisions for Adaptation*, 2009.
- [17] R. Bremer, "Outliers in statistical data," *Technometrics*, vol. 37, pp. 117–118, 1995.
- [18] J. F. González-Rouco, J. L. Jiménez, V. Quesada, and F. Valero, "Quality control and homogeneity of precipitation data in the southwest of Europe," *Journal of Climate*, vol. 14, no. 5, pp. 964–978, 2001.
- [19] A. C. Costa and A. Soares, "Homogenization of climate data: review and new perspectives using geostatistics," *Mathematical Geosciences*, vol. 41, no. 3, pp. 291–305, 2009.
- [20] M. A. Kohler, "Double-mass analysis for testing the consistency of records and for making adjustments," *Bulletin of the American Meteorological Society*, vol. 30, pp. 188–189, 1949.
- [21] S. M. Deni, J. Suhaila, W. Z. W. Zin, and A. A. Jemain, "Trends of wet spells over Peninsular Malaysia during monsoon seasons," *Sains Malaysiana*, vol. 38, no. 2, pp. 133–142, 2009.
- [22] K. Chaouche, L. Neppel, C. Dieulin et al., "Analyses of precipitation, temperature and evapotranspiration in a French Mediterranean region in the context of climate change," *Comptes Rendus: Geoscience*, vol. 342, no. 3, pp. 234–243, 2010.
- [23] D. Machiwal and M. K. Jha, "Time series analysis of hydrologic data for water resources planning and management: a review," *Journal of Hydrology and Hydromechanics*, vol. 54, pp. 237–257, 2009.
- [24] H. Verworn, S. Krämer, M. Becker, and A. Pfister, "The impact of climate change on rainfall runoff statistics in the Emscher-Lippe region," in *Proceedings of the 11th International Conference on Urban Drainage*, pp. 1–10, Edinburgh, UK, 2008.
- [25] X. Yang, L. Xu, K. Liu, C. Li, J. Hu, and X. Xia, "Trends in temperature and precipitation in the zhangweinan river basin during the last 53 years," *Procedia Environmental Sciences*, vol. 13, pp. 1966–1974, 2012.
- [26] O. E. Scarpati, L. B. Spescha, J. A. F. Lay, and A. D. Capriolo, "Soil water surplus in salado river basin and its variability during the last forty years (buenos aires province, argentina)," *Water*, vol. 3, pp. 132–145, 2011.
- [27] R. Sneyers, *On the Statistical Analysis of Series of Observations*, WMO, 1991.
- [28] T. Partal and E. Kahya, "Trend analysis in Turkish precipitation data," *Hydrological Processes*, vol. 20, no. 9, pp. 2011–2026, 2006.
- [29] H. Theil, "A rank-invariant method of linear and polynomial regression analysis," in *Henri Theil's Contributions to Economics and Econometrics*, pp. 345–381, Springer, 1992.
- [30] Y. Dinpashoh, D. Jhajharia, A. Fakheri-Fard, V. P. Singh, and E. Kahya, "Trends in reference crop evapotranspiration over Iran," *Journal of Hydrology*, vol. 399, no. 3–4, pp. 422–433, 2011.
- [31] D. Karpouzou, S. Kavalieratou, and C. Babajimopoulos, "Trend analysis of precipitation data in Pieria region (Greece)," *European Water*, vol. 30, pp. 31–40, 2010.
- [32] C. J. Martinez, J. J. Maleski, and M. F. Miller, "Trends in precipitation and temperature in Florida, USA," *Journal of Hydrology*, vol. 452–453, pp. 259–281, 2012.
- [33] M. Santos and M. Frago, "Precipitation variability in Northern Portugal: data homogeneity assessment and trends in extreme precipitation indices," *Atmospheric Research*, vol. 131, pp. 34–45, 2013.

- [34] H. von Storch and A. Navarra, *Analysis of Climate Variability: Applications of Statistical Techniques*, Springer, 1999.
- [35] D. H. Burn, J. M. Cunderlik, and A. Pietroniro, "Hydrological trends and variability in the Liard River basin," *Hydrological Sciences Journal*, vol. 49, no. 1, pp. 53–68, 2004.
- [36] T. Stocker, D. Qin, G. Plattner et al., *Summary for Policymakers*, Cambridge University Press, New York, NY, USA, 2013.
- [37] N. Palizdan, Y. Falamarzi, Y. F. Huang, T. S. Lee, and A. H. Ghazali, "Regional precipitation trend analysis at the Langat River Basin, Selangor, Malaysia," vol. 117, no. 3-4, pp. 589–606, 2014.

## Research Article

# Dominant Large-Scale Atmospheric Circulation Systems for the Extreme Precipitation over the Western Sichuan Basin in Summer 2013

Yamin Hu,<sup>1,2</sup> Panmao Zhai,<sup>2</sup> Lihong Liu,<sup>2</sup> Yang Chen,<sup>2</sup> and Yanju Liu<sup>3</sup>

<sup>1</sup>Guangdong Climate Center, Guangzhou 510080, China

<sup>2</sup>State Key Laboratory of Severe Weather, Chinese Academy of Meteorological Sciences, Beijing 100081, China

<sup>3</sup>National Climate Center, Beijing 100081, China

Correspondence should be addressed to Panmao Zhai; [pmzhai@cma.gov.cn](mailto:pmzhai@cma.gov.cn)

Received 21 October 2014; Accepted 3 December 2014

Academic Editor: Jieshun Zhu

Copyright © 2015 Yamin Hu et al. This is an open access article distributed under the Creative Commons Attribution License, which permits unrestricted use, distribution, and reproduction in any medium, provided the original work is properly cited.

The western Sichuan Basin (WSB) is a rainstorm center influenced by complicated factors such as topography and circulation. Based on multivariable empirical orthogonal function technique for extreme precipitation processes (EPP) in WSB in 2013, this study reveals the dominant circulation patterns. Results indicate that the leading modes are characterized by “Saddle” and “Sandwich” structures, respectively. In one mode, a TC from the South China Sea (SCS) converts into the inverted trough and steers warm moist airflow northward into the WSB. At the same time, WPSH extends westward over the Yangtze River and conveys a southeasterly warm humid flow. In the other case, WPSH is pushed westward by TC in the Western Pacific and then merges with an anomalous anticyclone over SCS. The anomalous anticyclone and WPSH form a conjunction belt and convey the warm moist southwesterly airflow to meet with the cold flow over the WSB. The configurations of WPSH and TC in the tropic and the blocking and trough in the midhigh latitudes play important roles during the EPPs over the WSB. The persistence of EPPs depends on the long-lived large-scale circulation configuration steady over the suitable positions.

## 1. Introduction

A particular challenge to operational weather forecasters is extreme precipitation processes (EPPs) forecasting, and especially those topography-related events are more complicated, such as over the Taiwan [1–3], the Mediterranean [4], the Rocky Mountains [5].

The western Sichuan Basin (WSB) (102°–108°E, 28°–33°N) is well-known as a rainy region in the western China, which is also one of rainstorm centers in China [6]. Some studies concentrated the effects of the topography of the Sichuan Basin and the Tibetan Plateau on the precipitation events by numerical simulation and observation analyses [7–11].

Numerous studies paid more attention to the favorable weather systems for the formation and maintenance of heavy rainfall over the WSB, such as the mid-high latitude blocking and trough, the Western Pacific Subtropical High (WPSH) [12–15], the southwest vortex [16–18], the South Asia high

[19], and other mesoscale synoptic systems [20]. Shi et al. [14] pointed out that 84% of rainstorm processes could be associated with the WPSH during June–September from 1998 to 2008 over Sichuan. However, most rainstorm processes are influenced by the different position of the WPSH [21]. During the rainy season (May 1 to September 30), four typical circulation patterns were summarized over the WSB [22], including the plateau vortex pattern, the shortwave trough pattern in the westerlies, one trough between two ridge patterns and the shear line pattern over the Yangtze-Huaihe region. More interestingly, both the circulation systems of one trough between the double blocking highs [13, 22, 23] and those of one ridge between the double troughs [24–26] could be beneficial to the production of heavy precipitation over WSB. Why could the seemingly contradictory or different configurations be favorable for heavy rainfall over WSB?

Furthermore, the above mentioned researches mainly focus on the importance of the mid-high latitude circulation

systems. Chen et al. [27] addressed that the depression in the tropic also played an important role in EPPs over Sichuan on July 26–30, 2001, July 30–August 1, 2002, and September 23–26, 2008. Few studies of EPPs over WSB, however, gave enough consideration to the circulation systems from the low latitudes and the circulation configurations from the different latitude.

Recently, more attentions have been paid to EPPs because they have the potential to become hazardous virtually anywhere in the world. Doswell et al. [4] investigated three cases of project ANOMALIA with heavy precipitation in the western Mediterranean region. Their evaluation showed the unique characteristics of each event, as well as some limited similarities.

During summer 2013, WSB was frequently attacked by EPPs, especially the earthquake-hit areas (i.e., Wenchuan and Ya'an). Extreme precipitations resulted in serious natural disasters, like mountain torrents and landslides. The severe floods and their associated natural disasters caused lots of human life and property damage as well. There were 358 large-scale geological disasters. The unusually heavy rain caused flash floods in the Minjiang River, the Tuojiang River, and so on. In addition, statistics data reported that 16 million people were affected by the flood which also caused direct economic loss of 41.5 billion Yuan (RMB). That catastrophe has undoubtedly intensified the disaster over geologically vulnerable regions such as Wenchuan, Ya'an, and other earthquake-hit areas. However, what are the dominant circulation systems and how do they match up to result in the EPPs over WSB during summer 2013? What are the similarities among the circulation systems during the EPPs?

In this study, we will focus on the above questions. Firstly, by exploring the daily anomalous circulation of the 500-hPa geopotential height and the water vapor transport features, the main impacting circulation systems are analyzed. Further, by applying the multivariable empirical orthogonal function (MV-EOF) technique, two dominant patterns and their corresponding atmospheric circulation configurations, as well as their conceptual models, are demonstrated.

The rest of this paper is organized as follows. Descriptions of data and analysis method are given in Section 2. The extreme precipitation processes overviews are discussed in Section 3. In Section 4, large-scale circulation and water vapor transport features for each process are investigated, so as to capture their impacting systems in common. In Section 5, the two dominant modes of the EPPs and their conceptual models are concluded. A summary and discussion of the obtained results are provided in Section 6. This study will offer forecasters some useful knowledge in understanding extreme precipitation occurred over the WSB.

## 2. Data and Analysis Methods

A dataset including 2,480 stations for daily precipitation data is provided by the National Meteorological Information Centre, China Meteorological Administration (CMA). The daily reanalysis data are provided by the National Centers for Environmental Prediction and National Center for Atmospheric Research (NCEP/NCAR) with a horizontal resolution

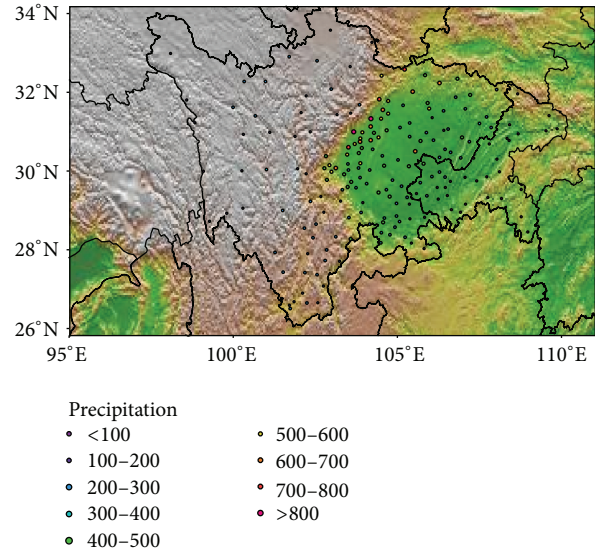


FIGURE 1: Rainfall spatial distributions during the period June 18–July 19, 2013 (unit: mm).

of  $2.5^\circ \times 2.5^\circ$  and 17 vertical levels [28]. To handle the complexity of circulation features of all the extreme precipitation processes, the paper computed the correlation coefficient between precipitation and the 500-hPa geopotential height field, and then rainfall and 7 high-correlated circulation indices were dealt with the multivariable empirical orthogonal function (MV-EOF) technique to extract the dominant circulation modes of EPPs.

We also introduced several other indices, including the Balkhash Lake Depression (BalkhaD), the Baikal Blocking High (BaikaBH), the Okhotsk Sea Depression (OkhotSD), the Continent Sector of the West Pacific Subtropical High (CSWPSH), the Indian Depression (IndiaD), the South China Sea Depression (SCSD), and the West Pacific Tropical Cyclone (WPTC), defined as the area-averaged 500-hPa geopotential height over regions of ( $48^\circ$ – $55^\circ$ N,  $78^\circ$ – $85^\circ$ E), ( $48^\circ$ – $58^\circ$ N,  $98^\circ$ – $108^\circ$ E), ( $47^\circ$ – $53^\circ$ N,  $130^\circ$ – $137^\circ$ E), ( $27^\circ$ – $32^\circ$ N,  $114^\circ$ – $119^\circ$ E), ( $20^\circ$ – $26^\circ$ N,  $81^\circ$ – $90^\circ$ E), ( $12^\circ$ – $20^\circ$ N,  $108^\circ$ – $117^\circ$ E), and ( $14^\circ$ – $20^\circ$ N,  $128^\circ$ – $136^\circ$ E), respectively. The standard deviation was denoted by  $\sigma$  in this study.

## 3. Overviews of the Extreme Precipitation Events in 2013

From mid-June to mid-July in 2013, precipitation mainly concentrated over the WSB with frequent process, extreme intensity, and long duration, which resulted in multiple floods, especially in the western region. Maximum daily rainfall exceeded 800 mm, which was remarkably above normal (Figure 1). On regional average, daily precipitation was  $2\sigma$  above normal frequently. The region recorded 4 EPPs during the period June 19–22, June 30–July 2, July 3–5, and July 8–11, respectively (Figure 2). In particular, during the last process, precipitation was heaviest and rainstorm duration persisted three days longer. Such extremes occurred in

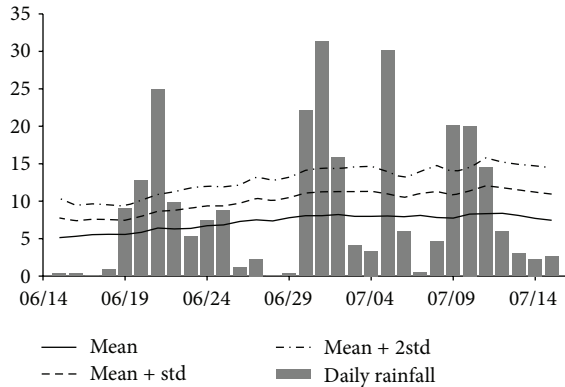


FIGURE 2: Daily regional precipitation ( $102^{\circ}$ – $108^{\circ}$ E,  $28^{\circ}$ – $33^{\circ}$ N) during the period June 15–July 15, 2013 (the bar represents daily rainfall, the solid line is daily climatological average, and the dash/dash-dot line is over onefold/twofold standard deviation above normal, resp.) (unit: mm).

the neighborhood of 7 stations with daily rainfall over 50 mm. That process has set the record in the Sichuan Basin since 1951 and was strictly in accordance with the regional persistent rainstorm events as defined by Chen and Zhai [29].

#### 4. Large-Scale Atmospheric Circulation and Water Vapor Transport Features

The atmospheric circulation provides a basic background for understanding mechanism of extreme event. *Some recent studies [30–32] indicated that in summer 2013, SSTs in the Western Pacific Warm Pool region was higher than normal. At that background, the East Asia summer monsoon is stronger than normal and the West Pacific subtropical high (WPSH) frequently strengthened and westward expanded. More than normal tropical cyclones were observed in the South China Sea. Furthermore, weaker East Asia troughs frequently occurred in the mid-high latitudes. All such circulation features are favorable for forming the “Saddle” and “Sandwich” structures thus eventually causing precipitation in WSB.*

In the following, we discuss main features as shown in the 500-hPa geopotential height and water vapor transport anomaly field for the four EPPs. It is noted that the terrains of the Tibetan Plateau and the Sichuan Basin, as well as the southwest vortex and the South Asia High, also can contribute to the extreme precipitation process in WSB, which, however, are not discussed in this study.

##### 4.1. The First Process during June 19–22 (Figure Not Shown).

One ridge (over the Baikal Lake) between the double troughs (over the Balkhash Lake and the Okhotsk Sea) exhibited over the mid-high latitudes in 500-hPa geopotential height. The WPSH was larger than normal and stretched westward over the mid-lower reaches of the Yangtze River (MLRYR). Its continental sector formed an anomalous anticyclone over the Yangtze-Huaihe Rivers region. Because of the WPSH favorable position, the westerlies trough conveyed cold-dry air from the mid-high latitudes into the Sichuan Basin. At

the same time, the tropical storm “Bebinca,” locating over the South China Sea (SCS), transported the warm moist airflow from the south. Therefore, the water vapor convergence over the WSB stemmed from the “Bebinca” and the WPSH.

##### 4.2. The Second Process during June 30–July 2 (Figure 3).

In the mid-high latitudes, there existed a low and a high system over the western and eastern Eurasia in the 500-hPa geopotential height field, respectively. In particular, the high pressure barrier developed over the northeast side of Sichuan Basin. This held back the cold airflow into the Sichuan Basin. On the other hand, the WPSH intensified and extended westward near  $110^{\circ}$ E and its northwestern flank was located over the WSB. Meanwhile, the tropical cyclone (TC) “Rumbia” moved into the SCS. Both WPSH and TC transported a large amount of warm water vapor into the WSB. And the terrains of the Tibetan Plateau provided favorable conditions for the moist airflow to be lifted and to release conditional or convective instabilities. Therefore, the combination of WPSH and TC played an important role in transferring the warm moist flow.

##### 4.3. The Third Process during July 3–5 (Figure Not Shown)

. This process was different from the others, which was a widespread extreme precipitation rather than a persistent precipitation in the WSB. It was a typical large-scale frontal precipitation, especially on July 5. During the process, a deep mid-latitude trough developed over the north side of the Sichuan Basin and a blocking high located over the Okhotsk Sea. Meanwhile, the WPSH intensified and extended westward, but its ridge location was more southward than normal. At this moment, the warmer stream from the WPSH confronted the colder air from the rear of the mid-high latitudes deep trough over the Sichuan Basin. Such feature created a region scale moist airflow convergence. Because there was no depression over the SCS or Western Pacific (WP), the water vapor could not be persistently supplied to the WSB. On 6 July, the mid-high latitude circulations have rectified and the WPSH retreated eastward. Therefore, the precipitation-favorable circulation could not long-lived maintain over the Sichuan Basin.

##### 4.4. The Fourth Process during July 8–11 (Figure 4).

The precipitation during this process was heaviest and the rainstorm duration persisted more than three days in the neighborhood of 7 stations with daily rainfall over 50 mm. However, the high latitude circulation feature was seemingly opposite to the first precipitation process. The trough and ridge were active in the westerlies zone. The WPSH intensified and its continental sector extended westward near  $105^{\circ}$ E. Moreover, the tropical storm “Souluk” made the WPSH more northward of normal. The persistent extreme precipitation process owned to the convergence between the cold airflow behind the blocking high in Baikal Lake and the warm southeasterly airflow from the westward-extending and northward-shifting WPSH over MLRYR.

In summary, four extreme precipitation processes happened over the WSB in summer 2013, including three persistent EPPs. The impacting large-scale atmospheric circulation

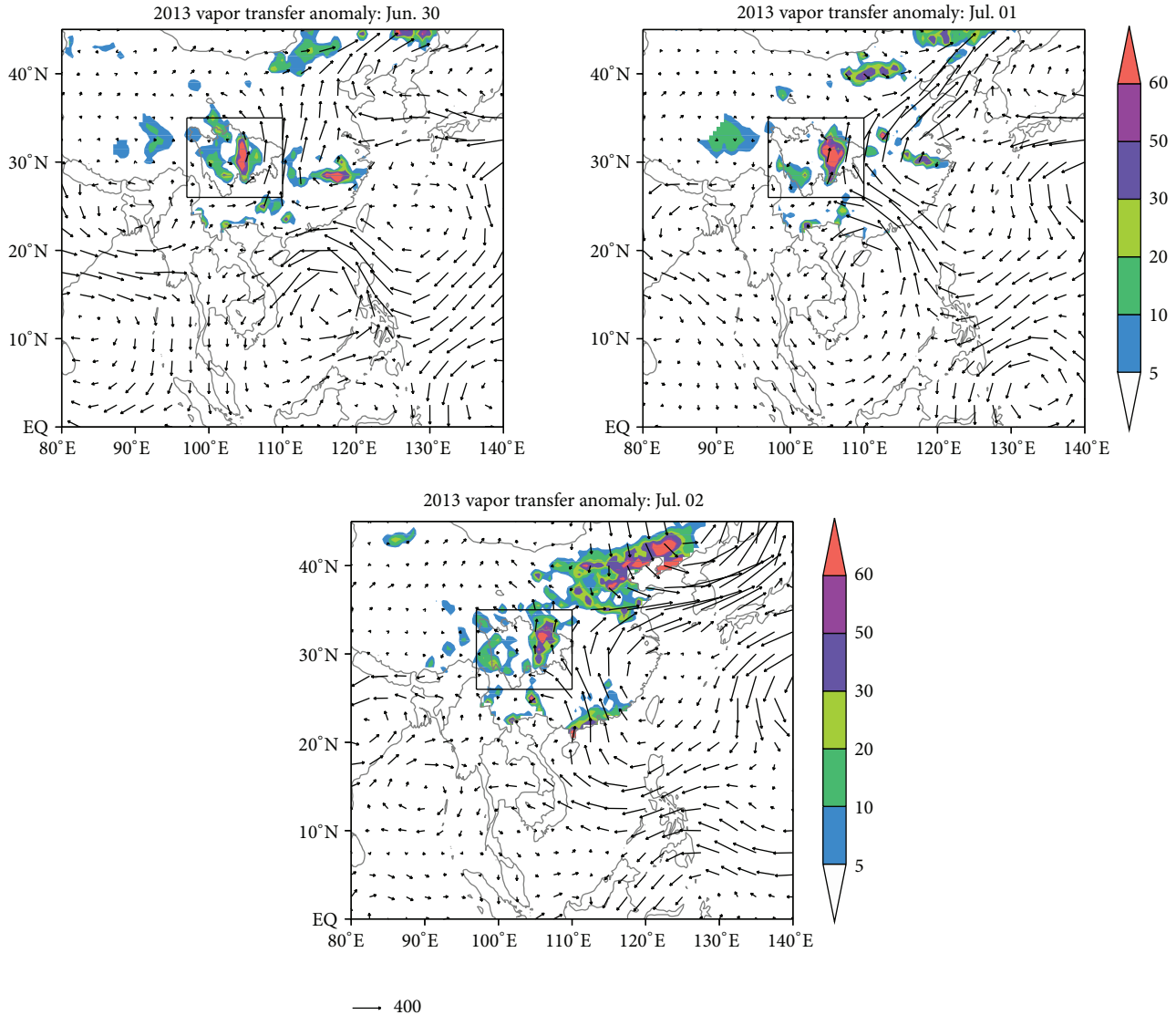


FIGURE 3: Vertically integrated water vapor transport anomaly ( $\text{kg}\cdot\text{m}^{-1}\cdot\text{s}^{-1}$ ) (shading: rainfall > 5 mm) for the 2nd process during the period June 30–July 2, 2013.

and water vapor transport features are very complicated. The EPPs tend to happen over the WSB under the following two circumstances: (a) one ridge between the double troughs (the 1st process) or a low/high value system in the western/eastern Eurasian (the 2nd process) exhibits over the mid-high latitudes. This feature combines the occurrences of a TC and the strengthening and westward-extending WPSH. (b) A blocking high develops in the high latitudes (the 3rd process) or a deep trough occurs in the westerlies zone (the 4th process). Such circulation cooperates with an anomalous anticyclone (the 3rd and 4th processes) over SCS and the strengthening, westward-extending, and northward-shifting WPSH. Therefore, both the WPSH and the TC contribute to four EPPs over the WSB in summer 2013. Chen et al. [27] draw a similar conclusion in Sichuan on July 26–30, 2001, July 30–August 1, 2002, and September 23–26, 2008. Still in another condition, the above mentioned two types

of opposite circulation pattern—an anomalous cyclone (the 1st and 2nd processes) and an anomalous anticyclones (the 3rd and 4th processes) over SCS seem to be both favorable for the rainstorm process in the WSB. But how can such contradictory conditions lead to the EPPs?

## 5. Dominant Impacting System Pattern Configurations of EPPs in the WSB

The atmospheric circulation systems, which lead to four extreme precipitation processes in the WSB in summer 2013, are too complicated to capture their similarities. To solve this difficulty, correlation coefficients between daily precipitation over the WSB and 500-hPa geopotential height field were computed from June 18 to July 20, 2013 (Figure 5). Seven high correlated key circulation systems are identified, including

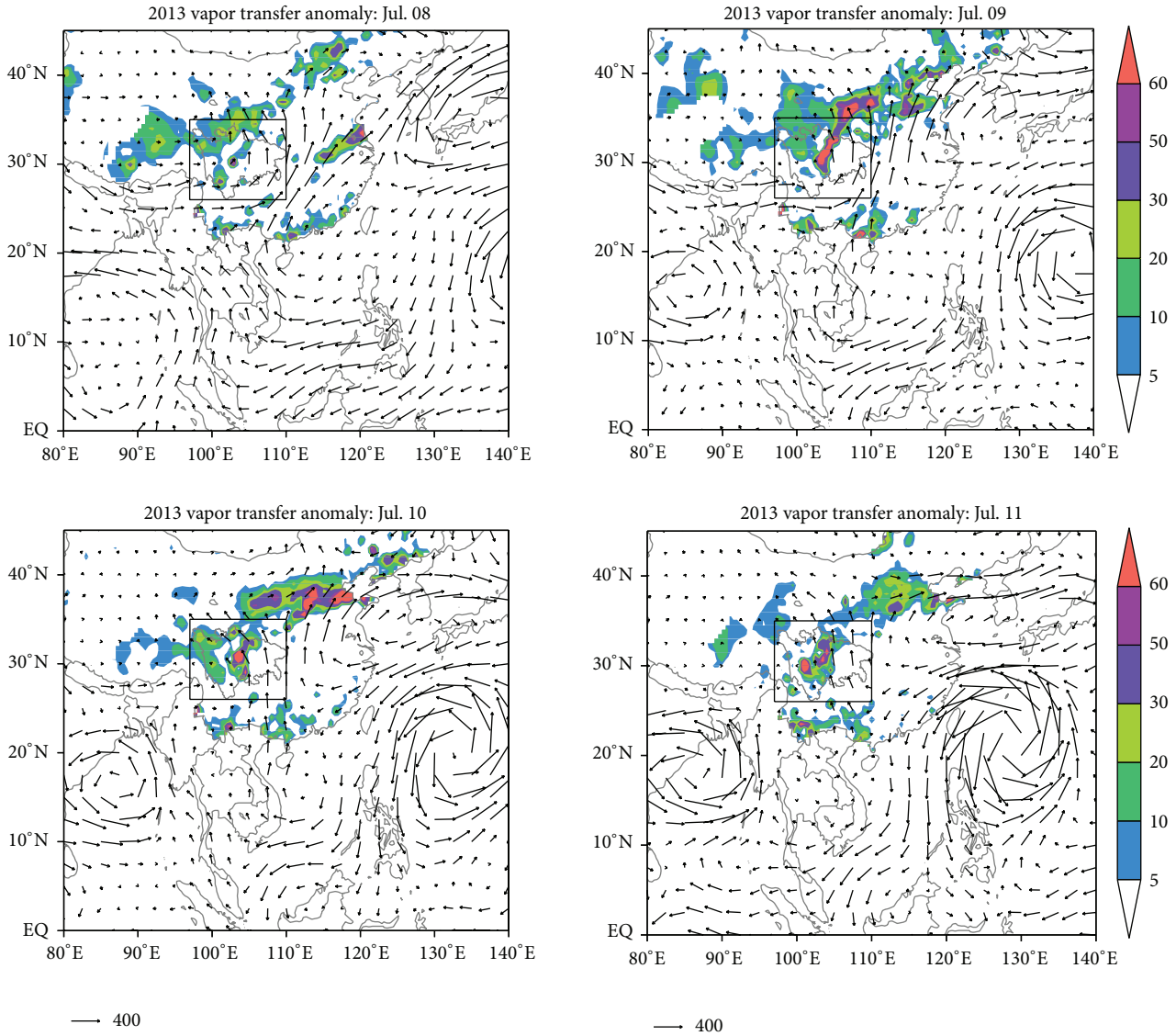


FIGURE 4: Same as in Figure 3, but for the 4th process during the period July 8–11, 2013.

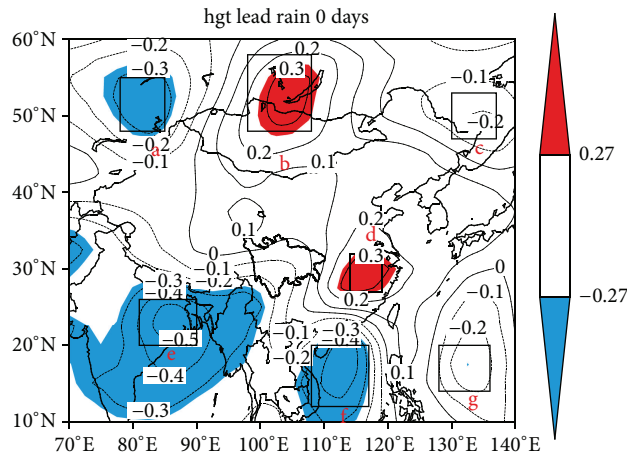


FIGURE 5: Correlation pattern between the WSB precipitation and the 500-hPa geopotential height field. The shaded regions denote correlation coefficients exceeding the 95% confidence level on the basis of Student's *t*-test.

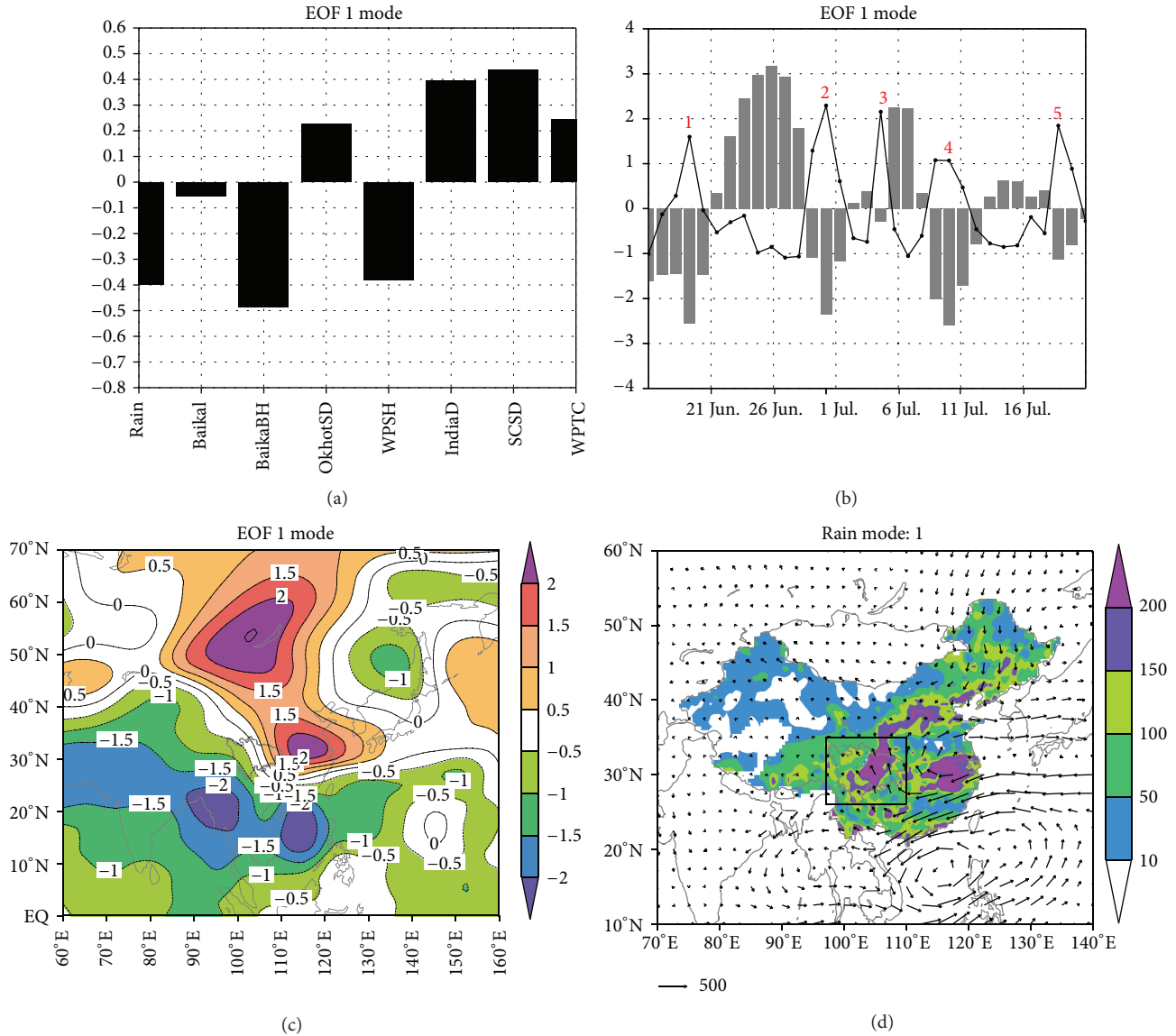


FIGURE 6: (a) Spatial pattern (the bar) and (b) time series (the bar) of the first mode of the MV-EOF analysis (the solid line denotes the normalized daily precipitation). (c) Composite of 500-hPa normalized geopotential height anomaly. (d) Composite of vertically integrated water vapor transport anomaly ( $\text{kg}\cdot\text{m}^{-1}\cdot\text{s}^{-1}$ ) (shading: rainfall > 10 mm).

(a) BalkhaD, (b) BaikaBH, (c) OkhotSD, (d) CSWPSH, (e) IndiaD, (f) SCSD, and (g) WPTC. The multiple linear regression equation between daily precipitation and the seven key factors exceeded the 95% confidence level on the basis of Student's  $t$ -test with multiple-correlation coefficient reaching 0.45. 35.1% of the daily precipitation variance can be explained by all the factors, among which the BalkhaD, CSWPSH, and SCSD are more significant than others.

Secondly, daily rainfall and the aforementioned 7 high-correlated circulation indices are dealt with by the MV-EOF analysis. Figures 6(a), 6(b), 7(a), and 7(b) depict the first two leading modes and the corresponding principal components (PCs). They account for 35.5% and 18.3% of the total variance, respectively, with a sum of 53.8%. According to the rule given by North et al. [33], the first and the second modes

are statistically distinguished from each other. Therefore, the first two leading modes and their corresponding atmospheric circulations are further analyzed so as to draw a common conclusion for the four EPPs.

**5.1. The First Mode.** Figures 6(a) and 6(b) show the spatial pattern and PC of the MV-EOF first mode. The main factors are BaikaBH, CSWPSH, IndiaD, and SCSD, which act on the first, second, and fourth EPPs. And the PC shows the three precipitation processes are persistent. Figures 6(c) and 6(d) present the composite of 500-hPa normalized geopotential height and the vertically integrated water vapor transport anomaly with PC value  $> 1\sigma$ . In 500-hPa geopotential height field, the anomaly pattern is characterized by a “saddle” field (Figure 6(c)). It is concluded that the most importance is that

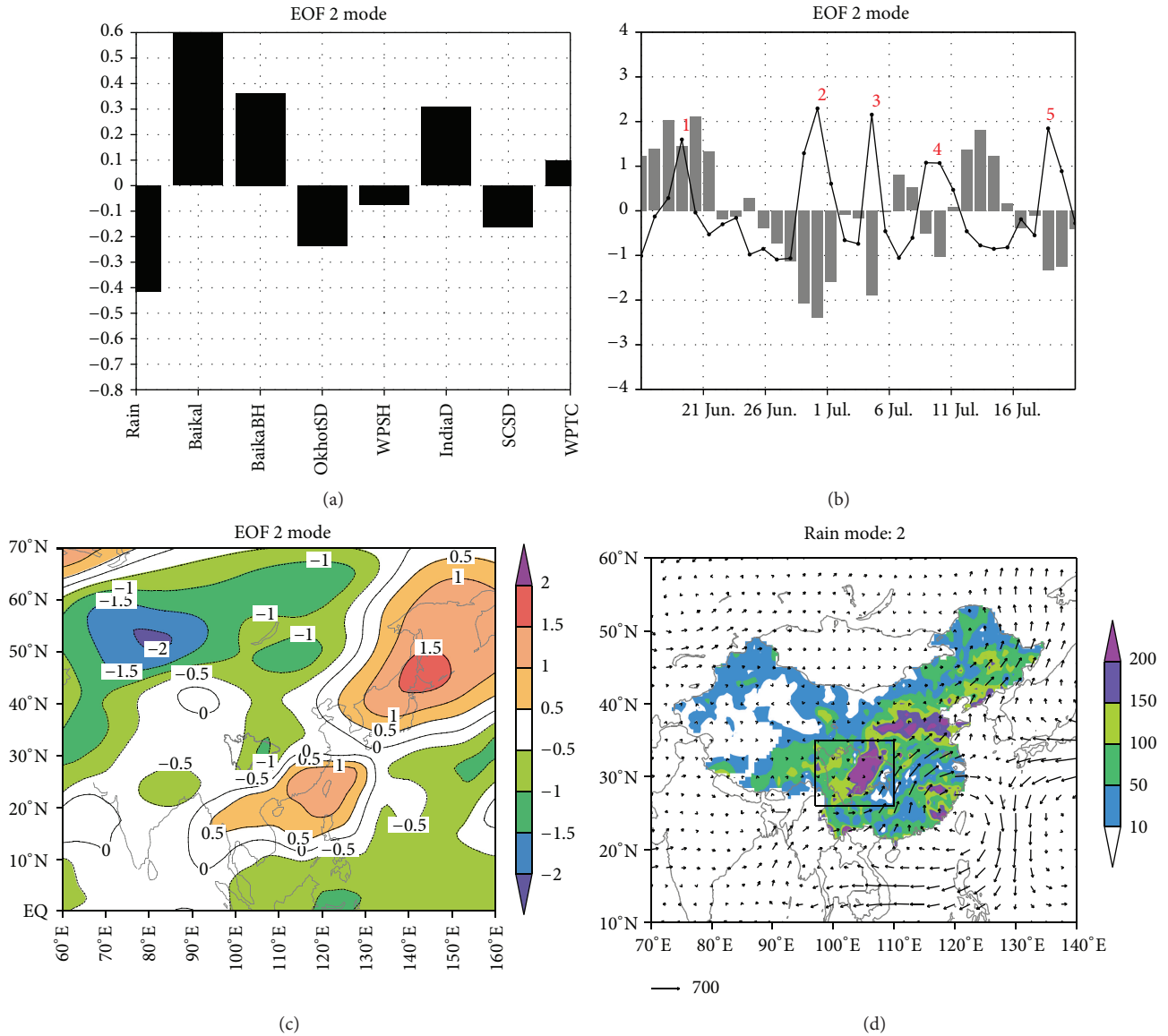


FIGURE 7: Same as in Figure 6, but for the second mode of the MV-EOF analysis.

circulation systems should match up with each other for EPPs over the WSB. When a blocking high occurring over Baikal Lake in the high latitudes, the WPSH strengthening and extending westward over MLRYR, an immense depression maintaining over the tropic region and a TC controlling over the SCS, the EPPs prefer to occur. The cold and warm airflow confront from the eastside of Sichuan Basin. This kind of circulation pattern could maintain for several days so as to produce a persistent precipitation. And this is consistent with Chen et al.'s [27] previous studies according to statistics of 22 typical summer rainstorm events in Sichuan from 1981 to 2000.

5.2. *The Second Mode.* Figures 7(a) and 7(b) show the spatial pattern and PC of the second mode. It is different from the first one. The key factors are the Balkhash Lake

depression, the Baikal Lake depression, the Okhotsk Sea blocking high, and the Indian depression, as well as the conjunction of the SCS anticyclone and the WPSH. The circulation configuration is in favor of the second, third, and fourth precipitation processes. The composite spatial pattern of 500-hPa normalized geopotential height is characterized by a "Sandwich" structure (Figure 7(c)). All the anomalous circulation systems present southwest-northeast oriented distribution pattern. Two low systems inhabit from the Ural Mountain to the Baikal Lake in high latitudes and from the southern SCS to the WP in the tropics. Nevertheless, there is a high one over the northern SCS and South China, through Japan up to the Okhotsk Sea. A TC in WP pushes the WPSH westward into the SCS. Furthermore, the SCS anomalous anticyclone also attracts the WPSH westward-extending and southward-shifting so as to the two high systems form

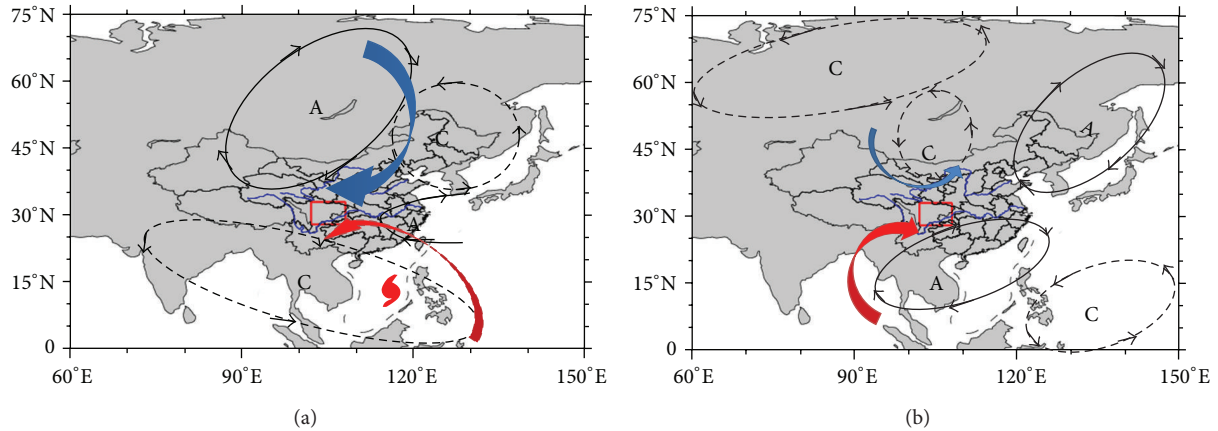


FIGURE 8: The conceptual model for the first (a) and second (b) mode of the MV-EOF analysis. The letters “A” and “C” represent anticyclone and cyclone and the red and blue arrows are warm and cold airflow, respectively.

a winning combination. Therefore, the warm stream comes from the west side of the conjunction. And the cold airflow is from the small trough over the north side of Sichuan Basin. This kind of circulation pattern is so steady that it could persist for a few days.

As can be seen in Figures 8(a) and 8(b), the conceptual models from the MV-EOF first and second mode are shown. In comparison, the WPSH is the same system in the mid-latitude, but it plays a different role in these two modes. It depends on whether a depression is over SCS or WP. For the first mode, a TC over the SCS converts into the inverted trough and steers the warm airflow northward into the WSB. Locating over the MLRYR, the WPSH makes vapor convergence zone westward and conveys southeastward warm current. In the second mode, the WPSH is pushed westward by a TC in WP. Moreover, the anomalous anticyclone over the SCS attracts the WPSH westward-shifting so as to the two high value systems combine a conjunction belt. Such conjunction belt advects southwestward warm moist airflow to merge with the cold current from the trough in the mid-high latitude. Therefore, not only do the precipitation events over the WSB depend on a blocking and/or a trough in the high latitude, but also rely on the WPSH in the mid-latitude and a TC from the tropics. The occurrence of EPPs should depend on the circulation systems matching up with each other [24, 29, 34].

## 6. Summary and Discussion

From mid-June to mid-July in 2013, four EPPs occur during the period June 19–22, June 30–July 2, July 3–5, and July 8–11 over the WSB, respectively. Daily precipitation totals are occasionally  $2\sigma$  above normal. Through daily large-scale circulation analysis, the results underscore that EPPs happen under the different steady circulation configurations. The WPSH and TC play crucial roles in EPPs over the WSB. Using MV-EOF technique, the first two leading modes are characterized by a “saddle” and a “Sandwich” pattern with accounting for 35.5% and 18.3% of the total variance, respectively. As a result, we draw the following conclusions.

- (1) Both TC and WPSH play a different role in the two modes by MV-EOF. In the first mode, TC over the SCS converts into the inverted trough and steers the warm airflow northward into the WSB. Locating over the MLRYR, the WPSH make vapor convergence zone westward and convey southeastward warm airflow. In the second mode, a TC in WP pushes the WPSH westward-extending. Simultaneously, an anomalous anticyclone over the SCS attracts the WPSH. Consequently, the WPSH and the SCS anomalous anticyclone form a conjunction belt, which advects the southwesterly warm moist airflow to merge with the cold current over the WSB.
- (2) Not only do the precipitation events over the WSB depend on a blocking and/or a trough in high latitude, but also rely on the WPSH in mid-latitude and a TC in the tropics. The EPPs events depend on the circulation systems matching up with each other. Especially, “Saddle” and “Sandwich” patterns are favorable for EPPs over WSB in summer 2013.
- (3) Four EPPs include three persistent EPPs. The persistence of EPPs depends on the long-lived circulation systems steady over the suitable position. The third process is different from the others and is a typical large-scale frontal precipitation. Because there is no depression over the SCS or the WP, the water vapor could not be persistently supplied; meanwhile, the mid-high latitude circulations rectify on July 6, 2013. Therefore, the precipitation-favorable circulation could not long-lived maintain over the Sichuan Basin.

Our cases exemplify a situation that might be relevant for the 2013a case. During the 4 EPPs, the pretty clear indications is that the circulation systems should match up with each other and the persistence of EPPs depends on the long-lived large-scale circulation configuration steady over the suitable positions. Clearly, 4 cases are not sufficient to make overly broad generalizations. We hope eventually to be able to get the dominant impacting system configuration patterns of

EPPs in WSB, based on a much larger set of cases than we have considered here. To clearly explain the cause and effect, a further study seems to be needed to perform numerical simulations with “imposed” such two modes at 500 hPa to explore the impact on the precipitation distribution in future.

It is well known that the affecting factors of EPPs over WSB are very complicated, including the trough, the blocking, the WPSH, the TCs, the monsoon, the South Asian high, the southwest vortex, and the low-level shear line, as well as the other mesoscale synoptic systems. The Sichuan Basin and the Tibetan Plateau terrains make the precipitation processes more complex. Therefore, the persistent precipitation physics mechanisms are a challenge to deeply understand. Further investigation of the multiscale interaction among the atmospheric circulation, the external forcing role of the Tibetan Plateau terrain and the air-land-sea interaction and so on, may also be important and essential to understand the EPPs.

### Conflict of Interests

The authors declare that there is no conflict of interests regarding the publication of this paper.

### Acknowledgments

This paper was jointly supported by the National Basic Research and Development (973) Program of China (2012CB417205 and 2013CB430202), the National Natural Science Foundation of China (40905043 and 41375091), and the Open Program of State Key Laboratory of Severe Weather (2013LASW-B12).

### References

- [1] C.-S. Chen, W.-C. Chen, Y.-L. Chen, P.-L. Lin, and H.-C. Lai, “Investigation of orographic effects on two heavy rainfall events over southwestern Taiwan during the Mei-yu season,” *Atmospheric Research*, vol. 73, no. 1-2, pp. 101-130, 2005.
- [2] C.-S. Chen, Y.-L. Lin, N.-N. Hsu, C.-L. Liu, and C.-Y. Chen, “Orographic effects on localized heavy rainfall events over Southwestern Taiwan on 27 and 28 June 2008 during the post-Mei-Yu period,” *Atmospheric Research*, vol. 101, no. 3, pp. 595-610, 2011.
- [3] C.-S. Chen, Y.-L. Lin, H.-T. Zeng, C.-Y. Chen, and C.-L. Liu, “Orographic effects on heavy rainfall events over northeastern Taiwan during the northeasterly monsoon season,” *Atmospheric Research*, vol. 122, pp. 310-335, 2013.
- [4] C. A. Doswell, C. Ramis, R. Romero, and S. Alonso, “A diagnostic study of three heavy precipitation episodes in the Western Mediterranean region,” *Weather and Forecasting*, vol. 13, no. 1, pp. 102-124, 1998.
- [5] D. A. Ahijevych, C. A. Davis, R. E. Carbone, and J. D. Tuttle, “Initiation of precipitation episodes relative to elevated terrain,” *Journal of the Atmospheric Sciences*, vol. 61, no. 22, pp. 2763-2769, 2004.
- [6] R. Y. Lu and H. Ye, “Decreasing trend in summer precipitation over the western Sichuan Basin since the 1950s,” *Atmospheric and Oceanic Science Letters*, vol. 4, no. 2, pp. 114-117, 2011.
- [7] S. H. Yu, J. M. Teng, and G. B. He, “The numerical experiment of plateau terrain influencing for a suddenly arising torrential rain in the west of Sichuan Basin,” *Scientia Atmospherica Sinica*, vol. 22, no. 3, pp. 379-383, 1998.
- [8] G. B. He, “Simulation of impact of steep terrain on east side of Qinghai-Xizang plateau on mesoscale vortex and rain storm over the basin,” *Plateau Meteorology*, vol. 25, no. 3, pp. 430-441, 2006 (Chinese).
- [9] C. Li, J. Chen, and G. B. He, “Impact of the steep terrain of Eastern Qinghai-Xizang Plateau on the genesis and development of extreme heavy rainfall event,” *Plateau Meteorology*, vol. 25, no. 3, pp. 442-450, 2006 (Chinese).
- [10] G. X. Wu, Y. Liu, T. Wang et al., “The influence of mechanical and thermal forcing by the Tibetan Plateau on Asian climate,” *Journal of Hydrometeorology*, vol. 8, no. 4, pp. 770-789, 2007.
- [11] A. M. Duan, G. X. Wu, Y. M. Liu, Y. M. Ma, and P. Zhao, “Weather and climate effects of the Tibetan Plateau,” *Advances in Atmospheric Sciences*, vol. 29, no. 5, pp. 978-992, 2012.
- [12] S. H. Yu, “Resultant analysis of large-scale heavy rain storm over Sichuan Basin,” *Plateau Meteorology*, vol. 3, no. 1, pp. 58-67, 1984 (Chinese).
- [13] C. Y. Zhou, Y. Q. Li, Q. L. Bu, and J. Peng, “Features of drought-flood coexistence in West and East of Sichuan-Chongqing Basin in midsummer and its relating background of atmospheric circulation,” *Plateau Meteorology*, vol. 30, no. 3, pp. 620-727, 2011 (Chinese).
- [14] R. Shi, Y. R. Chen, and C. G. Wang, “Comparative analysis of the influence of the Subtropical high on the torrential rainfall in Sichuan Basin,” *Plateau and Mountain Meteorology Research*, vol. 30, no. 4, pp. 18-25, 2010 (Chinese).
- [15] D. Q. Hu, R. Y. Lu, Q. Su, and G. Z. Fan, “Interannual variation in the mid-summer rainfall over the western Sichuan Basin and the associated circulation anomalies,” *Chinese Journal of Atmospheric Sciences*, vol. 38, no. 1, pp. 13-20, 2014 (Chinese).
- [16] D. Chen, Y. Q. Li, and R. H. Huang, “The physical process analyses of the Southwest vortex development and its effect on heavy rainfall in Eastern Sichuan under the saddle pattern background of large-scale circulations,” *Chinese Journal of Atmospheric Sciences*, vol. 31, no. 2, pp. 185-201, 2007 (Chinese).
- [17] S. X. Zhao and S. M. Fu, “An analysis on the southwest vortex and its environment fields during heavy rainfall in eastern Sichuan Province and Chongqing in September 2004,” *Chinese Journal of Atmospheric Sciences*, vol. 31, no. 6, pp. 1059-1074, 2007 (Chinese).
- [18] C. H. Huang, G. P. Li, J. L. Niu, L. Luo, and W. Zhang, “Moist helicity analysis of a heavy rainstorm in Sichuan Basin induced by Plateau vortex moving eastward,” *Plateau Meteorology*, vol. 30, no. 6, pp. 1427-1434, 2011 (Chinese).
- [19] Y. R. Chen, Y. Q. Li, C. G. Wang, and R. Y. Deng, “Study on the relationship between South Asia High and rainfall of Sichuan-Chongqing regions in summer,” *Plateau Meteorology*, vol. 28, no. 3, pp. 539-548, 2009 (Chinese).
- [20] Y. H. Kuo, L. S. Cheng, and R. A. Anthes, “Mesoscale analyses of the Sichuan flood catastrophe, 11-15 July 1981,” *Monthly Weather Review*, vol. 114, no. 11, pp. 1984-2003, 1986.
- [21] H. Y. Xiao and S. H. Yu, “Subtropical high activity and Sichuan rainstorm,” *Journal of Sichuan Meteorology*, vol. 23, no. 2, pp. 2-12, 2003 (Chinese).
- [22] Sichuan Provincial Meteorological Bureau, *Handbook of Short-Term Weather Forecasting in Sichuan Province*, China Meteorological Press, Beijing, China, 2015, (Chinese).
- [23] Y. F. Zhu and R. C. Yu, “Interannual variation of summer precipitation in the west of Sichuan Basin and its relationship

- with large-scale circulation,” *Chinese Journal of Atmospheric Sciences*, vol. 27, no. 6, pp. 1045–1056, 2003 (Chinese).
- [24] Y. Chen and Y. H. Ding, “Cold air activities in July 2004 and its impacts on intense rainfalls over Southwest China,” *Acta Meteorologica Sinica*, vol. 64, no. 6, pp. 743–759, 2006 (Chinese).
- [25] B. Zhou and J. F. Wen, “Circulation of a persistent heavy rain and its diabatic heating characteristics over the North of Chongqing and the east of Sichuan in 2004,” *Journal of Applied Meteorological Science*, vol. 17, supplement, pp. 71–78, 2006 (Chinese).
- [26] Q. Y. Gu, D. X. Xiao, and C. H. Huang, “Trigger role of the low-level jet for the continuous rainstorm in the northwest side of subtropical high,” *Meteorological Monthly*, vol. 35, no. 4, pp. 59–67, 2009 (Chinese).
- [27] D. Chen, L. Gu, and X. W. Jiang, “Characteristics of large-scale circulation background of summer heavy rainfall in Sichuan during 1981 to 2000,” *Transactions of Atmospheric Sciences*, vol. 33, no. 4, pp. 443–450, 2010 (Chinese).
- [28] E. Kalnay, M. Kanamitsu, R. Kistler et al., “The NCEP/NCAR 40-year reanalysis project,” *Bulletin of the American Meteorological Society*, vol. 77, no. 3, pp. 437–471, 1996.
- [29] Y. Chen and P. Zhai, “Persistent extreme precipitation events in China during 1951–2010,” *Climate Research*, vol. 57, no. 2, pp. 143–155, 2013.
- [30] Z. Q. Gong, Y. J. Wang, Z. Y. Wang, L. J. Ma, C. H. Sun, and S. Q. Zhang, “Briefly analysis on climate anomalies and causations in summer 2013,” *Meteorological Monthly*, vol. 40, no. 1, pp. 119–125, 2014 (Chinese).
- [31] F. Zhang and L. F. He, “Analysis of the June 2013 atmospheric circulation and weather,” *Meteorological Monthly*, vol. 39, no. 9, pp. 1227–1232, 2013 (Chinese).
- [32] Y. C. Lin, J. Xu, and F. H. Zhang, “Analysis of the July 2013 atmospheric circulation and weather,” *Meteorological Monthly*, vol. 39, no. 10, pp. 1379–1384, 2013 (Chinese).
- [33] G. R. North, T. L. Bell, and R. F. Cahalan, “Sampling errors in the estimation of empirical orthogonal functions,” *Monthly Weather Review*, vol. 110, no. 7, pp. 699–706, 1982.
- [34] Y. Chen and P. M. Zhai, “Two types of typical circulation patterns for the persistent extreme precipitation in Central Eastern China,” *Quarterly Journal of the Royal Meteorological Society*, vol. 140, no. 682, pp. 1467–1478, 2014.

## Research Article

# Fuzzy Clustering-Based Ensemble Approach to Predicting Indian Monsoon

Moumita Saha,<sup>1</sup> Pabitra Mitra,<sup>1</sup> and Arun Chakraborty<sup>2</sup>

<sup>1</sup>Department of Computer Science and Engineering, Indian Institute of Technology Kharagpur, Kharagpur, Paschim Medinipur, West Bengal 721302, India

<sup>2</sup>Centre for Oceans, Rivers, Atmosphere and Land Sciences, Indian Institute of Technology Kharagpur, Kharagpur, Paschim Medinipur, West Bengal 721302, India

Correspondence should be addressed to Moumita Saha; moumita.saha2012@gmail.com

Received 2 January 2015; Revised 31 March 2015; Accepted 3 April 2015

Academic Editor: Xiaolong Jia

Copyright © 2015 Moumita Saha et al. This is an open access article distributed under the Creative Commons Attribution License, which permits unrestricted use, distribution, and reproduction in any medium, provided the original work is properly cited.

Indian monsoon is an important climatic phenomenon and a global climatic marker. Both statistical and numerical prediction schemes for Indian monsoon have been widely studied in literature. Statistical schemes are mainly based on regression or neural networks. However, the variability of monsoon is significant over the years and a single model is often inadequate. Meteorologists revise their models on different years based on prevailing global climatic incidents like El-Niño. These indices often have degree of severity associated with them. In this paper, we cluster the monsoon years based on their fuzzy degree of associativity to these climatic event patterns. Next, we develop individual prediction models for the year clusters. A weighted ensemble of these individual models is used to obtain the final forecast. The proposed method performs competitively with existing forecast models.

## 1. Introduction

Monsoon is a complex phenomenon of a climatic system. It is influenced by multiple climatic parameters and sea-atmosphere interactions. Prediction of monsoon is challenging due to large variability present in its patterns. Indian Meteorological Department (*IMD*) performs forecast of Indian summer monsoon rainfall (*ISMR*) since 1886. Indian monsoon forecast was initiated by Blanford [1] as early as 1882. The success of forecasts in span of 1882–1885 encouraged Blanford to design operational long range forecast model for monsoon in 1886. Subsequently, Walker [2] developed models studying the statistical correlations between rainfall and different global climate parameters. Thapliyal and Kulshrestha [3] introduce regression model in predicting south-west Indian monsoon rainfall. Gowariker et al. [4] propose power regression model for long-term forecast of monsoon, which provided accurate forecast for a long period, but failed to predict the extreme condition of

2002. In 2004, Rajeevan et al. [5] reassess different climatic parameters and introduce four new parameters to design statistical model for issuing long-range forecast of Indian monsoon. Succeeding in 2007, Rajeevan et al. [6] built models using ensemble multiple regression and pursuit projection regression to forecast Indian rainfall and proved to be superior to past *IMD* models. Schewe and Levermann [7] explain the change in distribution of Indian rainfall and also explain the reasons behind failure of monsoon in certain years. Wu et al. [8] propose a linear Markov model to predict short-term climate variability of East Asian monsoon. Fan et al. [9] develop two statistical prediction schemes for seasonal forecast of East Asian summer monsoon. The schemes take the direct outputs of the existing models and give better prediction of the summer monsoon.

Artificial neural networks (*ANN*) [10] are widely used in modelling the nonlinearity present in monsoon process. Sahai et al. [11] use *ANN* techniques with error backpropagation to forecast Indian summer monsoon rainfall. Hong [12]

predicts Indian summer monsoon utilizing recurrent neural network and also demonstrates successful employment of support vector machine in solving nonlinear regression and time series problems. Three different backpropagation neural learning rules, namely, momentum learning, conjugate gradient descent learning, and Levenberg-Marquardt learning, are used by S. Chattopadhyay and G. Chattopadhyay [13] to perform a comparative study of different neural network method to predict rainfall time series.

Presence of large variability in monsoon patterns makes it difficult for a single model to predict its distribution. A number of uncertainties including boundary condition, parameter, and structural uncertainties are involved in construction of these models. Thus, it remains fundamentally challenging to have a single model for prediction. Multimodel ensembles are proposed to overcome the weakness of single model, which combine the outcome of different models to produce efficient results [14, 15]. In addition, monsoon shows different characteristics over years. There exist groups of years where variation of climatic parameters and pattern of rainfall are similar. We use fuzzy clustering to cluster the similar years together and model them separately. The motivation behind using fuzzy clustering is that each year manifests a mixture of physical climatic events. We cannot hard cluster a year into a specific group; years have their membership of belongingness to every cluster. Fuzzy clustering is used to enclose the characteristics of different events being related to a year of study. We use the same set of climatic parameters as predictor set for every cluster but frame different models for each cluster.

A number of prediction models, namely, multiple regression (*MR*), multilayer perceptron (*MLP*), recurrent neural network (*RNN*), and generalized regression neural network (*GRNN*) models, are used for prediction of Indian monsoon for the year clusters. There exists viable reasons for using neural networks like *MLP*, *RNN*, and *GRNN* for modelling: (i) Indian monsoon is a complex process, which cannot be adequately modelled by linear models, (ii) nonlinearity in the time-series pattern can be well captured by neural network learning, (iii) climatic events are much closely related to near years parameters disturbance as compared to distant years, and neural network enables attaching weight to the year parameter in appropriate manner.

In this work, climatic parameters that are strongly correlated with Indian monsoon are identified at the onset, which is followed by fuzzy clustering of years into groups with degree of belongingness of each year to the clusters. Then we model each cluster with four types of models, namely, *MR*, *MLP*, *RNN*, and *GRNN*, to forecast rainfall. Weighted ensemble of forecasts given by respective models for each cluster is considered as final predicted rainfall. Analysis and comparisons are performed on aggregate Indian rainfall and finally, a meteorological interpretation of the obtained clusters is presented.

The paper is organised in the following manner. We discussed the details of data and predictor climatic parameters in Sections 2 and 3. Proposed clustering based approach, prediction model, and ensemble technique are presented in Section 4 with experimental results in Section 5.

Meteorological significance is discussed in Section 6 and finally, conclusions are provided in Section 7.

## 2. Data Sets Used

We consider the annual Indian summer monsoon rainfall (*ISMR*), occurring in four months of June, July, August, and September. Annual *ISMR* is considered during period 1948–2013 for our study. The long period average (*LPA*) (1948–2013) of *ISMR* is 891.8 mm. *ISMR* is expressed as percentage of the *LPA* value. The data is obtained from Indian Institute of Tropical Meteorology, Pune (<http://www.imdpune.gov.in/research/ncc/longrange/data/data.html>) [16].

Predictor parameters sea level pressure (*SLP*) ([http://www.esrl.noaa.gov/psd/gcos\\_wgsp/Gridded/data.noaa.erslp.html](http://www.esrl.noaa.gov/psd/gcos_wgsp/Gridded/data.noaa.erslp.html)) and sea surface temperature (*SST*) (<http://www.esrl.noaa.gov/psd/data/gridded/data.noaa.ersst.html>) data are provided by the NOAA/OAR/ESRL/PSD, at spatial resolution of  $2^\circ \times 2^\circ$  [17]. Surface pressure (*SP*) and zonal wind velocity (*WV*) data are collected from *NCEP* Reanalysis Derived data provided by the NOAA/OAR/ESRL PSD (<http://www.esrl.noaa.gov/psd/data/gridded/data.ncep.reanalysis.derived.surface.html>) [18], available at resolution of  $2.5^\circ \times 2.5^\circ$ . Finally, Niño 3.4 data, which is the sea surface temperature anomaly for the spatial coverage of  $5^\circ\text{S}$  to  $5^\circ\text{N}$  and  $170^\circ\text{W}$  to  $120^\circ\text{W}$  in Pacific Ocean region is acquired from National Center for Atmospheric Research ([http://www.cpc.ncep.noaa.gov/products/analysis\\_monitoring/ensostuff/ensoyears.shtml](http://www.cpc.ncep.noaa.gov/products/analysis_monitoring/ensostuff/ensoyears.shtml)) [19]. All the above monthly data are considered for the period 1948–2013 in our study and analysis.

## 3. Global Climatic Parameters Influencing Indian Monsoon

Indian monsoon is strongly influenced by several global climatic parameters, occurring at places distant from Indian subcontinent. Identification of predictor parameters relies on physical understanding of monsoon event and wind pattern flow. We have selected the climatic parameters based on the parameters used by Indian meteorological department's models [5, 6], studying their correlation with Indian summer monsoon rainfall (*ISMR*) during our period of study (1948–2013). In the data preprocessing phase, climatic anomaly data are evaluated by calculating the deviation of parameter value from long-term average value of the parameter exclusively for each month, followed by correlation study between *ISMR* and the climatic parameters for a lag of zero to twelve months. We consider the best lagged predictor month having high correlation with *ISMR*. The predictor climatic parameters and their correlation values with Indian monsoon are shown in Table 1. Figure 1 shows the geographic location of climatic parameters influencing Indian monsoon.

*Predictor Sets of Climatic Parameters.* Based on the correlation with Indian monsoon, we have built five predictor sets for forecasting. Different combinations of the identified climatic parameters (Table 1) form the predictor sets. The predictor sets are shown in Table 2.

TABLE 1: Climatic parameters (CP) influencing Indian monsoon with geographical location, correlation values, and correlated month (0 signifies same years and -1 signifies previous year).

CP	CP name	Location	Correlation values	Correlated months
CP1	North Atlantic Ocean SST anomaly	20°N–30°N, 100°W–80°W	0.242	Jan (0)
CP2	North Atlantic Ocean surface pressure anomaly	20°N–30°N, 100°W–80°W	0.256	April (0)
CP3	East Asia SLP anomaly	35°N–45°N, 120°E–130°E	0.337	May (0)
CP4	East Asia surface pressure anomaly	35°N–45°N, 120°E–130°E	0.341	Mar (0)
CP5	Equatorial South Eastern Indian ocean SST anomaly	20°S–10°S, 100°E–120°E	0.200	Sept (-1)
CP6	Pressure gradient between Madagascar and Tibet	—	0.253	May (0)
CP7	Niño 3.4 SST anomaly	5°S–5°N, 170°W–120°W	0.311	Sept (-1)
CP8	Equatorial Pacific Ocean SLP anomaly	5°S–5°N, 120°E–80°W	0.272	Aug (-1)
CP9	North West Europe surface pressure anomaly	55°N–65°N, 20°E–40°E	0.183	Jan (0)
CP10	North Central Pacific zonal wind anomaly	5°N–15°N, 180°E–150°W	0.457	May (0)

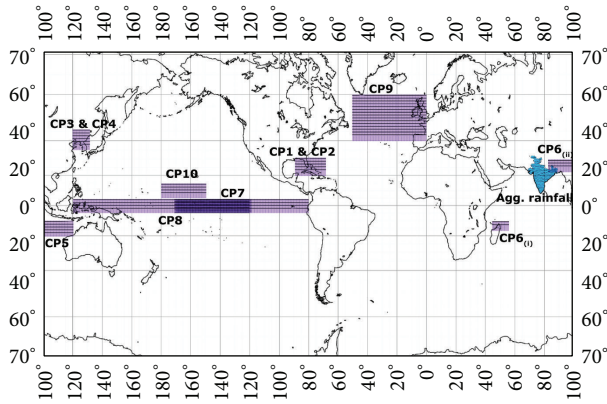


FIGURE 1: Climatic parameters over the globe governing Indian monsoon (purple patches signify the location of climatic parameters taken, and blue patch represents the Indian region);  $CP_i$  represents parameter  $i$  in Table 1.

TABLE 2: Predictor sets with climatic parameters.

Predictor sets	Climatic parameters
<i>PredSet1</i>	CP1, CP4, CP5, CP6
<i>PredSet2</i>	CP4, CP5, CP6, CP7
<i>PredSet3</i>	CP2, CP4, CP10
<i>PredSet4</i>	CP2, CP4, CP7, CP10
<i>PredSet5</i>	CP3, CP7, CP8, CP9

## 4. Methodology

We propose fuzzy clustering of monsoon years into groups followed by building models for each group separately and finally predicting Indian summer monsoon rainfall (*ISMR*) as weighted ensemble of forecasts provided by cluster models. The block diagram of the proposed fuzzy clustering-based approach to prediction of *ISMR* is shown in Figure 2. Detailed steps are described in the following subsections.

**4.1. Motivation: Variability of Monsoon Patterns.** Trends and distributions of monsoon vary to a large extent over years. It

is thus necessary to group the years into clusters which have similar patterns of predictor climatic parameters affecting monsoon. The approach of clustering the years is effective as we can build separate models for each cluster. These cluster models will be more accurate as variation within cluster is less. Finally, ensemble of forecasts of these cluster models results in better prediction of Indian monsoon. As an example consider two clusters of years corresponding to strong El-Niño and North Atlantic Oscillation, respectively. A drought year has correlation with both events and hence might have significant degree of belongingness to both clusters.

**4.2. Fuzzy Clustering of Monsoon Years.** Fuzzy  $c$ -means clustering is used for grouping the similar years together. Fuzzy  $c$ -means (*FCM*) is a method of clustering which allows one instance of input to belong to more than one cluster with some membership of belongingness. *FCM* attempts to partition a set of  $N$  elements  $Y = \{y_1, \dots, y_n\}$  into a collection of  $c$  fuzzy clusters  $C = \{cen_1, \dots, cen_c\}$  and a partition matrix  $W = w_{ij} \in [0, 1]$ ,  $i = 1, \dots, n$ ,  $j = 1, \dots, c$ , where  $w_{ij}$  gives the degree of belongingness of element  $y_i$  to cluster with center  $cen_j$ .

*FCM* aims to minimize an objective function of (1). The update of partition matrix and centers occur in accordance with (2) and (3), respectively:

$$J_m = \sum_{i=1}^N \sum_{j=1}^c w_{ij}^m \|y_i - cen_j\|^2, \quad 1 \leq m \leq \infty \quad (1)$$

$$w_{ij} = \frac{1}{\sum_{k=1}^c (\|y_i - cen_j\| / \|y_i - cen_k\|)^{2/(m-1)}} \quad (2)$$

$$cen_j = \frac{\sum_{i=1}^N w_{ij}^m \cdot x_i}{\sum_{i=1}^N w_{ij}^m}, \quad (3)$$

where  $m$  denotes the level of cluster fuzziness.

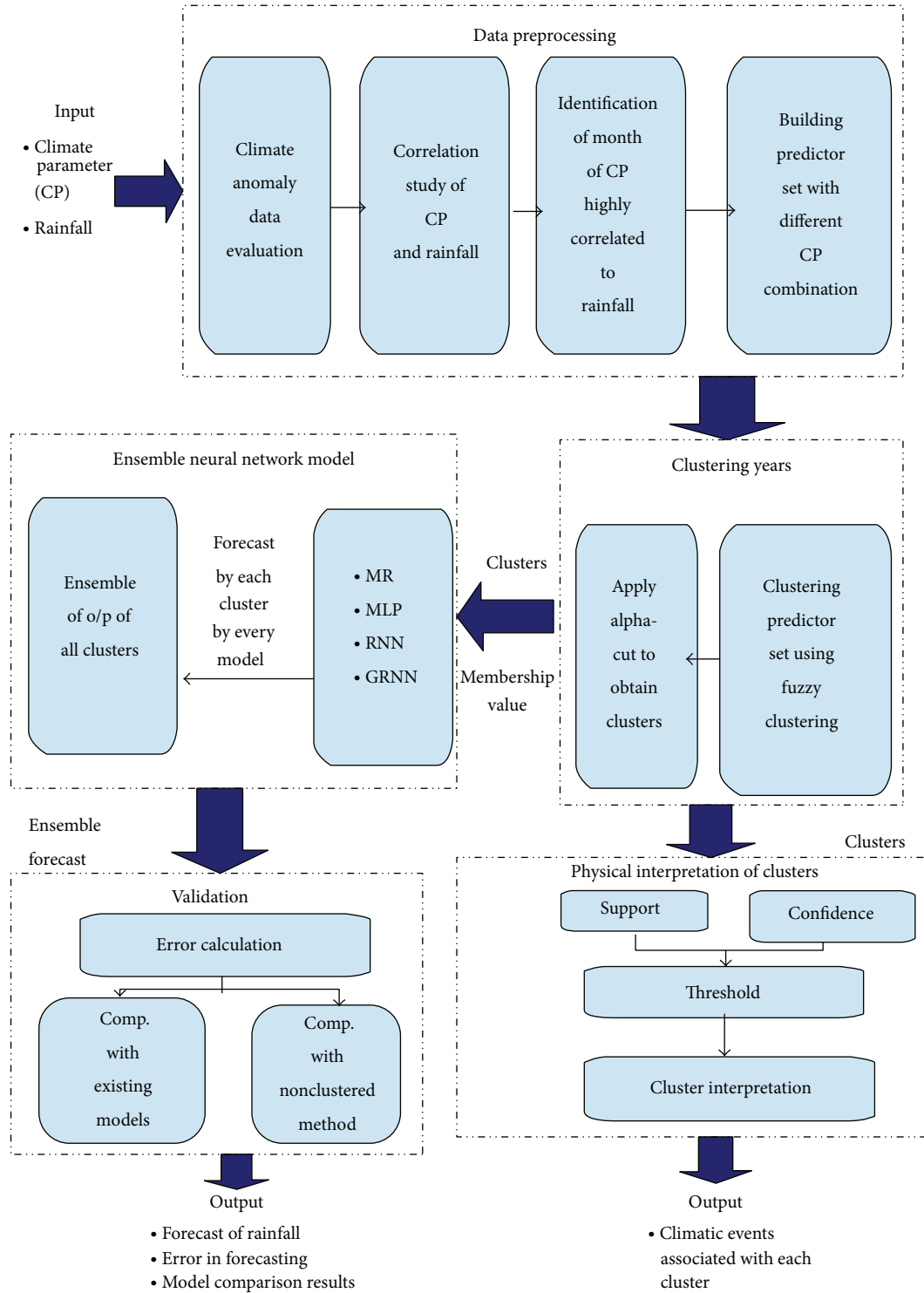


FIGURE 2: Proposed fuzzy clustering-based ensemble approach for prediction of Indian summer monsoon rainfall.

4.3. Prediction Models. Multiple regression and three models of artificial neural networks (ANN), namely, multilayer perceptron, recurrent neural network, and generalized regression neural network, are used to design prediction models for each cluster exclusively. Forecast of annual ISMR is provided by each cluster model separately and also by ensemble of all

the clusters' model forecast. We describe below the models used.

4.3.1. Multiple Regression (MR). Multiple regression model is used to learn the relationship between several independent predictor variables ( $X_i$ s) and a dependent variable ( $Y$ ).

TABLE 3: Model parameter setting for MLP models.

Parameter set	Hidden layers	Training years	Training method
<i>ParSet1</i>	[3 5]	20	BFGS quasi-Newton backpropagation
<i>ParSet2</i>	[3 5 10]	15	Conjugate gradient backpropagation with Powell-Beale restarts
<i>ParSet3</i>	[5 10]	10	Scaled conjugate gradient backpropagation
<i>ParSet4</i>	[3 5]	15	Resilient backpropagation

Multiple regression model having  $p$  independent variables is shown in

$$y_i = \beta_1 x_{i1} + \beta_2 x_{i2} + \dots + \beta_p x_{ip} + \varepsilon_i, \quad (4)$$

where  $x_{ij}$  is the  $i$ th observation of  $j$ th independent variable, where the first independent variable takes the value 1 for all  $i$  and  $\varepsilon$  represents the residual.

**4.3.2. Multilayer Perceptron Neural Network (MLP).** Multilayer perceptron neural network is a class of ANN where connections between the neurons do not form a directed cycle. In this network, the information propagates in only one direction, from input nodes, through hidden nodes, and to the output nodes. The independent and dependent variables constitute the input and output layers, respectively. Number of hidden layers with corresponding nodes must be determined empirically for each prediction task. Four different parameter sets are considered empirically for model designed to forecast ISMR, shown in Table 3.

**4.3.3. Recurrent Neural Network (RNN).** Recurrent neural network is a class of ANN which creates an internal state of the network to exhibit dynamic temporal behaviour. Climatic changes or events occurring in near or same time period are highly correlated. Similarly, rainfall patterns are more correlated to influencing factors in the near years as compared to the distant years. This phenomenon is well captured by RNN which gives weights in decreasing order to the values in near to distant years during training of network. Thus, it assists in modelling the system dynamics in much natural manner. Same set of climatic parameters as MLP network (Table 3) is considered with delay span of 2 units.

**4.3.4. Generalized Regression Neural Network (GRNN).** Generalized regression neural network is a variant of radial basis function network. GRNN has three layers of artificial neurons: input, hidden, and output. The hidden layer has radial basis neurons, while neurons in the output layer have linear transfer function. Output of radial basis neurons is the input scaled by the spread factor. Given  $p$  input-output pairs  $x_i, y_j \in \mathfrak{R}^n \times \mathfrak{R}^1$ , with  $n$  input variables and  $i = 1, 2, \dots, p$ ,  $y_j$  represents the output from each hidden unit. The GRNN output for a test point,  $x \in \mathfrak{R}^n$ , is described by

$$\widehat{y}(x) = \sum_{i=1}^p W_i y_i, \quad (5)$$

where

$$W_i = \frac{\exp(-\|x - x_i\|^2 / 2\sigma^2)}{\sum_{k=1}^p \exp(-\|x - x_k\|^2 / 2\sigma^2)}. \quad (6)$$

The reasons behind modelling using GRNN are (i) only one tunable design parameter (spread factor), (ii) one-pass algorithm (less time consuming), and (iii) accurately approximate functions from sparse data.

Optimal training year is ascertained for MR and GRNN models by varying training years from 5 to 30 and validating against least absolute error in prediction during validation period (1984–1993). A training of  $m$  years specifies that, for predicting  $r$ th year rainfall, available preceding  $m$  number of years  $r - 1, r - 2, \dots, r - m$  present in a particular cluster are considered for training.

**4.4. Ensemble of Predictors.** Complexity in monsoon process makes it difficult for a single model to predict rainfall accurately. We design separate models for each cluster of years obtained by fuzzy clustering using four predictors described in Section 4.3. Finally, annual ISMR is presented as weighted ensemble of forecasts of model designed for each cluster. Weight is taken as the fuzzy membership of belongingness of the test year in different clusters:

$$\text{Ensemble prediction}^t = \sum_{i=1}^c W_i^t \cdot P_i, \quad (7)$$

where  $P_i$  represents the prediction given by a model for cluster  $i$ ,  $W_i^t$  is the fuzzy membership of  $t$ th test year to cluster  $i$ , and  $c$  is the total number of clusters.

**4.5. Validation of Proposed Approach.** The study is performed on data for the period 1948–2013. Fuzzy clustering is performed over the period to cluster it into *three* groups. The number of clusters is decided based on cluster quality. Separate prediction models are designed for all three clusters and ensemble of forecasts of these models is provided as predicted Indian summer monsoon rainfall. Test period 2001–2013 is considered to evaluate the forecasting skills of our proposed approach.

The forecast models for annual ISMR are chiefly evaluated in terms of mean absolute error. Other error statistics, namely, root mean square error, prediction yields, Pearson correlation, and Willmott index of agreement, are also evaluated to judge the efficacy of our proposed approach for prediction. They are described below.

- (i) *Mean Absolute Error (MAE)*. Mean absolute error for prediction of annual *ISMR* is calculated in the following way:

$$\text{MAE} = \frac{\sum_{i=1}^N |Y - X|}{N}, \quad (8)$$

where  $X$  and  $Y$  are the actual and predicted *ISMR* series for test period and  $N$  denotes the total number of test years.

- (ii) *Root Mean Square Error (RMSE)*. Root mean square error calculates the differences between model predicted output and actual values. They are a good measure to compare forecasting errors of various models:

$$\text{RMSE} = \sqrt{\frac{(Y - X)^2}{N}}. \quad (9)$$

- (iii) *Prediction Yield (PY)*. Prediction yields are evaluated at three different error categories (5%, 10%, and 15% errors) to assess the overall prediction results by judging percent of predicted years within each allowed range of errors.
- (iv) *Pearson Correlation Coefficient (PC)*. Pearson correlation coefficient measures the strength of linear association between actual and predicted values, where the value of 1 means a perfect positive correlation and the value of  $-1$  means a perfect negative correlation:

$$\text{PC} = \frac{\sum_{i=1}^N (X_i - \bar{X})(Y_i - \bar{Y})}{\sqrt{\sum_{i=1}^N (X_i - \bar{X})^2} \sqrt{\sum_{i=1}^N (Y_i - \bar{Y})^2}}, \quad (10)$$

where  $X$  and  $Y$  are the actual and predicted *ISMR* series for test period and  $\bar{X}$  and  $\bar{Y}$  are their corresponding mean.

- (v) *Willmott Index of Agreement (WI)*. Willmott index of agreement is a standardized measure of the degree of model prediction error. It varies between 0 and 1 with higher values indicating a better fit of the model for prediction:

$$\text{Index of agreement} = 1 - \frac{\sum_{i=1}^N |X_i - Y_i|^2}{\sum_{i=1}^N (|Y_i - \bar{X}| + |X_i - \bar{X}|)^2}. \quad (11)$$

## 5. Experimental Results and Analysis

In this section we present the evaluation of our proposed fuzzy clustering-based approach. We first present the results of fuzzy clustering of the monsoon years for different predictor sets. Forecasting skills are evaluated for all cluster and the ensemble model in terms of mean absolute errors for test period 2001–2013. In addition, other measures like root mean square errors in prediction, correlation between predicted

TABLE 4: Cluster size (number of years) by fuzzy  $c$ -means clustering with  $\alpha$ -cut of 0.3 over the period 1948–2013.

Predictor set	Cluster1	Cluster2	Cluster3
<i>PredSet1</i>	16	38	30
<i>PredSet2</i>	30	17	40
<i>PredSet3</i>	32	14	38
<i>PredSet4</i>	42	31	21
<i>PredSet5</i>	15	37	26

and actual rainfall, prediction yields, and agreement index between actual and predicted rainfall are also estimated to establish the efficiency of our proposed approach to prediction of Indian summer monsoon rainfall.

**5.1. Clustering of Monsoon Years.** Fuzzy clustering is performed over period 1948–2013 to cluster the data into *three* clusters. We have performed an  $\alpha$ -cut, with value  $\alpha = 0.3$  to assign the data instances to the clusters. The value is ascertained empirically such that the distribution of elements within clusters is regular. A data instance can be assigned to more than one cluster simultaneously. The cluster sizes are shown in Table 4 while considering various predictor sets.

**5.2. Prediction Accuracy.** We predict annual rainfall considering for all five predictor sets (Table 2) separately using four models, namely, *MR*, *MLP*, *RNN*, and *GRNN*. Test period is considered from 2001 to 2013.

**5.2.1. Multiple Regression Model (MR).** Multiple regression models are built for every cluster by ascertaining optimal training period for each predictor set. Optimal training period is evaluated by varying training years and validating them for least absolute error in prediction during validation period (1984–1993). Individual cluster based as well as weighted ensemble models are considered for prediction. Table 5 gives the mean absolute error for individual cluster based and ensemble models for test period 2001–2013. The model provides mean absolute error of 6.2% for *PredSet4* (Table 2). It is observed that the ensemble model outperforms all the single cluster models for every predictor set. Figure 3 shows the interannual variability of actual and ensemble predicted rainfall as percent of long period average (*LPA*).

**5.2.2. Multilayer Perceptron Neural Network Model (MLP).** Multilayer perceptron neural network model is designed with four different sets of parameters described in Table 2. Mean absolute errors of all cluster and ensemble models are shown in Table 6. *MLP* model reports an error of 4.0% for *PredSet4* (Table 2) with *MLP* parameters *ParSet1* (Table 3). The actual and predicted rainfall by models built for clusters and ensemble model is shown in Figure 4. Ensemble predicted rainfall closely follows actual rainfall.

**5.2.3. Recurrent Neural Network Model (RNN).** Mean absolute errors for prediction of annual rainfall by recurrent neural network model for the test period 2001–2013 are

TABLE 5: Mean absolute errors (%) for annual Indian summer monsoon rainfall prediction by individual MR cluster models and ensemble model for test period 2001–2013. Reports minimum error of 6.2%.

Predictor set	Training years	Cluster1 error (%)	Cluster2 error (%)	Cluster3 error (%)	Ensemble error (%)
<i>PredSet1</i>	20	9.4	9.3	10.9	<b>8.6</b>
<i>PredSet2</i>	20	11.0	7.5	9.4	<b>8.3</b>
<i>PredSet3</i>	15	10.9	6.5	9.2	<b>6.7</b>
<i>PredSet4</i>	15	10.4	10.1	6.8	<b>6.2</b>
<i>PredSet5</i>	15	7.6	8.5	8.4	<b>7.9</b>

TABLE 6: Mean absolute errors (%) for annual Indian summer monsoon rainfall prediction by individual MLP cluster models and ensemble model for test period 2001–2013. Reports minimum error of 4.0%.

Predictor set	Parameter set	Cluster1 error (%)	Cluster2 error (%)	Cluster3 error (%)	Ensemble error (%)
<i>PredSet1</i>	<i>ParSet4</i>	13.8	18.1	16.9	<b>8.2</b>
<i>PredSet2</i>	<i>ParSet3</i>	16.0	7.9	11.0	<b>5.2</b>
<i>PredSet3</i>	<i>ParSet1</i>	8.0	7.8	6.5	<b>6.5</b>
<i>PredSet4</i>	<i>ParSet1</i>	9.3	10.7	4.5	<b>4.0</b>
<i>PredSet5</i>	<i>ParSet1</i>	8.5	15.3	13.7	<b>11.0</b>

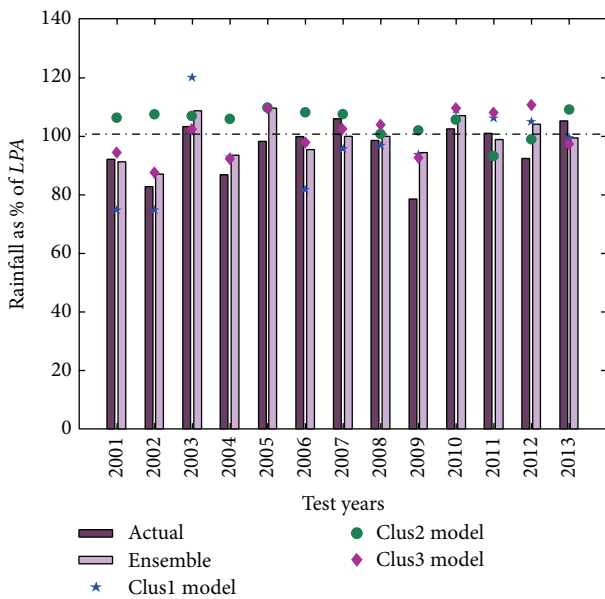


FIGURE 3: Performance of forecasts by proposed fuzzy clustering-based ensemble model and its respective three clusters models by MR for *PredSet4*. The deep and light purple bars represent the actual and predicted ISMR in terms of percent of LPA. The symbols represent forecasts given by individual cluster models. The results are shown for test period 2001–2013.

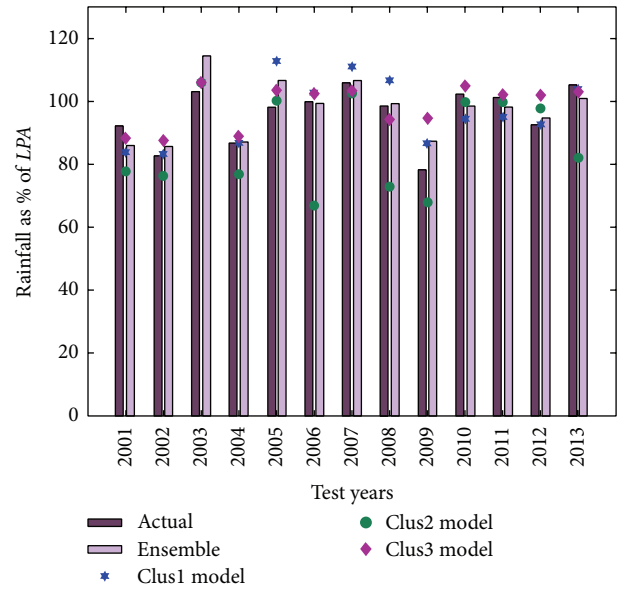


FIGURE 4: Performance of forecasts by proposed fuzzy clustering-based ensemble model and its respective three clusters models by MLP for *PredSet4*. The deep and light purple bars represent the actual and predicted ISMR in terms of percent of LPA. The symbols represent forecasts given by individual cluster models. The results are shown for test period 2001–2013.

presented in Table 7. *PredSet3* (Table 2) with RNN parameters *ParSet1* (Table 3) gives error of 5.1%. RNN gives weights in decreasing order of their distance from test year to the training years. The pattern of actual and ensemble predicted rainfall in terms of percentage of LPA is shown in Figure 5.

5.2.4. Generalized Regression Neural Network Model (GRNN). Generalized regression neural network ensemble and

individual cluster models’ errors in terms of mean absolute errors are presented in Table 8. The model reports an error of 6.1% for *PredSet3* (Table 2). Figure 6 shows the interannual variations of ensemble forecast of rainfall by GRNN ensemble model along with actual rainfall pattern in terms of percentage of LPA for period 2001–2013. It is observed that the predicted values are close to actual rainfall patterns. Prediction by models designed for clusters is shown by different symbols.

TABLE 7: Mean absolute errors (%) for annual Indian summer monsoon rainfall prediction by individual RNN cluster models and ensemble model for test period 2001–2013. Reports minimum error of 5.1%.

Predictor set	Parameter set	Cluster1 error (%)	Cluster2 error (%)	Cluster3 error (%)	Ensemble error (%)
<i>PredSet1</i>	<i>ParSet1</i>	11.3	7.1	16.8	<b>7.0</b>
<i>PredSet2</i>	<i>ParSet1</i>	13.2	13.5	12.6	<b>8.5</b>
<i>PredSet3</i>	<i>ParSet1</i>	12.9	5.4	6.0	<b>5.1</b>
<i>PredSet4</i>	<i>ParSet1</i>	12.3	6.4	4.7	<b>5.9</b>
<i>PredSet5</i>	<i>ParSet2</i>	15.1	16.1	13.4	<b>8.8</b>

TABLE 8: Mean absolute errors (%) for annual Indian summer monsoon rainfall prediction by individual GRNN cluster models and ensemble model for test period 2001–2013. Reports minimum error of 6.1%.

Predictor set	Training years	Cluster1 error (%)	Cluster2 error (%)	Cluster3 error (%)	Ensemble error (%)
<i>PredSet1</i>	20	10.0	7.6	7.6	<b>6.4</b>
<i>PredSet2</i>	30	7.1	8.9	7.6	<b>6.4</b>
<i>PredSet3</i>	20	5.8	9.2	6.0	<b>6.1</b>
<i>PredSet4</i>	20	6.3	6.6	7.2	<b>6.3</b>
<i>PredSet5</i>	25	7.1	9.4	11.9	<b>6.6</b>

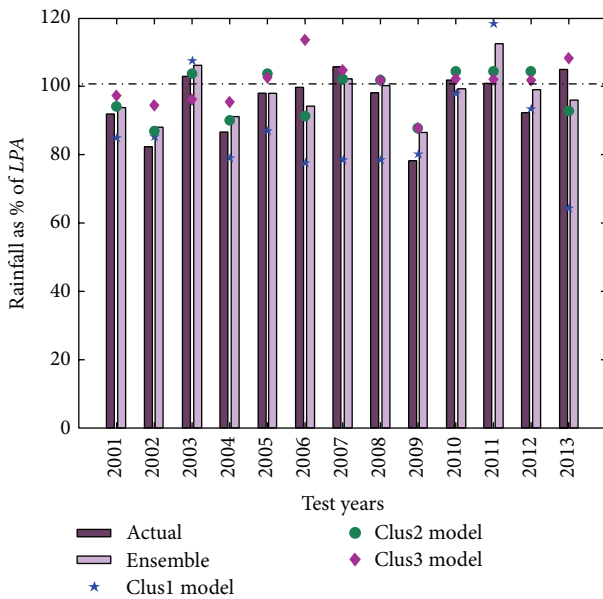


FIGURE 5: Performance of forecasts by proposed fuzzy clustering-based ensemble model and its respective three clusters models by RNN for *PredSet3*. The deep and light purple bars represent the actual and predicted ISMR in terms of percent of LPA. The symbols represent forecasts given by individual cluster models. The results are shown for test period 2001–2013.

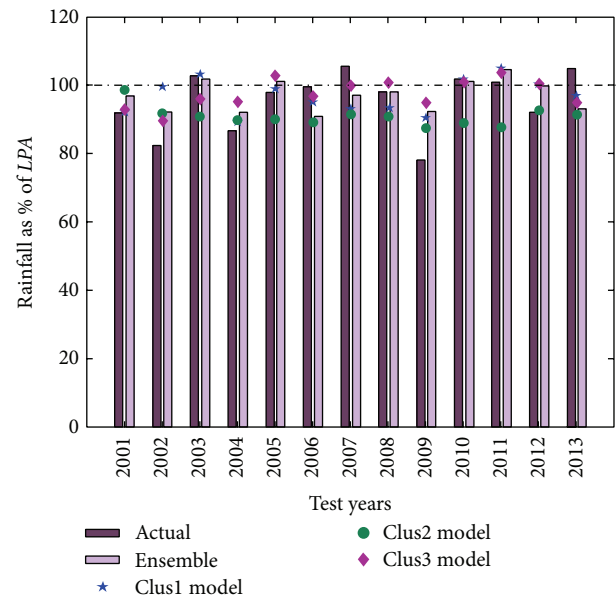


FIGURE 6: Performance of forecasts by proposed fuzzy clustering-based ensemble model and its respective three clusters models by GRNN for *PredSet3*. The deep and light purple bars represent the actual and predicted ISMR in terms of percent of LPA. The symbols represent forecasts given by individual cluster models. The results are shown for test period 2001–2013.

### 5.3. Statistical Measures for Validation of Proposed Approach.

Next, we validate the models in terms of other accuracy measures besides mean absolute error. Table 9 shows different forecast verification statistics for ensemble models during test period 2001–2013. We summarize the observations below.

- (i) *Root Mean Square Error (RMSE)*. MLP ensemble model gives RMSE of 5.3%, followed by RNN ensemble model with 6.4%. GRNN and MR models give RMSE of 7.4% and 8.4%, respectively.

- (ii) *Prediction Yield (PY)*. PY for 5% error category of MR, MLP, RNN, and GRNN ensemble models is 46%, 69%, 53%, and 46%, respectively. They give prediction yield of 76%, 92%, 92%, and 84% for allowed error of 10% category. Finally at error category of 15%, MR, MLP, RNN, and GRNN ensemble models give yield of 92%, 100%, 92%, and 100%, respectively. Thus, none of the predicted years show abrupt deviation from corresponding actual rainfall pattern.

TABLE 9: Prediction evaluation statistics for ensemble models during test period 2001–2013 (Section 4.5).

Verification measures	MR	MLP	RNN	GRNN
RMSE for forecast (%)	8.4	<b>5.3</b>	6.4	7.4
PY (%) at allowed error 5%	46	<b>69</b>	53	46
PY (%) at allowed error 10%	76	<b>92</b>	<b>92</b>	84
PY (%) at allowed error 15%	92	<b>100</b>	92	<b>100</b>
PC between actual and predicted rainfall	0.61	<b>0.81</b>	0.71	0.49
WI between actual and predicted rainfall	0.71	<b>0.89</b>	0.81	0.62

TABLE 10: Comparison of absolute errors for rainfall prediction by proposed ensemble models (Ensm) with clustering (WC) approach to standard method with same models without clustering (NC) approach.

Predictor set	MR		MLP		RNN		GRNN	
	Tot. error (NC) (%)	Ensm error (WC) (%)	Tot. error (NC) (%)	Ensm error (WC) (%)	Tot. error (NC) (%)	Ensm error (WC) (%)	Tot. error (NC) (%)	Ensm error (WC) (%)
<i>PredSet1</i>	8.9	<b>8.6</b>	10.0	<b>8.2</b>	11.7	<b>7.0</b>	6.9	<b>6.4</b>
<i>PredSet2</i>	9.2	<b>8.2</b>	12.8	<b>5.2</b>	10.7	<b>8.5</b>	7.2	<b>6.4</b>
<i>PredSet3</i>	7.4	<b>6.7</b>	6.7	<b>6.5</b>	6.2	<b>5.1</b>	6.1	<b>6.1</b>
<i>PredSet4</i>	6.7	<b>6.2</b>	5.8	<b>4.0</b>	6.0	<b>5.5</b>	6.3	<b>6.3</b>
<i>PredSet5</i>	8.2	<b>7.9</b>	9.7	11.0	8.9	<b>8.8</b>	9.0	<b>6.7</b>

(iii) *Pearson Correlation (PC)*. PC of 0.61, 0.81, 0.71, and 0.49 is observed for prediction by MR, MLP, RNN, and GRNN ensemble models, respectively. It is noticed that predicted rainfall by MLP ensemble model is highly correlated to actual values, while correlation for GRNN forecast is least.

(iv) *Willmott Index of Agreement (WI)*. WI for MR, MLP, RNN, and GRNN ensemble models is 0.71, 0.89, 0.81, and 0.62, respectively. The index shows that the agreement between actual and predicted rainfall is high for MLP and RNN ensemble models.

All of the mentioned statistical measures (Table 9) as well as mean absolute error (Table 6) in prediction of monsoon ascertain MLP model to be the best among all four proposed models.

#### 5.4. Comparison of Results

**5.4.1. Comparison with State-of-the-Art Methods.** Proposed fuzzy clustering-based ensemble prediction models are compared with the models used by Indian Meteorological Department (IMD). It is compared with existing 16-parameter power regression model [4] and Rajeevan et al. [5] 8- and 10-parameter models. Test period of seven years from 1996 to 2002 is considered. IMD models give root mean square errors of 10.8%, 7.6%, and 6.4%, respectively. The MR, MLP, RNN, and GRNN ensemble models give 6.0%, 3.4%, 4.4%, and 5.5% root mean square errors, respectively, outperforming all three IMD models. The results are shown as a bar graph in Figure 7.

**5.4.2. Improvement of Cluster-Based Models over Conventional Models.** Ensemble model error obtained by combining all clusters' model output is compared with error obtained by

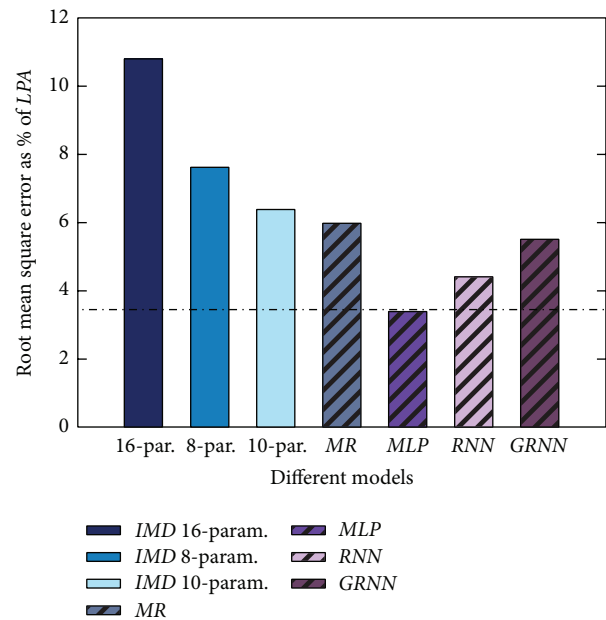


FIGURE 7: Comparison of MR (grey), MLP (purple), RNN (light purple), and GRNN (dark purple) models with IMD existing 16-param. (dark blue), 10-param. (blue), and 8-param. (light blue) models for time period of 1996–2002 [4, 5]. Striped bars represent errors by our proposed models.

same model (parameter), trained on the whole dataset without clustering. The mean absolute error for various models and predictor sets combinations are shown in Table 10. The result clearly depicts the improvement in prediction by clustering and ensemble method over nonclustered conventional method.

TABLE 11: Physical climatic events under study.

Climatic event	Number of years	Years associated with the event
Drought	13	1951, 1965, 1966, 1968, 1972, 1974, 1979, 1982, 1986, 1987, 2002, 2004, 2009
Flood	11	1953, 1956, 1958, 1959, 1961, 1964, 1970, 1975, 1983, 1988, 1994
El-Niño	23	1951, 1953, 1957, 1958, 1963, 1965, 1966, 1968, 1969, 1972, 1977, 1982, 1983, 1986, 1987, 1991, 1992, 1994, 1997, 2002, 2004, 2006, 2009
La-Niña	22	1950, 1954, 1955, 1956, 1964, 1970, 1971, 1973, 1974, 1975, 1984, 1985, 1988, 1989, 1995, 1998, 1999, 2000, 2007, 2008, 2010, 2011
Positive IOD	12	1957, 1961, 1963, 1967, 1972, 1977, 1982, 1983, 1994, 1997, 2006, 2007
Negative IOD	10	1958, 1960, 1964, 1971, 1974, 1975, 1989, 1992, 1993, 1996

TABLE 12: Threshold of support and confidence measures for associating obtained clusters with physical climatic events.

Predictor set	Support threshold	Confidence threshold
<i>PredSet1</i>	0.37	0.30
<i>PredSet2</i>	0.25	0.46
<i>PredSet3</i>	0.21	0.43
<i>PredSet4</i>	0.29	0.61
<i>PredSet5</i>	0.21	0.54

5.5. *Prediction of the Year 2014.* Annual Indian summer monsoon rainfall for the year of 2014 is 781.7 mm, which is 87.8% of *LPA* value. Proposed clustering-based ensemble *MR*, *MLP*, *RNN*, and *GRNN* models predict rainfall of 2014 as 96.1%, 80.3%, 80.0%, and 95.3% of *LPA*, respectively. Thus, proposed models show absolute error of 7.0% for forecasting rainfall of 2014.

## 6. Meteorological Analysis

Next, we try to visualize each cluster in terms of physical climatic events. The clusters obtained by fuzzy clustering are physically interpreted as being characterized by some global climatic events. The climatic events considered and studied during the time period 1948 to 2013 (period considered for clustering in our work) are El-Niño, La-Niña (<http://ggweather.com/enso/oni.htm>), positive and negative Indian ocean dipole (<http://bom.gov.au/climate/IOD>), drought, and flood, shown in Table 11.

Figure 8 shows the El-Niño and La-Niña years associated with drought, normal, and excess rainfall years during 1948–2013. The years having rainfall 10% above *LPA* are excess rainfall years and years having rainfall 10% below *LPA* are drought years. The El-Niño and La-Niña years are shown by color codes (*light green and green*) in the figure. The chart helps to visualize the cooccurrence of El-Niño and La-Niña events with extremities of *ISMR*.

6.1. *Measuring Association between Climatic Events and ISMR.* Support and confidence measures are considered to relate physical climatic event to the clusters generated by fuzzy clustering. They are defined below.

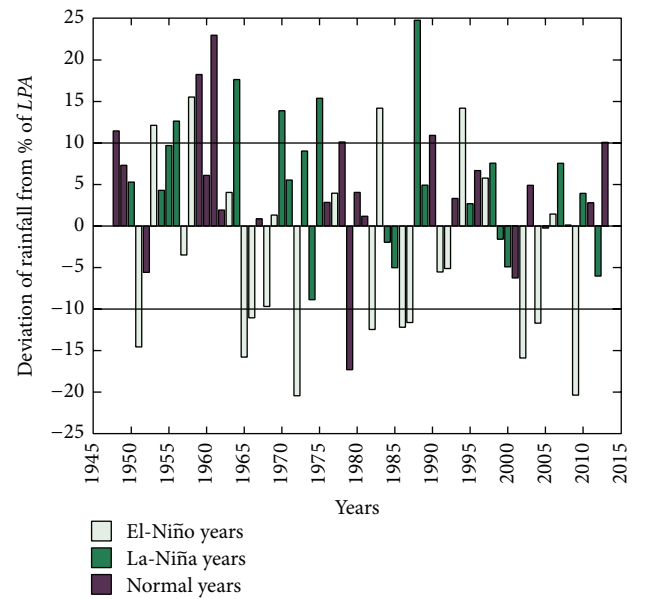


FIGURE 8: El-Niño (light green) and La-Niña (green) years association with drought (years below 10% of *LPA* rainfall), normal (years between +10% and –10% of *LPA* rainfall), and excess (years above 10% of *LPA* rainfall) years during period 1948–2013.

- (i) *Support.* Support is defined as percentage of total number of years in the cluster corresponding to the climatic event:

$$\text{Support} = \frac{x_{ce}}{N}, \quad (12)$$

where  $x_{ce}$  denotes the number of years associated with a specific climatic event in the cluster and  $N$  is the total count of years in the cluster.

- (ii) *Confidence.* Confidence is defined as percentage of years associated with the climatic event in the cluster to the total number of such event years:

$$\text{Confidence} = \frac{x_{ce}}{T_{ce}}, \quad (13)$$

where  $T_{ce}$  is the number of years associated with the climatic event during the period 1948–2013.

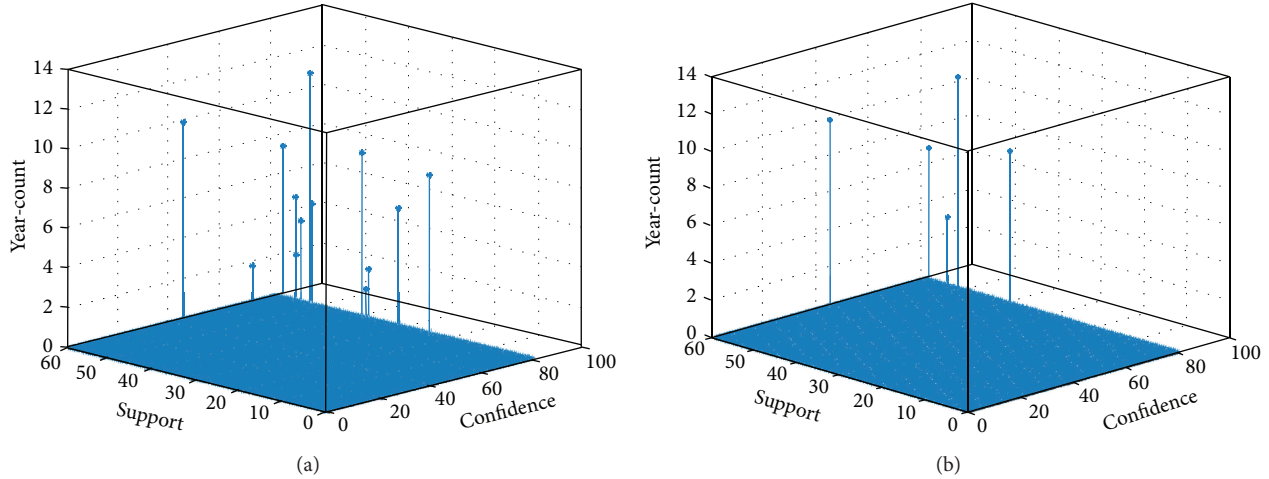


FIGURE 9: Histogram of the confidence and support measures as bins of year-count before (a) and after (b) thresholding for *PredSet1*.

TABLE 13: Identified physical climatic events being associated with clusters obtained by fuzzy clustering.

Predictor	Cluster1	Cluster2	Cluster3
<i>PredSet1</i>	Drought, El-Niño	La-Niña	La-Niña
<i>PredSet2</i>	Flood, La-Niña	Drought	Drought, El-Niño, La-Niña
<i>PredSet3</i>	El-Niño, positive IOD	Drought	Drought, El-Niño
<i>PredSet4</i>	La-Niña	Flood, La-Niña	Drought
<i>PredSet5</i>	—	Drought, El-Niño	Flood

We relate a cluster to a physical climatic event described in Table 11, if both support and confidence measures attain the corresponding thresholds. The thresholds are chosen in a way that 50% of years of study are under consideration. A low threshold compromises the importance of a climatic event being related to a particular cluster; on the other hand if even less number of years are taken, then threshold values should be high, which in turn will leave out most of the clusters. Therefore, as an optimal between the extremes, 50% of years are considered. Figure 9 shows histograms with confidence and support as bins of year-count for cases before and after threshold process, respectively, for predictors *PredSet1* (Table 2). The threshold values obtained for predictor sets are presented in Table 12. For each predictor set, we associate the clusters with physical climatic events, if they satisfy both support and confidence thresholds. The climatic events corresponding to cluster are shown in Table 13. Results establish coexistence of events of *La-Niña* and *flood*. It also puts light on high probability of occurrence of *El-Niño*, *drought*, and *positive IOD* events simultaneously.

## 7. Conclusion

Monsoon is an important phenomenon for economic development of agricultural-land like India. Large variability of monsoon over years makes prediction of rainfall a challenging task. The paper attempts to address this problem by clustering the years into similar groups and finally, multimodel

ensemble forecast is provided for Indian summer monsoon rainfall.

Different climatic parameters with best correlated month value are identified and five different predictor sets are built for prediction of Indian monsoon. Four different models, namely, *MR*, *MLP*, *RNN*, and *GRNN*, are designed for each cluster exclusively. The final forecast is provided by weighted ensemble of forecasts by each cluster’s model, where weight is considered as fuzzy membership of belongingness in each cluster. Multilayer perceptron ensemble model provides mean absolute error of 4.0% for prediction of annual rainfall, which is appreciable for forecasting complex monsoon process. Proposed fuzzy clustering-based ensemble approach surpasses the conventional approach. Performance of proposed clustering-based ensemble models is superior to existing *IMD*’s models [4, 5]. The error statistics also ascertain the superiority of multilayer perceptron model over other three proposed models. Lastly, in meteorological context the clusters are linked with global climatic events.

In the future, large number of climatic parameters influencing Indian monsoon can be explored and different predictor set can be used for different clusters of years to provide even better forecasting accuracy.

## Conflict of Interests

The authors declare that there is no conflict of interests regarding the publication of this paper.

## Acknowledgment

This work is supported by RBU project through RESPOND program of ISRO through KCSTC, IIT Kharagpur.

## References

- [1] H. F. Blanford, "On the connexion of the Himalaya snowfall with dry winds and seasons of drought in India," *Proceedings of the Royal Society of London*, vol. 37, no. 232–234, pp. 3–22, 1884.
- [2] G. T. Walker, "Correlation in seasonal variations of weather—IV, a further study of world weather," *Memoirs of the India Meteorological Department*, vol. 24, pp. 275–332, 1924.
- [3] V. Thapliyal and S. M. Kulshrestha, "Recent models for long range forecasting of South-West monsoon rainfall in India," *Mausam*, vol. 43, no. 3, pp. 239–248, 1992.
- [4] V. Gowariker, V. Thapliyal, S. M. Kulshrestha, G. S. Mandal, N. Sen Roy, and D. R. Sikka, "A power regression model for long range forecast of southwest monsoon rainfall over India," *Mausam*, vol. 42, no. 2, pp. 125–130, 1991.
- [5] M. Rajeevan, D. S. Pai, S. K. Dikshit, and R. R. Kelkar, "IMD's new operational models for long-range forecast of southwest monsoon rainfall over India and their verification for 2003," *Current Science*, vol. 86, no. 3, pp. 422–431, 2004.
- [6] M. Rajeevan, D. S. Pai, R. A. Kumar, and B. Lal, "New statistical models for long-range forecasting of southwest monsoon rainfall over India," *Climate Dynamics*, vol. 28, no. 7–8, pp. 813–828, 2007.
- [7] J. Schewe and A. Levermann, "A statistically predictive model for future monsoon failure in India," *Environmental Research Letters*, vol. 7, no. 4, Article ID 044023, 2012.
- [8] Q. Wu, Y. Yan, and D. Chen, "A linear markov model for east asian monsoon seasonal forecast," *Journal of Climate*, vol. 26, no. 14, pp. 5183–5195, 2013.
- [9] K. Fan, Y. Liu, and H. Chen, "Improving the prediction of the east asian summer monsoon: new approaches," *Weather & Forecasting*, vol. 27, no. 4, pp. 1017–1030, 2012.
- [10] F. Mekanik, M. A. Imteaz, S. Gato-Trinidad, and A. Elmahdi, "Multiple regression and artificial neural network for long-term rainfall forecasting using large scale climate modes," *Journal of Hydrology*, vol. 503, pp. 11–21, 2013.
- [11] A. K. Sahai, M. K. Soman, and V. Satyan, "All India summer monsoon rainfall prediction using an artificial neural network," *Climate Dynamics*, vol. 16, no. 4, pp. 291–302, 2000.
- [12] W.-C. Hong, "Rainfall forecasting by technological machine learning models," *Applied Mathematics and Computation*, vol. 200, no. 1, pp. 41–57, 2008.
- [13] S. Chattopadhyay and G. Chattopadhyay, "Comparative study among different neural net learning algorithms applied to rainfall time series," *Meteorological Applications*, vol. 15, no. 2, pp. 273–280, 2008.
- [14] N. Acharya, S. C. Kar, M. A. Kulkarni, U. C. Mohanty, and L. N. Sahoo, "Multi-model ensemble schemes for predicting northeast monsoon rainfall over peninsular India," *Journal of Earth System Science*, vol. 120, no. 5, pp. 795–805, 2011.
- [15] V. R. Durai and R. Bhardwaj, "Improving precipitation forecasts skill over India using a multi-model ensemble technique," *Geofizika*, vol. 30, no. 2, pp. 119–141, 2013.
- [16] B. Parthasarathy, A. A. Munot, and D. R. Kothawale, "Monthly and seasonal rainfall series for All-India homogeneous regions and meteorological subdivisions, 1871–1994," Tech. Rep. RR-065, Indian Institute of Tropical Meteorology, 1995.
- [17] G. P. Compo, J. S. Whitaker, P. D. Sardeshmukh et al., "The twentieth century reanalysis project," *Quarterly Journal of the Royal Meteorological Society*, vol. 137, no. 654, pp. 1–28, 2011.
- [18] E. Kalnay, M. Kanamitsu, R. Kistler et al., "The NCEP/NCAR 40-year reanalysis project," *Bulletin of the American Meteorological Society*, vol. 77, no. 3, pp. 437–471, 1996.
- [19] E. M. Rasmusson and T. H. Carpenter, "Variations in tropical sea surface temperature and surface wind fields associated with the Southern Oscillation/El Niño," *Monthly Weather Review*, vol. 110, no. 5, pp. 354–384, 1982.

## Research Article

# Analysis on the Extreme Heat Wave over China around Yangtze River Region in the Summer of 2013 and Its Main Contributing Factors

Jin Li,<sup>1</sup> Ting Ding,<sup>2</sup> Xiaolong Jia,<sup>2,3</sup> and Xianchan Zhao<sup>4</sup>

<sup>1</sup>91867 Troops of PLA, Yiwu 322000, China

<sup>2</sup>Laboratory for Climate Studies, National Climate Center, China Meteorological Administration, Beijing 100081, China

<sup>3</sup>Collaborative Innovation Center on Forecast and Evaluation of Meteorological Disasters, Nanjing University of Information Science & Technology, Nanjing 210044, China

<sup>4</sup>Yiwu Meteorological Bureau, Yiwu 322000, China

Correspondence should be addressed to Ting Ding; [dingting@cma.gov.cn](mailto:dingting@cma.gov.cn)

Received 12 January 2015; Revised 15 June 2015; Accepted 21 June 2015

Academic Editor: Guillermo Baigorria

Copyright © 2015 Jin Li et al. This is an open access article distributed under the Creative Commons Attribution License, which permits unrestricted use, distribution, and reproduction in any medium, provided the original work is properly cited.

In the summer of 2013, a rare extreme heat wave occurred in the middle and lower reaches of the Yangtze River in China. Based on high resolution reanalysis data from ECMWF, comprehensive analyses on the associated atmospheric circulation and the sea surface temperature anomaly (SSTA) were provided. The stable and strong West Pacific Subtropical High (WPSH) was the direct cause for the heat wave. The WPSH had four westward extensions, which brought about four hot spells in southern China. The South Asia High (SAH) at 150 hPa was more eastward and more northward than normal. The strong Hadley circulation in the central and western Pacific and the anomalous easterlies at 500 hPa and 250 hPa in the middle and high latitudes were favorable for more hot days (HDs). The total HDs in the middle and lower reaches of the Yangtze River had close relationships with the zonal wind anomalies in the middle and high latitudes, the SSTA in the Indian Ocean and Pacific, and the dry soil conditions of the Yangtze River Valley in spring and summer. The anomalies of the tropical, subtropical, and polar circulation and the underlying surfaces could be responsible for this extreme heat wave.

## 1. Introduction

The Fifth Assessment Report of Intergovernmental Panel on Climate Change (IPCC) indicates that new analyses continue to support the Fourth Assessment Report and IPCC Special Report on Managing the Risks of Extreme Events and Disasters to Advance Climate Change Adaptation (SREX) conclusions that there is medium confidence that globally the length and frequency of warm spells, including heat waves, have increased since the middle of the 20th century although it is likely (high confidence) that heatwave frequency has increased during this period in large parts of Europe, Asia, and Australia [1]. The heat wave stressed the delivery of water and energy resources and had significant morbidity and mortality impacts on humans and livestock [2–5]. Therefore,

heat wave events have attracted considerable attention during recent years.

In recent years, especially after the European heat wave in 2003, many studies analyzed the magnitudes, durations, impacts associated with heat waves, and the causes of hot spells. The main features of European heat wave in 2003 summer were described and discussed in detail in the study by Feudale and Shukla [6]. Model simulations indicated that hot summers could be more frequent in a future warmer climate, and, therefore, the European heat wave of 2003 summer might give an indication of the nature of heat waves that could occur due to global warming [7–9]. Sea surface temperature anomaly (SSTA) was one of the possible factors in enhancing the heat wave in Europe [6, 10]. The anomalous 2010 Russian heat wave that caused adverse

impacts exceeded the amplitude and spatial extent of the previous hottest summer in 2003 [11–13]. The principal factor contributing to the heat wave magnitude was a severe rainfall deficit during antecedent and concurrent seasons related to a La Niña event [14].

There were a large number of previous studies on heat wave events and the associated atmospheric circulation in China. Significant increasing trend of the frequencies of heat waves in China was found in recent decades [15–17]. It was advantageous to the occurrences of high temperature events in the south of the Yangtze Valley and South China when the Tibetan Plateau High sustained, reinforced, and continually expanded eastward and westward [18, 19]. The continuous hot weather over southern China was associated with the variation of the West Pacific Subtropical High (WPSH). Heat wave events occurred when the WPSH manifested intensely over most of southern China from late July to August stably [20, 21]. The descending motion provided a sunny weather in favor of the solar radiation directly down to the ground surface that led to remarkable sensible heat flux and long-wave radiation near the surface, which was favorable for the persistent heat wave event in South China in the summer of 2003 [22]. The polar vortex leaning to the western hemisphere for a long time led to weakening of the cold air which influenced China, and this was one of the important reasons why the WPSH was abnormally strong and the temperature was persistently high in the south of China [23]. Weak cold air transport, northward locations of subtropical high ridgeline, and less snow cover over the Tibetan Plateau in the winter and spring of 2005/2006 were the three main direct causes for the extremely hot and dry weather over the Chongqing and Sichuan areas of China in the summer of 2006 [24]. Low-level divergence, subtropical westerly jet axis shifting northward, and the westward jet center were conducive to the occurrence and maintenance of high temperature in China in the summer of 2009 [25].

From July to August in 2013, a long-lasting high temperature event occurred in East China, in a zone extending from North China southward to the midlower reaches of the Yangtze River and to the south of the lower reaches of the Yangtze River [26]. The number of consecutive hot days (HDs) and daily maximum temperature (DMT) in many regions broke the historical extreme records and caused moderate to severe droughts in Guizhou, Hunan, Chongqing, and other provinces. Due to few rain days, little precipitation, high solar radiation, and high evaporation in the south of the Yangtze River, drought brought about devastating impact to many aspects of social life. 1610 million people and crops of 18720 km<sup>2</sup> in Hunan province were affected, and 353.5 million people and 1.417 million livestock were in the shortage of drinking water [27]. 3520 km<sup>2</sup> crops had no harvest, and direct economic losses were 14.3 billion [27]. However, there were few studies on the anomaly of the thorough meteorological situation associated with the heat wave event in 2013. Here, we take a comprehensive diagnostic analysis on the 2013 summer heat wave in the middle and lower reaches of the Yangtze River in China. This paper will mainly focus on the characteristics and causes of this extreme heat wave event,

in order to provide a reference to the forecasting of extreme hot spell events in the future.

## 2. Data

The temperature records were chosen from the daily observations of 752 stations during the period 1951–2013 from the National Meteorological Information Center of the China Meteorological Administration [28–30]. The datasets had been quality-controlled and used in numerous previous studies [31–37]. The stations were evenly distributed in the plains to the east of 95°E. Because of numerous missing data before 1961 [38], the daily series of summer for 1961–2013 were analyzed in the present paper. Stations with more than 1-day missing records during June–August in every month were excluded. Finally, 533 stations were used for subsequent analysis. The analyses of atmospheric circulation in association with heat waves were based on the latest ECMWF ERA-Interim global reanalysis data with 0.75° × 0.75° spatial resolution on 60 vertical levels from the surface up to 0.1 hPa and 6 h temporal resolution for 1979–2013, and the sea surface temperature (SST) analyses were also chosen from the ERA-Interim data, which were downloaded from <http://www.ecmwf.int/en/research/climate-reanalysis/browse-reanalysis-datasets>.

Relative indices of high temperature extremes were considered in the present paper. A hot day (HD) was defined if the temperature exceeded the 90th percentile of the local daily temperature climatology, as applied in IPCC [39] and many previous studies [40–44]. The least squares method was applied to fit the linear trend and the statistical *t*-test was used to test the significance of correlation coefficient for two time series [45, 46]. The climatic value was the average of values during 1981–2010.

## 3. The Characteristics of the Heat Wave in 2013

In 2013, the summer average temperature in China was 21.7°C, which was 0.7°C above normal [47]. The average summer temperature in 2006 and 2010 was also 21.7°C, which was the highest since 1961 [47]. For 8 provinces from the south of the Yellow River to the middle and lower reaches of the Yangtze River, the average temperature (28.0°C) was the highest since 1961, with 1.6°C above normal [47]. The average temperature, the average maximum temperature and the average minimum temperature over the middle and lower reaches of the Yangtze River broke the records in the late 50 years [48]. In 23 provinces of the Yangtze River Valley, extreme high temperature events occurred in 530 meteorological stations, and 206 stations reached the highest level in the past 50 years (the highest daily maximum temperature of 44.1°C was recorded in Xinchang in the south of the Yangtze River). Record-breaking consecutive extreme hot temperature events were observed in 144 stations, including Changsha (48 days), Hengshan (48 days), and Anren (45 days) [47]. According to the report of China Meteorology Daily, the heat wave covered an area of 3.177 million km<sup>2</sup> for

the period ending on 30 July 2013 [49]. Therefore, the heat wave over the middle and lower reaches of the Yangtze River Valley in China was long-lasting, severe, and affected a large area with great harm in the summer of 2013.

In order to characterize the magnitude and duration of the 2013 summer hot spell, the analysis approach in Figure 1 was similar to the previous study on heat wave by Barriopedro et al. [11]. Figure 1 shows the spatial pattern of the highest value of DMT anomalies averaging in different time scales and the anomaly of the total HDs in 2013 summer in China. Figures 1(a) to 1(e) revealed that the center of the exceptional warmth at all temporal scales was along the reaches of the Yangtze River. The daily and weekly positive anomalies were particularly pronounced, exceeding the 90th percentile during 1961–2013 by above 2°C. The biweekly to seasonal positive anomalies exceeded the 90th percentile by about 1°C. In Figure 1(f), the spatial distribution of the HD anomaly in 2013 was similar to the distribution in Figures 1(a) to 1(e). The center of positive anomaly for HDs mainly located along the reaches of the Yangtze River, with 10 days more than the climatic average and about one week more than the 90th percentile threshold. In Chongqing, Shanghai, and the middle and northern of Zhejiang province, the HDs exceeded the climatic average by more than 25 days and exceeded the 90th percentile by over 10 days. Because of the sparse distribution of observation stations in the upper reaches of the Yangtze River, region A (26.4°N–34.2°N, 105°E–122°E) in Figure 1(f) was selected to analyze the hot spells over the middle and lower reaches of the Yangtze River in the paper.

#### 4. The Anomaly of the Atmospheric Circulation and SST in the Summer of 2013

**4.1. The Anomaly of WPSH.** The likelihood of passing into the HD threshold was more frequently reached in South China when WPSH manifested intensely over the region in the summer [21]. For the 2013 heat wave, Peng [49] indicated that the anomaly of WPSH was the major and direct reason. Figure 2 revealed that the average geopotential height anomaly series of 500 hPa over region A had high positive correlation with the total HDs for all the stations in region A in the summer during 1979–2013. The correlation coefficient is 0.58, significant at the 0.01 level. The average geopotential height anomaly of region A in the summer of 2013 was the second highest for 1979–2013, and the total HDs in 2013 were the peak in recent years. In Figure 2, the total HDs in region A presented an increasing trend. The strong heat wave events in South China became more frequent and stronger significantly in the 54 years [26]. The heat wave in the summer of 2013 may also be partly due to the global warming. Global warming altered the climatic distribution of extreme heat events, such that heat wave might become more likely to occur.

Figure 3 shows the longitude and latitude profiles of the 500 hPa geopotential height departure from 5880 gpm in region A in the summer of 2013. The WPSH at 500 hPa first strengthened in region A in mid-June and intensified in mid-July with higher geopotential height anomaly than that in mid-June. The positive geopotential height anomaly

over region A reached the highest in late July to mid-August. In the end of August, the WPSH enhanced for a few days. The number of HD stations in region A increased while the positive geopotential height anomalies over region A were observed and reduced while the positive anomalies decreased. The four intensifications of the WPSH indicated the four hot spells in the middle and lower reaches of the Yangtze River in the summer of 2013, and the third hot spell from late July to mid-August was the most severe. This was consistent with analyses by Tang et al. [48].

The position of the WPSH ridge line at 500 hPa was compared with the climatic position for the summer in 2013 (Figure 4). The WPSH ridge line was more northward than the climatic position in early to mid-June, and more southward from the second half of July to early August and in late August. In mid-June, the WPSH ridge line arrived near 28–31°N, which was 5–8 latitudes more northward than the climatic position. From late July to early August, the ridge line was 4–6 latitudes more southward than the climatic position and stabilized in the vicinity of 25–26°N. The WPSH ridge line was 2 latitudes more northward than the climatic position in June, 1 latitude more southward in July, and 1.5 latitudes more southward in August. The WPSH was maintained in the vicinity of 25–30°N during the whole summer, which caused the long-lasting heat wave in region A. Meanwhile, the anomalous position of the WPSH precluded its susceptibility to weakening by tropical easterly wave or typhoons, which could disrupt or end the heat wave. The easterly wave represented a kind of wave migrating westward through deep easterlies on the south side of a subtropical high over the western Pacific and South Asia [50]. Tropical easterly waves were a type of atmospheric trough oriented north to south, which moved from east to west across the tropics and sometimes could lead to typhoons in western Pacific Ocean.

**4.2. The Anomaly of the South Asia High.** South Asia High (SAH) was a strong and steady atmospheric anticyclone in the upper troposphere and lower stratosphere over southern Asia in the summer and had close relationship with the atmospheric circulation of northern hemisphere and Asia [51–56]. In particular, it had great impacts on the summer heat waves in China [18, 19, 25, 56]. The studies by Wu et al. [53] and Li et al. [57] revealed that the descending air motion prevailed in the Yangtze Valley while the ridge line of the SAH was more northward. Zhu et al. [58] pointed out that the WPSH strengthened and extended westward, when the SAH strengthened and moved eastward. The precipitation was above normal in northern China and below normal in southern China in the summer of 2013 [47]. The release of the latent heat of condensation over the northern part of China enhanced the geopotential height anomaly and caused the divergence in the upper troposphere and lower stratosphere [47]. The southward divergent air flows descended over the WPSH and made the WPSH continue to be strong and westward [47]. Figure 5 shows the distribution of geopotential height and the anomaly at 150 hPa in the summer of 2013, and the 14360 gpm isoline represents the climatological position of SAH. The center of the SAH was located near 80°E, and the high value of geopotential height anomaly in Figure 5 was

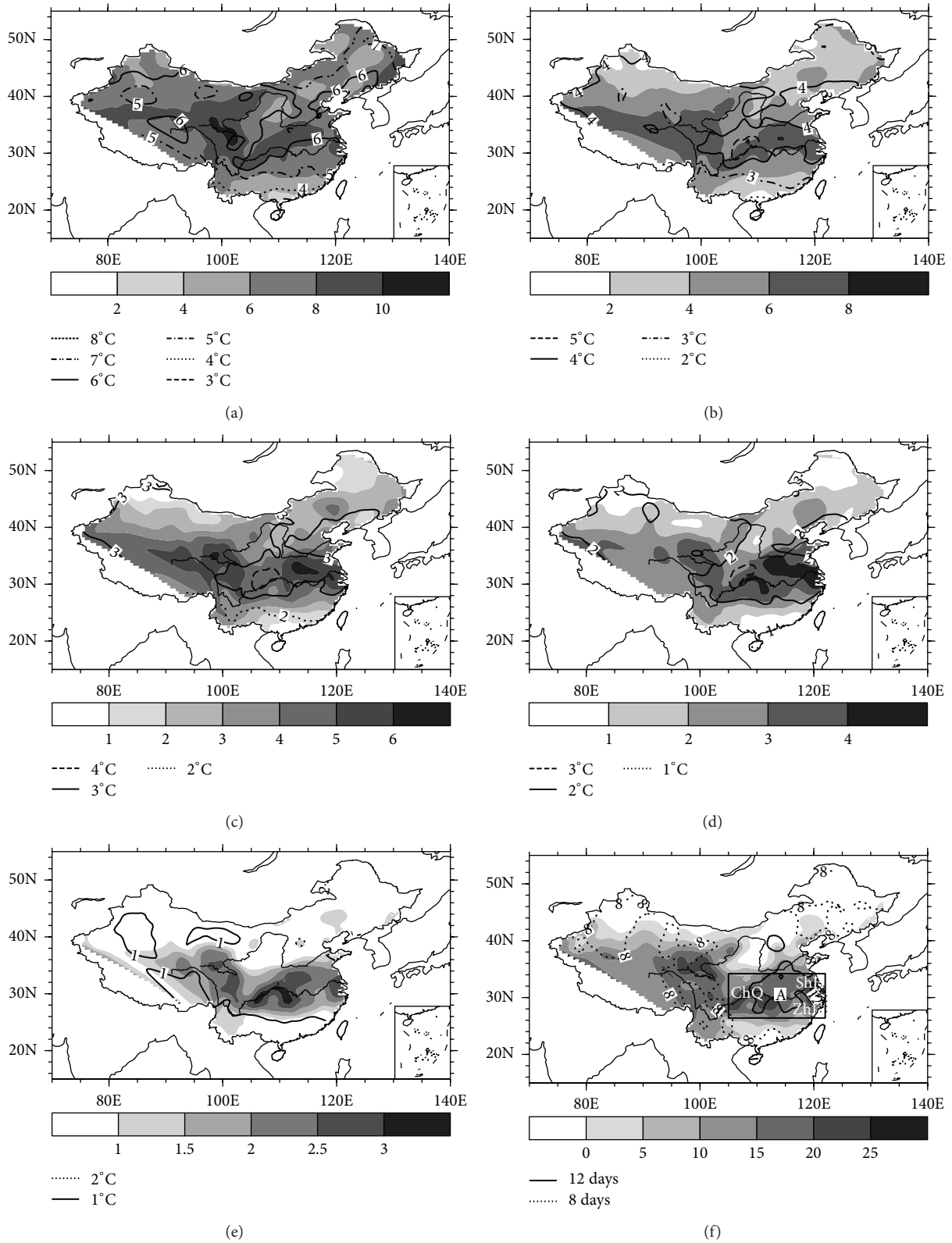


FIGURE 1: The distribution of the highest value of DMT anomalies ( $^{\circ}\text{C}$ ) running-averaging (a) daily, (b) weekly, (c) biweekly, (d) monthly, and (e) seasonally and in the anomaly of the total HDs (days) in 2013 summer in China (f). The shaded areas denote the highest value of DMT anomaly, and the lines denote the 90th percentile threshold of DMT anomaly for 1961–2013 for the corresponding time scales. The rectangle ( $26.4^{\circ}\text{N}$ – $34.2^{\circ}\text{N}$ ,  $105^{\circ}\text{E}$ – $122^{\circ}\text{E}$ ) in Figure 1(f) indicates region A. “ChQ,” “ShH,” and “Zhj” in (f) indicate the geographical location of Chongqing, Shanghai, and Zhejiang province.

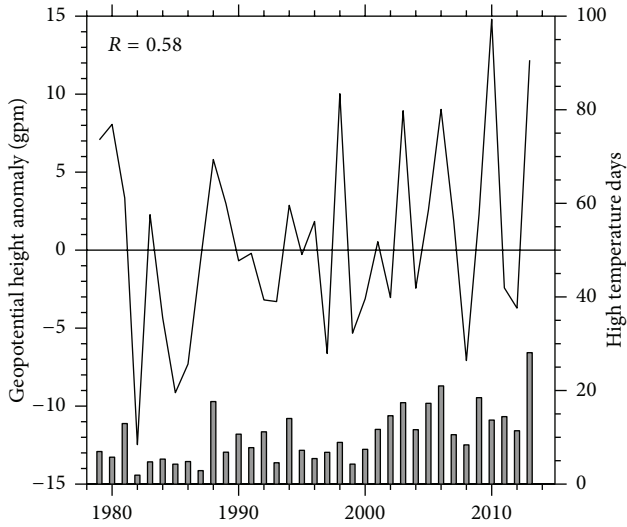


FIGURE 2: The anomaly of 500 hPa average geopotential height (gpm, solid line) and the total HDs (days) of observation stations (bar) in region A in the summer of 1979–2013. The total HDs are reduced 100 times.

located in the region of the Yellow River Valley. Compared with the climatological position of SAH, it was found that the SAH was more eastward and more northward than usual in the summer of 2013. Accompanied by the abnormal location and strengthening of the SAH, the WPSH was stronger and more westward in this summer.

In order to reveal the interrelation between troposphere and stratosphere, Figure 6 shows the time-height section of the geopotential height anomaly averaged in region A in the summer of 2013. There were positive anomalies from 700 hPa up to 50 hPa during the most time of the summer. The maximum of geopotential height anomaly was mainly found at about 150 hPa, and the downward expansion of the upper-level positive height anomaly existed. The anomaly of SAH was found in the bottom of the stratosphere and the anomaly of WPSH in the midupper troposphere. In Figure 6, four eastward extensions and strengthening of the SAH were found at 150 hPa in the second half of June, the first half of July, late July, and late August. Meanwhile, the WPSH strengthened and expanded to the west (Figure 3) and then resulted in the increasing HDs in southern China.

**4.3. The Anomaly of Zonal and Meridional Flows.** The zonal and meridional winds were the main components of air movement, and the atmospheric circulation anomaly and the occurrences of many extreme events were associated with the anomalies of wind [21, 59–66].

**4.3.1. The Anomaly of Zonal Wind.** Figure 7 shows the correlation coefficient distribution between the total HDs in region A and u-component anomaly and the distribution of u-component anomaly in 2013 summer. At 250 hPa, the significant negative correlation was found over the northern Kazakhstan northeastward to the north of Lake Baikal and the Yangtze River Valley, while significant positive correlation

was found over Uzbekistan eastward to Northeast China. In the summer of 2013, the anomalous easterlies were observed in two regions at 250 hPa, in north of 50°N and south of 36°N, with the maximum anomalies exceeding 6 m/s and 4 m/s, respectively. The anomalous westerly was found in the region of 38–48°N, with the maximum anomaly above 12 m/s. Comparing Figure 7(a) with Figure 7(b), the distribution of zonal wind anomaly at 250 hPa in the summer of 2013 was favorable for HDs in region A. In Figures 7(c) and 7(d), the distribution of correlation coefficient during 1979–2013 and u-wind anomaly in 2013 summer at 500 hPa was similar to those at 250 hPa. At 700 hPa, the significant positive correlation was found in the south of the Balkhash Lake (located in southeastern Kazakhstan in Central Asia within the domain 73–80°E, 45–48°N) and from Northeast China to the Korean Peninsula. For the mean climatology, the subtropical monsoon prevails from Southeast China to Northeast China at 700 hPa in summer. The HDs were more in region A and the WPSH was more westward, when the westerly wind was stronger from Northeast China to the Korean Peninsula. The zonal air flow in the middle and high latitudes of the northern hemisphere had close relationship with the heat waves in region A.

**4.3.2. The Anomaly of Meridional Wind.** In summer, the WPSH often weakened and moved eastward during the period of tropical cyclones, and the generation and tracks of tropical cyclones were closely associated with the intertropical convergence zone (ITCZ) [21]. Yang and Li [21] found that the anomaly of cross-equatorial airflow in the middle and western Pacific was one of the important causes for the extreme high temperature in southern China in the summer of 2003. In Figure 8(a), the strong southerly anomaly at the top of troposphere transported northward from the southern hemisphere to near 20°N and then descended, while the northerly anomaly at the bottom of troposphere blew to near 10°N and then ascended. The strong ascending branch was mainly located near 10°S. The Hadley circulation of northern hemisphere was stronger in the middle and western Pacific in the summer of 2013, which contributed to the strengthening and extending westward of WPSH. The northerly anomaly in the central and western Pacific was favorable for weaker ITCZ [21]. In the summer of 2013, the northerly anomaly prevailed in the lower troposphere between 10°S and 20°N in the middle and western Pacific. The weakening of the southerly was unfavorable for the generation and development of tropical cyclones and was against the weakening of the WPSH. The average numbers of tropical cyclones generating in the ITCZ in July and August were 5.6 and 7.2, respectively, while the numbers in July 2013 and August 2013 were smaller than the climate mean, with 3 and 4, respectively [67]. At the same time, in the northern troposphere of about 28°N (Figure 8(a)), there was an anticlockwise circulation. The strong descending branch lied in the southern of 30°N, and the anticlockwise circulation also strengthened the WPSH.

Figure 8(b) shows that in Southeast Asia, the northerly anomaly prevailed below 500 hPa between 10°S and 15°N in the summer of 2013, while the southerly anomaly mainly appeared in the north of 15°N. The South China Sea monsoon

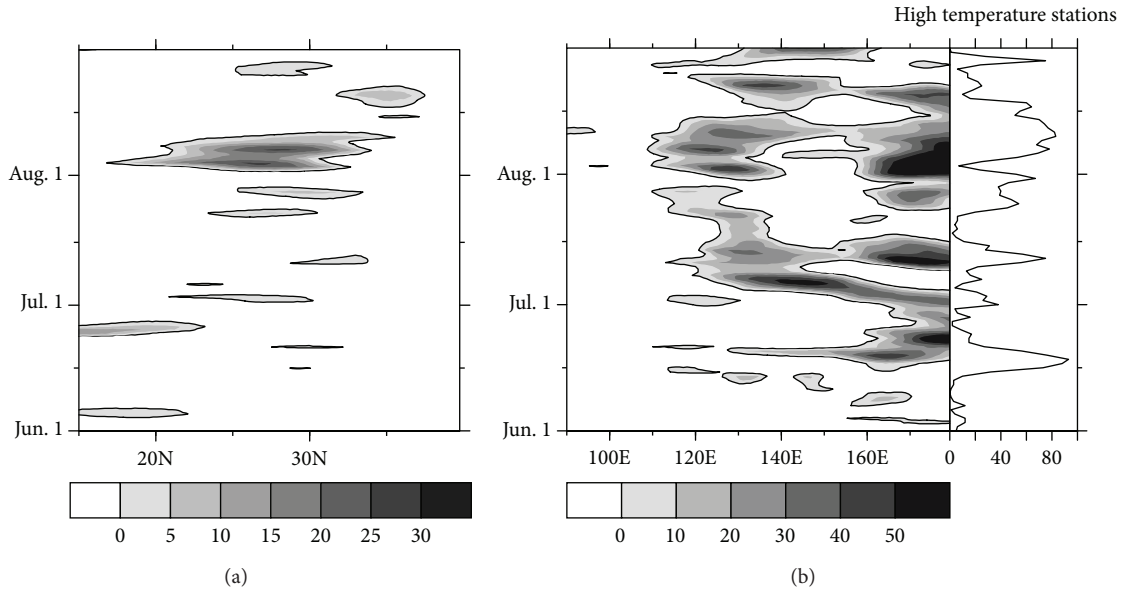


FIGURE 3: The 500 hPa geopotential height departure from 5880 gpm (shaded area, gpm) of (a) the time-latitude profile and (b) the time-longitude profile and stations affected by the heat wave in region A in the summer of 2013. In (b), the right figure denotes the number of daily total stations affected by the heat wave.

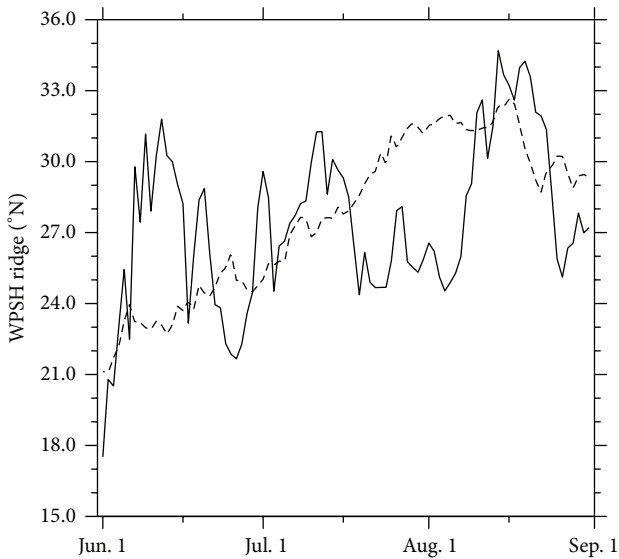


FIGURE 4: The variation of the climatic position (dashed line) and the position in the summer of 2013 (solid line) for WPSH ridge line at 500 hPa.

was weaker than usual, and the subtropical monsoon was stronger in the summer of 2013. The WPSH was more westward in summer accompanied by weak South China Sea monsoon and strong subtropical monsoon [68].

The southerly anomaly from surface to 300 hPa was found in 26–36°N (the middle and lower reaches of the Yangtze River) in the summer of 2013 (Figure 8(c)). The center of the southerly anomaly tilted northward with height.

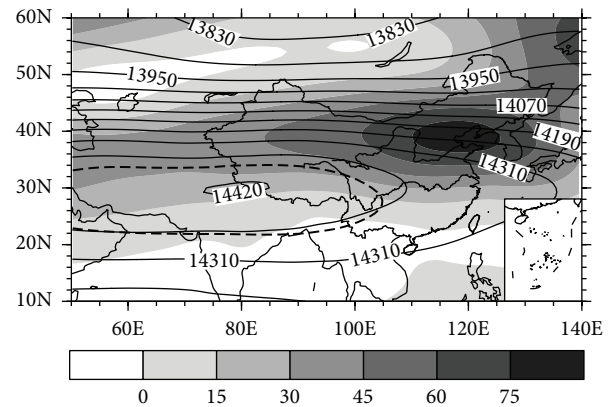


FIGURE 5: The distribution of geopotential height (solid line) and the anomaly (shaded area) at 150 hPa in the summer of 2013 (gpm). The dashed line (14360 gpm) indicates the climatological position of SAH.

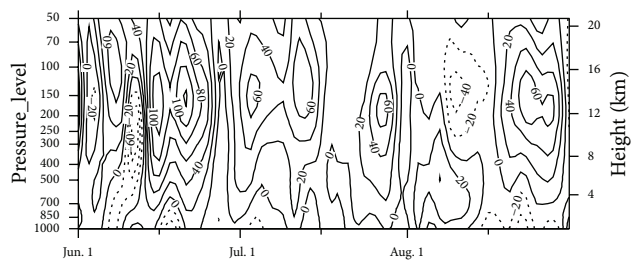


FIGURE 6: The time-height section of geopotential height anomaly averaged in the region A in the summer of 2013 (gpm).

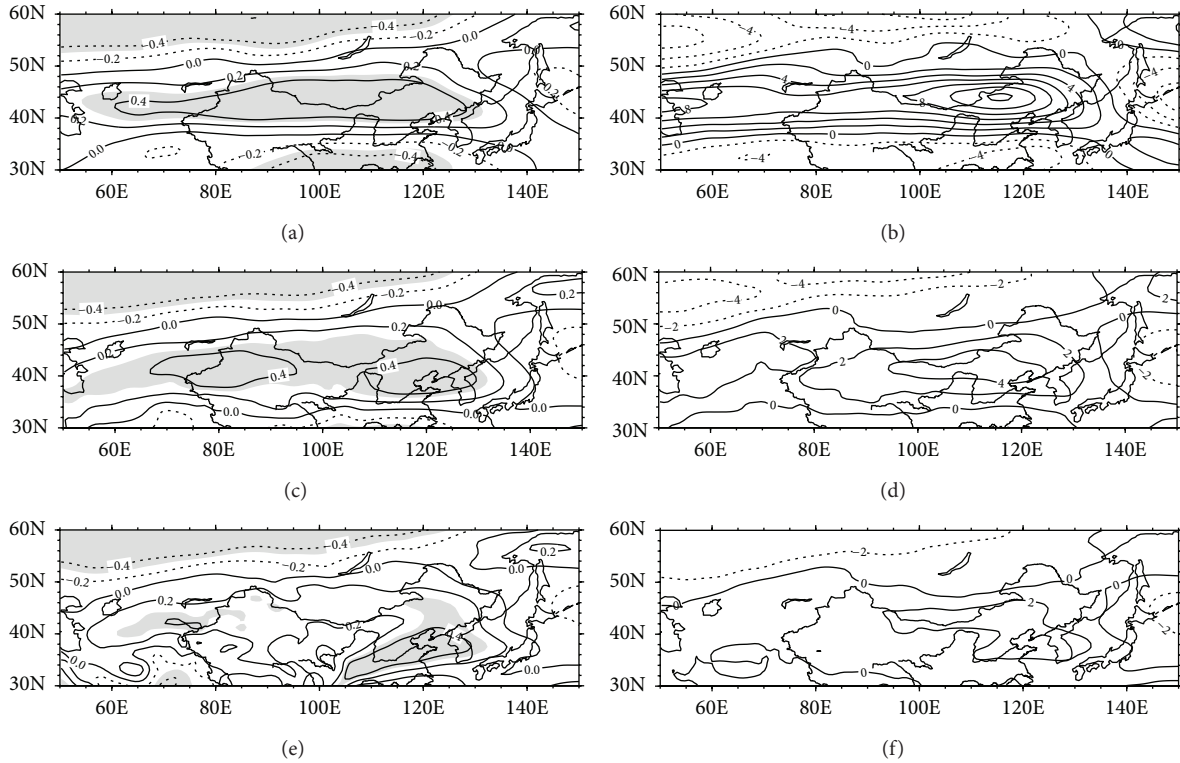


FIGURE 7: The correlation coefficient distribution between the total HDs in region A and u-component anomaly (m/s) at (a) 250 hPa, (c) 500 hPa, and (e) 700 hPa during 1979–2013 summer, and the distribution of u-component anomaly of (b) 250 hPa, (d) 500 hPa, and (f) 700 hPa in the summer of 2013. In (a, c, and e), the long-term trend is removed, and shaded area denotes the correlation coefficient significant at the 0.05 level.

The anomalous southerlies brought heat transport to the middle and lower reaches of the Yangtze River and contributed to the long-lasting heat wave. The northerly anomaly in the lower troposphere was located north of  $44^{\circ}\text{N}$  in the summer of 2013. The transport of cold air in the middle and high latitudes was more northward, and it was difficult for the cold air to reach the middle and lower reaches of the Yangtze River. The weak transport of cold air from north was one of the direct causes of the severe heat wave in the middle of the Yangtze River in the summer of 2006 [24]. Xiang et al. [67] also indicated that the transport of cold air in the Yangtze River Valley was weaker and more northward than usual during the hot spell in 2013.

**4.4. The Anomaly of Arctic Polar Vortex.** The Arctic polar vortex was a deep atmospheric system in the middle and high latitudes of northern hemisphere and played a vital role in global climate. As early as in 1949, Willett [69] took into consideration the impact of the expanding and reducing of the Arctic polar vortex on weather and climate. Meteorologists in China noticed that the Arctic polar vortex played a significant role on climate change in China in the 1980s, especially on temperature [70]. There was a close relationship between the area and intensity of the Arctic polar vortex and the position of subtropical high and summer rainfall belt in China [71]. The intensity of the Arctic polar vortex and the WPSH were the major reasons for the flood

and drought disasters in the Yangtze River and Huaihe River Valley [72]. Weak Arctic polar vortex and strong WPSH were favorable for hot spell in China [73]. In the summer of 2003, the Arctic polar vortex was in the western hemisphere for a long time, and weak cold air and persistent high temperature were observed in southern China [23].

Figure 9 shows the distribution of climate mean geopotential height at 500 hPa in the northern hemisphere and the anomaly in the summer of 2013. For the climate mean, the center of the Arctic polar vortex concentrated in the Arctic pole, and four troughs extending from the polar vortex were located in northern Canada, northern Qinghai-Tibet Plateau, the central Pacific, and the west coast of Europe, respectively, while four ridges were situated between the troughs. The North American trough located in northern Canada was the deepest, and the trough located in the west coast of Europe was the shallowest. Besides the westerly troughs stretching out from the polar vortex, there were also troughs in the middle and high latitudes near the Black Sea, northeastern Inner Mongolia, and the west coast of North America. Compared with the climate mean, the intensity of the Arctic polar vortex was obviously stronger in the summer of 2013, with the center of the anomaly lower than  $-70$  gpm. The polar vortex obviously extended to the western hemisphere, and the negative anomaly was concentrated in northeastern Canada and Greenland, while the positive anomaly circled around the negative anomaly. In the summer

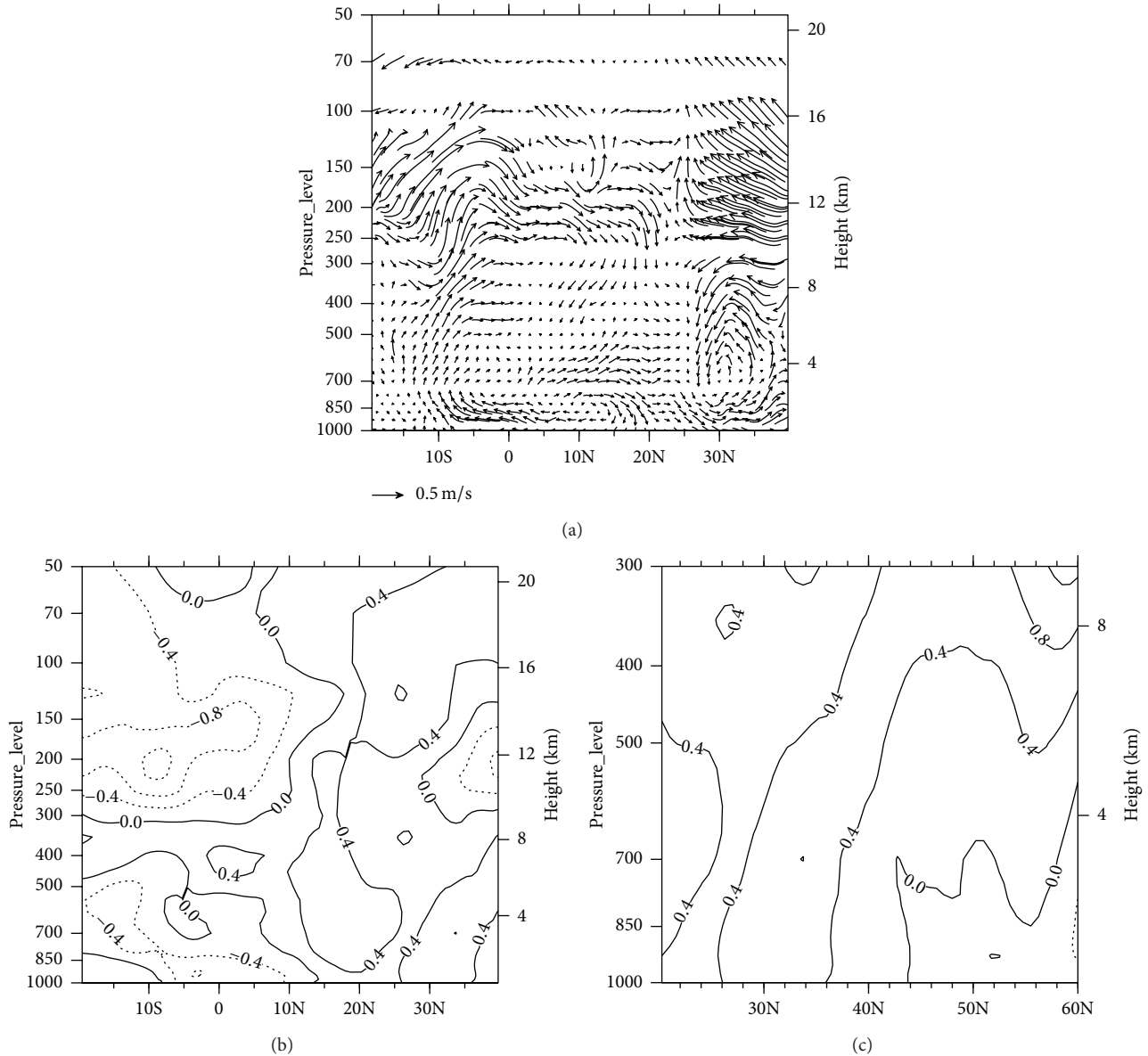


FIGURE 8: The pressure-latitude profiles of v-w wind anomaly (m/s) in (a) West Pacific (110°E–180°E) and v-component anomaly (m/s) in (b) Southeast Asia (90°E–130°E) and (c) Northeast Asia (90°E–130°E).

of 2013, the ridges lying in these positive anomaly zonal regions would be stronger, and the troughs would be weaker than normal, so the northern part of trough in northern Qinghai-Tibet Plateau and the trough in central Pacific were weaker than normal. At the same time, the northern part of the westerly trough in northern Qinghai-Tibet Plateau was more eastward, and the southern part was more westward and merged into one trough with the trough near the Black Sea, combined with the climatic trough in the northeastern Inner Mongolia; a very broad trough in southwest-northeast direction was found in the middle and high latitudes of Eurasia (figure omitted). The westerly in the broad trough was straight and mostly affected the large area north of 40°N. The straight westerly (enhanced westerly) blocked southward intrusion of the Arctic air mass, and this was unfavorable

for the weakening of WPSH and disrupt of heat wave. The straight westerly was unfavorable for the cold air invading southward to the middle and lower reaches of the Yangtze River.

The area of the Asian polar vortex (AAPV) in 60°E~150°E at 500 hPa in the summer of 2013 was calculated. It was found that in June the AAPV was smaller than normal, and the south border of the Asian polar vortex was more northward, while in July and August the AAPV was larger and the south border was more southward. Ji et al. [74] pointed out that, in summer, the ridge of the WPSH was more southward when the AAPV over 500 hPa was larger; on the contrary the ridge was more northward. In June 2013, the ridge of the WPSH was more northward locating in the middle and lower reaches of the Yangtze River. Compared with the abrupt

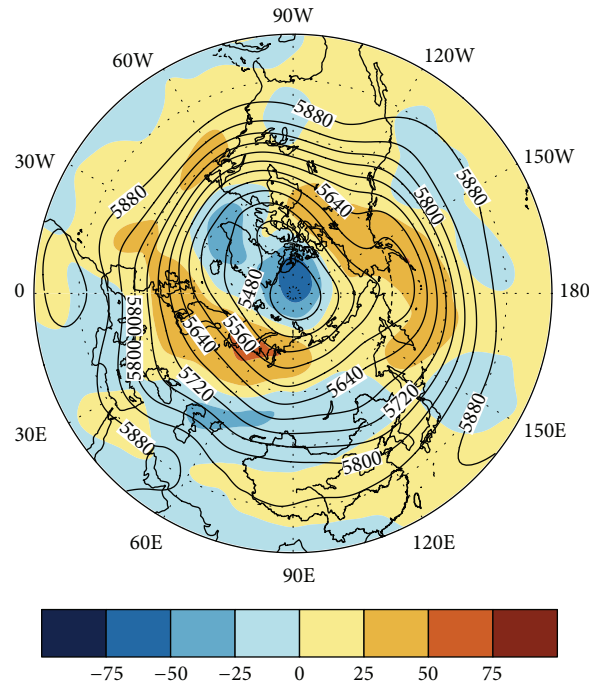


FIGURE 9: The distribution of climate mean geopotential height (solid line) and the anomaly (shaded area) in the summer 2013 at 500 hPa in the northern hemisphere (gpm).

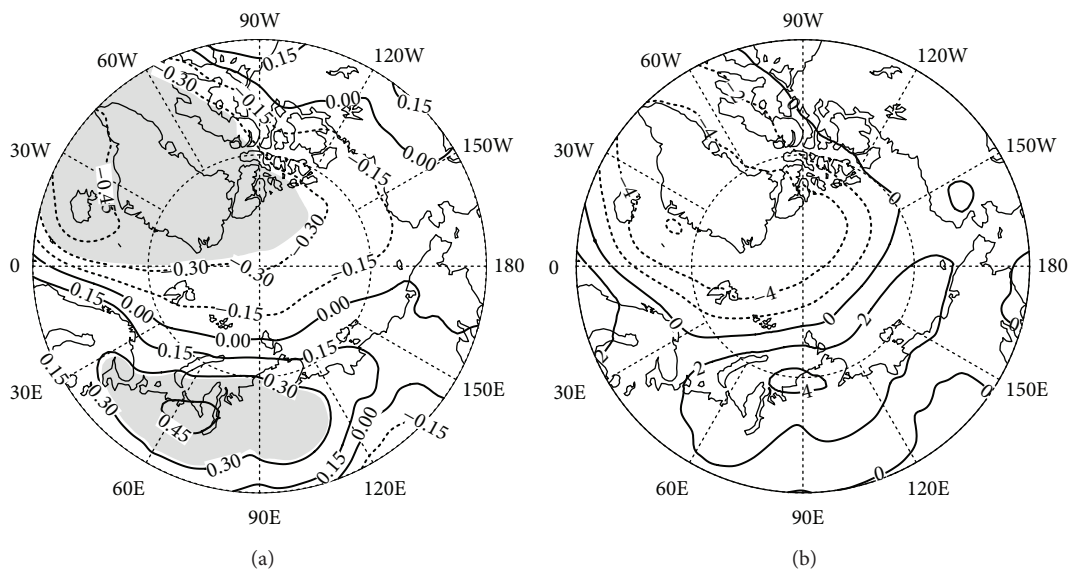


FIGURE 10: (a) The correlation coefficient distribution between the SLP anomaly in the Arctic region and the total HDs in region A during 1979–2013 summer, and (b) the distribution of the SLP anomaly (hPa) in the summer of 2013. In (a), long-term trend is removed, and shaded area denotes the correlation coefficient significant at the 0.05 level.

northward movement to the lower reaches of the Yellow River and the Huaihe River Valley in normal years, the ridge in July and August of 2013 was more southward, still locating in the middle and lower reaches of the Yangtze River. The ridge of the WPSH sustained in the middle and lower reaches of the Yangtze River, as shown in Figure 4, resulting in the rare persistent hot spell.

Figure 10 shows the correlation coefficient distribution between the sea-level pressure (SLP) anomaly and the total HDs and the distribution of the SLP anomaly in the summer of 2013. The SLP anomaly in northeastern Canada, Greenland, and Iceland was significantly negatively correlated with the total HDs in region A, and the correlation coefficient near Iceland was below  $-0.45$ . Significant positive correlation

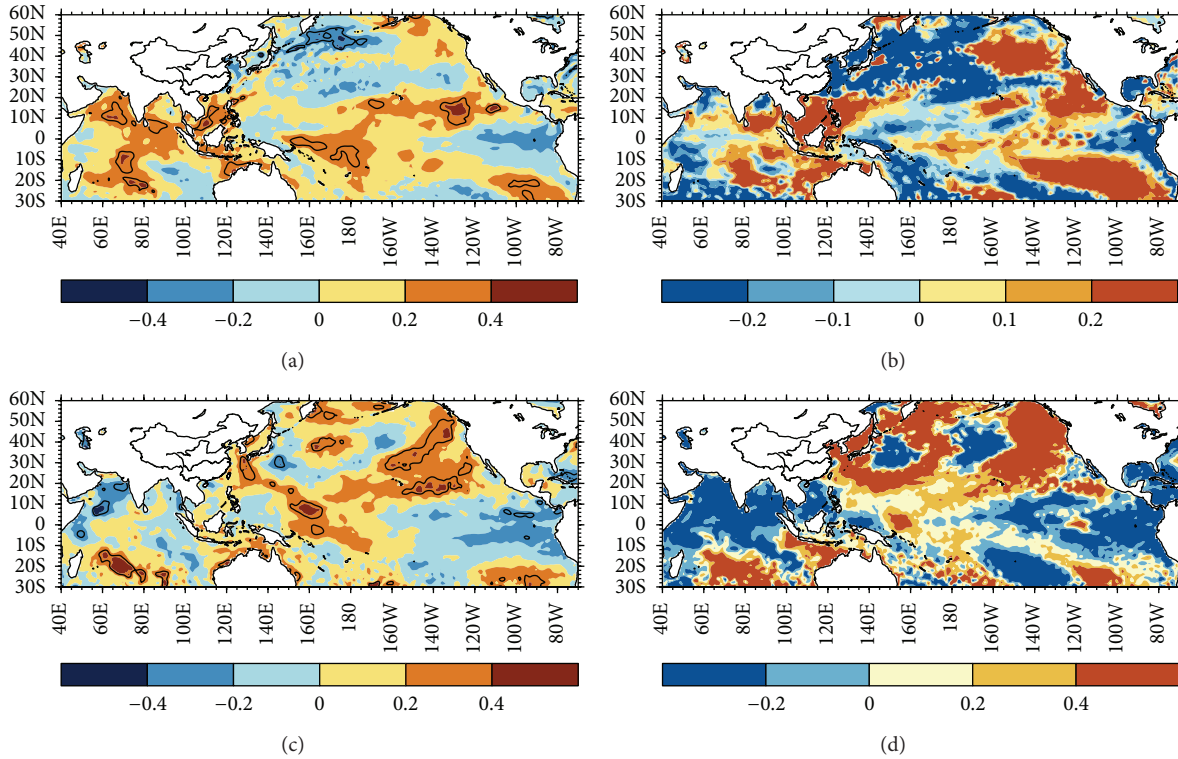


FIGURE 11: The correlation coefficient distribution between the total HDs in region A in summer and SSTA in (a) spring and (c) summer during 1979–2013, and the distribution of SSTA ( $^{\circ}\text{C}$ ) in (b) spring and (d) summer in 2013. In (a and c), long-term trend is removed, and solid line denotes the correlation coefficient significant at the 0.05 level.

coefficient was found in the middle and northern East Europe and Siberia. The negative SLP anomalies were observed near Greenland in the summer of 2013, with  $-6$  hPa lower than normal. The Arctic polar vortex was strong and biased towards Greenland, making the polar cold air active in this region. In summer, the continental low pressure was evident over the Eurasian continent. The continental low was weaker than normal in the summer of 2013, as positive SLP anomalies were located in northern Siberia with the highest anomaly above 4 hPa. This was un conducive to the strong cold air invading southward to the middle and lower reaches of the Yangtze River.

#### 4.5. The Anomaly of SST in the Indian Ocean and the Pacific.

In China, many meteorologists studied the impacts of SSTA on the WPSH and found that the SSTA in the Indian Ocean and the Pacific had a close relationship with the WPSH [75–80]. Areas of high positive correlation between WPSH and SSTA were located at the equatorial middle and eastern Pacific and the Indian Ocean [76]. When the western tropical Pacific warm pool is warming, the convection is intensified from the area around the Philippines to the Indo-China Peninsula through the South China Sea, the WPSH may shift northward, and the summer rainfall may be below normal in the Yangtze River Valley [75]. Three coupled ocean-atmosphere phenomena in the Indo-Pacific Oceans, El Niño, El Niño Modoki, and the Indian Ocean Dipole (IOD) had possible influences on summer climate in China [81].

SSTA in the spring and summer in 2013 were favorable for more HDs in region A. SSTAs in the Indian Ocean and the Pacific in spring were related to the heat wave in region A in summer. As Figure 11(a) shows, significant positive correlation was found between the total HDs in region A in summer and SSTA in spring in the warm pool of western equatorial Pacific, the South China Sea, the Arabian Sea, and the south of the Bengal Bay. In the spring of 2013, there were above  $0.2^{\circ}\text{C}$  positive anomalies from western Pacific to the South China Sea and the southern Bengal Bay (Figure 11(b)).

Figure 11(c) shows the distribution of the correlation coefficient between the SSTA in summer and the total HDs in region A. Significant positive correlation was found from the warm pool of the western equatorial Pacific to the northwestern Pacific. Significant negative correlation was found in the eastern equatorial Pacific and the Arabian Sea. Figure 11(d) shows that there were above  $0.4^{\circ}\text{C}$  positive anomalies from the warm pool of western equatorial Pacific to the northwestern Pacific, while below  $-0.2^{\circ}\text{C}$  negative anomalies in the eastern equatorial Pacific and the northern Indian Ocean. The thermal state in the tropical western Pacific warm pool and the convection over the warm pool play an important role in the summer climate anomalies in East Asia [75]. When the western tropical Pacific warm pool is warming, the upward motion is intensified in the tropical western Pacific, and the downward motion is intensified in the subtropical region, as shown in Figure 8(a). The WPSH may strengthen and HDs may be frequent in the Yangtze

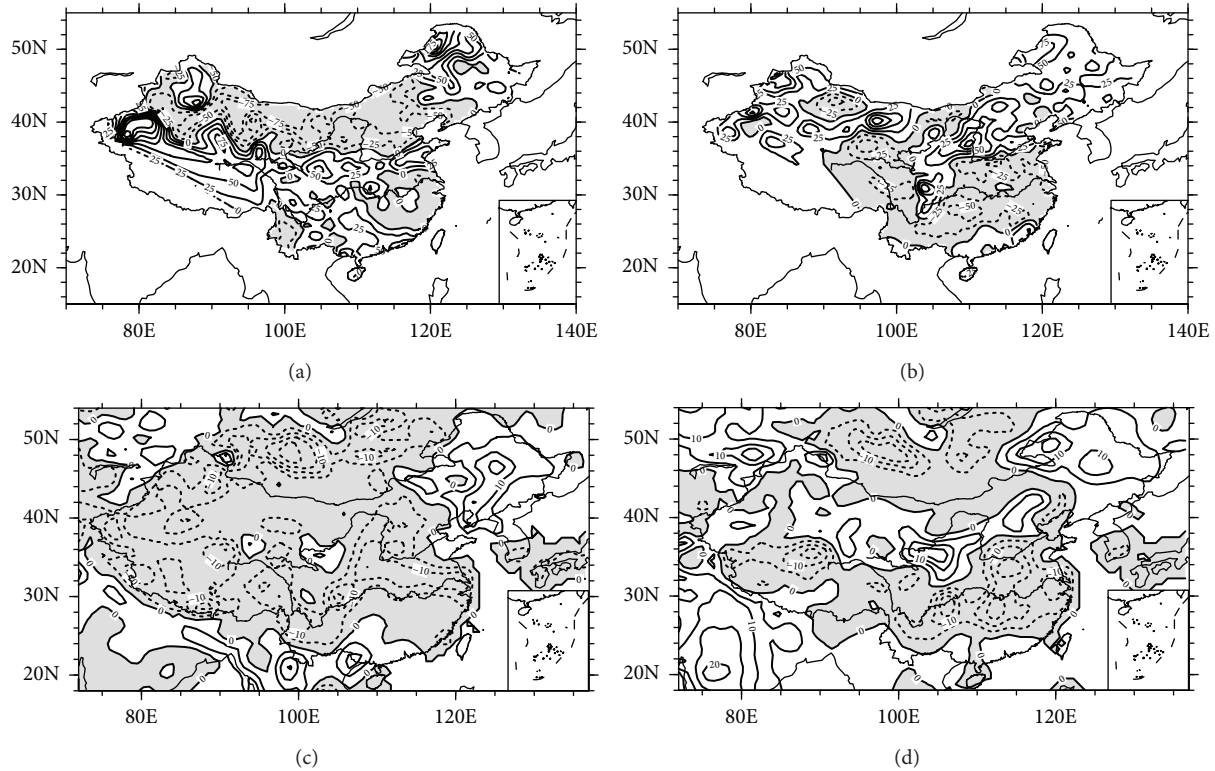


FIGURE 12: The percentage of precipitation anomalies in China in (a) spring and (b) summer of 2013 and the percentage of volumetric soil water anomalies in China in (c) spring and (d) summer of 2013. Shaded area denotes the negative percentage of precipitation and volumetric soil water anomalies.

River Valley. Besides, from a large scale over the tropical Indo-Pacific Oceans, above-normal SSTA is found in the tropical western Pacific in the summer of 2013, while below-normal SSTA in the tropical central and eastern Pacific and the tropical Indian Ocean. In association with SSTA in the tropical Indo-Pacific Oceans, the convection was stronger in the tropical western Pacific and weaker in the tropical central and eastern Pacific and tropical Indian Ocean (figures omitted). The distribution of SSTA in the tropical Indo-Pacific Oceans in the summer of 2013 favors the upward motion over the tropical western Pacific and helps the Hadley cell enhancement and the strengthening of the WPSH.

**4.6. The Anomaly of the Soil Moisture.** In the spring of 2013, the precipitation in the middle and lower reaches of the Yangtze River was less than normal and in some areas even 25% less (Figure 12(a)). In the summer of 2013, Meiyu began later and ended earlier than normal in the middle and lower reaches of the Yangtze River [82, 83], and the precipitation brought by typhoons was also less [67, 80]. The percentage of precipitation anomaly around the Yangtze River region in summer was 25% ~50% less than normal (Figure 12(b)). Accordingly in the spring and summer, the volumetric soil water around the Yangtze River region was about 10% less than normal and in some regions even 15% less (Figures 12(c) and 12(d)). Heat waves can be amplified by the dry soil conditions in the regions with precipitation deficits [82–86]. The moisture deficits in soil in spring and summer

made the heat wave more serious in the middle and lower reaches of the Yangtze River. Besides, the clouds in wet regions reduce the incoming solar radiation resulting in lower surface temperature, and dry conditions under subtropical high system favor more sunshine resulting in higher surface temperature [81]. A good negative correlation was found between summer rainfall and high temperature anomalies in South China [15].

## 5. Summary and Conclusions

An exceptional heat wave event occurred in southern China from June to August in 2013, and the total HDs were 25 days more than normal and exceeded the 90th percentile by over 10 days. In this paper, the 2013 heat wave was described, and the associated atmospheric circulations as well as the anomaly of the underlying surfaces were investigated.

The anomaly of the WPSH was the major and direct reason for the heat wave in 2013. In the summer of 2013, the WPSH underwent four westward extensions to the middle and lower reaches of the Yangtze River and brought about four hot spells to the Yangtze River Valley. The extension of the WPSH from late July to mid-August was the most westward. The ridge of the WPSH was more northward in June, more southward in July and August, and sustained between 25° and 30°N all summer. The anomalies of the WPSH ridge made the hot weather come earlier and sustain in the middle and lower reaches of the Yangtze River.

The anomaly of the WPSH was connected with the circulation anomaly in high latitudes and low latitudes. In high latitudes, the central position of the Arctic polar vortex was biased in the western hemisphere. In June 2013, the AAPV was smaller and the south border was more northward, while in July and August the AAPV was greater and the south border was more southward. The anomaly of AAPV made the WPSH ridge more northward in June, more southward in July and August, and sustain in the middle and lower reaches of the Yangtze River. At 500 hPa, the ridges lying in these zonal regions with positive anomaly became stronger, and the northern part of trough in the northern Qinghai-Tibet Plateau and the trough in the central Pacific were weaker than normal. The westerly trough was vast and flat in the northern China, and the zonal circulation was unfavorable for the weakening of the WPSH. At 700 hPa, the westerly wind was stronger from Northeast China to the Korean Peninsula and uncondusive to the strong cold air invading southward to the middle and lower reaches of the Yangtze River and weakening the heat wave.

In low latitudes, the center of the SAH at 150 hPa was located near 80°E in the summer of 2013, and the highest geopotential height anomaly at 150 hPa was in the Yellow River Valley. The SAH was overall more eastward and more northward in the summer of 2013, meanwhile the WPSH was more westward and stronger. Besides, the ITCZ in the central and western tropical Pacific was weaker during the whole summer of 2013. The northerly anomaly dominated in the lower troposphere in the tropical Pacific. The effects by tropical easterly waves (a kind of wave moving from east to west across the tropics) and typhoons in the south of the WPSH were weak when the ridge moved southward in the second half of July to early August, which were unfavorable for the weakening of heat wave. The strong southerly prevailed in the middle and lower reaches of the Yangtze River in the summer of 2013. The Hadley circulation in the northern hemisphere was stronger in the central and western Pacific. The upward motion in the central and western Pacific and downward motion in the subtropical region contributed to the strengthening of the WPSH. Meanwhile, anticyclone anomaly near 28°N indicated the strengthening of the WSPH.

The heat wave in the middle and lower reaches of the Yangtze River in the summer of 2013 was closely correlated with SSTA in the Indian and Pacific oceans. The positive SSTA was found in the warm pool of the western equatorial Pacific to the northwestern Pacific while negative anomalies in the eastern equatorial Pacific and the northern Indian Ocean in the summer of 2013 were found. The dynamical linkages between the SSTA in the Indian Ocean and the Pacific and the heat wave around Yangtze River regions were complex and worth further investigating. The convection and upward flow were stronger over the tropical western Pacific, while the convection was weak and downward flow was confined in the eastern Pacific and the tropical Indian Ocean. The warming in the warm pool of the tropical western Pacific could drive ascending anomalous flow in the tropical region and the enhancement of the Hadley circulation. Strong descending anomalous flow was observed in the subtropical region, connecting with the strengthening of the WPSH. However,

the positive SSTA over the northwestern Pacific within 20–30°N in the summer of 2013 might be favorable for an upward motion in the local area. The precise mechanism responsible for their association needs to be further investigated. Besides, statistically significant correlation values existed over remote areas such as the west of Mexico westward to the Hawaiian Islands, the southeastern Pacific near the Easter Island, and the central of the southern Indian Ocean. But it was not clear whether there was an important remote dynamical process (e.g., teleconnection) that could affect HDs in China. The numerical model will be applied in further study to see whether and how the SSTA in remote areas affects the atmospheric circulation and therefore influence the heat wave.

## Conflict of Interests

The authors declare that there is no conflict of interests regarding the publication of this paper.

## Acknowledgments

The authors thank the anonymous reviewers and editors for their helpful comments and suggestions. The authors thank Dr. Kaijun Wu for his help on data calculation and processing. This research was supported by the National Natural Science Foundation of China (Grant no. 41205039) and China Meteorological Administration Special Public Welfare Research Fund (GYHY201206017 and GYHY201306033).

## References

- [1] D. L. Hartmann, A. M. G. Klein Tank, M. Rusticucci et al., "Observations: atmosphere and surface," in *Climate Change 2013: The Physical Science Basis. Contribution of Working Group I to the Fifth Assessment Report of the Intergovernmental Panel on Climate Change*, Cambridge University Press, Cambridge, UK, 2013.
- [2] A. Davis, *Heat Claims As Many As 38 People, Tests State Energy Supply*, Associated Press, San Jose Mercury News, 2006.
- [3] K. Knowlton, M. Rotkin-Ellman, G. King et al., "The 2006 California heat wave: impacts on hospitalizations and emergency department visits," *Environmental Health Perspectives*, vol. 117, no. 1, pp. 61–67, 2009.
- [4] O. Munoz, *139 Deaths Later, Heat Wave Appears Over*, Associated Press, Forbes, New York, NY, USA, 2006.
- [5] USAgNet, California's cattle death toll surpasses 25000, 2006.
- [6] L. Feudale and J. Shukla, "Influence of sea surface temperature on the European heat wave of 2003 summer. Part I: an observational study," *Climate Dynamics*, vol. 36, no. 9–10, pp. 1691–1703, 2011.
- [7] C. Schär, P. L. Vidale, D. Lüthi et al., "The role of increasing temperature variability in European summer heatwaves," *Nature*, vol. 427, no. 6972, pp. 332–336, 2004.
- [8] M. Beniston, "The 2003 heat wave in Europe: a shape of things to come? An analysis based on Swiss climatological data and model simulations," *Geophysical Research Letters*, vol. 31, no. 2, 2004.

- [9] G. A. Meehl and C. Tebaldi, "More intense, more frequent, and longer lasting heat waves in the 21st century," *Science*, vol. 305, no. 5686, pp. 994–997, 2004.
- [10] L. Feudale and J. Shukla, "Influence of sea surface temperature on the European heat wave of 2003 summer. Part II: a modeling study," *Climate Dynamics*, vol. 36, no. 9–10, pp. 1705–1715, 2011.
- [11] D. Barriopedro, E. M. Fischer, J. Luterbacher, R. M. Trigo, and R. García-Herrera, "The hot summer of 2010: redrawing the temperature record map of Europe," *Science*, vol. 332, no. 6026, pp. 220–224, 2011.
- [12] R. Dole, M. Hoerling, J. Perlwitz et al., "Was there a basis for anticipating the 2010 Russian heat wave?" *Geophysical Research Letters*, vol. 38, no. 6, Article ID L06702, 2011.
- [13] K. E. Trenberth and J. T. Fasullo, "Climate extremes and climate change: the Russian heat wave and other climate extremes of 2010," *Journal of Geophysical Research: Atmospheres*, vol. 117, no. 17, Article ID D17103, 2012.
- [14] M. Hoerling, A. Kumar, R. Dole et al., "Anatomy of an extreme event," *Journal of Climate*, vol. 26, no. 9, pp. 2811–2832, 2013.
- [15] T. Ding, W. H. Qian, and Z. W. Yanb, "Changes in hot days and heat waves in China during 1961–2007," *International Journal of Climatology*, vol. 30, no. 10, pp. 1452–1462, 2010.
- [16] T. Ding and W. Qian, "Geographical patterns and temporal variations of regional dry and wet heatwave events in China during 1960–2008," *Advances in Atmospheric Sciences*, vol. 28, no. 2, pp. 322–337, 2011.
- [17] Y. J. Wang, F. M. Ren, and X. B. Zhang, "Spatial and temporal variations of regional high temperature events in China," *International Journal of Climatology*, vol. 34, no. 10, pp. 3054–3065, 2014.
- [18] H. J. Ding, L. L. Zhou, B. Zha et al., "An analysis on the abnormal high temperature weather in the south Yangtze Valley during summer 2003," *Journal of Zhejiang University (Science Edition)*, vol. 34, no. 1, pp. 100–105, 2007 (Chinese).
- [19] R. Guo and X. F. Zhi, "Synoptic analysis of severe droughts during the summer 2003 in Southern China," *Journal of Nanjing Institute of Meteorology*, vol. 31, no. 2, pp. 234–241, 2008 (Chinese).
- [20] J. H. Sun, J. Wei, and X. L. Zhang, "The abnormal weather in the summer 2003 and its real-time prediction," *Climatic and Environmental Research*, vol. 9, no. 1, pp. 203–217, 2004 (Chinese).
- [21] H. Yang and C. Y. Li, "Diagnostic study of serious high temperature over South China in 2003 summer," *Climatic and Environmental Research*, vol. 10, no. 1, pp. 80–85, 2003 (Chinese).
- [22] Y. L. Fang and M. Q. Jian, "Diagnosis study of persistent heat waves in South China during summer 2003," *Journal of Tropical Oceanography*, vol. 30, no. 3, pp. 30–37, 2011 (Chinese).
- [23] R. P. Zhang, Y. F. Zhou, and K. Y. Guo, "The relation between the persistent high temperature in south of china in the summer of 2003 and the vortex's position," *Scientia Meteorologica Sinica*, vol. 25, no. 5, pp. 528–533, 2005 (Chinese).
- [24] X. K. Zou and H. Gao, "Analysis of severe drought and heat wave over the Sichuan Basin in the summer of 2006," *Advances in Climate Change Research*, vol. 3, no. 3, pp. 149–153, 2007 (Chinese).
- [25] M. Zhang, Q. J. Gao, and W. Jiang, "The preliminary analysis of heat wave in summer of 2009 in China," *Journal of the Meteorological Sciences*, vol. 31, no. 5, pp. 582–590, 2011 (Chinese).
- [26] T. Ding and Z. J. Ke, "Characteristics and changes of regional wet and dry heat wave events in China during 1960–2013," *Theoretical and Applied Climatology*, 2014.
- [27] H. X. Duan, S. P. Wang, and J. Y. Feng, "The national drought situation and its impacts and causes in the summer 2013," *Journal of Arid Meteorology*, vol. 31, no. 3, pp. 633–640, 2013 (Chinese).
- [28] China Meteorological Administration, *Surface Meteorological Observation Criteria*, China Meteorological Press, Beijing, China, 2003, (Chinese).
- [29] Q. Li, X. Liu, H. Zhang, T. C. Peterson, and D. R. Easterling, "Detecting and adjusting temporal inhomogeneity in Chinese mean surface air temperature data," *Advances in Atmospheric Sciences*, vol. 21, no. 2, pp. 260–268, 2004.
- [30] Q. X. Li, H. Z. Zhang, X. N. Liu, and J. Huang, "Urban heat island effect on annual mean temperature during the last 50 years in China," *Theoretical and Applied Climatology*, vol. 79, no. 3–4, pp. 165–174, 2004.
- [31] D.-Y. Gong, Y.-Z. Pan, and J.-A. Wang, "Changes in extreme daily mean temperatures in summer in eastern China during 1955–2000," *Theoretical and Applied Climatology*, vol. 77, no. 1–2, pp. 25–37, 2004.
- [32] Y. Tang, J. Gan, L. Zhao, and K. Gao, "On the climatology of persistent heavy rainfall events in China," *Advances in Atmospheric Sciences*, vol. 23, no. 5, pp. 678–692, 2006.
- [33] Z. Y. Wang and Y. H. Ding, "Climate change of the cold wave frequency of China in the last 53 years and the possible reasons," *Chinese Journal of Atmospheric Sciences*, vol. 30, pp. 14–22, 2006 (Chinese).
- [34] W. H. Qian, J. L. Fu, and Z. W. Yan, "Decrease of light rain events in summer associated with a warming environment in China during 1961–2005," *Geophysical Research Letters*, vol. 34, no. 11, Article ID L11705, 2007.
- [35] J. Shi, Y. H. Ding, and L. L. Cui, "Climatic characteristics and their changing law during summer high-temperature times in East China," *Acta Meteorologica Sinica*, vol. 63, no. 3, pp. 237–246, 2008 (Chinese).
- [36] T. Ding and W. H. Qian, "Statistical characteristics of heat wave precursors in China and model prediction," *Chinese Journal of Geophysics*, vol. 55, pp. 1472–1486, 2012 (Chinese).
- [37] W. H. Qian and T. Ding, "Atmospheric anomaly structures and stability associated with heat wave events in China," *Chinese Journal of Geophysics*, vol. 55, pp. 1487–1500, 2012 (Chinese).
- [38] S. Feng, Q. Hu, and W. H. Qian, "Quality control of daily meteorological data in China, 1951–2000: a new dataset," *International Journal of Climatology*, vol. 24, no. 7, pp. 853–870, 2004.
- [39] IPCC, *Climate Change 2007, Working Group I Contribution to the Fourth Assessment Report of the IPCC Intergovernmental Panel on Climate Change*, Cambridge University Press, Cambridge, UK, USA, 2007.
- [40] P. D. Jones, E. B. Horton, C. K. Folland, M. Hulme, D. E. Parker, and T. A. Basnett, "The use of indices to identify changes in climatic extremes," *Climatic Change*, vol. 42, no. 1, pp. 131–149, 1999.
- [41] X. H. Pan and P. M. Zhai, "Analysis of surface air temperature extremes," *Meteorological Monthly*, vol. 28, pp. 28–31, 2002 (Chinese).
- [42] Z. Yan, P. D. Jones, T. D. Davies et al., "Trends of extreme temperatures in Europe and China based on daily observations," *Climatic Change*, vol. 53, no. 1–3, pp. 355–392, 2002.

- [43] L. J. Hua, Z. G. Ma, and Z. M. Zeng, "The comparative analysis of the changes of extreme temperature and extreme diurnal temperature range of large cities and small towns in Eastern China," *Chinese Journal of Atmospheric Sciences*, vol. 30, pp. 80–91, 2006 (Chinese).
- [44] X. Q. Fang, A. Y. Wang, S.-K. Fong, W. Lin, and J. Liu, "Changes of reanalysis-derived Northern Hemisphere summer warm extreme indices during 1948–2006 and links with climate variability," *Global and Planetary Change*, vol. 63, no. 1, pp. 67–78, 2008.
- [45] J. Y. Huang, *Meteorological Statistical Analysis and Forecasting Method*, China Meteorological Press, Beijing, China, 2004, (Chinese).
- [46] T. Ding and Z. J. Ke, "A comparison of statistical approaches for seasonal precipitation prediction in Pakistan," *Weather and Forecasting*, vol. 28, no. 5, pp. 1116–1132, 2013.
- [47] Z. Q. Gong, Y. J. Wang, Z. Y. Wang et al., "Briefly analysis on climate anomalies and causations in summer 2013," *Meteorological Monthly*, vol. 40, no. 1, pp. 119–125, 2014 (Chinese).
- [48] T. Tang, R. H. Jin, X. Y. Peng et al., "Analysis on extremely high temperature over southern China in summer 2013," *Meteorological Monthly*, vol. 40, no. 10, pp. 1207–1215, 2014 (Chinese).
- [49] J.-B. Peng, "An investigation of the formation of the heat wave in Southern China in summer 2013 and the relevant abnormal subtropical high activities," *Atmospheric and Oceanic Science Letters*, vol. 7, no. 4, pp. 286–290, 2014.
- [50] R. Zhang, "Characteristics of soliton with dynamic constraints on its existence/propagation in tropical easterly wave," *Advances in Atmospheric Sciences*, vol. 13, no. 3, pp. 325–339, 1996.
- [51] Q. Zhang and Y. F. Qian, "Interannual and interdecadal variations of the South Asia High," *Chinese Journal of Atmospheric Sciences*, vol. 24, no. 1, pp. 67–78, 2000 (Chinese).
- [52] S. Y. Tao and F. K. Zhu, "The 100-MB flow patterns in Southern Asia in summer and its relation to the advance and retreat of the west-Pacific subtropical anticyclone over the Far East," *Acta Meteorologica Sinica*, vol. 34, no. 4, pp. 385–396, 1964 (Chinese).
- [53] G. X. Wu, J. F. Chou, Y. M. Liu, Q. Zhang, and S. Sun, "Review and prospect of the study on the subtropical anticyclone," *Chinese Journal of Atmospheric Sciences*, vol. 27, no. 4, pp. 503–517, 2003 (Chinese).
- [54] S. S. Huang, "Relationship between the development of subtropical high on summer ocean and Tibetan high," *Journal of Nanjing University: Science Edition*, vol. 1, pp. 141–146, 1977 (Chinese).
- [55] R. C. Ren and G. X. Wu, "On the short-term structure and formation of the subtropical anticyclone in the summer of 1998," *Acta Meteorologica Sinica*, vol. 61, no. 2, pp. 180–195, 2003 (Chinese).
- [56] B. K. Zhao, X. P. Yao, and G. X. Wu, "The structure and activity characteristics of the Western Pacific Subtropical anticyclone and its dynamical mechanism during the meiyu period over the Huaihe River basin in 2003," *Chinese Journal of Atmospheric Sciences*, vol. 29, no. 5, pp. 771–779, 2005 (Chinese).
- [57] Y. H. Li, J. M. Qing, Q. Li et al., "Inter-annual and inter-decadal variations of South Asian High in summer and its influences on flood/drought over western Southwest China," *Journal of Southwest University*, vol. 34, no. 9, pp. 1–11, 2012 (Chinese).
- [58] Q. G. Zhu, J. R. Lin, S. W. Shou et al., *The Principle and Method of Synoptic Meteorology*, China Meteorological Press, Beijing, China, 2007, (Chinese).
- [59] Q. Y. Zhang and S. Y. Tao, "The anomalous subtropical anticyclone in western Pacific and their association with circulation over East Asia during summer," *Chinese Journal of Atmospheric Sciences*, vol. 27, no. 3, pp. 369–380, 2003 (Chinese).
- [60] Y. Y. Bai and Z. Y. Guan, "Principal modes of summertime zonal-mean flow and their relations with AO and ENSO," *Acta Meteorologica Sinica*, vol. 65, no. 3, pp. 372–382, 2007 (Chinese).
- [61] J. Bjerknæs, "A possible response of the atmospheric Hadley circulation to equatorial anomalies of ocean temperature," *Tellus*, vol. 18, no. 4, pp. 820–829, 1966.
- [62] J. Bjerknæs, "Atmosphere teleconnection from the equatorial Pacific," *Monthly Weather Review*, vol. 97, no. 4, pp. 163–172, 1969.
- [63] Q. Y. Zhang and S. Y. Tao, "Influence of Asian mid-high latitude circulation on East Asian summer rainfall," *Acta Meteorologica Sinica*, vol. 56, no. 2, pp. 199–211, 1998 (Chinese).
- [64] Q. Y. Zhang and S. Y. Tao, "Tropical and subtropical monsoon over East Asia and its influence on the rainfall over eastern China in summer," *Quarterly Journal of Applied Meteorology*, vol. 9, supplement 1, pp. 17–23, 1998 (Chinese).
- [65] B. G. Bi, G. C. Zhang, and Z. C. Li, "The relationship of abnormal features of western pacific subtropical high and 2003 Huaihe River flood and cause exploration," *Journal of Tropical Meteorology*, vol. 20, no. 5, pp. 505–514, 2004 (Chinese).
- [66] W. Qian, J. Li, and X. Shan, "Application of synoptic-scale anomalous winds predicted by medium-range weather forecast models on the regional heavy rainfall in China in 2010," *Science China Earth Sciences*, vol. 56, no. 6, pp. 1059–1070, 2013.
- [67] S. Q. Xiang, S. F. Shu, X. Han et al., "Analysis of abnormal high temperature causes in the summer of 2013," *Climate Change Research Letters*, vol. 3, pp. 78–84, 2014 (Chinese).
- [68] D. D. Yu, R. Zhang, Y. C. H. Zhao et al., "Correlation between the subtropical high abnormal longitudinal position and the East Asian summer monsoon system," *Transactions of Atmospheric Sciences*, vol. 37, no. 3, pp. 304–312, 2014 (Chinese).
- [69] M. C. Willett, "Long-period fluctuations of general circulation of the atmosphere," *Journal of Meteorology*, vol. 6, pp. 34–50, 1949.
- [70] H. D. Zhang, S. T. Gao, and Y. Liu, "Advances of research on polar vortex," *Plateau Meteorology*, vol. 27, no. 2, pp. 452–461, 2008 (Chinese).
- [71] X. G. Zhang and F. Y. Wei, "The interrelation between the polar vortex and the subtropical high in north hemisphere," in *The Long-Term Weather Forecast Papers*, pp. 25–36, China Meteorological Press, Beijing, China, 1990, (Chinese).
- [72] Z. L. Shi, "The cause analysis of the typical drought and flood years in the area between the Yangtze River and Huaihe River in summer since 1990," *Meteorological Monthly*, vol. 22, no. 9, pp. 35–38, 1996 (Chinese).
- [73] L. Zhao, S. L. Li, F. H. Wang et al., "The character and cause analysis of high-temperature weather in the summer 2000 in the Daxinganling prefecture," *Heilongjiang Meteorology*, no. 4, pp. 4–5, 2001 (Chinese).
- [74] F. Ji, J.-H. Zhao, Q. Shen, R. Zhi, and Z.-Q. Gong, "The distribution of large-scale drought/flood of summer in China under different configurations of monsoon and polar vortex," *Acta Physica Sinica*, vol. 63, no. 5, Article ID 059201, 2014 (Chinese).
- [75] R. H. Huang and F. Y. Sun, "Impacts of the thermal state and convective activities in the Tropical Western Warm Pool on the summer climate anomalies in East Asia," *Scientia Atmospherica Sinica*, vol. 18, no. 2, pp. 456–464, 1994 (Chinese).

- [76] S. Sun and M. Ying, "Subtropical high anomalies over the western pacific and its relations to the asian monsoon and SST anomaly," *Advances in Atmospheric Sciences*, vol. 16, no. 4, pp. 559–568, 1999.
- [77] M. Ying and S. Q. Sun, "A study on the response of subtropical high over the Western Pacific on the SST anomaly," *Scientia Atmospherica Sinica*, vol. 24, no. 2, pp. 193–206, 2000.
- [78] G. R. Jiang, W. Y. Sha, and J. P. Cai, "Long-range variation relations between sea surface temperature over the north Pacific and Indian oceans and the west Pacific subtropical high in summer," *Marine Forecasts*, vol. 8, no. 1, pp. 16–23, 1991.
- [79] L. S. Hao, W. S. Lu, J. Z. H. Min et al., "Mechanism for the impact of tropical SSTA on general circulation in summer," *Journal of Nanjing Institute of Meteorology*, vol. 30, no. 2, pp. 178–185, 2007.
- [80] D. Si, Y. Yuan, T. Cui et al., "Anomalies of ocean and atmospheric circulation in 2013 and their impacts on climate in China," *Meteorological Monthly*, vol. 40, no. 4, pp. 494–501, 2014 (Chinese).
- [81] H. Y. Weng, G. X. Wu, Y. M. Liu, S. K. Behera, and T. Yamagata, "Anomalous summer climate in China influenced by the tropical Indo-Pacific Oceans," *Climate Dynamics*, vol. 36, no. 3, pp. 769–782, 2011.
- [82] L. Ferranti and P. Viterbo, "The European summer of 2003: sensitivity to soil water initial conditions," *Journal of Climate*, vol. 19, no. 15, pp. 3659–3680, 2006.
- [83] Z. J. Ke, Y. G. Wang, and Z. S. Gong, "Review of the precursor and its application in summer climate prediction in 2013," *Meteorological Monthly*, vol. 40, no. 4, pp. 502–509, 2014 (Chinese).
- [84] E. M. Fischer, S. I. Seneviratne, P. L. Vidale, D. Lüthi, and C. Schär, "Soil moisture-atmosphere interactions during the 2003 European summer heat wave," *Journal of Climate*, vol. 20, no. 20, pp. 5081–5099, 2007.
- [85] S. I. Seneviratne, T. Corti, E. L. Davin et al., "Investigating soil moisture-climate interactions in a changing climate: a review," *Earth-Science Reviews*, vol. 99, no. 3-4, pp. 125–161, 2010.
- [86] B. Mueller and S. I. Seneviratne, "Hot days induced by precipitation deficits at the global scale," *Proceedings of the National Academy of Sciences of the United States of America*, vol. 109, no. 31, pp. 12398–12403, 2012.

## Research Article

# Spatiotemporal Characteristics of Evapotranspiration Paradox and Impact Factors in China in the Period of 1960–2013

Huiping Huang,<sup>1,2</sup> Yuping Han,<sup>1</sup> Mingming Cao,<sup>2</sup> Jinxi Song,<sup>2</sup>  
Heng Xiao,<sup>1</sup> and Weili Cheng<sup>1</sup>

<sup>1</sup>School of Resources and Environment, North China University of Water Resources and Electric Power, Zhengzhou 450045, China

<sup>2</sup>College of Urban Environmental Science, Northwest University, Xi'an 710127, China

Correspondence should be addressed to Yuping Han; han0118@163.com

Received 16 December 2014; Accepted 30 January 2015

Academic Editor: Fred Kucharski

Copyright © 2015 Huiping Huang et al. This is an open access article distributed under the Creative Commons Attribution License, which permits unrestricted use, distribution, and reproduction in any medium, provided the original work is properly cited.

Downward trend of potential evaporation accompanied with upward of air temperature which is denoted as evaporation paradox has been reported in many regions over the past several decades in the world. In this paper, evaporation paradox and key factors attributed to  $ET_0$  changes are systematically analyzed based on data from 599 meteorological stations during 1960–2013. Results show that (1) Evaporation paradox exists in all regions in 1960–2013 and 1960–1999 except SWRB in 1960–2013 but no evaporation paradox in 2000–2013. (2) Evaporation paradox exists in large areas in spring and summer, the extent and range fall in autumn, and there is no evaporation paradox in winter. (3) The evaporation paradox area accounts for 73.7% of China in 1960–2013 and 91.2% in 1969–1999. (4) Sunshine hours, humidity, wind speed, and maximum temperature appear to be the most important variables which contributed to  $ET_0$  change in China.

## 1. Introduction

Climate change characterized by global warming has been the focus of diversified research fields such as water resource, agriculture, ecosystem, and human health. It is widely accepted that global air temperature had been increasing in recent decades, it has risen by about 0.85 (0.65–1.06)°C from 1951 to 2012, and the average rising rate was 0.12 (0.08–0.14)°C (IPCC [1]). In China, temperature has increased by about 0.5–0.8°C and precipitation has large regional fluctuation but no significant trend in the recent 100 years (Wang et al. [2]).

Potential evapotranspiration ( $ET_0$ ) is one of the most important components of the hydrological system which refers to “the quantity of water evaporated per unit area, per unit time from an idealized, extensive free water surface under existing atmospheric conditions.” It is an important indicator of atmospheric evaporative demand for estimating terrestrial evaporation and crop water requirements. There have been many discussions on methods of calculating  $ET_0$  (Penman [3], Hargreaves and Samani [4], Pereira and Pruitt [5]), the spatial-temporal variations (Irmak et al. [6],

Dinpashoh et al. [7], Liang et al. [8], Croitoru et al. [9]), and its influencing factors (Feng et al. [10], Liu and Yang [11], Harmsen et al. [12], Tang et al. [13]). Declining trends in both pan evaporation (McVicar et al. [14]) and potential evaporation ( $ET_0$ ) have been reported to be occurring simultaneously in many regions with increasing trends of air temperature, which has been denoted as the evaporation paradox (Roderick and Farquhar [15]) and it has been one of the hot issues of hydrological system. Over the past several decades evaporation paradox had been verified in many regions of the world such as the former Soviet Union (Peterson et al. [16]), the United States (Golubev et al. [17]), China (Thomas [18], Ma et al. [19]), India (Chattopadhyay et al. [14]), Thailand (Tebakari et al. [20]), Italy (Moonen et al. [21]), Romania (Croitoru et al. [9]), Australia, New Zealand (Roderick and Farquhar [22]), Canada (Burn and Hesch [23]). But there existed exception to this rule (Cohen et al. [24]). In China both at national scale (Yin et al. [25], Han et al. [26]) and at regional scale such regions as the Northwest China (Liang et al. [8]), the YeRB (Wang et al. [27]), the HaRB (Xing et al. [28]), the YaRB (Xu et al. [29]), the Northwest

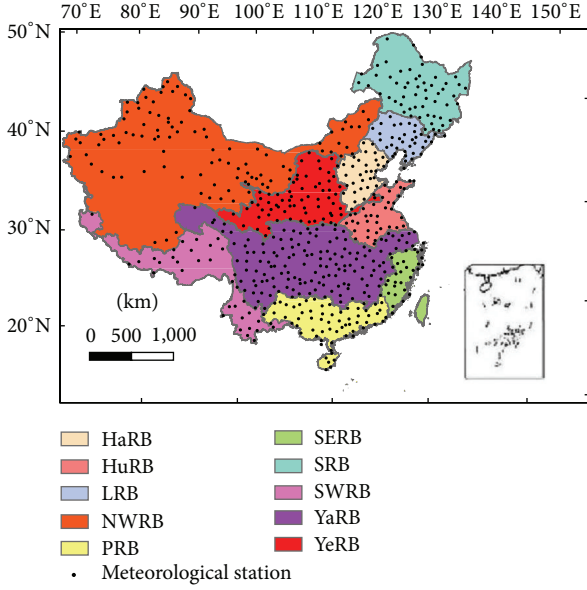


FIGURE 1: Spatial distribution of meteorological stations and first-order basin in China.

China (Yang et al. [30]), the Loess Plateau (Li et al. [31]), and the Tibet Plateau (Liu et al. [32]) evaporation paradox had been found.

In fact pan evaporation observations mostly ended in 2001 in China; evaporation paradox was concluded based on annual pan evaporation of 1960–2000 (H. Yang and D. Yang [33]) or potential evaporation from 1960–2010 without no data segment. However, change of temperature and potential evaporation transformed around 2000. In this paper observed meteorological variables are divided into two parts taking year 2000 as the boundary and the objectives of this study are (1) to investigate changes in  $ET_0$  and temperature in China since 1960s; (2) to examine the existence of evaporation paradox in different periods and regions; (3) to determine potential key factors attributed to  $ET_0$  changes in the whole country as well as different river basins.

## 2. Data and Methodology

**2.1. Data.** Daily meteorological data were obtained from 754 stations from the China Meteorological Administration (CMA) and National Meteorological Information Center of China (NMIC); 599 stations (Figure 1) of these had complete records of all climatic factors calculating  $ET_0$  in time series of 1960–2013. The daily meteorological data included precipitation, relative humidity, sunshine hours, vapor pressure, wind speed, maximum, minimum, and mean air temperature. A few missing data (mainly in 1967, 1968, 1969) were estimated by averaging the value of the other years observed at the same station.

In the data set, the 10 river basins are the first-order basin in China (Figure 1). 56 stations are in the Songhua River basin (SRB), 36 are in the Liao River basin (LRB), 33 are in the Hai River basin (HaRB), 67 are in the Yellow River

basin (YeRB), 38 are in the Huai River basin (HuRB), 143 are in the Yangtze River basin (YaRB), 28 are in the southeast rivers basin (SERB), 67 are in the Pearl River basin (PRB), 35 are in the southwest rivers basin (SWRB), and 97 are in the Northwest Rivers Basin (NWRB). In the 599 stations, the Taiwan Island is the one that we could not collect observation data from; therefore, it is excluded from the study region.

### 2.2. Methodology

**2.2.1. Penman-Monteith Method.** In this paper, potential evapotranspiration ( $ET_0$ ) was estimated using the Penman-Monteith (PM) method (Allen et al. [34]); the formula is given as

$$ET_0 = \frac{0.408\Delta(R_n - G) + \gamma(900/(T + 273))U_2(e_s - e_a)}{\Delta + \gamma(1 + 0.34U_2)}, \quad (1)$$

where  $ET_0$  is the daily potential evapotranspiration ( $\text{mm d}^{-1}$ ), and the yearly and monthly value of  $ET_0$  will be used in this paper;  $R_n$  is the net radiation at the top surface ( $\text{MJ}\cdot\text{m}^{-2}\cdot\text{d}^{-1}$ );  $G$  is the soil heat flux density ( $\text{MJ}\cdot\text{m}^{-2}\cdot\text{d}^{-1}$ );  $T$  is the mean daily air temperature at 2 m height ( $^{\circ}\text{C}$ );  $U_2$  is daily average wind speed at 2 m height ( $\text{m}\cdot\text{s}^{-1}$ );  $e_s$  is the saturation vapor pressure (kPa);  $e_a$  is the actual vapor pressure (kPa);  $\Delta$  is the slope of the vapor pressure curve ( $\text{kPa}^{\circ}\text{C}^{-1}$ );  $\gamma$  is the psychrometric constant ( $\text{kPa}^{\circ}\text{C}^{-1}$ ). In the model the radiation term was calculated by experience formula and its accuracy depends on the experience coefficients which were often only effective in particular regions. In this paper,  $ET_0$  was calculated by corrected radiation. The correcting net radiation is as follows (Yin et al. [35]):

$$R_n = 0.77 \times \left(0.2 + 0.79 \frac{n}{N}\right) R_{sa} - \delta \left[ \frac{T_{x,k}^4 + T_{n,k}^4}{2} \right] \times (0.56 - 0.25\sqrt{e}) \left(0.1 + 0.9 \frac{n}{N}\right), \quad (2)$$

where  $\delta$  is constant of Stefan-Boltzmann ( $4.903 \times 10^{-9} \text{MJ}\cdot\text{K}^{-4}\cdot\text{m}^{-2}\cdot\text{d}^{-1}$ ),  $T_{x,k}$ ,  $T_{n,k}$  is the absolute maximum and minimum temperature (K),  $n$  is the actual sunshine hours (h),  $N$  is the duration of possible sunshine (h), and  $R_{sa}$  is the Sunny radiation ( $\text{MJ}\cdot\text{m}^{-2}$ ). Soil heat flux  $G$  is small compared with the relative net radiation and  $G \approx 0$  in the day time scale.

**2.2.2. Trend Analysis Method.** The simple linear regression method was used to estimate the trend magnitudes (slope) in  $ET_0$  and other climatic variables. The linear equation is

$$\widehat{X}_i = a + b \cdot t_i, \quad (3)$$

where  $\widehat{X}_i$  is the simulated value of climatic variables;  $b \times 10$  is the trend which denoted the change trend of climatic variables per decade; and  $t$  is the time series (Yang et al. [36]). Meanwhile, the nonparametric Mann-Kendall

TABLE 1: Change trends of temperature and potential evapotranspiration ( $ET_0$ ) in China.

	$ET_0$						Temperature					
	1960–2013		1960–1999		2000–2013		1960–2013		1960–1999		2000–2013	
	<i>a</i>	<i>b</i>	<i>a</i>	<i>b</i>	<i>a</i>	<i>b</i>	<i>c</i>	<i>d</i> (%)	<i>c</i>	<i>d</i> (%)	<i>c</i>	<i>d</i> (%)
China	-3.9*	59.1	-14.78**	75.1	10.08	43.7	0.24**	97.8	0.21**	90	-0.08	41.4
YaRB	-2.51	58.7	-17.64**	86	52.27	16.8	0.18**	96.5	0.07	74.3	0.16	62.2
SERB	3.61	60.7	-20.93**	89.3	19.37	21.4	0.21**	100	0.1	92.9	-0.14	46.4
HaRB	-9.21**	75.8	-18.08**	84.8	-17.05	72.7	0.28**	97	0.3**	97	-0.41	39.4
HuRB	-5.95	60.5	-8.16	65.8	-17.24	60.5	0.2**	97.4	0.17*	97.4	-0.1	39.5
YeRB	1.02	61.2	-5.94	55.2	-6.22	53.7	0.27**	97	0.23**	98.5	-0.1	13.4
LRB	-10.68*	52.8	-12.67	80.6	-78.2	86.1	0.23**	100	0.31**	100	-0.51	2.7
SRB	-4.04	70.9	-3.77	58.2	-74.26	90.9	0.33**	100	0.44**	98.2	-0.36	27.3
NWRB	-11.13**	69.1	-27.65**	81.4	26.69	39.2	0.34**	99	0.31**	94.8	0	45.4
SWRB	3.89	48.6	-3.26	60	102.4	5.7	0.28**	100	0.22**	88.6	0.4	97.1
PRB	-1.01	44.8	-14.65**	76.1	5.74	43.3	0.14**	98.5	0.11**	88.1	-0.28	25.4

*a* slope of  $ET_0$  (mm per decade); *b* percent of downward (%); *c* slope of temperature ( $^{\circ}\text{C}$  per decade); *d* percent of upward; \* $\alpha = 0.05$ , \*\* $\alpha = 0.01$ , the significance in 2000–2013 was not calculated because of the short time.

(M-K) method (Mann [37], Kendall et al. [38]) is highly recommended by the World Meteorological Organization for analyzing hydrological series as it did not need any distributional assumption for the data and it was used to detect the significance of the trend.

**2.2.3. Stepwise Regression.** The basic idea is to introduce the influencing factors into regression equation one by one. Significant test is carried out when introducing one variable into the model, retaining the significant factors and rejecting the insignificant ones until there are no variables introduced into the model and no one rejected. This method can eliminate the variables which contribute little to principal component or those existing linear relations and can overcome the multicollinearity based on guaranteeing the regression effects.

**2.2.4. Region Average of Variables.** In previous researches, regional value was obtained by using an arithmetic mean method from meteorological station. However, meteorological stations are not distributed evenly but dense in the east and sparse in the west in China. Therefore, it is necessary to assign different weights for different stations when evaluating climate change accurately for different regions. When calculating the average value of an area, the weight of a station is determined by the percentage of the Thiessen polygon in the whole area. Thiessen polygon method was more accurate than simple mean method and less workload grid data set method.

### 3. Results

**3.1. Observed Changes of Temperature and  $ET_0$ .** In 1960–2013, 98.2% of the 599 stations show upward trend (91.2% of all stations are at 95% significance level). The average daily temperature in China as a whole (Figure 2) rises at the rate of  $0.24^{\circ}\text{C}$  per decade (95% significance level). Corresponding with significant warming trend, the mean national  $ET_0$  declines at the rate of  $-3.9$  mm per decade (95% significance

level), so there exists evaporation paradox in China as a whole.

**3.2. Temporal Trends of Evaporation Paradox.** According to Figure 2, the mean annual temperature climaxed in around year 2000 and then decreased slowly, and  $ET_0$  reached the lowest value around 1993 and then rose slowly. Taking the change into account comprehensively, this paper took the year 2000 as the dividing line. At the same time in order to compare with the proceeding results of other researchers, we analyzed the characteristics of evaporation paradox in the period of 1960–2013, 1960–1999, and 2000–2013 (Table 1). In 1960–2013 and 1960–1999, the annual temperature increased significantly, while  $ET_0$  decreased significantly at the rate  $-3.9$  mm per decade (58.4% of all stations) and  $-14.78$  mm per decade (75.1% of all stations); in 2000–2013, temperature decreased (58.6% of all stations) with the rate being  $-0.08^{\circ}\text{C}$  per decade while  $ET_0$  increased (56.3%) with the rate being  $10.08$  mm per decade. In 1960–1999,  $ET_0$  of 75.1% stations dropped and temperature of 90% stations rose and the opposite change of temperature and  $ET_0$  between 1960–1999 and 2000–2013 made the range of temperature rise and  $ET_0$  dropping moderate and evaporation paradox weaken in 1960–2013.

The mean annual temperature in the 10 river basins all rose at 95% significance level and  $ET_0$  all showed downward trend except in SERB, YeRB, and SWRB in 1960–2013; all river basins indicated upward in temperature and downward in  $ET_0$  in 1960–1999. The maximum downward in  $ET_0$  and upward in temperature appeared in NWRB and SRB with values being  $-27.65$  mm per decade and  $0.44^{\circ}\text{C}$  per decade, respectively, in 1960–1999. In 2000–2013,  $ET_0$  in YaRB, SERB, SWRB, NWRB, and PRB increased while temperature in SWRB and PRB decreased. In other basins the trend in temperature and  $ET_0$  was the same. In this period temperature only in YaRB and SWRB increased, whether the increase was a fluctuation in the whole upward process or the beginning of decrease needs further investigation.

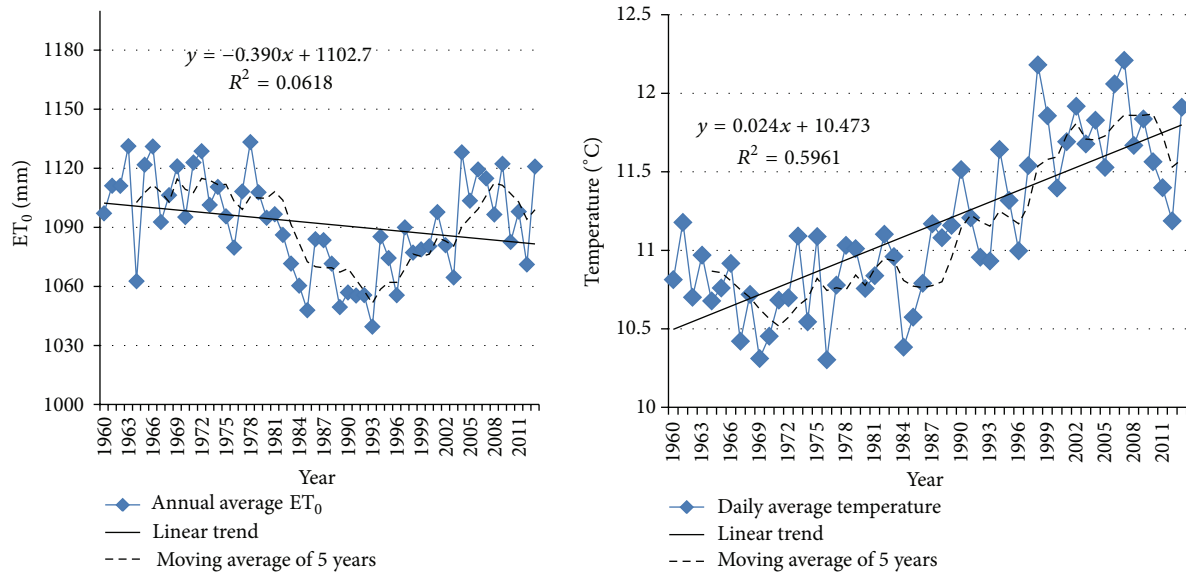


FIGURE 2: Interannual changes of temperature and  $ET_0$  in 1960–2013.

**3.3. Seasonal Change of Evaporation Paradox.** Figure 3 showed trends of evaporation paradox in 4 seasons.

Spring (March to May): in 1960–2013, evaporation paradox existed in HaRB, LRB, SRB, NWRB, SWRB, PRB, and China as a whole. In 1960–1999, evaporation paradox existed in all regions except SRB; in 2000–2013, there was no evaporation paradox; change of temperature and  $ET_0$  was the same in eight river basins and temperature in 5 river basins dropped. The opposite changes of temperature and  $ET_0$  in 1960–1999 and 2000–2013 weakened the evaporation paradox of 1960–2013.

Summer (June to August): in 1960–2013,  $ET_0$  and temperature were the highest values in a whole year; the slope of  $ET_0$  and percent of downward stations were the highest values too.  $ET_0$  descended in YaRB, HaRB, HuRB, YeRB, LRB, NWRB, and China as a whole; temperature rose in all regions, except HuRB which was at 99% confidence level. In 1960–1999, evaporation paradox existed in all river basins except SWRB and HuRB; in China as a whole the percent of  $ET_0$  downward climaxed 77% and 8 river basins were more than 70%, and so evaporation paradox was the most prominent in all statistical periods. In 2000–2013, the variation of  $ET_0$  and temperature was the same except the HuRB.

Autumn (September to November): the slope and range of  $ET_0$  decline reduced in autumn comparing with that of spring and summer. In 1960–2013,  $ET_0$  in HaRB, LRB, SERB, SRB, and NWRB decreased and temperature increased significantly. The phenomenon existed in the 5 river basins in 1960–1999 too. In 2000–2013, HuRB, LRB, SRB, and PRB showed evaporation paradox.

Winter (December to February next year): change in temperature was the most severe compared with the other seasons. Except in PRB in 1960–1999, temperature in 1960–2013 and 1960–1999 all rose significantly. Opposite to the severe increase in temperature, decrease of  $ET_0$  in winter was moderate. In 1960–2013,  $ET_0$  only in HuRB, HaRB,

LRB, and NWRB declined slightly and other regions showed upward trend. In 1960–1999,  $ET_0$  in HaRB, HuRB, PRB, YaRB, NWRB, and China as a whole insignificantly decreased. In 2000–2013, temperature showed biggest fall and only SWRB showed upward trend. In winter  $ET_0$  changed the smallest in the four seasons and evaporation paradox was moderate.

**3.4. Spatial Distribution of Evaporation Paradox.** In 1960–2013 and 1960–1999, the percent of rising stations in temperature exceeded 90%, so stations in which  $ET_0$  decreased can be judged as where evaporation paradox existed (Figure 4). The evaporation paradox distribution can be obtained from the interpolation of  $Z$  statistic of  $ET_0$ . In 1960–2013, 57.6% of the site of annual  $ET_0$  decreased in China, the regions where  $ET_0$  increased were mainly located in the northeast of the NWRB, northwest of SRB, three rivers sources regions, middle reach in YeRB, northeast and southeast of HuRB, SWRB, coastal area of PRB, middle of YaRB, and so on. Overall coastal areas in the south of  $37^\circ\text{N}$ , most of the regions between  $30^\circ\text{N}$  and  $40^\circ\text{N}$ ,  $90^\circ\text{E}$ – $110^\circ\text{E}$ , northwestern of the northeast China, and southeastern of SWRB were the areas where evaporation paradox does not exist. The evaporation paradox area accounted for 73.7% of the 10 river basins. In 1960–1999,  $ET_0$  of 75.1% stations showed downward trend; northwestern of SRB, Ningxia and middle Shaanxi section of the YeRB, three rivers sources regions and northeastern of HuRB, there is no evaporation paradox in such areas. The evaporation paradox area accounted for 91.2%. In 2000–2013,  $ET_0$  and temperature of 223 stations change oppositely and 322 stations were the same; 54 stations of  $Z$  statistics of  $ET_0$  or temperature were 0.

## 4. Discussion

**4.1. Relationship between  $ET_0$  and Precipitation.** Precipitation and  $ET_0$  were two important segments of the hydrologic



TABLE 2: Results of the stepwise regression.

China	YaRB	SERB	HaRB	HuRB	YeRB	LRB	SRB	NWRB	SWRB	PRB
$V$	$H$	$V$	$T_{\max}$	$H$	$V$	$H$	RH	$H$	$V$	$H$
$H$	RH	RH	RH	RH	$T_{\max}$	RH	$H$	$V$	RH	RH
RH	$V$	$T_{\max}$	$V$	$V$	$P$	$T_{\max}$	$T_{\max}$	$T_{\text{mean}}$	$T_{\max}$	$T_{\min}$
$T_{\max}$	$T_{\min}$	$H$				$V$	$V$	$P$	$H$	$V$

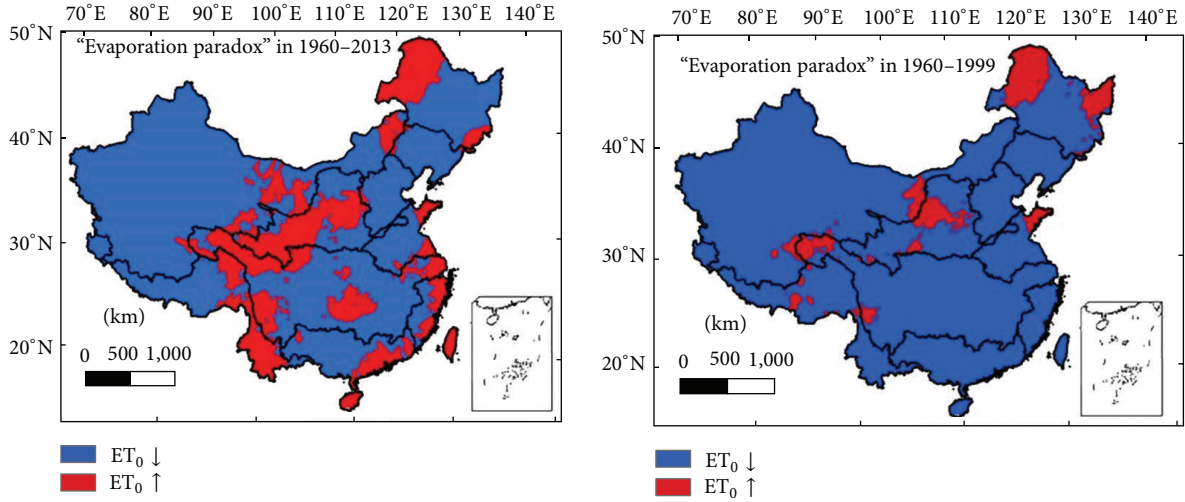


FIGURE 4: Distribution of evaporation paradox in different periods.

cycle;  $ET_0$  will decline with the increase of precipitation according to the Bouchet assumption. The annual average precipitation is 808 mm in China during 1960–2013; it rose insignificantly and the rising percent was 48.4%. The annual average precipitation was 811 mm in 1960–1999 and the insignificant rising percent was 55.9%; in 2000–2013 the average value was 799.5 mm; change of  $ET_0$  and precipitation in China were consistent with the Bouchet hypothesis and Figure 5 showed the relationship of them. In 1960–2013, reverse trend stations were 301 and were located in NWRB, SERB, three rivers sources regions, lower reaches of YaRB, northwestern of SRB, HuRB, and PRB where precipitation increased. Precipitation and  $ET_0$  drop sites were mainly located in LRB, HaRB, YeRB, upper reaches of PRB, southeastern of SRB, and the middle reaches of the YaRB. Decreased stations of precipitation in 1960–1999 were more than that of 1960–2013, but its distribution was basically the same. The two factors both indicated upward trend in 2000–2013, whose precipitation rose in 330 stations, unchanged in 45 sites. 352 stations showed opposite change of them which accounted for 58.8% of the whole stations. Regions where precipitation decreased were mainly located in NWRB, SRB, LRB, HaiRB, and the middle reaches of the YeRB.

**4.2. Impacts of Meteorological Factors on  $ET_0$ .** Meteorological factors change had profound impacts on  $ET_0$ ; in this paper stepwise regression was used to extract the influencing factors of  $ET_0$ . Yearly  $ET_0$  and 7 meteorological factors such as mean temperature ( $T_{\text{mean}}$ ), maximum temperature ( $T_{\max}$ ),

minimum temperature ( $T_{\min}$ ), relative humidity (RH), sunshine hours ( $H$ ), average wind speed ( $V$ ), and average water pressure ( $P$ ) were firstly normalized in order to remove the impacts of inconsistent units. The entering order of climate variability was showed in Table 2.  $V$  was the primary contributor which caused  $ET_0$  change in China as a whole, SERB, YeRB, and SWRB and the standardized coefficients were 0.75, 0.54, 0.87, and 0.54, respectively.  $H$  contributed most to  $ET_0$  change in YaRB, HuRB, LRB, and PRB with the standardized coefficients of 0.56, 0.66, 0.82, and 0.70.  $T_{\max}$  had maximum impact on  $ET_0$  in HaRB with standardized coefficients being 0.80. The largest contribution in SRB was RH which was negative with  $ET_0$ .

Table 2 indicated that  $H$ ,  $T_{\max}$ ,  $V$ , and RH were the most important factors influencing  $ET_0$ . Table 3 showed slope of the listed meteorological elements and  $ET_0$  in different statistical period. In 1960–2013,  $ET_0$  decreased in all regions except SERB, YeRB, and SWRB; in NWRB, LRB and HaRB  $ET_0$  decreased at 99% level of confidence. In 1960–1999,  $ET_0$  decreased in all regions and the decline rate was much more than that of 1960–2013; in 2000–2013,  $ET_0$  in 5 river basins was downward trend.  $V$  which was in positive relationship with  $ET_0$  decreased at the rate of  $-0.11 \text{ m s}^{-1}$  per decade significantly in China as a whole and it was found to be the primary contributor which caused  $ET_0$  to decrease in the past 54 years; except PRB in 1960–2013,  $V$  decreased in all regions significantly.  $H$  which was in positive relationship with  $ET_0$  too had decreased with a significant trend of  $-0.11 \text{ h}$  per decade in 1960–2013 and  $-0.13 \text{ h}$  per decade in 1960–1999 at 99% confidence level and the decline led  $ET_0$  to decrease

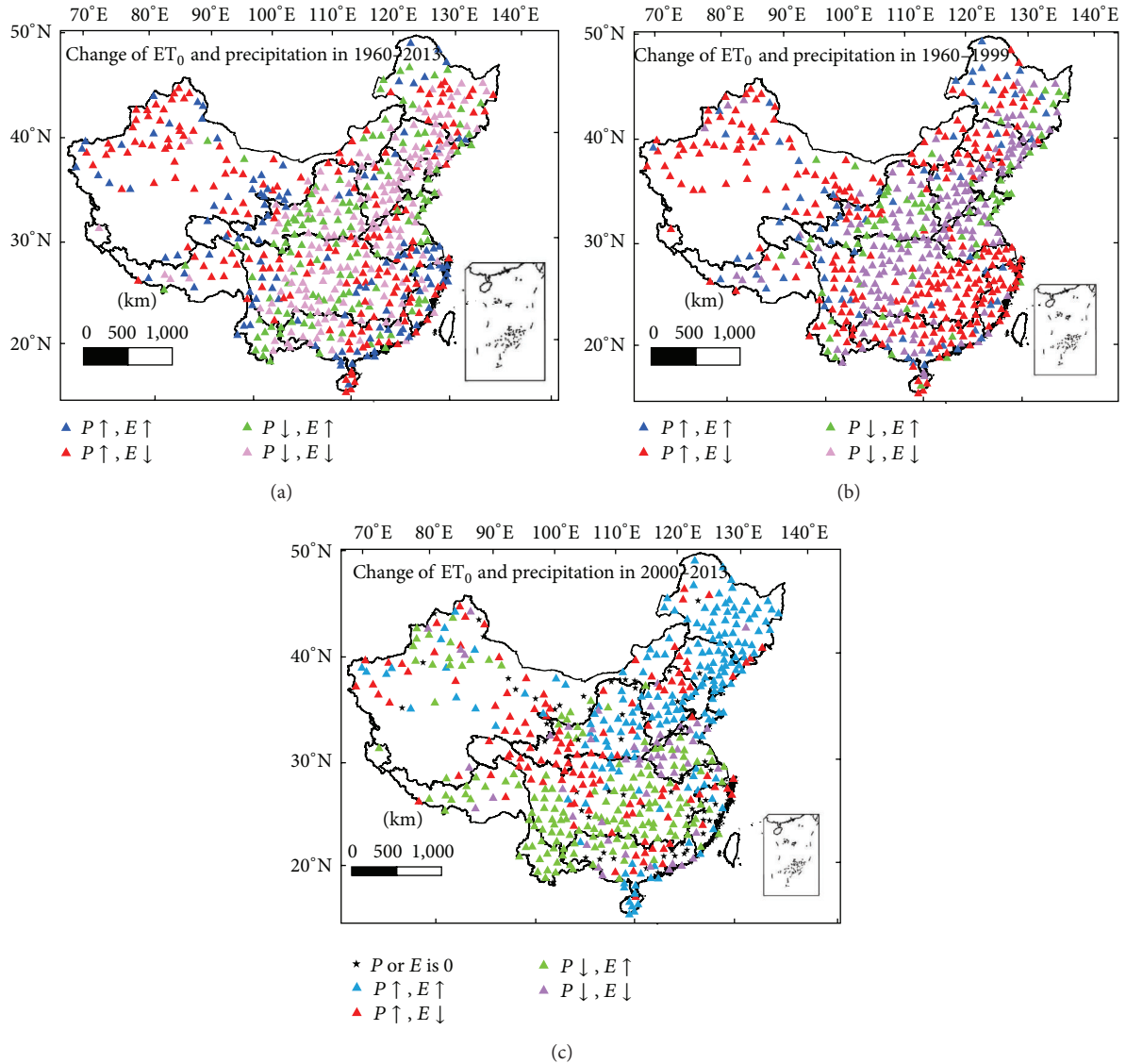


FIGURE 5: Change of precipitation and  $ET_0$  in China.

in China as a whole; in the 10 river basins,  $H$  decreased significantly except SWRB. The range and scope of  $H$ ,  $V$  decline both diminished in 2000–2013.  $T_{max}$  contributing positive impact on  $ET_0$  growth increased in all regions in 1960–1999 and the increase was significant except HuRB in 1960–2013; the most dramatic change occurred in  $T_{max}$  in 2000–2013 among the 4 variables; it changed into decrease from increase in SERB, HaRB, HuRB, YeRB, LRB, SRB, PRB, and China as a whole. RH only increased in YaRB, NWRB, and SWRB in 1960–1999 and LRB and SRB in 2000–2013. The change of  $ET_0$  was influenced comprehensively by all these factors;  $ET_0$  was in a positive relationship with  $H$ ,  $V$ ,  $T_{max}$  and negative relationship with RH. In China, the decline of  $V$ ,  $H$  made  $ET_0$  reduce and decline RH and ascension of  $T_{max}$  made  $ET_0$  ascend. The comprehensive effect of the four elements was the decline of  $ET_0$ . In 1960–1999, the decline rate of  $H$ ,  $V$  strengthened corresponding to the weakness

in  $T_{max}$  rising and RH decreasing strengthened the decline rate of  $ET_0$  to  $-14.78$  mm per decade. In 2000–2013, the trend of meteorological factors changed compared with that of 1960–1999, decline rate of  $H$ ,  $V$  reduced greatly,  $T_{max}$  switched from increase into decrease, and decline rate of RH increased substantially. The combination caused  $ET_0$  switch from decrease to increase.

## 5. Conclusions

- (1) In 1960–2013, temperature in 98.2% stations of 599 stations increased in China. The decline rate of annual national  $ET_0$  was  $-3.9$  mm per decade so evaporation paradox existed. In 1960–1999,  $ET_0$  of 75.1% stations was downward and temperature of

TABLE 3: Slope of climate variables and  $ET_0$  in China.

		China	YaRB	SERB	HaRB	HuRB	YeRB	LRB	SRB	NWRB	SWRB	PRB
$ET_0$ (mm per decade)	1960–2013	-3.9*	-2.51	3.61	-9.21**	-5.95	1.02	-10.68*	-4.04	-11.13**	3.89	-1.01
	1960–1999	-14.78**	-17.64**	-20.93**	-18.08**	-8.16	-5.94	-12.67	-3.77	-27.65**	-3.26	-14.65**
	2000–2013	10.08	52.27	19.37	-17.05	-17.24	-6.22	-78.2	-74.26	26.69	102.4	5.74
$H$ ( $h\ d^{-1}$ per decade)	1960–2013	-0.11**	-0.11**	-0.16**	-0.23**	-0.18**	-0.08*	-0.08*	-0.09**	-0.04**	0	-0.13**
	1960–1999	-0.13**	-0.16**	-0.28**	-0.2**	-0.16**	-0.1*	-0.12**	-0.11**	-0.06*	-0.01	-0.19**
	2000–2013	-0.04	0.09	-0.05	-0.17	0.08	-0.13	-0.14	-0.43	0.07	0.23	-0.25
RH (% per decade)	1960–2013	-0.43**	-0.53**	-0.83**	-0.6**	-0.87**	-0.5*	-0.11	-0.46**	-0.12	-0.34	-0.63**
	1960–1999	-0.02	0.12	0	-0.33	-0.26	-0.17	-0.11	-0.42*	0.21	0.21	-0.23*
	2000–2013	-2.08	-3.18	-2.8	-2.41	-5.22	-1.93	2.14	1.35	-2.58	-5.9	-1.3
$T_{max}$ ( $^{\circ}C$ per decade)	1960–2013	0.18**	0.16**	0.18**	0.19**	0.08	0.25**	0.16**	0.19**	0.25**	0.24**	0.09*
	1960–1999	0.11	0	0.03	0.18*	0.1	0.19	0.2*	0.27**	0.18*	0.11	0.02
	2000–2013	-0.11	0.25	-0.21	-0.41	-0.46	-0.02	-0.72	-0.69	0.02	0.74	-0.41
$V$ ( $m\ s^{-1}$ per decade)	1960–2013	-0.11**	-0.08**	-0.13**	-0.16**	-0.1**	-0.07**	-0.18**	-0.18**	-0.14**	-0.05**	0.04
	1960–1999	-0.12**	-0.09**	-0.15**	-0.19**	-0.11**	-0.07**	-0.18**	-0.17**	-0.18**	-0.02	-0.07**
	2000–2013	-0.02	0.03	-0.13	0.01	-0.2	-0.06	-0.14	-0.21	-0.02	0.12	0.12

90% stations was upward which indicated the most prominent evaporation paradox. In 2000–2013 there was no evaporation paradox. The opposite change of temperature and  $ET_0$  in 1960–1999 and 2000–2013 weaken the evaporation paradox in 1960–2013 compared with that of 1960–1999.

- (2) In 1960–2013, evaporation paradox existed in spring, summer, and autumn in China as a whole; it existed in 6, 6, 5, and 4 river basins in spring, summer, autumn, and winter; the decline rate of  $ET_0$  and percent of temperature downward climaxed in summer. In 1960–1999, except SRB in spring, SWRB in summer, HaRB, HuRB, and YeRB in autumn, HuRB, YeRB, LRB, and SRB in winter evaporation paradox exists in other times. In 2000–2013, there was no evaporation paradox.
- (3) There was no evaporation paradox in the southeastern coastal areas south of  $37^{\circ}N$ , most of areas in  $30^{\circ}N$ – $40^{\circ}N$ ,  $90^{\circ}E$ – $110^{\circ}E$ , northwestern in SRB, and southeastern of SWRB in China in 1960–2013; the area accounted for 26.3% of the 10 river basins. No evaporation paradox area was only in NWRB, northeastern of SRB, middle reach of YeRB, three river source regions, and northeastern of HuRB which accounted for 8.8% merely.
- (4) Precipitation in NWRB, SERB, three river source regions, lower reaches of YaRB, northwestern of SRB, northwestern of HuRB, and lower reaches of PRB increased and in such regions  $ET_0$  decreased in 1960–2013. Most of stations in which  $ET_0$  and precipitation change inversely were located south of  $27^{\circ}N$  and north of  $32^{\circ}N$ ; the number of the stations was 346 in 1960–1999. In 2000–2013, the stations which precipitation increased were located in north

of  $32^{\circ}N$  and the number of stations in which  $ET_0$  and precipitation change inversely was 352.

- (5)  $H$ ,  $T_{max}$ ,  $V$ , RH were the most important variations affecting  $ET_0$  change;  $H$ ,  $V$ ,  $T_{max}$  were positive and RH was negative relationship with  $ET_0$ ;  $H$ ,  $V$ , RH mainly decreased and  $T_{max}$  mainly increased in China and the comprehensive function of them made  $ET_0$  decrease in 1960–2013 and 1960–1999 and increase in 2000–2013.

## Conflict of Interests

The authors declare that there is no conflict of interests regarding the publication of this paper.

## Acknowledgments

This study was supported by the National Natural Science Foundation of China (Grant no. 51279063); Program for Innovative Research Team (in Science and Technology) in University of Henan Province (15IRTSTHN030); and Program for New Century Excellent Talents in University (Grant no. NCET-13-0794).

## References

- [1] IPCC, *Climate Change 2013: The Physical Science Basis, Working Group I Contribution to Fifth Assessment Report of Intergovernmental Panel on Climate Change*, Cambridge University Press, Cambridge, UK, 2013.
- [2] S. Wang, J. Ye, D. Gong et al., “Construction of mean annual temperature series for the last one hundred years in China,” *Quarterly Journal of Applied Meteorology*, vol. 9, no. 4, pp. 392–401, 1998.

- [3] H. L. Penman, "Natural evaporation from open water, bare soil and grass," *Proceedings of the Royal Society of London. Series A*, vol. 193, pp. 120–145, 1948.
- [4] G. H. Hargreaves and Z. A. Samani, "Reference crop evapotranspiration from temperature," *Applied Engineering in Agriculture*, vol. 1, no. 2, pp. 96–99, 1985.
- [5] A. R. Pereira and W. O. Pruitt, "Adaptation of the Thornthwaite scheme for estimating daily reference evapotranspiration," *Agricultural Water Management*, vol. 66, no. 3, pp. 251–257, 2004.
- [6] S. Irmak, I. Kabenge, K. E. Skaggs, and D. Mutiibwa, "Trend and magnitude of changes in climate variables and reference evapotranspiration over 116-yr period in the Platte River Basin, central Nebraska–USA," *Journal of Hydrology*, vol. 420–421, pp. 228–244, 2012.
- [7] Y. Dinpashoh, D. Jhajharia, A. Fakheri-Fard, V. P. Singh, and E. Kahya, "Trends in reference crop evapotranspiration over Iran," *Journal of Hydrology*, vol. 399, no. 3–4, pp. 422–433, 2011.
- [8] L. Q. Liang, L. J. Li, and Q. L. Liu, "Temporal variation of reference evapotranspiration during 1961–2005 in the Taoer River basin of Northeast China," *Agricultural and Forest Meteorology*, vol. 150, no. 2, pp. 298–306, 2010.
- [9] A.-E. Croitoru, A. Piticar, C. S. Dragotă, and D. C. Burada, "Recent changes in reference evapotranspiration in Romania," *Global and Planetary Change*, vol. 111, pp. 127–132, 2013.
- [10] J. Feng, D. Yan, C. Li, F. Yu, and C. Zhang, "Assessing the impact of climatic factors on potential evapotranspiration in droughts in North China," *Quaternary International*, vol. 336, pp. 6–12, 2014.
- [11] Q. Liu and Z. Yang, "Quantitative estimation of the impact of climate change on actual evapotranspiration in the Yellow River Basin, China," *Journal of Hydrology*, vol. 395, no. 3–4, pp. 226–234, 2010.
- [12] E. W. Harmsen, N. L. Miller, N. J. Schlegel, and J. E. Gonzalez, "Seasonal climate change impacts on evapotranspiration, precipitation deficit and crop yield in Puerto Rico," *Agricultural Water Management*, vol. 96, no. 7, pp. 1085–1095, 2009.
- [13] B. Tang, L. Tong, S. Kang, and L. Zhang, "Impacts of climate variability on reference evapotranspiration over 58 years in the Haihe river basin of north China," *Agricultural Water Management*, vol. 98, no. 10, pp. 1660–1670, 2011.
- [14] T. R. McVicar, M. L. Roderick, R. J. Donohue et al., "Global review and synthesis of trends in observed terrestrial near-surface wind speeds: implications for evaporation," *Journal of Hydrology*, vol. 416–417, pp. 182–205, 2012.
- [15] M. L. Roderick and G. D. Farquhar, "The cause of decreased pan evaporation over the past 50 years," *Science*, vol. 298, no. 5597, pp. 1410–1411, 2002.
- [16] T. C. Peterson, V. S. Golubev, and P. Y. Groisman, "Evaporation losing its strength," *Nature*, vol. 377, no. 6551, pp. 687–688, 1995.
- [17] V. S. Golubev, J. H. Lawrimore, P. Y. Groisman et al., "Evaporation changes over the contiguous United States and the former USSR: a reassessment," *Geophysical Research Letters*, vol. 28, no. 13, pp. 2665–2668, 2001.
- [18] A. Thomas, "Spatial and temporal characteristics of potential evapotranspiration trends over China," *International Journal of Climatology*, vol. 20, no. 4, pp. 381–396, 2000.
- [19] X. Ma, M. Zhang, S. Wang, Q. Ma, and S. Pan, "Evaporation paradox in the Yellow River Basin," *Acta Geographica Sinica*, vol. 67, no. 5, pp. 645–656, 2012.
- [20] T. Tebakari, J. Yoshitani, and C. Suvanpimol, "Time-space trend analysis in pan evaporation over Kingdom of Thailand," *Journal of Hydrologic Engineering*, vol. 10, no. 3, pp. 205–215, 2005.
- [21] A. C. Moonen, L. Ercoli, M. Mariotti, and A. Masoni, "Climate change in Italy indicated by agrometeorological indices over 122 years," *Agricultural and Forest Meteorology*, vol. 111, no. 1, pp. 13–27, 2002.
- [22] M. L. Roderick and G. D. Farquhar, "Changes in New Zealand pan evaporation since the 1970s," *International Journal of Climatology*, vol. 25, no. 15, pp. 2031–2039, 2005.
- [23] D. H. Burn and N. M. Hesch, "Trends in evaporation for the Canadian Prairies," *Journal of Hydrology*, vol. 336, no. 1–2, pp. 61–73, 2007.
- [24] S. Cohen, A. Ianetz, and G. Stanhill, "Evaporative climate changes at Bet Dagan, Israel, 1964–1998," *Agricultural and Forest Meteorology*, vol. 111, no. 2, pp. 83–91, 2002.
- [25] Y. Yin, S. Wu, G. Chen, and E. Dai, "Attribution analyses of potential evapotranspiration changes in China since the 1960s," *Theoretical and Applied Climatology*, vol. 101, no. 1, pp. 19–28, 2010.
- [26] S. Han, D. Xu, and S. Wang, "Decreasing potential evaporation trends in China from 1956 to 2005: accelerated in regions with significant agricultural influence?" *Agricultural and Forest Meteorology*, vol. 154–155, pp. 44–56, 2012.
- [27] W. Wang, Q. Shao, S. Peng et al., "Reference evapotranspiration change and the causes across the Yellow River Basin during 1957–2008 and their spatial and seasonal differences," *Water Resources Research*, vol. 48, no. 5, pp. 27–35, 2012.
- [28] W. Xing, W. Wang, Q. Shao et al., "Changes of reference evapotranspiration in the Haihe River Basin: present observations and future projection from climatic variables through multi-model ensemble," *Global and Planetary Change*, vol. 115, pp. 1–15, 2014.
- [29] C.-Y. Xu, L. Gong, T. Jiang, D. Chen, and V. P. Singh, "Analysis of spatial distribution and temporal trend of reference evapotranspiration and pan evaporation in Changjiang (Yangtze River) catchment," *Journal of Hydrology*, vol. 327, no. 1–2, pp. 81–93, 2006.
- [30] Y. Yang, Z. Feng, H. Q. Huang, and Y. Lin, "Climate-induced changes in crop water balance during 1960–2001 in Northwest China," *Agriculture, Ecosystems & Environment*, vol. 127, no. 1–2, pp. 107–118, 2008.
- [31] Z. Li, F.-L. Zheng, and W.-Z. Liu, "Spatiotemporal characteristics of reference evapotranspiration during 1961–2009 and its projected changes during 2011–2099 on the Loess Plateau of China," *Agricultural and Forest Meteorology*, vol. 154–155, pp. 147–155, 2012.
- [32] X. Liu, H. Zheng, M. Zhang, and C. Liu, "Identification of dominant climate factor for pan evaporation trend in the Tibetan Plateau," *Journal of Geographical Sciences*, vol. 21, no. 4, pp. 594–608, 2011.
- [33] H. Yang and D. Yang, "Climatic factors influencing changing pan evaporation across China from 1961 to 2001," *Journal of Hydrology*, vol. 414–415, pp. 184–193, 2012.
- [34] R. G. Allen, L. S. Pereira, D. Raes, and M. Smith, "Crop evapotranspiration guidelines for computing crop water requirements," FAO Irrigation and Drainage Paper 56, FAO, Rome, Italy, 1998.
- [35] Y. Yin, S. Wu, D. Zheng, and Q. Yang, "Radiation calibration of FAO56 Penman-Monteith model to estimate reference crop

- evapotranspiration in China,” *Agricultural Water Management*, vol. 95, no. 1, pp. 77–84, 2008.
- [36] Y. Yang, X. Zhou, and B. Wu, “Urban expansion prediction for Zhangzhou city based on GIS and spatiotemporal logistic regression model,” *Journal of Geo-Information Science*, vol. 13, no. 3, pp. 374–382, 2011.
- [37] H. B. Mann, “Nonparametric tests against trend,” *Econometrica*, vol. 13, pp. 245–259, 1945.
- [38] M. G. Kendall, *Rank Correlation Methods*, Griffin, London, UK, 1975.

## Research Article

# Impact of Stratospheric Sudden Warming on East Asian Winter Monsoons

**Quanliang Chen, Luyang Xu, and Hongke Cai**

*College of Atmospheric Science, Chengdu University of Information Technology and Plateau Atmospheric and Environment Laboratory of Sichuan Province, Chengdu 610225, China*

Correspondence should be addressed to Quanliang Chen; chenql@cuit.edu.cn

Received 15 January 2015; Revised 22 March 2015; Accepted 29 March 2015

Academic Editor: Jieshun Zhu

Copyright © 2015 Quanliang Chen et al. This is an open access article distributed under the Creative Commons Attribution License, which permits unrestricted use, distribution, and reproduction in any medium, provided the original work is properly cited.

Fifty-two Stratospheric sudden warming (SSW) events that occurred from 1957 to 2002 were analyzed based on the 40-year European Centre for Medium-Range Weather Forecasts Reanalysis dataset. Those that could descent to the troposphere were composited to investigate their impacts on the East Asian winter monsoon (EAWM). It reveals that when the SSW occurs, the Arctic Oscillation (AO) and the North Pacific Oscillation (NPO) are both in the negative phase and that the tropospheric circulation is quite wave-like. The Siberian high and the Aleutian low are both strengthened, leading to an increased gradient between the Asian continent and the North Pacific. Hence, a strong EAWM is observed with widespread cooling over inland and coastal East Asia. After the peak of the SSW, in contrast, the tropospheric circulation is quite zonally symmetric with negative phases of AO and NPO. The mid-tropospheric East Asian trough deepens and shifts eastward. This configuration facilitates warming over the East Asian inland and cooling over the coastal East Asia centered over Japan. The activities of planetary waves during the lifecycle of the SSW were analyzed. The anomalous propagation and the attendant altered amplitude of the planetary waves can well explain the observed circulation and the EAWM.

## 1. Introduction

Stratospheric sudden warming (SSW) is an intriguing phenomenon of winter stratospheric circulation. Since it was first discovered in 1952 by Scherhag [1], it has been recognized as one of the critical phenomena that could influence hemispheric circulation patterns. Polar stratospheric temperature rises sharply when SSW occurs, and stratospheric circulation patterns linked to temperature changes shift dramatically. SSW events can be divided into major and minor warming events, based on the degree of warming. Charlton and Polvani [2] classified major warming events into those that either do or do not split the stratospheric polar vortex based on the zonal wind at 60°N and 10 hPa. Matthewman et al. [3] found that vortex-splitting events are typically barotropic, with the vortex split occurring nearly simultaneously over a large altitude range (20–40 km), while displacement events are characterized by a very clear baroclinic structure.

Abnormal circulation caused by some specific SSW events is able to propagate downward to influence the

tropospheric weather and climate. Early in the 1970s, Quiroz [4] found that anomalous stratospheric zonal anticyclonic circulation in high latitudes occurs along with SSW, and this anomaly extends from the stratosphere to the ground and affects tropospheric weather systems. Baldwin and Dunkerton [5] considered that Arctic Oscillation (AO), which is the critical mode that couples the stratosphere and troposphere, has a significant relationship with SSW. They suggested that SSW causes the AO index to become negative and return to positive slowly. They also pointed out the potential role of the stratosphere in the tropospheric weather forecasts during both the weak and strong vortex events. Later, Baldwin et al. [6, 7] further found that SSW could lead to higher temperature and geopotential height in the polar region and weaken the stratospheric AO.

Major SSW events can cause significant changes in the stratospheric polar region and lead to the anomaly of Northern Hemispheric AO transmission to the troposphere, thereby affecting weather and climate in the troposphere. Li et al. [8] found that, after a major SSW event, temperature

and height anomalies in the polar stratosphere can lead to downward AO, which may result in stronger Siberian high and Aleutian low, and a deeper westward shifted mid-tropospheric East Asian trough. Deng et al. [9] analyzed the linkage between the SSW and AO and found that the upper-tropospheric East Asian jet stream is strengthened and the East Asian trough is deepened during SSW. Mitchell et al. [10] developed a new classification technique of weak vortex events based on the distribution of potential vorticity and further divided such events into vortex displacements and vortex splits. They suggested that vortex splitting events are correlated with surface weather and can lead to positive temperature anomalies that exceed 1.5 K over eastern North America and negative anomalies that exceed -3 K over Eurasia and that the corresponding signals are weaker during displacement events. Wang and Chen [11] studied the cold winter in 2009 and suggested that this event is accounted for by the extreme negative AO at surface level and that some relatively weaker stratospheric anomalies can also propagate downward and influence the troposphere. From the perspective of mass circulation, some recent studies provided a clear physical picture on the linkage between the stratospheric circulation anomalies and the Northern Hemispheric cold air outbreaks [12, 13].

China is located in East Asia, and the East Asian winter monsoon (EAWM) is the world's strongest winter monsoon system [14, 15]. The EAWM is generally considered to be the driver of the East Asian atmospheric circulation and is related to cold air moving eastward and southward from the Siberian high [14]. Previous scholars have shown that many factors including external forces and internal dynamic processes can affect the EAWM [14, 15]. Some recent studies [16–20] suggested that the changes of EAWM are closely linked to the winter AO. The EAWM is strong during the negative phase of AO and vice versa. The North Pacific Oscillation (NPO) and its tropospheric embodiment, the western Pacific (WP) pattern, are other important factors that influence the EAWM [21–23]. They are featured with an equivalent barotropic structure in summer but tilt slightly westward with height during the other three seasons [21]. The positive phase of NPO favors significant southerly anomalies along the coasts of East Asia during the boreal winter and may bring warm moist air from the south [21].

It is well known that the troposphere and the stratosphere are dynamically coupled because of the vertical transmission of atmospheric planetary waves in the boreal winter. After Thompson and Wallace discovered AO [24, 25], observation and simulation results both indicate that the anomalies that occur in the stratosphere are able to propagate downward to the troposphere, affecting climate and weather when accompanied by the AO signal [26–28]. However, not all the stratospheric AO events and SSW events are linked with the subsequent tropospheric cold events or low temperature events [26–28]. Besides, most of these studies focused on North America or Europe, and fewer studies were carried on for East Asia. In fact, the EAWM has a very close relationship with the AO and the stratosphere [16–20, 29], implying that the stratosphere is very likely to influence the EAWM. Moreover, it is interesting to explore this issue because the

long-lasting stratospheric anomalies may provide valuable information for the medium-range weather prediction of the EAWM. Therefore, this study aims to explore the possible relationship between the SSW (stratospheric AO) and the EAWM, focusing on the period of both during and after the peak of the SSW. Specifically, we divided the 52 SSW events during 1957–2002 into those that could and could not propagate downward to the troposphere and analyzed the changes of the East Asian winter monsoon during and after the peak of the downward propagating SSW events. In order to understand the mechanism that links the EAWM and the SSW, the activity of planetary waves and the associated Eliassen-Palm (EP) flux were also investigated.

## 2. Data and Methods

Data used in this study are from the 40-year European Centre for Medium-Range Weather Forecast Reanalysis (ERA-40) dataset that contains 45 years (1957–2002). It has a horizontal resolution of  $2.5^\circ \times 2.5^\circ$  and extends from 1000 to 1 hPa with 23 pressure levels. The data used in this study include the geopotential field, the temperature field, and the zonal and meridional wind fields.

According to the World Meteorological Organization's stipulation in 1963, in order for a warming event to be qualified as SSW, it needs to meet two criteria: (1) a zonal mean temperature of  $60^\circ\text{N}$  to polar reverses its meridional gradient at 10 hPa or lower and (2) the polar vortex weakens and moves south, while, since the polar region is controlled by a warm high, the circulation turns easterly instead of westerly. These criteria can be expressed as follows:

$$\begin{aligned}\Delta [T] &= [T]_{90^\circ\text{N}} - [T]_{60^\circ\text{N}} \\ \Delta [H] &= [H]_{90^\circ\text{N}} - [H]_{60^\circ\text{N}},\end{aligned}\tag{1}$$

where  $[\ ]$  indicates the zonal mean. When  $\Delta [T] > 0$ ,  $\Delta [H] > 0$ —that is, both zonal mean temperature and the corresponding zonal mean geopotential meridional gradient reverse in  $60^\circ\text{N}$  to polar regions; we define it as a major SSW event. If only  $\Delta [T] > 0$ , but  $\Delta [H] < 0$ , then the event is defined as a minor SSW event. Thirty-one strong and 21 minor SSW events were identified and analyzed for the 45 winters during 1957–2002, according to the definition above (see Table 1).

In addition, we define an SSW event as a downward propagating event if it meets both of the following criteria [30].

- (1) The maximum anomalies of geopotential height in the polar region ( $70^\circ \sim 90^\circ\text{N}$ ) at 10 hPa lag behind the maximum anomalies of 1 hPa by at least one day.
- (2) The maximum anomalies of geopotential height in the polar region ( $70^\circ \sim 90^\circ\text{N}$ ) at 10 hPa lead the maximum anomalies of 100 hPa by at least one day.

Twenty-eight downward propagating events were selected from the 52 SSW events according to the criteria above, and they are listed in Table 1. As we can see, 21 out of 31 major SSW events could propagate downward, but only

TABLE 1: All SSW events and the downward propagating SSW events.

Year	Onset of major SSW	Termination of major SSW	Onset of minor SSW	Termination of minor SSW
1958	2-6, 11-22 <sup>▲</sup>	2-14, 12-12 <sup>▲</sup>	—	—
1960	1-4 <sup>▲</sup> , 12-9	1-24 <sup>▲</sup> , 12-26	—	—
1962	—	—	2-4, 12-8	2-23, 12-17
1963	1-25 <sup>▲</sup>	2-11 <sup>▲</sup>	—	—
1965	12-4	12-23	—	—
1967	12-30 <sup>▲</sup>	1968-1-25 <sup>▲</sup>	—	—
1968	11-18	12-3	—	—
1970	1-1 <sup>▲</sup>	2-1 <sup>▲</sup>	—	—
1971	1-10	1-28	—	—
1972	—	—	2-21	3-7
1973	1-28 <sup>▲</sup>	2-26 <sup>▲</sup>	—	—
1974	2-26	3-27	—	—
1975	—	—	1-1, 12-24	2-6, 12-28
1976	12-20 <sup>▲</sup>	12-26 <sup>▲</sup>	—	—
1977	1-3 <sup>▲</sup>	1-18 <sup>▲</sup>	—	—
1978	—	—	1-17 <sup>▲</sup> , 1-30	1-20 <sup>▲</sup> , 2-3
1979	2-20	3-5	1-23, 2-6, 11-24	1-28, 2-11, 12-7
1981	11-30 <sup>▲</sup>	12-8 <sup>▲</sup>	1-29, 2-16	2-9, 2-27
1982	—	—	1-24 <sup>▲</sup>	2-4 <sup>▲</sup>
1983	2-23 <sup>▲</sup>	3-4 <sup>▲</sup>	1-27 <sup>▲</sup>	2-16 <sup>▲</sup>
1984	2-19 <sup>▲</sup> , 12-30	3-20 <sup>▲</sup> , 1985-1-16	—	—
1986	—	—	1-20, 2-15	1-24, 2-22
1987	1-16 <sup>▲</sup> , 12-7 <sup>▲</sup>	2-5 <sup>▲</sup> , 12-19 <sup>▲</sup>	—	—
1989	2-12 <sup>▲</sup>	2-28 <sup>▲</sup>	—	—
1990	—	—	2-5 <sup>▲</sup>	2-27 <sup>▲</sup>
1991	1-20 <sup>▲</sup>	2-16 <sup>▲</sup>	—	—
1992	—	—	1-11 <sup>▲</sup>	1-24 <sup>▲</sup>
1993	12-30 <sup>▲</sup>	1994-1-8 <sup>▲</sup>	2-15	2-22
1995	2-9 <sup>▲</sup>	2-15 <sup>▲</sup>	—	—
1996	—	—	2-17	3-6
1997	—	—	12-19 <sup>▲</sup>	1-11 <sup>▲</sup>
1998	1-5 <sup>▲</sup> , 12-14 <sup>▲</sup>	1-11 <sup>▲</sup> , 1999-1-14 <sup>▲</sup>	—	—
1999	2-23 <sup>▲</sup>	3-6 <sup>▲</sup>	—	—
2001	1-31 <sup>▲</sup> , 12-23	2-21 <sup>▲</sup> , 2002-1-10	—	—
2002	2-13 <sup>▲</sup>	3-5 <sup>▲</sup>	—	—

Note: <sup>▲</sup> an SSW downward propagating event; #-# the date of an SSW event in the form of month-day.

6 out of 21 minor SSW events could propagate downward. This indicates that major SSW events spread more easily downward to the troposphere than minor ones do.

Figure 1 shows the composite of geopotential height anomalies in the polar region for the downward propagating and the nondownward propagating SSW events, respectively, during the 120-day period centered on the SSW events. Here day 0 is defined as the day of the maximum anomaly at 10 hPa. The vertical axis represents the height and the horizontal axis the lead (negative) or lag (positive) of the 10 hPa maximum anomalies' geopotential height. The selected abnormal downward propagating events (Figure 1(a)) have apparent downward positive anomalies below 150 hPa after day 0, while the nondownward propagating events (Figure 1(b)) show negative anomalies below the 150 hPa height. This result

suggests that the above method to select downward and nondownward propagating events is efficient and valid.

This study also considered planetary wave propagation in the vertical direction with two-dimensional EP flux calculations, using the EP flux of planetary waves. The EP flux is defined as follows [31]:

$$F = \left( -\rho a \cos \varphi \overline{u'v'}, \rho a \cos \varphi \frac{Rf}{HN^2} \overline{v'T'} \right), \quad (2)$$

where  $F$  is the EP flux,  $\rho$  the air density,  $a$  the radius of the Earth,  $\varphi$  the latitude,  $R$  the constant of the air,  $f$  the Coriolis parameter,  $H$  the scale height,  $u$  and  $v$  the zonal and meridional winds, respectively, and  $T$  the temperature. In this study, the wavenumbers 1-3 are extracted with Fourier analysis method. Composite analyses are performed and the

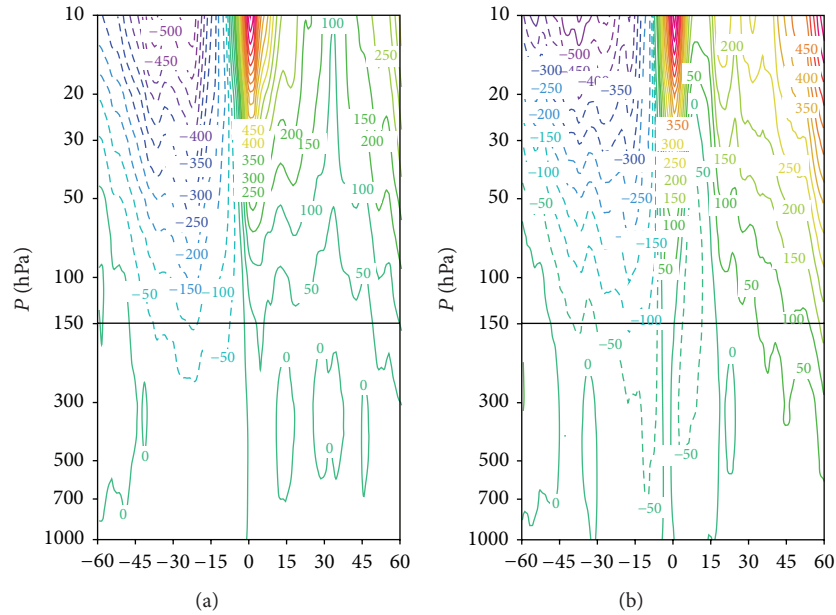


FIGURE 1: Composite of geopotential height anomalies of downward propagating SSW and nondownward propagating events: (a) downward propagating events; (b) nondownward propagating events. The time axis extends from 60 days before day 0 until 60 days afterward. The contour intervals are 50 gpm.

confidence levels are evaluated with a two-tailed Student's  $t$ -test.

### 3. Impact of SSW on the Middle and Lower Troposphere

During a major SSW event, the stratospheric circulation changes dramatically, and the westerly zonal winds that prevail at 10 hPa become the easterly winds [1–3]. After the SSW event, the stratospheric anomalies may propagate downward to the troposphere in the middle and high latitudes [4, 5]. Such features are well captured by the zonal-mean zonal wind anomalies shown in Figure 2, which is the composite based on the 28 downward propagating SSW events. During the peak (day  $-10 \sim +10$ ) of the SSW events, there are clear easterly anomalies that center at  $60^\circ\text{N}$  at about 1 hPa (Figure 2(a)). These easterly anomalies are originally confined in the stratosphere at the middle and high latitudes, and the easterly anomalies in the troposphere are very weak (Figure 2(a)). The center of the easterly anomalies propagates downward to about 10 hPa afterwards (Figure 2(b)). During day  $+10 \sim +40$ , the maximum easterly anomalies appear at 10 hPa height at  $60^\circ\text{N}$ , and clear easterly anomalies can be observed in the troposphere and even near the surface (Figure 2(b)). Meanwhile, the westerly winds are gradually restored at 1 hPa from about  $45^\circ\text{N}$ . Although the easterly circulation is in its slipping stage in the middle stratosphere, it still dominates the lower stratosphere and the whole troposphere.

In order to investigate the impact of the SSW on the EAWM, we composited the atmospheric circulation anomalies during (day  $-10 \sim +10$ ) and after (day  $+10 \sim +40$ ) the downward propagation of the SSW signals. Figure 3 shows the distribution of the 1000 hPa geopotential height anomalies

during (day  $-10 \sim +10$ ) and after (day  $+10 \sim +40$ ) the SSW. During the peak of the SSW events (Figure 3(a)), the 1000 hPa geopotential height field features significant positive anomalies region over the eastern part of the Eurasian continent and negative anomalies over the North Pacific, exhibiting clear wave-like structure. These anomalies overlap the Siberian high and the Aleutian low, indicating that both systems are strengthened. This is reasonable because, during the SSW events, the planetary waves are more active and have larger amplitude. Given that the Siberian high and the Aleutian low are manifestations of the planetary waves at the surface [29], the two systems both amplified during this process. In this situation, the pressure gradient between the Asian continent and the North Pacific is significantly enhanced and facilitates the strengthening of the EAWM. After the peak of the SSW (Figure 3(b)), the wave-like structure diminished. Instead, the polar region and the mid-latitude region are occupied by positive and negative geopotential height anomalies, respectively. This structure is quite zonal-symmetric and resembles the negative phase of AO. A slight difference of this structure from the conventional AO [21, 22] is that the anomalies over the North Pacific are stronger than those over the North Atlantic (Figure 3(b)), so it resembles the NPO [19] to some extent. In this situation, the Siberian high weakens significantly, but the Aleutian low amplifies over its southern part. Therefore, the pressure gradient in between is enhanced along the coasts and weakened in the East Asian inland.

Another significant feature of the East Asian winter atmospheric circulation is the deep coastal trough in the mid-troposphere [32, 33], so we further examined the East Asian trough during and after the SSW. Figure 4 shows the 500 hPa geopotential height anomalies during and after the peak of the SSW. During the peak of the SSW (Figure 4(a)), a roughly

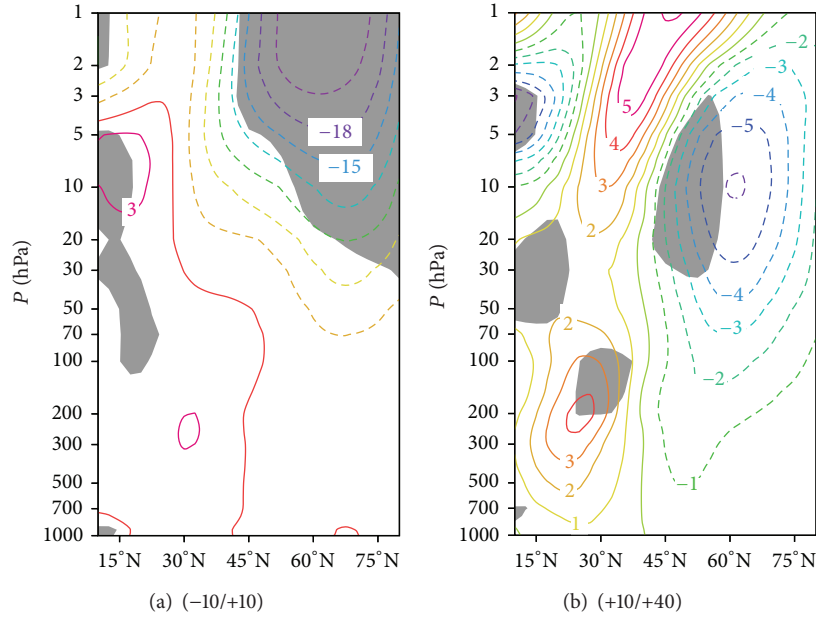


FIGURE 2: Distribution of zonal mean wind anomalies during and after the peak of SSW: (a) day -10~+10 mean; (b) day +10~+40 mean. Unit:  $m s^{-1}$ .

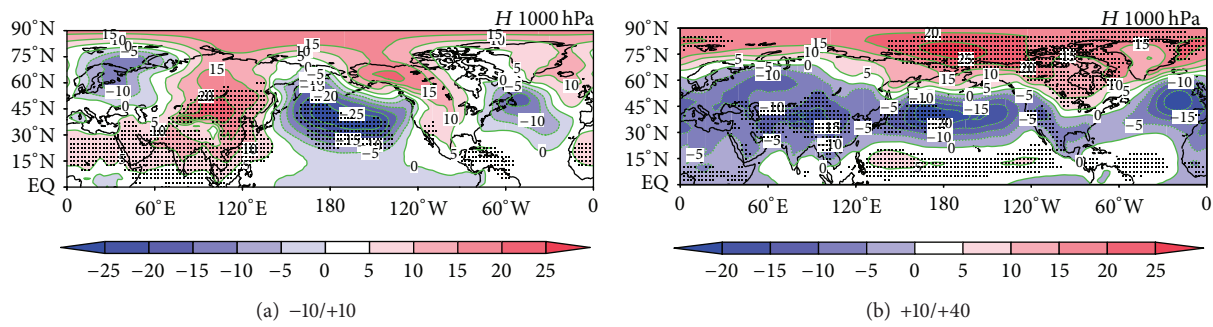


FIGURE 3: Distribution of 1000 hPa geopotential height anomalies during and after the peak of SSW: (a) day -10~+10 mean; (b) day +10~+40 mean. Unit: gpm; the dots indicate 99% confidence levels; the contour and the shading both indicate the geopotential height anomalies.

wavenumber-3 pattern is observed north of 45°N, corresponding to the wave-like pattern of 1000 hPa (Figure 3(a)). The geopotential height field is significantly negative around Japan (Figure 4(a)), indicating the enhanced East Asian trough and thereby the EAWM. After the peak of the SSW, the circulation at 500 hPa is more zonally symmetric and the wavenumber-3 pattern is slightly weakened, resembling the negative phase of both AO and NPO (Figure 4(b)). The NPO/WP pattern is especially clear and it exhibits a meridional dipole over the North Pacific. Compared with the peak of the SSW (Figure 4(a)), the anomalous negative geopotential height center over the Pacific is located more eastward (Figure 4(b)). Hence, it suggests that the East Asian trough not only deepens but also shifts eastward. This configuration is conducive to cold episode along the coastal areas of East Asia in the lower troposphere [33].

The decreased temperature anomalies during and after the peak of the SSW are shown in Figure 5. During the peak of the SSW (Figure 5(a)), the northern and central parts of East

Asia show quite significant cooling. This is consistent with the strong Siberian high (Figure 3(a)) and East Asian trough (Figure 4(b)). After the peak of the SSW (Figure 5(b)), East Asia shows quite contrasting temperature patterns between inland and coastal regions. The inland and the Southeast regions show clear warming, whereas the coastal areas and Japan show significant cooling. The inland warming can be attributed to the weakened Siberian high (Figure 3(b)). The coastal cooling can be attributed to the enhanced Aleutian low over its southern portion and the attendant enhanced pressure gradient (Figure 3(b)), as well as the deepened and eastward shifted East Asian trough (Figure 4(b)).

To get a clearer picture of the above interpretation, the wind anomalies at 850 hPa are shown in Figure 6. During the peak of SSW (Figure 6(a)), significant northerly anomalies prevail in a wide longitudinal range from northeast China to the coast of East Asia and even east of Japan. This configuration can carry cold air from the higher latitudes and result in lower-than-normal temperatures in all of East

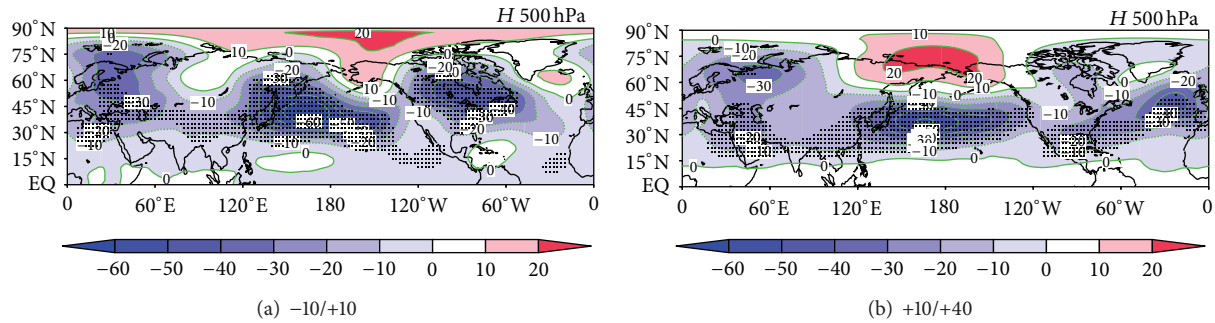


FIGURE 4: Distribution of 500 hPa geopotential height anomalies during and after the peak of SSW: (a) day  $-10\sim+10$  mean; (b) day  $+10\sim+40$  mean. Unit: gpm; the dots indicate 99% confidence levels; the contour and the shading both indicate the geopotential height anomalies.

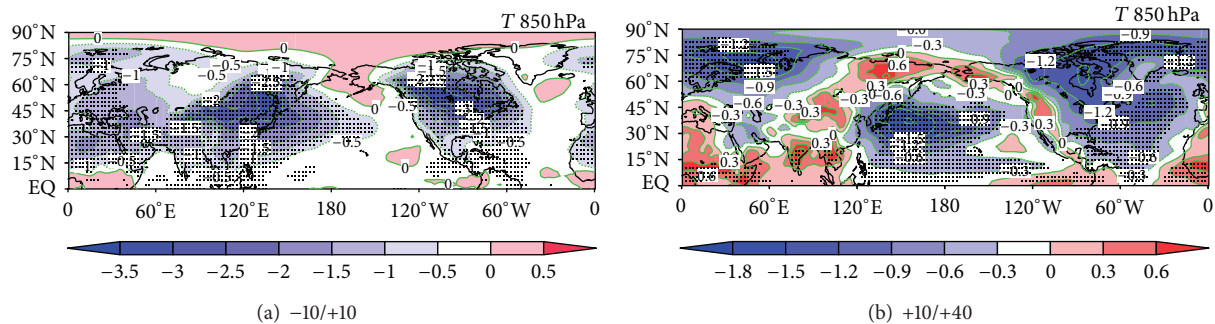


FIGURE 5: Distribution of 850 hPa temperature anomalies during and after the peak of SSW: (a) day  $-10\sim+10$  mean; (b) day  $+10\sim+40$  mean. Unit: K; the dots indicate 99% confidence levels; the contour and the shading both indicate the temperature anomalies.

Asia (Figure 5(a)). After the peak of the SSW (Figure 6(b)), in contrast, the northerly anomalies only prevail around and to the east of Japan, and southerly anomalies are observed over Southeast Asia. Therefore, cooling is only confined to the coastal region and around Japan, while warming is observed in the inland of East Asia (Figure 5(b)).

#### 4. Activity of Planetary Waves during the Lifecycle of the SSW

It is well known that a planetary wave generated in the troposphere can propagate upward, especially in winter, and can pass through the tropopause into the stratosphere [34] causing the stratosphere and troposphere to couple together. AO signals are able to propagate downward and impact the troposphere under some certain conditions as well [35, 36]. Furthermore, because the NPO/WP has a quasi-positive structure [21], it may cause changes in the lower atmosphere when its high levels trigger some adjustments in Pacific geopotential height. Therefore, in this section, the activities of planetary waves in the downward propagating process of the SSW anomaly are studied by means of its corresponding EP flux and wave amplitude.

Figure 7 shows the anomalies of EP flux for wavenumbers 1-3 during different periods of the SSW. Twenty days before the SSW, stronger-than-normal EP flux is observed to propagate continuously into the stratosphere (Figures 7(a)-7(d)). This propagation is especially strong in the week before the peak of the SSW (Figure 7(d)). These anomalously

upward propagating planetary waves converge in the polar stratosphere, leading to the deceleration of the stratospheric westerly winds. After 20 days of a decelerating effect on the stratospheric westerly circulation, the strength of the stratospheric polar vortex significantly decreases. When the decelerating effect reaches its maximum, the westerly turns to easterly and SSW occurs. When the SSW occurs, the establishment of the easterly circulation in the polar regions is not conducive to the upward propagation of planetary waves, so that further dispersion of the tropospheric wave energy into the stratosphere is suppressed. This process can be seen clearly from the EP flux diagrams. When the SSW begins (Figure 7(e)) the EP flux into the stratosphere weakens rapidly and anomalous downward EP flux is observed in the subpolar region (Figures 7(f)-7(i)). In this situation, it is conducive to the diabatic adjustments, and a radiative balance develops. Then, the westerly of polar night jet accelerates and the westerly circulation gradually resumes. However, the upward propagation of planetary waves remains weak (Figures 7(f)-7(i)) in both the stratosphere and the upper troposphere, and the decelerating effect of planetary waves on the polar night jet is still effective in the middle and high latitudes. This will facilitate a weak circumpolar vortex, which helps the negative phase of AO to maintain and propagate downward and thereby results in changes in the lower atmospheric circulation.

Figure 8 shows the amplitude anomalies of planetary waves for wavenumbers 1 to 3. Before the peak of the SSW (Figure 8(a)), the amplitude of planetary increases in

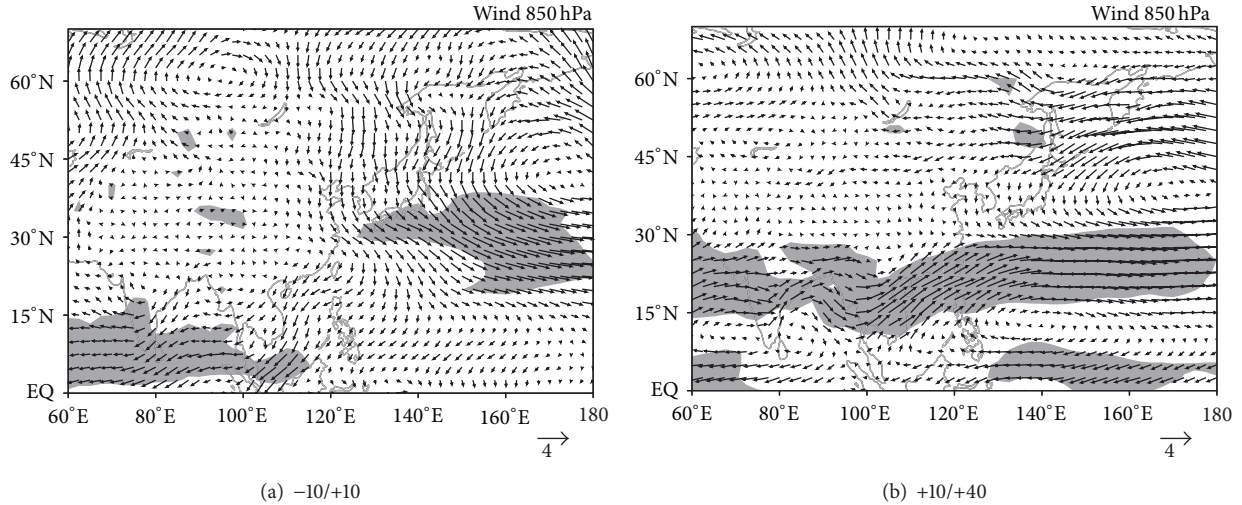


FIGURE 6: Distribution of 850 hPa wind anomalies during and after the peak of SSW: (a) day  $-10\sim+10$  mean; (b) day  $+10\sim+40$  mean. Unit:  $\text{m s}^{-1}$ ; the shadings indicate 99% confidence levels.

the region of  $45^{\circ}\text{N}\sim 70^{\circ}\text{N}$  with the maximum being located between 300 and 200 hPa and decreases in the regions of  $30^{\circ}\text{N}\sim 45^{\circ}\text{N}$ . The increase of wave amplitude at high latitudes is consistent with the enhanced upward propagation of planetary waves (Figures 7(a)–7(d)) that implies enhanced activity of planetary waves. After the peak of the SSW (Figure 8(b)), the pattern of amplitude of planetary waves remains similar but has opposite signs. That is, reduced amplitude is observed in  $45^{\circ}\text{N}\sim 70^{\circ}\text{N}$ , while enhanced amplitude is observed at  $30^{\circ}\text{N}\sim 45^{\circ}\text{N}$ . This is also consistent with the suppressed upward propagation of planetary waves (Figures 7(f)–7(i)) that implies weakened activity of planetary waves. The reduced wave amplitude at high latitudes ( $45^{\circ}\text{N}\sim 70^{\circ}\text{N}$ ) corresponds to a weakened Siberian high [37] and the increased wave amplitude at  $30^{\circ}\text{N}\sim 45^{\circ}\text{N}$  corresponds to the enhanced Aleutian low in its southern portion. Therefore, these results suggest that the planetary wave play an important role in linking the SSW and the EAWM.

## 5. Discussion and Conclusions

The traditional view is that the stratosphere is only passively influenced by the troposphere, and that it is difficult for the stratosphere to influence the troposphere. However, studies over the past ten years have discovered that the stratosphere not only accepts waves and energy from the troposphere, but also sends anomalies back to the troposphere [4–11]. A key connector between the stratosphere and troposphere is the activities of planetary waves. In this study, we investigated the unique phenomenon of SSW and its impacts on the troposphere, focusing on the impacts on the EAWM.

Based on composite analysis of selected SSW events whose signals can propagate downward to the troposphere, it is found that the stratospheric polar night jet is significantly weakened during the peak of the SSW. During this period, the planetary wave-like structure in the troposphere is very strong and the enhanced amplitude of planetary waves

corresponds to strong Siberian high and Aleutian low. This configuration facilitates strong northerly anomalies from Northeast China to North Pacific. Therefore, the EAWM is intensified and significant cooling is observed over all of East Asia especially over inland. After the peak of the SSW, the stratospheric easterly anomalies descend to the troposphere, while the easterly anomalies in the upper stratosphere begin to diminish and restore towards the westerly circulation. During this period, the tropospheric circulation anomalies are quite zonally symmetric and feature clear negative phases of AO and NPO. The Siberian high is weakened but the southern portion of the Aleutian low is strengthened. The mid-tropospheric East Asian trough deepens and shifts eastward. In this situation, the 850 hPa northerly anomalies are only observed around and to the east of Japan. Therefore, significant cooling is observed over coastal East Asia centered over Japan whereas clear warming is observed in the East Asian inland.

The activities of planetary waves were also examined during the lifecycle of the SSW. Before the occurrence of the SSW, there is stronger-than-normal upward propagating EP flux of planetary waves towards the polar stratosphere, leading to a decrease of the stratospheric circumpolar westerly winds. When the SSW occurs, the upward propagation of EP flux weakens because the significantly weakened stratospheric westerly makes it difficult for the planetary wave to propagate upward. The decreased upward propagation of planetary waves favors an adjustment of the diabatic radiation balance to develop, and it produces westerly acceleration in the upper stratosphere and a gradual recovery of westerly circulation. Nevertheless, the westerly circulation continues to slow down in the lower stratosphere and upper troposphere, being conducive to the downward propagation of the negative AO signal from the stratosphere to the troposphere. Thus, the SSW could affect the atmospheric circulation of the lower troposphere. Accompanied with the above-mentioned anomalous propagation of the planetary waves, the amplitude

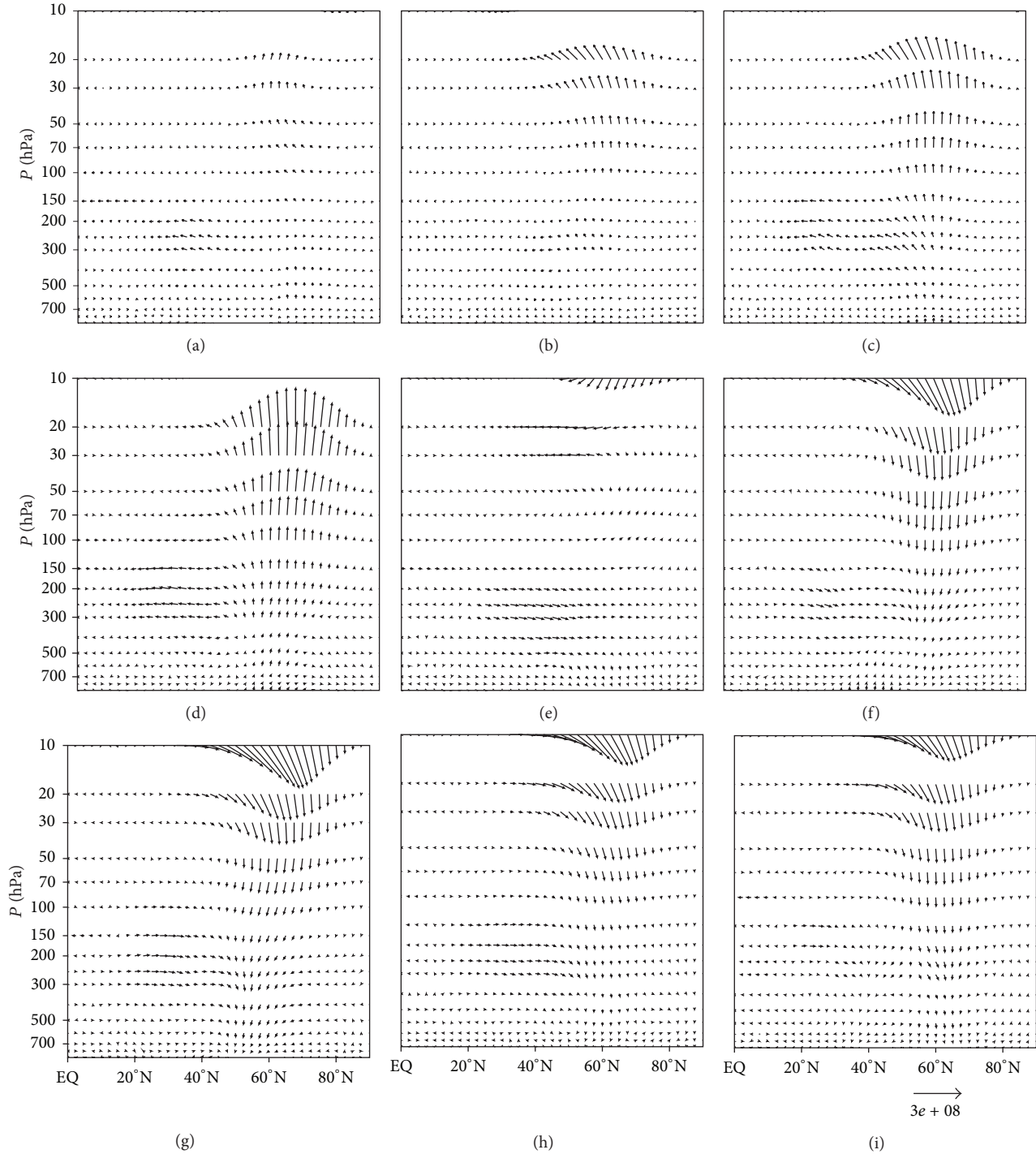


FIGURE 7: Evolution of EP flux during the lifecycle of SSW: (a) day  $-22\sim-18$  mean; (b) day  $-17\sim-13$  mean; (c) day  $-12\sim-8$  mean; (d) day  $-7\sim-3$  mean; (e) day  $-2\sim+2$  mean; (f) day  $+3\sim+7$  mean; (g) day  $+8\sim+12$  mean; (h) day  $+13\sim+17$  mean; (i) day  $+18\sim+22$  mean. Unit:  $\text{m}^2 \text{s}^{-2}$ .

of the planetary waves decreases after the SSW at  $45^\circ\text{N}\sim 70^\circ\text{N}$  and increases at  $30^\circ\text{N}\sim 45^\circ\text{N}$ . It weakens the Siberian high and strengthens the southern portion of the Aleutian low, leading to the observed cooling around Japan and warming over East Asian inland.

In this study, the temperature anomalies over East Asia during and after the SSW events are investigated and

explained from a point of view of altered atmospheric circulations. The wave-like circulation during the peak of the SSW and the zonally symmetric circulation after the peak of the SSW are quite contrasting. The different activities of planetary waves are suggested to be crucial in this process. Nevertheless, the mechanism of the downward propagation of the AO signal from the stratosphere to the troposphere

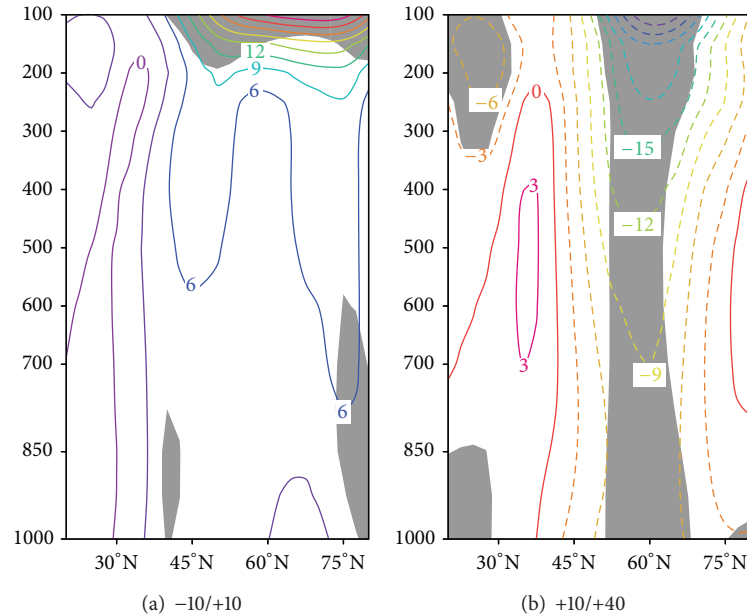


FIGURE 8: The anomalous amplitude of planetary wave numbers 1 to 3 before and after the peak of SSW: (a) day  $-10\sim-40$  mean; (b) day  $+10\sim+40$  mean. Unit: gpm.

remains unanswered. This is a difficult and intriguing issue that needs more theoretical studies.

### Conflict of Interests

The authors declare that there is no conflict of interests regarding the publication of this paper.

### Acknowledgments

This work was supported by National Natural Science Foundation of China (41475037, 41405031) and Sichuan Youth Fund (2014JQ0019).

### References

- [1] R. Scherhag, "Die explosionsartigen Stratosphärenwärnungen des Spätwinters 1951/52," *Berichte des Deutschen Wetterdienstes in der US-Zone*, vol. 6, no. 38, pp. 51–63, 1952.
- [2] A. J. Charlton and L. M. Polvani, "A new look at stratospheric sudden warmings. Part I. Climatology and modeling benchmarks," *Journal of Climate*, vol. 20, no. 3, pp. 449–469, 2007.
- [3] N. J. Matthewman, J. G. Esler, A. J. Charlton-Perez, and L. M. Polvani, "A new look at stratospheric sudden warmings. Part III: polar vortex evolution and vertical structure," *Journal of Climate*, vol. 22, no. 6, pp. 1566–1585, 2009.
- [4] R. S. Quiroz, "The tropospheric-stratospheric polar vortex breakdown of January 1977," *Geophysical Research Letters*, vol. 4, no. 4, pp. 151–154, 1977.
- [5] M. P. Baldwin and T. J. Dunkerton, "Propagation of the Arctic Oscillation from the stratosphere to the troposphere," *Journal of Geophysical Research D: Atmospheres*, vol. 104, no. 24, pp. 30937–30946, 1999.
- [6] M. P. Baldwin, D. B. Stephenson, D. W. J. Thompson, T. J. Dunkerton, A. J. Charlton, and A. O'Neill, "Stratospheric memory and skill of extended-range weather forecasts," *Science*, vol. 301, no. 5633, pp. 636–640, 2003.
- [7] M. P. Baldwin and D. W. J. Thompson, "A critical comparison of stratosphere-troposphere coupling indices," *Quarterly Journal of the Royal Meteorological Society*, vol. 135, no. 644, pp. 1661–1672, 2009.
- [8] L. Li, C.-Y. Li, Y.-K. Tan, and C.-H. Chen, "Stratospheric sudden warming impacts on the weather climate in China and its role in the influences of ENSO," *Chinese Journal of Geophysics*, vol. 53, no. 7, pp. 1529–1542, 2010 (Chinese).
- [9] S. Deng, Y. Chen, T. Luo, Y. Bi, and H. Zhou, "The possible influence of stratospheric sudden warming on East Asian weather," *Advances in Atmospheric Sciences*, vol. 25, no. 5, pp. 841–846, 2008.
- [10] D. M. Mitchell, L. J. Gray, J. Anstey, M. P. Baldwin, and A. J. Charlton-Perez, "The influence of stratospheric vortex displacements and splits on surface climate," *Journal of Climate*, vol. 26, no. 8, pp. 2668–2682, 2013.
- [11] L. Wang and W. Chen, "Downward Arctic Oscillation signal associated with moderate weak stratospheric polar vortex and the cold December 2009," *Geophysical Research Letters*, vol. 37, no. 9, 2010.
- [12] M. Cai and C.-S. Shin, "A total flow perspective of atmospheric mass and angular momentum circulations: boreal winter mean state," *Journal of the Atmospheric Sciences*, vol. 71, no. 6, pp. 2244–2263, 2014.
- [13] Y. Yu, M. Cai, R. Ren, and H. M. van den Dool, "Relationship between warm airmass transport into the upper polar atmosphere and cold air outbreaks in winter," *Journal of the Atmospheric Sciences*, vol. 72, no. 1, pp. 349–368, 2015.
- [14] J. C. L. Chan and C. Li, "The East Asia winter monsoon," in *East Asian Monsoon*, chapter 2, pp. 54–106, World Scientific, 2004, (Chinese).

- [15] R. Huang, J. Chen, L. Wang, and Z. Lin, "Characteristics, processes, and causes of the spatio-temporal variabilities of the East Asian monsoon system," *Advances in Atmospheric Sciences*, vol. 29, no. 5, pp. 910–942, 2012.
- [16] D.-Y. Gong, S.-W. Wang, and J.-H. Zhu, "East Asian winter monsoon and Arctic Oscillation," *Geophysical Research Letters*, vol. 28, no. 10, pp. 2073–2076, 2001.
- [17] B. Wu and J. Wang, "Possible impacts of winter Arctic Oscillation on Siberian High, the East Asian winter monsoon and sea-ice extent," *Advances in Atmospheric Sciences*, vol. 19, no. 2, pp. 297–320, 2002.
- [18] C. He and J. H. He, "Relation between arctic oscillation and North China air temperature in winter," *Journal of Nanjing Institute of Meteorology*, vol. 26, no. 1, pp. 1–7, 2003 (Chinese).
- [19] J. H. Ju, J. Z. Ren, and J. M. Lv, "Effect of interdecadal variation of arctic oscillation on temperature increasing in north of east Asian winter," *Plateau Meteorology*, vol. 23, no. 4, pp. 429–434, 2004 (Chinese).
- [20] J. P. Li, Y. Q. Yu, and W. Chen, "Physical significance of the arctic oscillation and its relationship with east Asian atmospheric circulation," in *Effect of Air-Sea Interaction on Climate Change in China*, pp. 169–176, Meteorological Press, Beijing, China, 2005, (Chinese).
- [21] L. Wang, W. Chen, S. Fong et al., "The seasonal March of the north pacific oscillation and its association with the interannual variations of China's climate in boreal winter and spring," *Chinese Journal of Atmospheric Science*, vol. 35, no. 3, pp. 393–402, 2011 (Chinese).
- [22] L. Wang and W. Chen, "An intensity index for the East Asian winter monsoon," *Journal of Climate*, vol. 27, no. 6, pp. 2361–2374, 2014.
- [23] D. W. J. Thompson and J. M. Wallace, "The Arctic oscillation signature in the wintertime geopotential height and temperature fields," *Geophysical Research Letters*, vol. 25, no. 9, pp. 1297–1300, 1998.
- [24] D. W. J. Thompson and J. M. Wallace, "Annular modes in the extratropical circulation. Part I: month-to-month variability," *Journal of Climate*, vol. 13, no. 5, pp. 1000–1016, 2000.
- [25] K. Kodera and Y. Kuroda, "Tropospheric and stratospheric aspects of the Arctic Oscillation," *Geophysical Research Letters*, vol. 27, no. 20, pp. 3349–3352, 2000.
- [26] M. P. Baldwin, D. W. J. Thompson, E. F. Shuckburgh, W. A. Norton, and N. P. Gillett, "Weather from the stratosphere?" *Science*, vol. 301, no. 5631, pp. 317–319, 2003.
- [27] B. Christiansen, "Downward propagation and statistical forecast of the near-surface weather," *Journal of Geophysical Research D: Atmospheres*, vol. 110, no. 14, pp. 1–10, 2005.
- [28] W. Chen, K. Wei, L. Wang, and Q. Zhou, "Climate variability and mechanisms of the East Asian winter monsoon and the impact from the stratosphere," *Chinese Journal of Atmospheric Sciences*, vol. 37, no. 2, pp. 425–438, 2013 (Chinese).
- [29] W. Chen and K. Wei, "Anomalous propagation of the quasi-stationary planetary waves in the atmosphere and its roles in the impact of stratosphere on the east Asian winter climat," *Advances in Earth Science*, vol. 24, no. 3, pp. 272–285, 2009 (Chinese).
- [30] W. Chen, M. Takahashi, and H. F. Graf, "Interannual variations of stationary planetary wave activity in the northern winter troposphere and stratosphere and their relations to NAM and SST," *Journal of Geophysical Research: Atmospheres*, vol. 108, no. D24, 2003.
- [31] W. Chen, S. Yang, and R.-H. Huang, "Relationship between stationary planetary wave activity and the East Asian winter monsoon," *Journal of Geophysical Research D: Atmospheres*, vol. 110, no. 14, 2005.
- [32] L. X. Chen, *East Asian Monsoon*, Meteorological Press, 1991.
- [33] L. Wang, W. Chen, W. Zhou, and R. Huang, "Interannual variations of East Asian trough axis at 500 hPa and its association with the East Asian winter monsoon pathway," *Journal of Climate*, vol. 22, no. 3, pp. 600–614, 2009.
- [34] W. Chen and R. H. Huang, "The propagation and transport effect of planetary waves in the Northern Hemisphere winter," *Advances in Atmospheric Sciences*, vol. 19, no. 6, pp. 1113–1126, 2002.
- [35] B. Christiansen, "Downward propagation of zonal mean zonal wind anomalies from the stratosphere to the troposphere: Model and reanalysis," *Journal of Geophysical Research D: Atmospheres*, vol. 106, no. 21, pp. 27307–27322, 2001.
- [36] R. X. Black, "Stratospheric forcing of surface climate in the Arctic oscillation," *Journal of Climate*, vol. 15, no. 3, pp. 268–277, 2002.
- [37] W. Chen, S. Yang, and R.-H. Huang, "Relationship between stationary planetary wave activity and the East Asian winter monsoon," *Journal of Geophysical Research D: Atmospheres*, vol. 110, no. D14, 2005.